ETH
Eidgenössische Technische Hochschule Zürich
Swiss Federal Institute of Technology Zurich

FNSNF
Fonds national suisse
Schweizerischer Nationalfonds
Fondo nazionale svizzero
Swiss National Science Foundation

Broadband imaging of anisotropy and composition in the Earth's mantle

Ludwig Auer

Institute of Geophysics – ETH Zürich

Committee: Domenico Giardini, Philippe Lognonné ,
Lapo Boschi, Tarje Nissen-Meyer

March 14th 2016

(1) Introduction: Tomography approach

Why broadband seismic information?

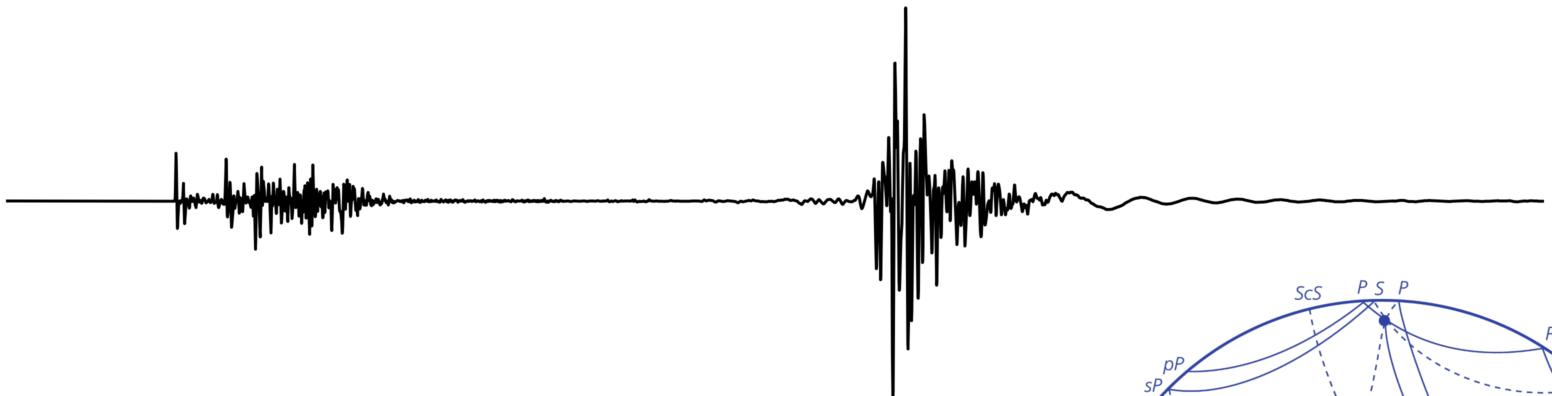

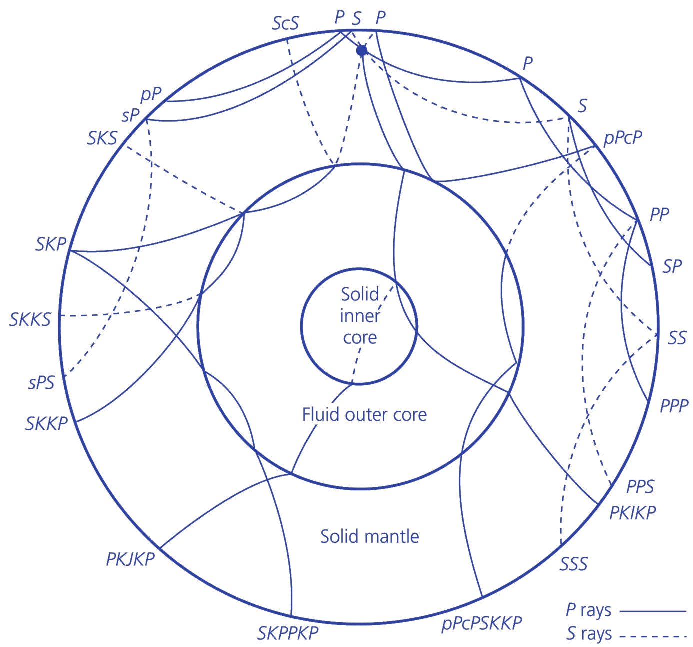

(1) Introduction: Tomography approach

Why broadband seismic information?

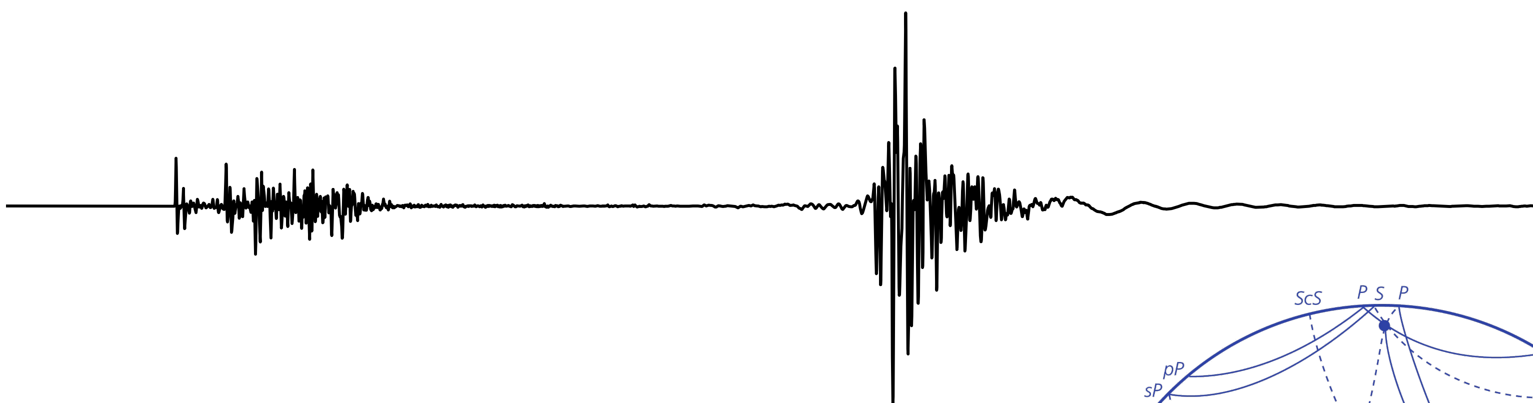

- Different time-frequency portions of the seismic record sense different regions

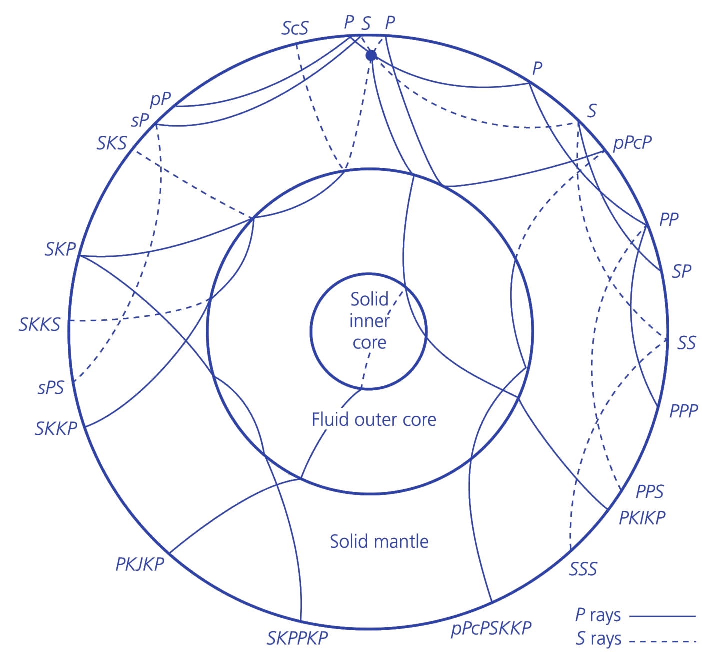

(1) Introduction: Tomography approach

Why broadband seismic information?

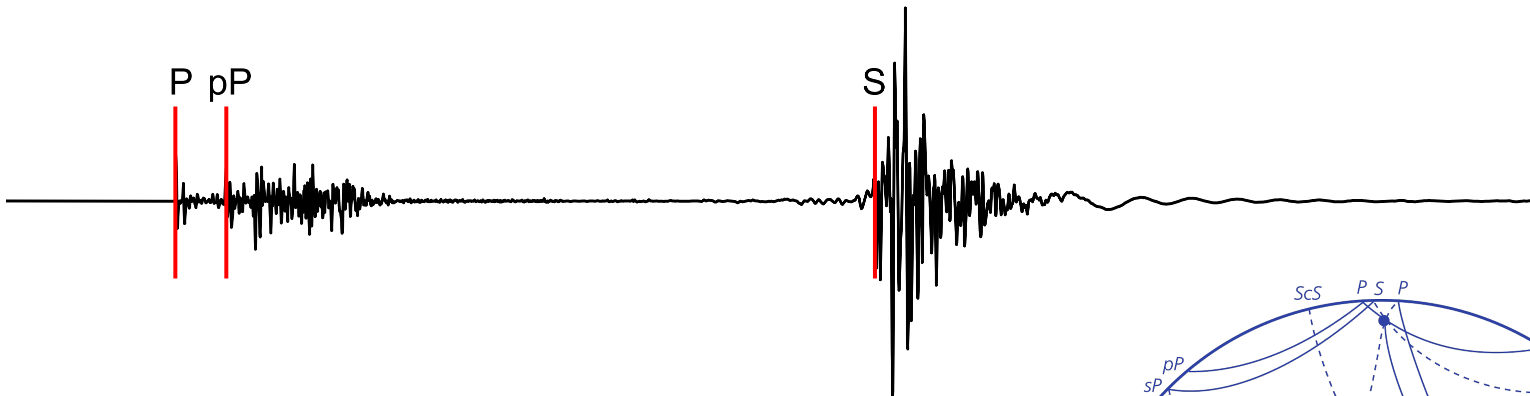

- Different time-frequency portions of the seismic record sense different regions

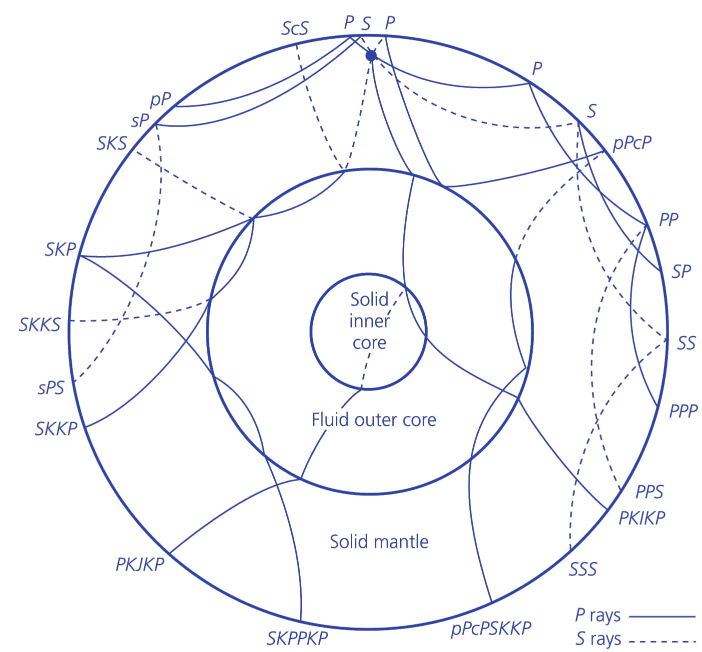

(1) Introduction: Tomography approach

Why broadband seismic information?

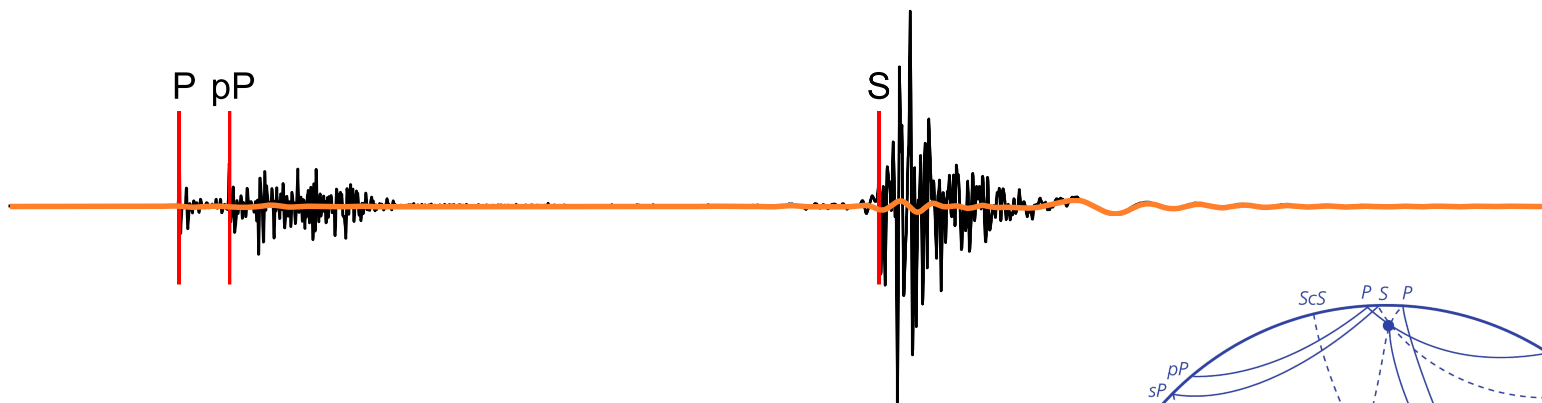

- Different time-frequency portions of the seismic record sense different regions

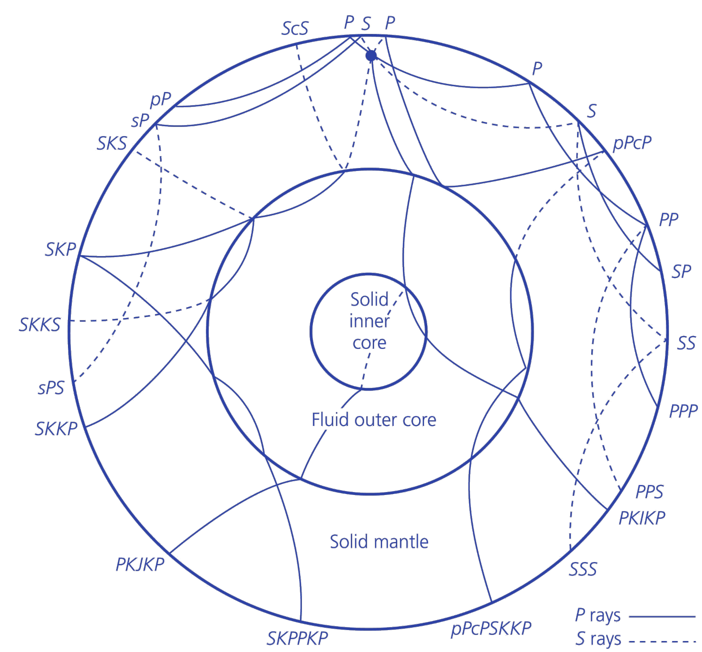

(1) Introduction: Tomography approach

Why broadband seismic information?

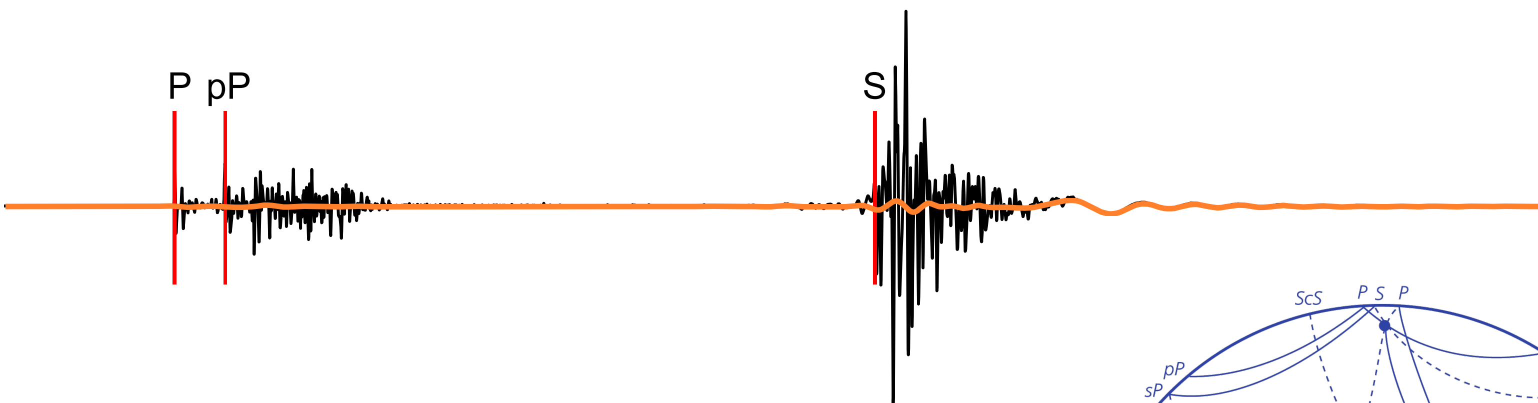

- Different time-frequency portions of the seismic record sense different regions
- Developing meaningful whole-mantle demands using high-frequency and lower-frequency information together

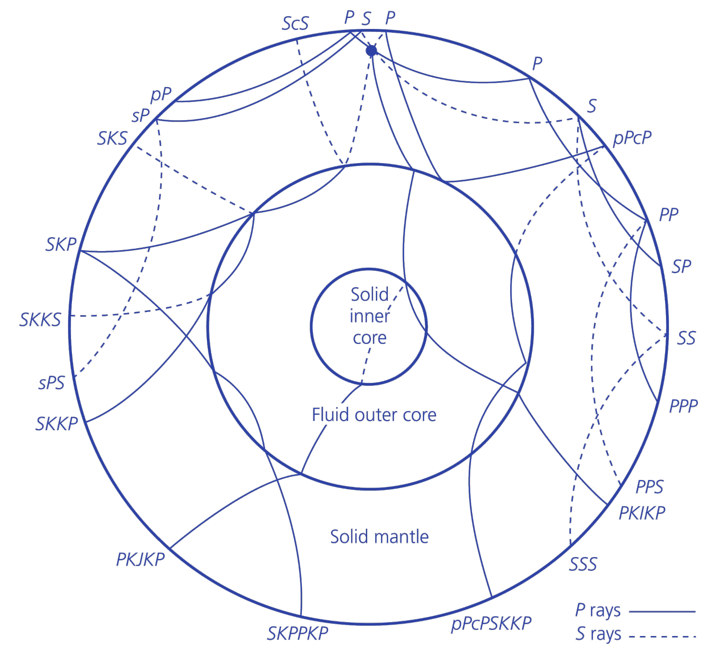

(1) Introduction: Tomography approach

Imaging multi-scale structure and dynamics

Global scale

Ray theoretical global model S40RTS, *(Ritsema 2011)*

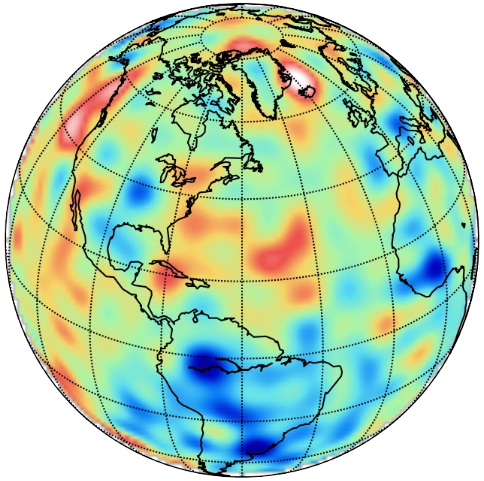

Approximate theory and 1D starting models

Regional scale

Adjoint tomography of Europe and the Middle East *(Fichtner 2012)*

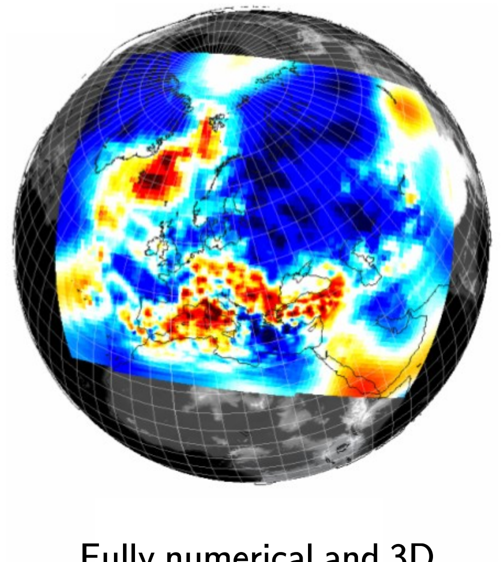

Fully numerical and 3D background models

(1) Introduction: Tomography approach

Imaging multi-scale structure and dynamics

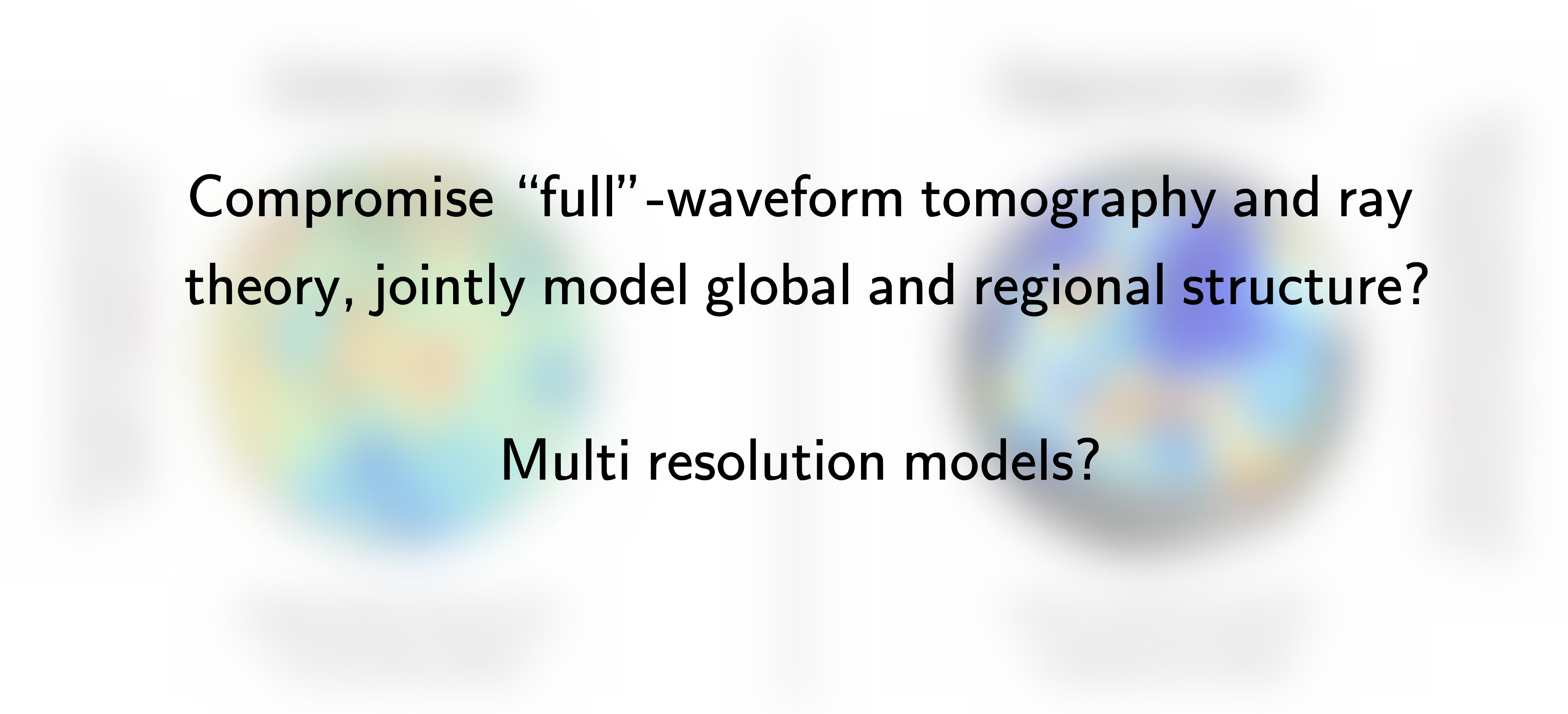

Compromise "full"-waveform tomography and ray theory, jointly model global and regional structure?

Multi resolution models?

(1) Introduction: Earth's 3D structure

SH model comparison (isotropic v_S)

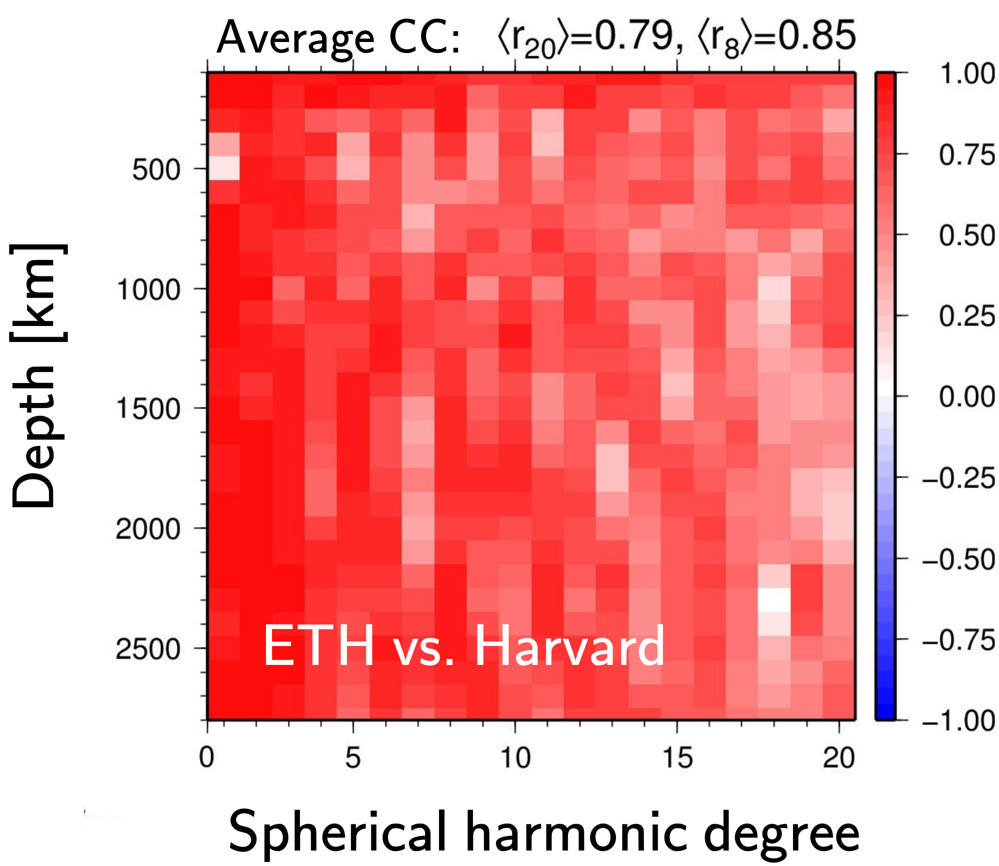

- Isotropic tomographic models correlate well for the SH harmonic degrees
- Model consistency validates modeling algorithms

(1) Introduction: Earth's 3D structure

Model congruency over the years

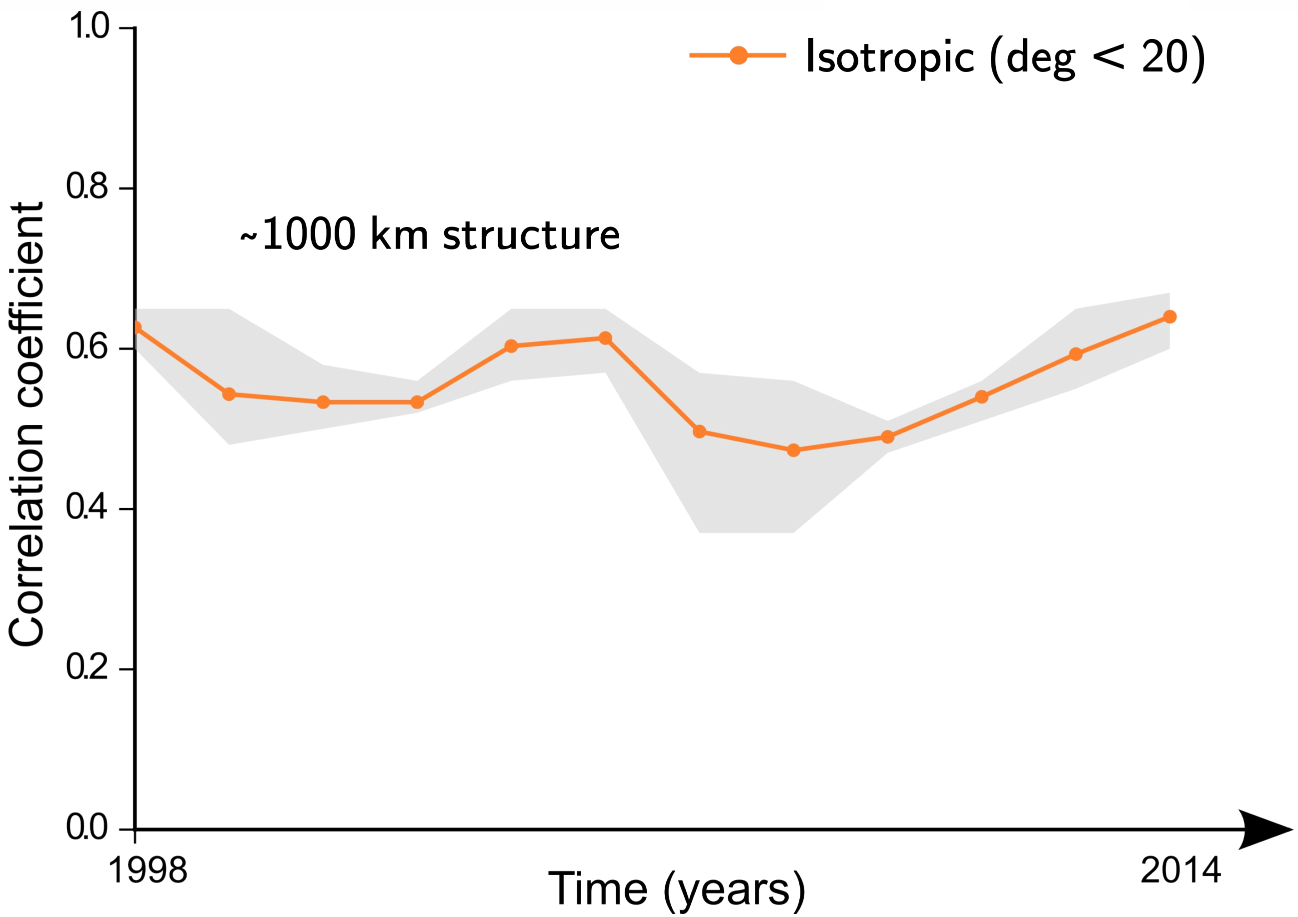

- Models still lack consistency at short spatial wavelength
- For Geodynamically relevant parameterizations situation is even worse
- E.g. anisotropy ...

(1) Introduction: Earth's 3D structure

Model congruency over the years

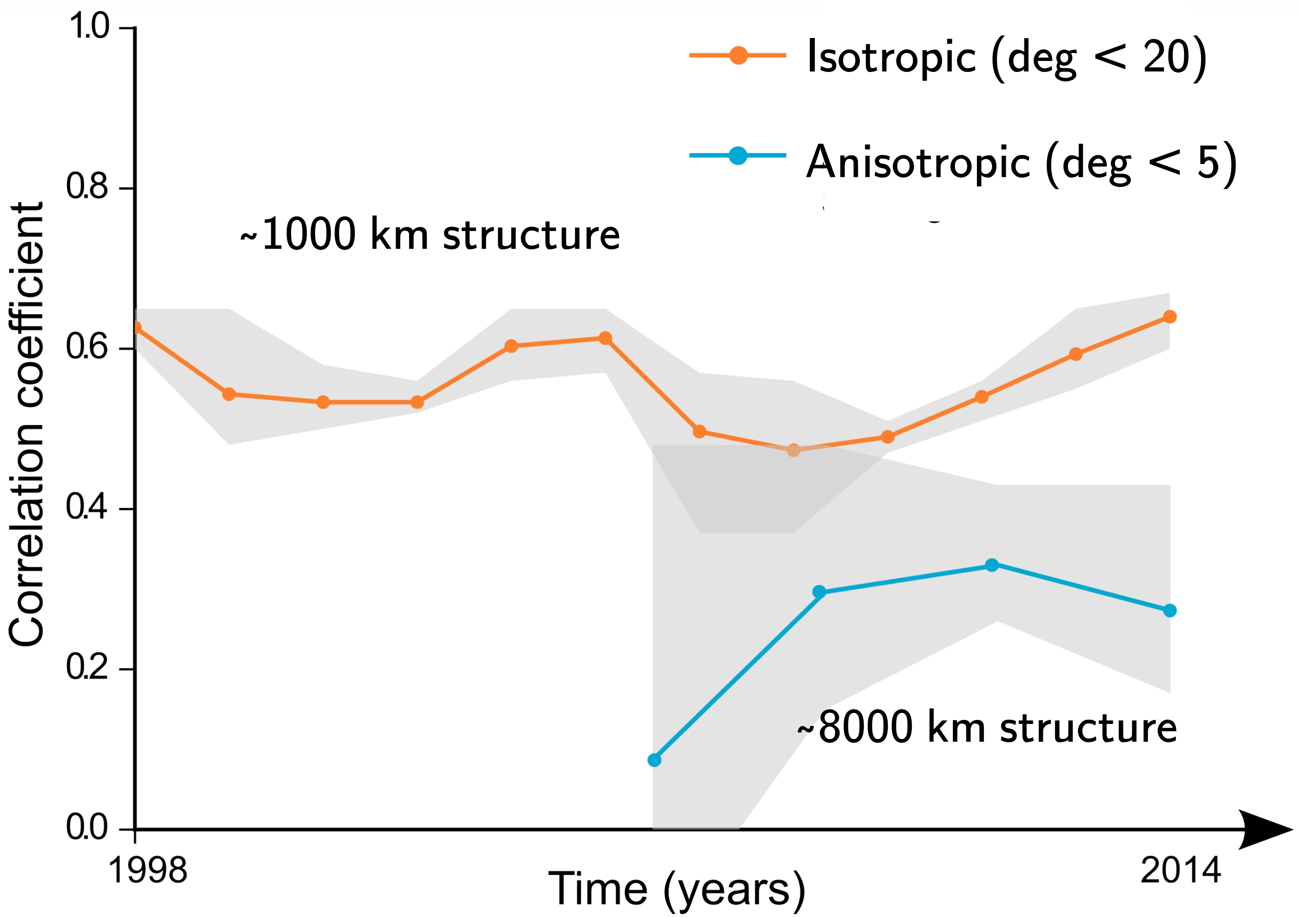

- Models still lack consistency at short spatial wavelength
- For Geodynamically relevant parameterizations situation is even worse
- E.g. anisotropy ...

(1) Introduction: Thesis outline

Chap.

2. Whole-mantle anisotropy from surface and body waves at adaptive resolution *(Auer et al. 2014)*

3. Thermal structure, anisotropy, and dynamics of oceanic boundary layers *(Auer et al. 2015)*

4. Joint inversion of P- and S-wave constraints, hydration of marginal basins *(Tesoniero et al. 2015)*

5. Hybrid full waveform tomography combining global and regional data *(Auer et al. 2016, in preparation)*

(2) Whole-mantle anisotropy

Summary of linear system d=Gm

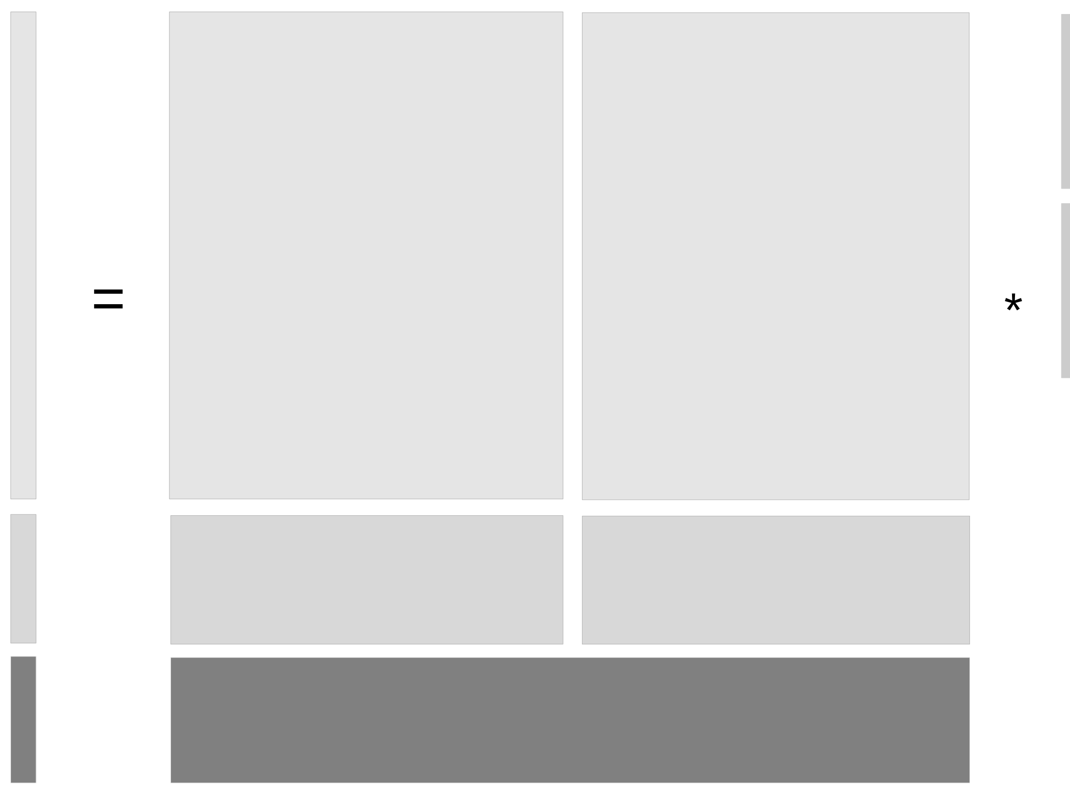

(2) Whole-mantle anisotropy

Summary of linear system d=Gm

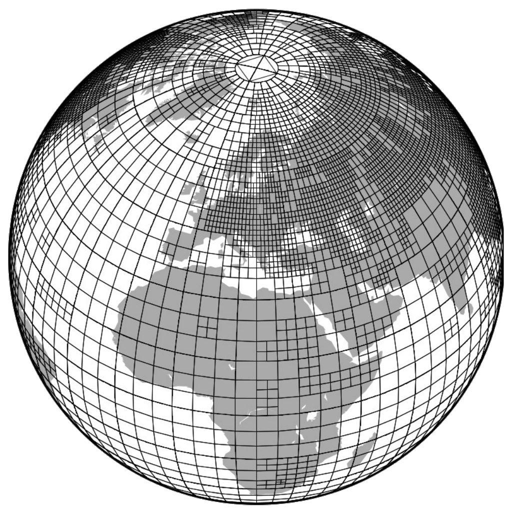

Voxel discretization

- Multi-scale
- Orthogonal
- Simple

(2) Whole-mantle anisotropy

Summary of linear system d=Gm

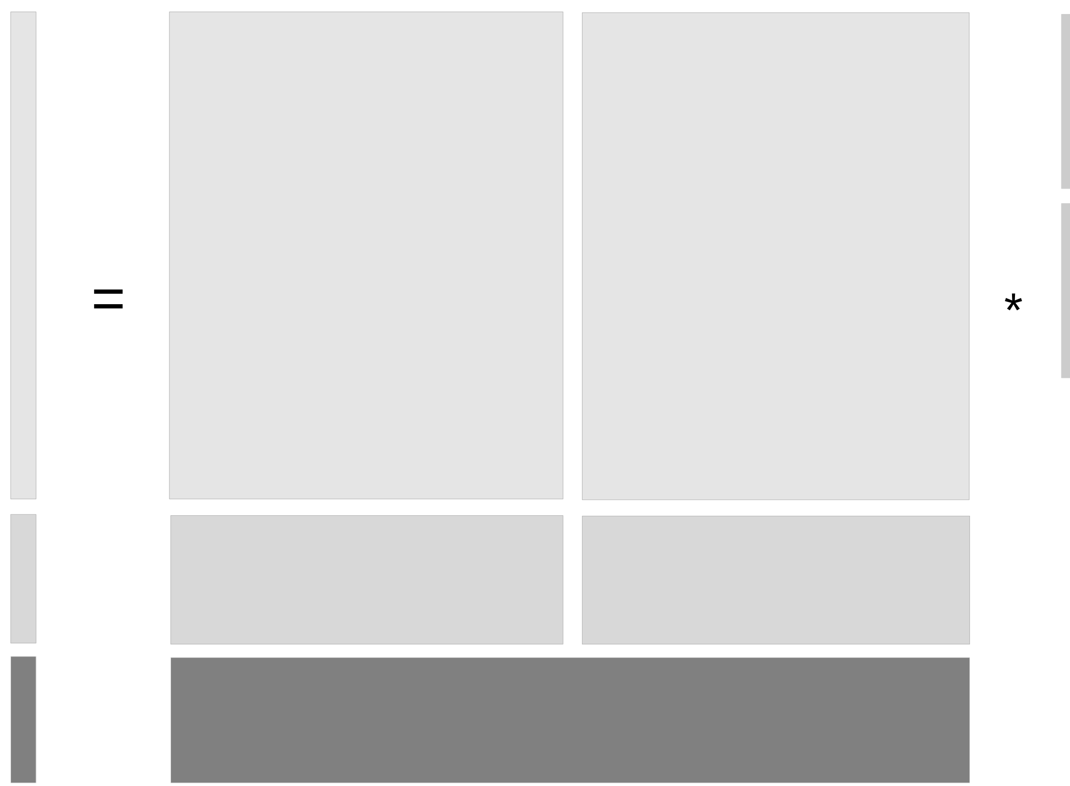

(2) Whole-mantle anisotropy

Summary of linear system d=Gm

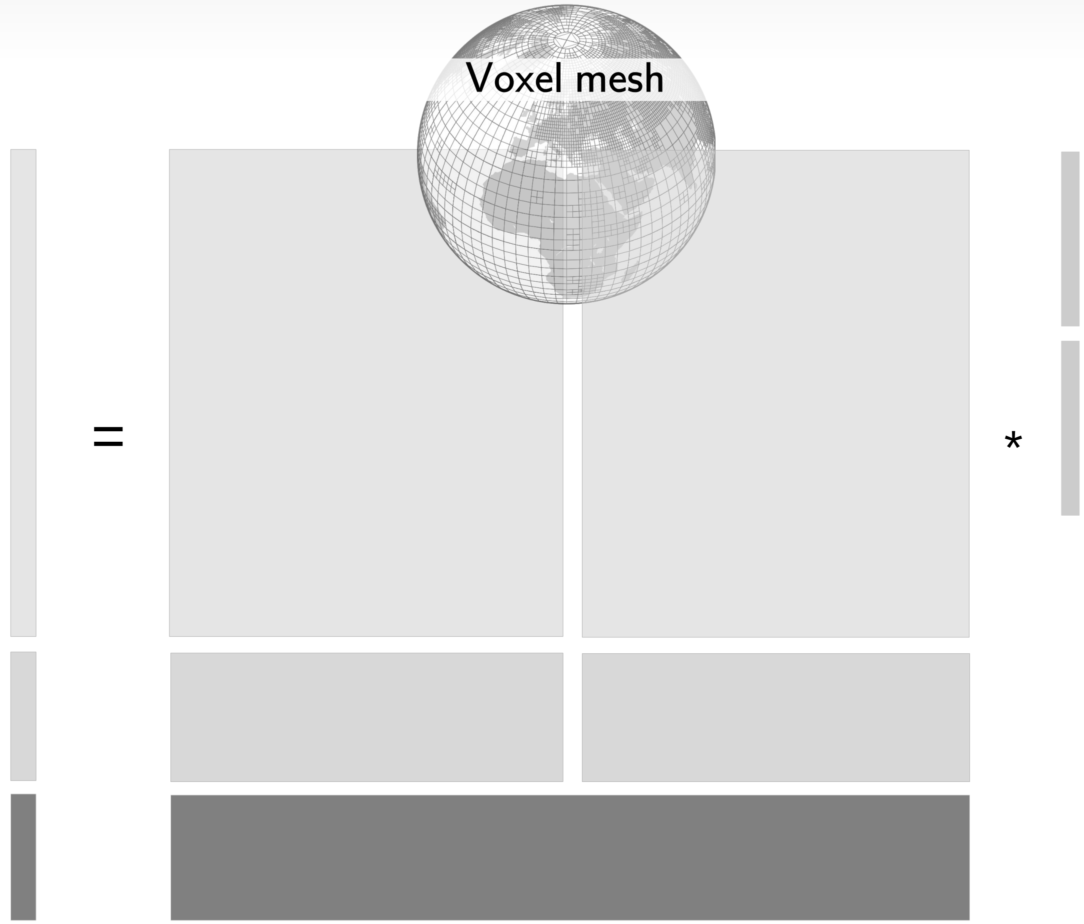

(2) Whole-mantle anisotropy

Summary of linear system d=Gm

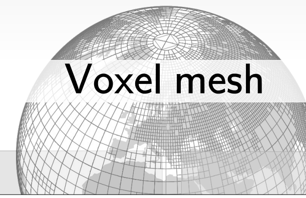

Surface wave dispersion

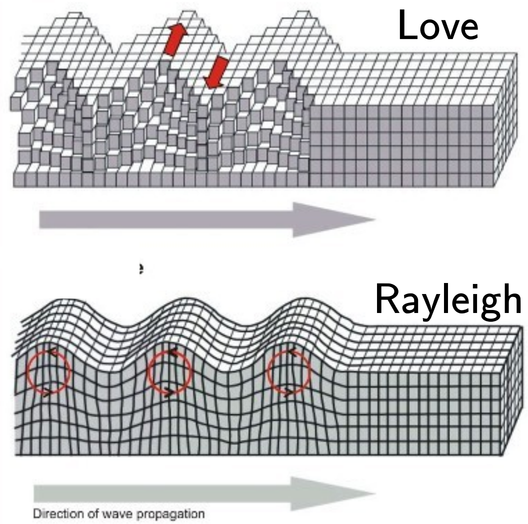

Published fundamental modes and overtones

Overview of surface and body wave datasets

Author	Spheroidal	s. rays	Toroidal	s. rays
Ritsema et al. (2004)	FM 37s-374s	2977971	FM 37s-375s	1605517
	1st OT 37s-274s	391495	1st OT 37s-269s	666057
	2nd OT 37s-365s	343398	2nd OT 37s-151s	242996
	3rd OT 37s-273s	316161	3rd OT 37s-100s	118018
	4th OT 37s-149s	300515	4th OT 37s-69s	54279
	5th OT 37s-114s	240256	5th OT 37s-56s	31106
	6th OT 37s-78s	162507		
Visser et al. (2008)	FM 35s-175s	477776	FM 35s-173s	399792
	1st OT 35s-172s	396431	1st OT 35s-176s	331168
	2nd OT 35s-149s	364140	2nd OT 35s-115s	250315
	3rd OT 35s-87s	253143	3rd OT 35s-78s	154160
	4th OT 35s-61s	159448	4th OT 35s-62s	81592
	5th OT 35s-56s	114037	5th OT 35s-56s	42756
	6th OT 37s-50s	71652		
Ekström (2011)	FM 25s-250s	1022706	FM 25-250s	342261

***Table 1**: Overview of surface wave datasets*

(2) Whole-mantle anisotropy

Summary of linear system d=Gm

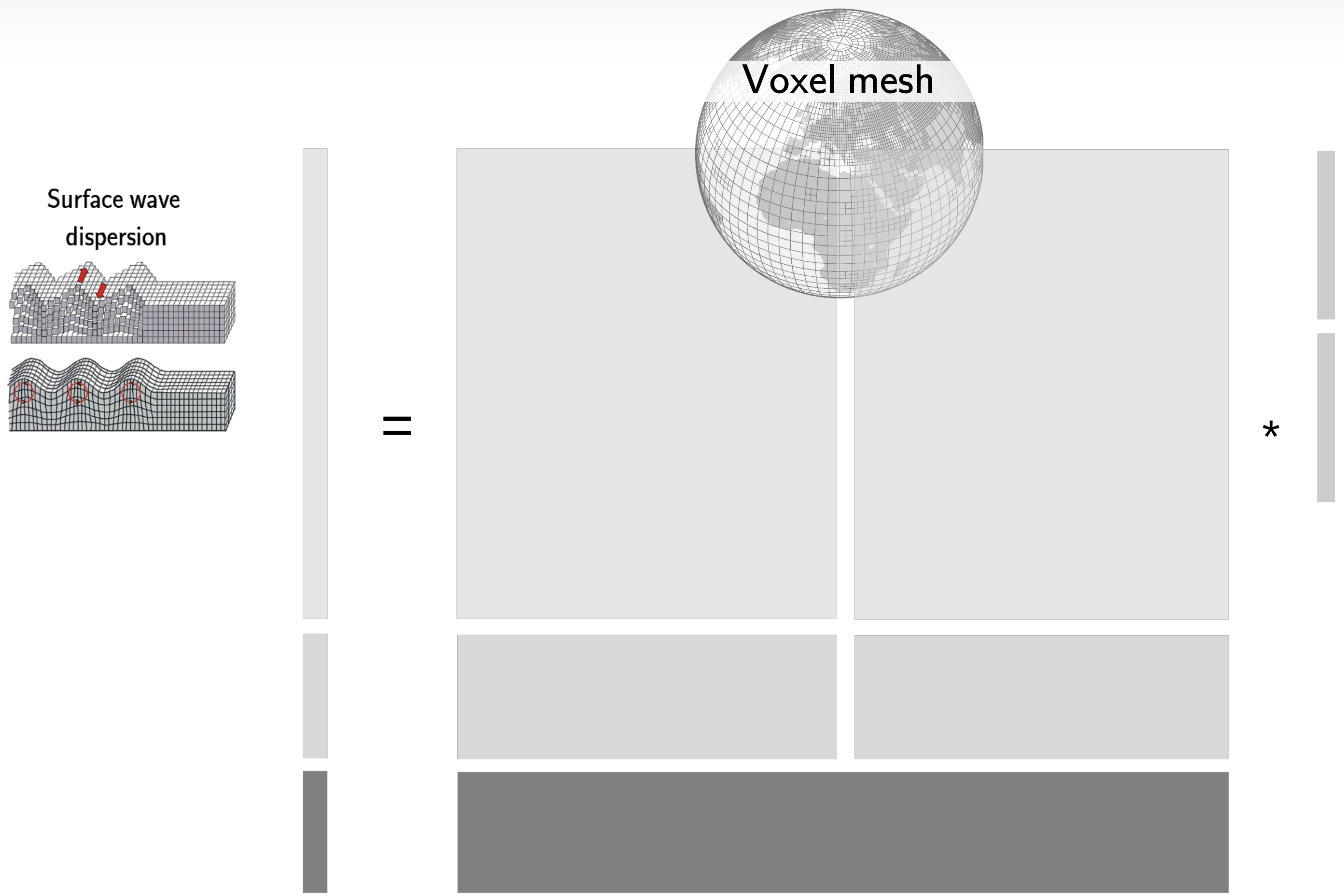

(2) Whole-mantle anisotropy

Summary of linear system d=Gm

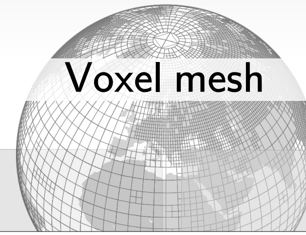

Surface wave dispersion

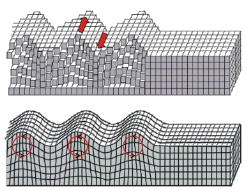

Teleseismic body wave traveltimes

Published cross-correlations
Around major S-wave phases

S,SS,SSS,ScS,ScS2,
ScS3,SKS,SKKS

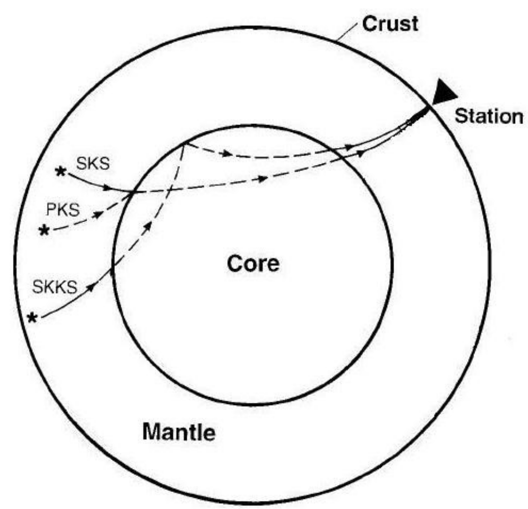

(2) Whole-mantle anisotropy

Summary of linear system d=Gm

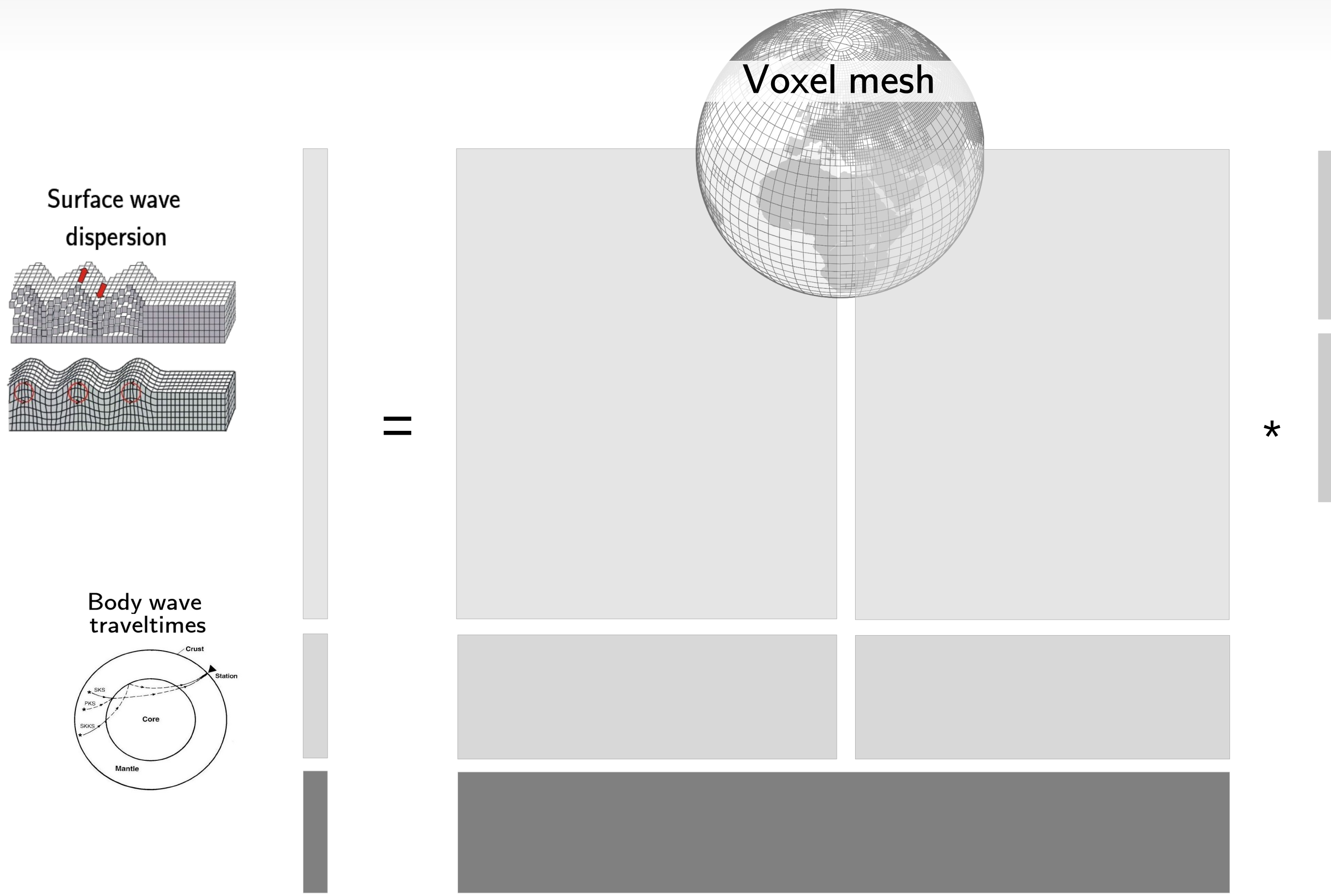

(2) Whole-mantle anisotropy

Summary of linear system d=Gm

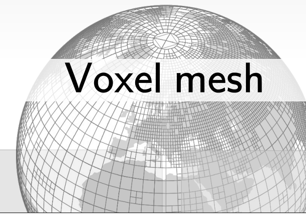

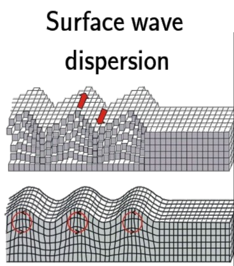

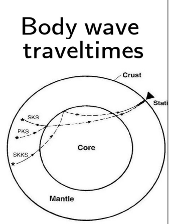

Transversely isotropy parameterization

$$\xi = \left(\frac{v_{SH}}{v_{SV}}\right)^2$$

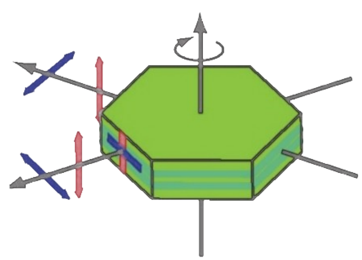

In case of simple A-type **olivine** lattice preferred orientation (**LPO**):

$\xi > 1$ horizontal flow
$\xi < 1$ vertical flow

(2) Whole-mantle anisotropy

Summary of linear system d=Gm

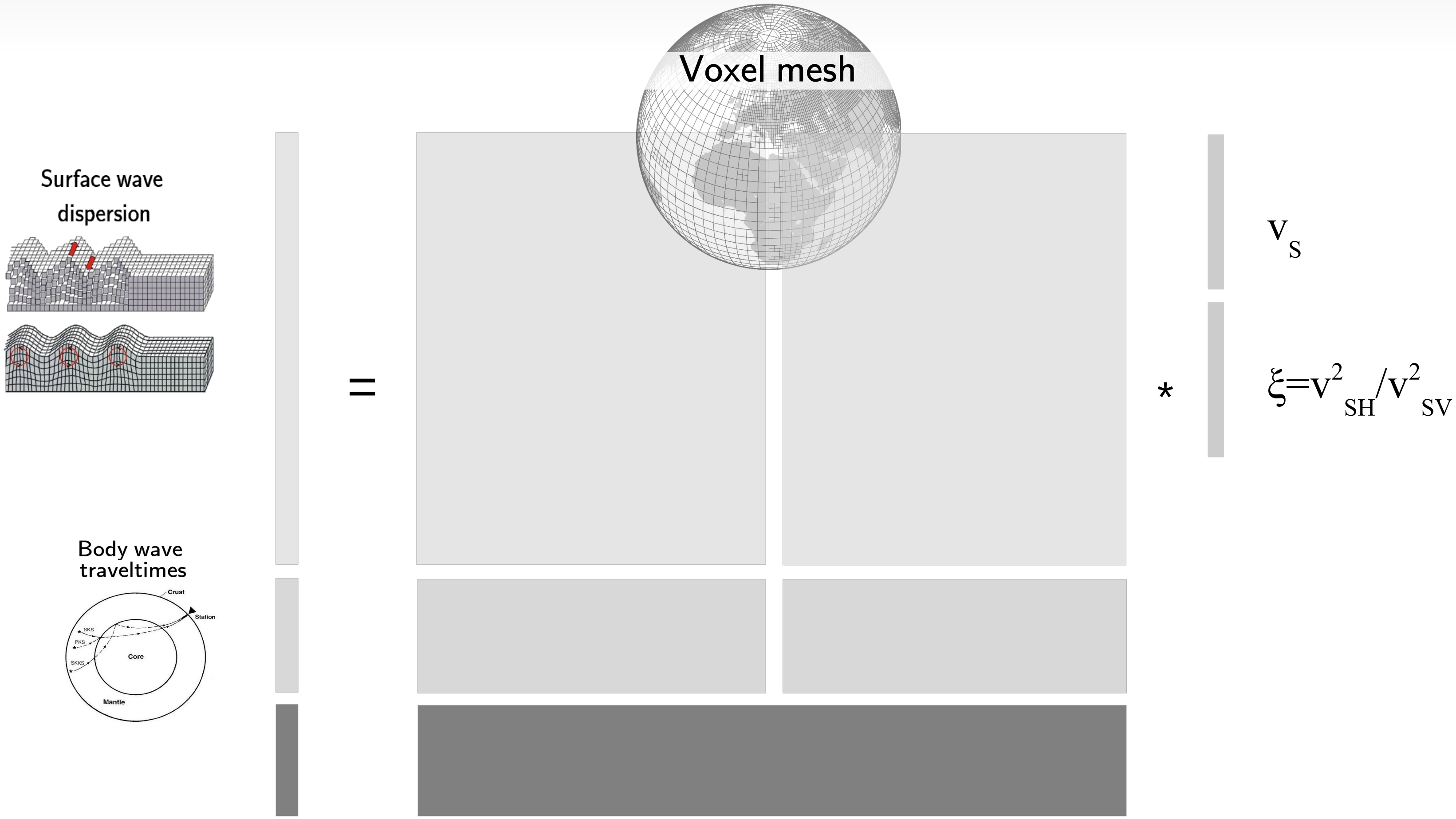

(2) Whole-mantle anisotropy

Summary of linear system d=Gm

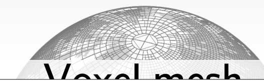

Surface wa
dispersion

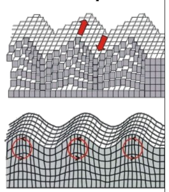

Body w
travelti

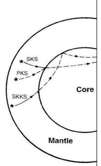

S

$=v^2_{SH}/v^2_{SV}$

Body wave ray theory

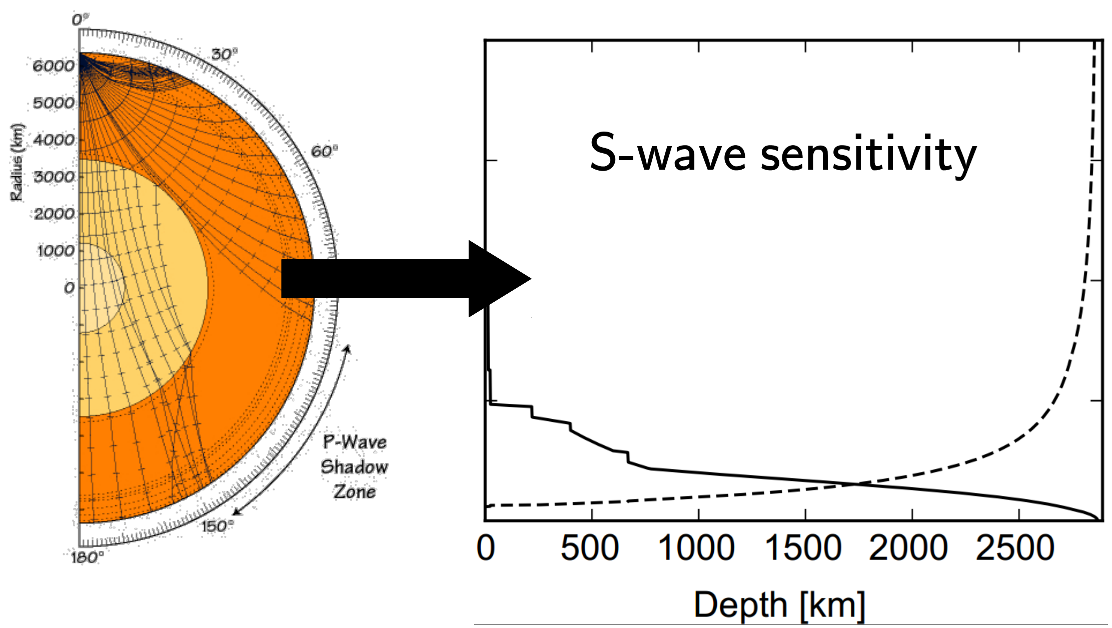

(2) Whole-mantle anisotropy

Summary of linear system d=Gm

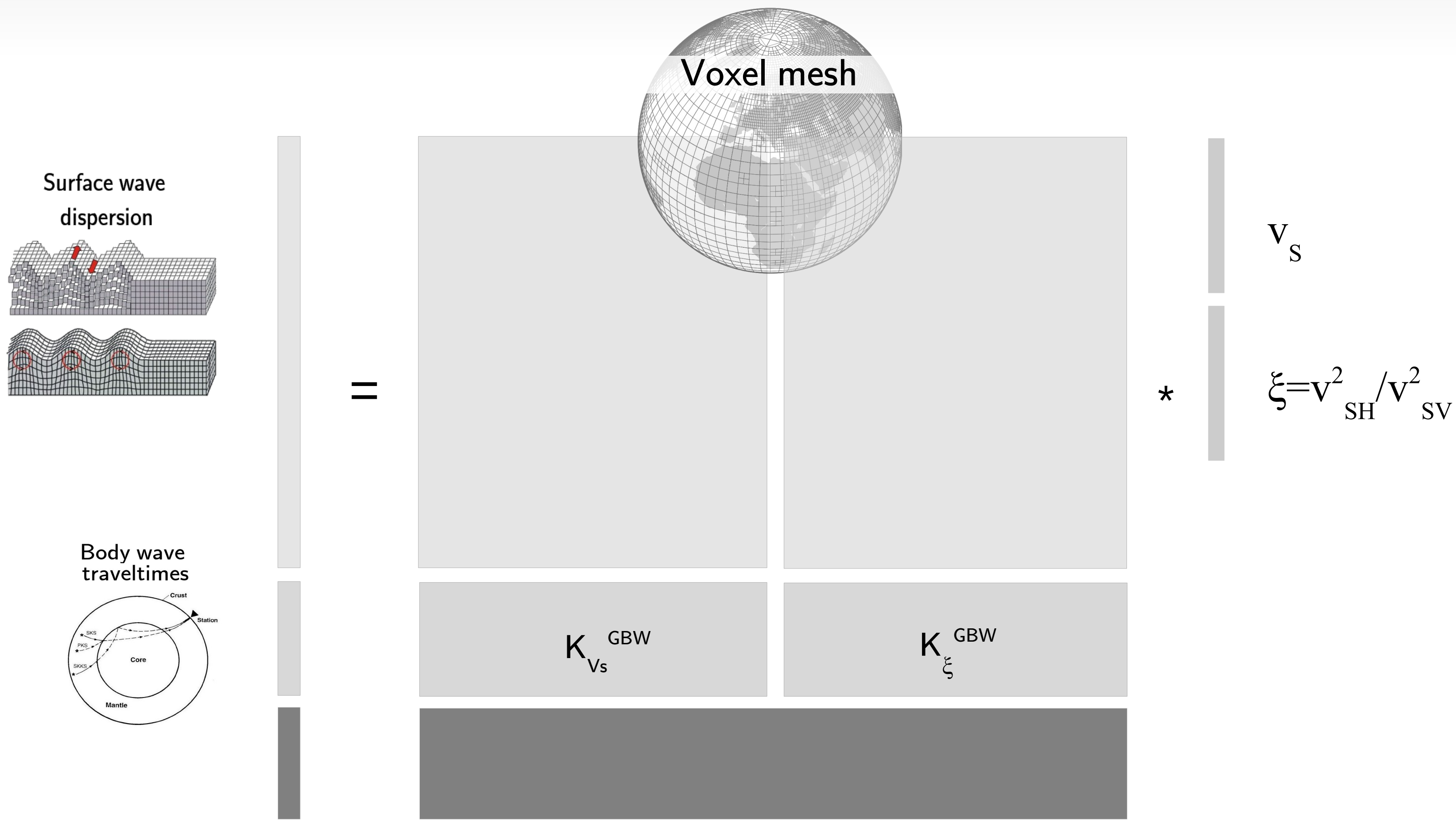

(2) Whole-mantle anisotropy

Summary of linear system d=Gm

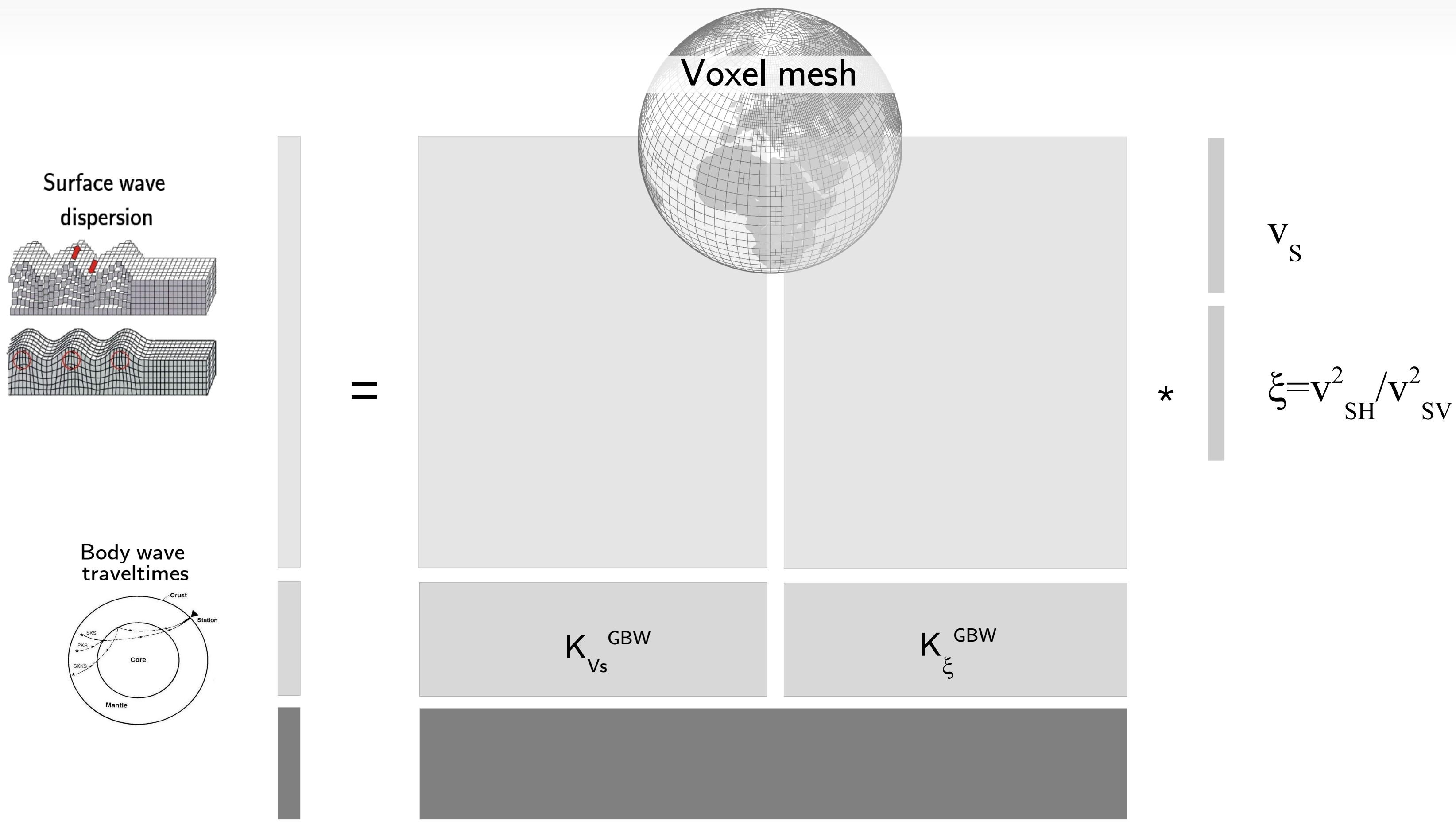

(2) Whole-mantle anisotropy

Summary of linear system d=Gm

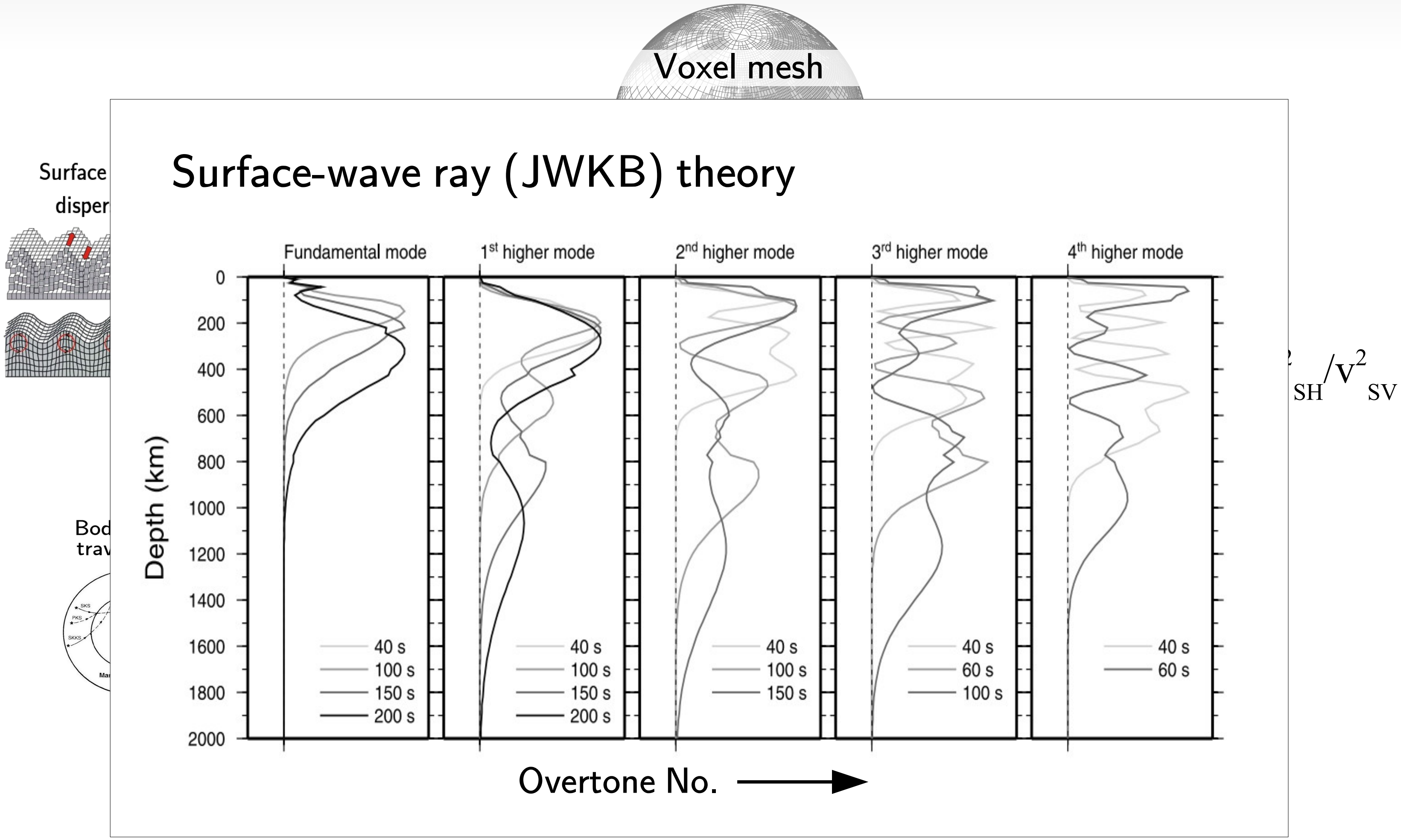

(2) Whole-mantle anisotropy

Summary of linear system d=Gm

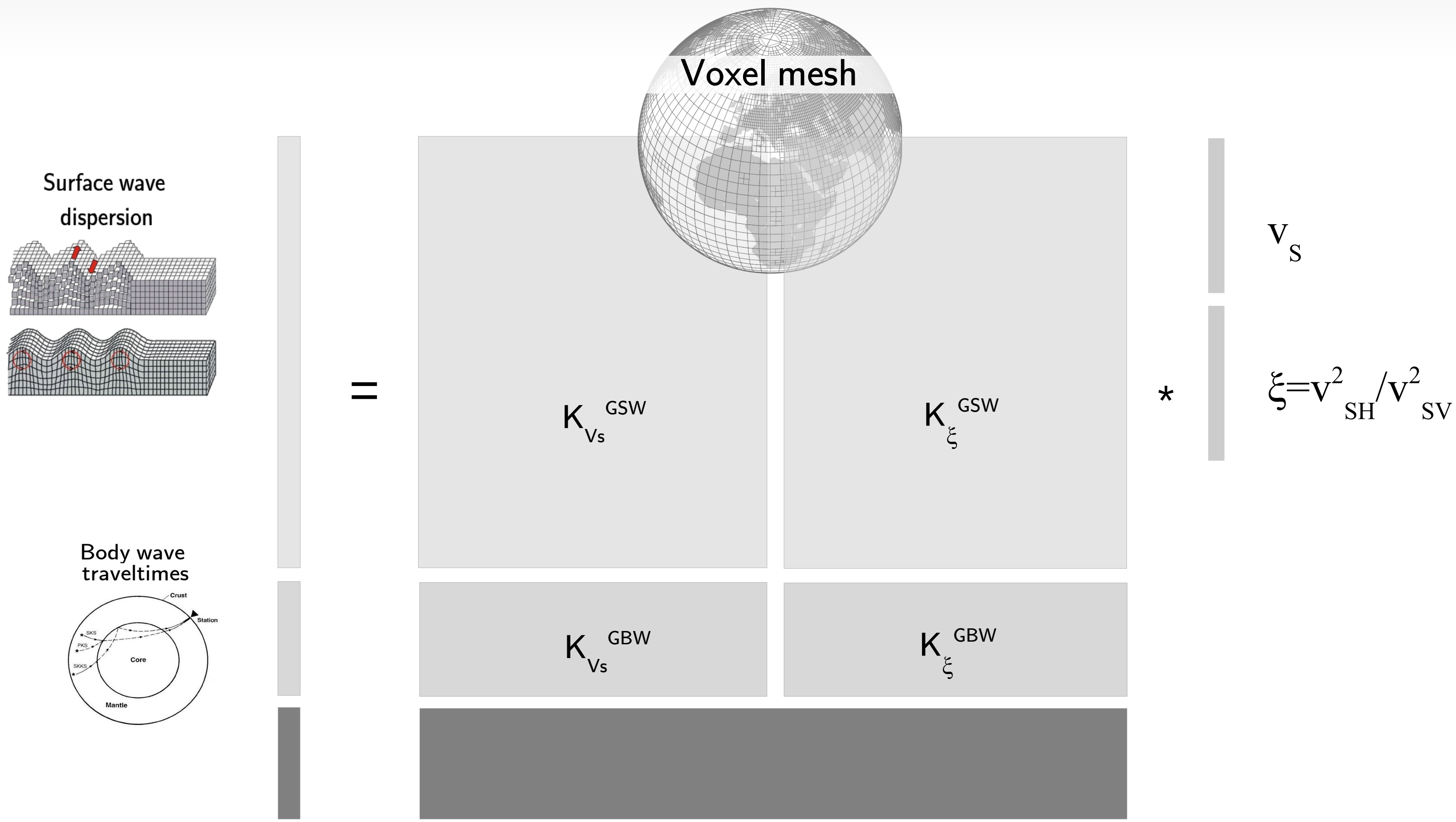

(2) Whole-mantle anisotropy

Summary of linear system d=Gm

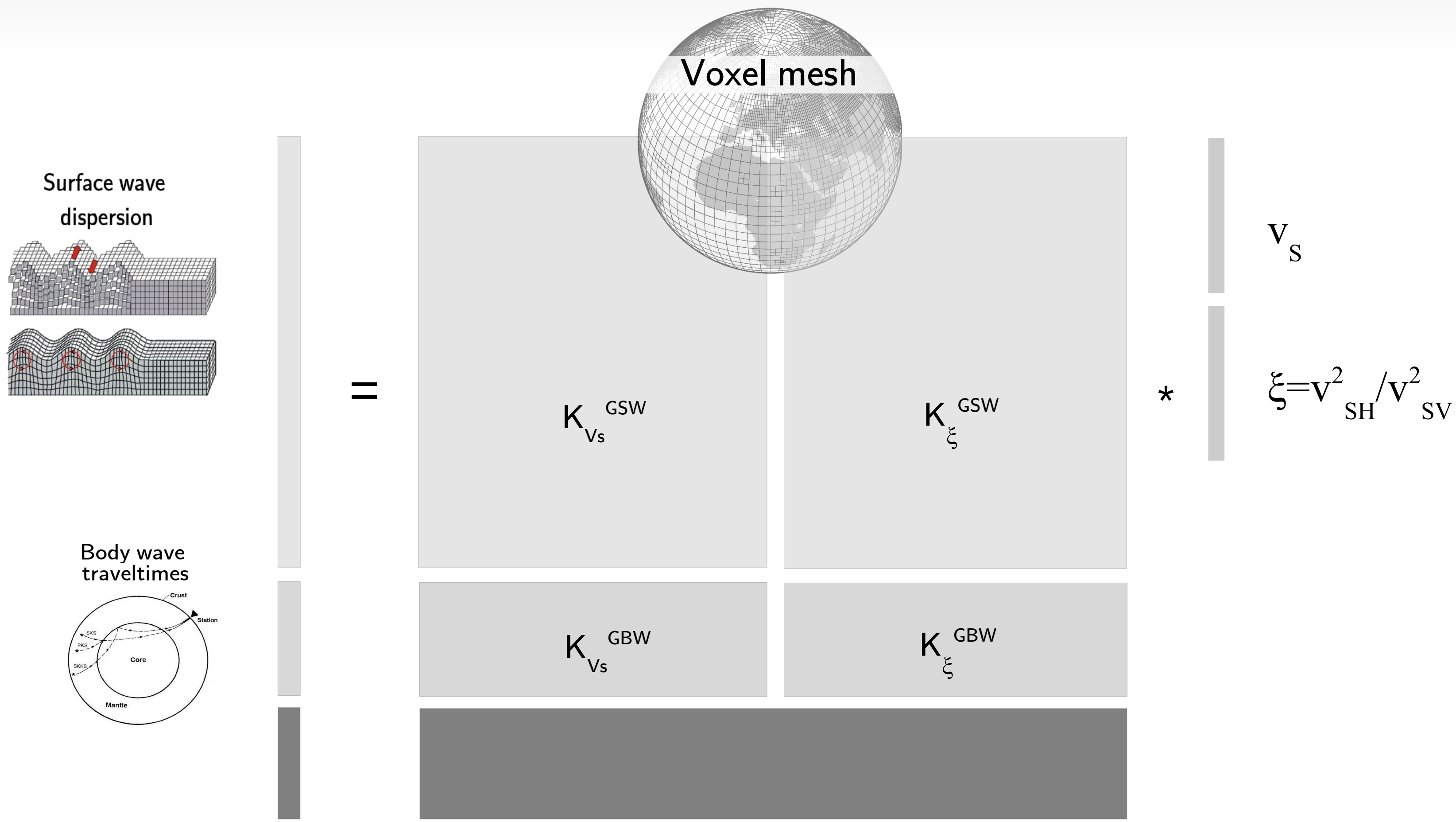

(2) Whole-mantle anisotropy

Summary of linear system d=Gm

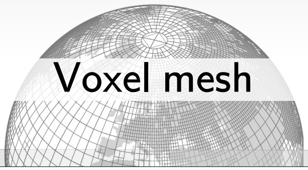

Surface wave dispersion

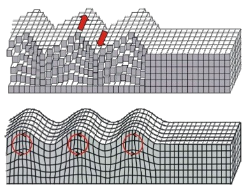

Body wave traveltimes

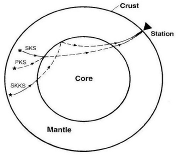

=

Regularization constraints

$$\mathbf{D} = \begin{pmatrix} \dots & 0 & 0 & 0 \\ -1 & 1 & 0 & 0 \\ 0 & -1 & 1 & 0 \\ 0 & 0 & -1 & 1 \\ 0 & 0 & 0 & \dots \end{pmatrix}$$

Penalize model roughness

*

v_S

$\xi = v^2_{SH}/v^2_{SV}$

(2) Whole-mantle anisotropy

Summary of linear system d=Gm

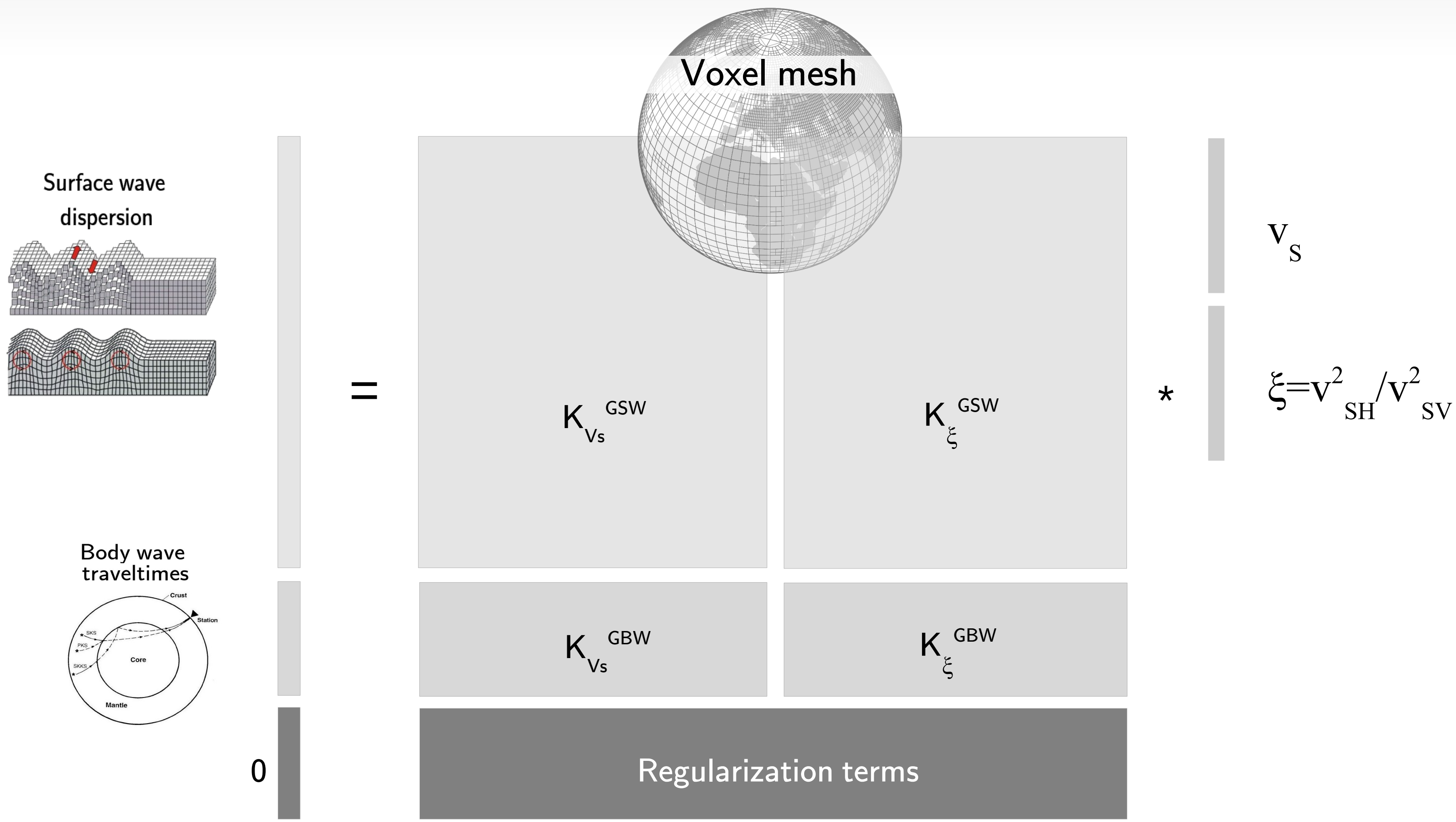

(2) Whole-mantle anisotropy

Solution of the inverse problem: d=Gm

We solve the normal equations ...

$$\delta\mathbf{m} = [\mathbf{G}^T\mathbf{C}_d^{-1}\mathbf{G} + \mathbf{C}_m^{-1}]\mathbf{G}^T\mathbf{C}_d^{-1}\delta\mathbf{d}$$

Using a tailored parallel solver based on PETSc available @ https://github.com/auerl/petscinv

(2) Whole-mantle anisotropy

Savani: a new, global, adaptive resolution model of radial shear-wave anisotropy

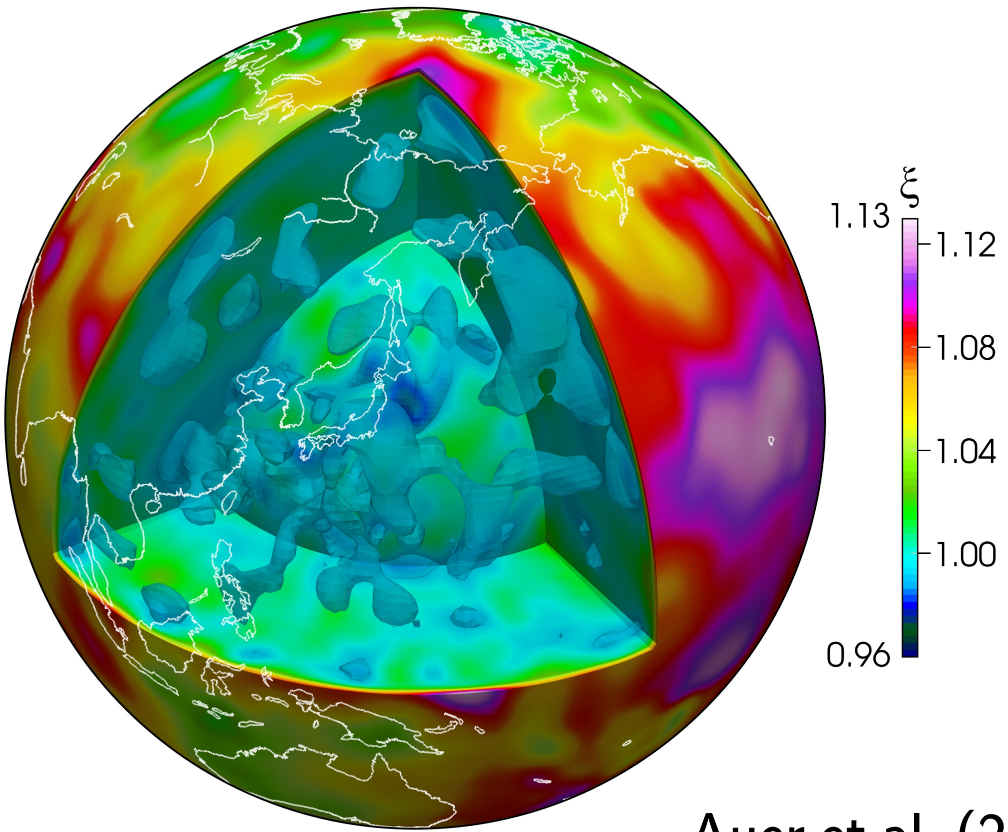

Auer et al. (2014)

(2) Whole-mantle anisotropy

Key features of savani

1) Variable, adaptive-resolution

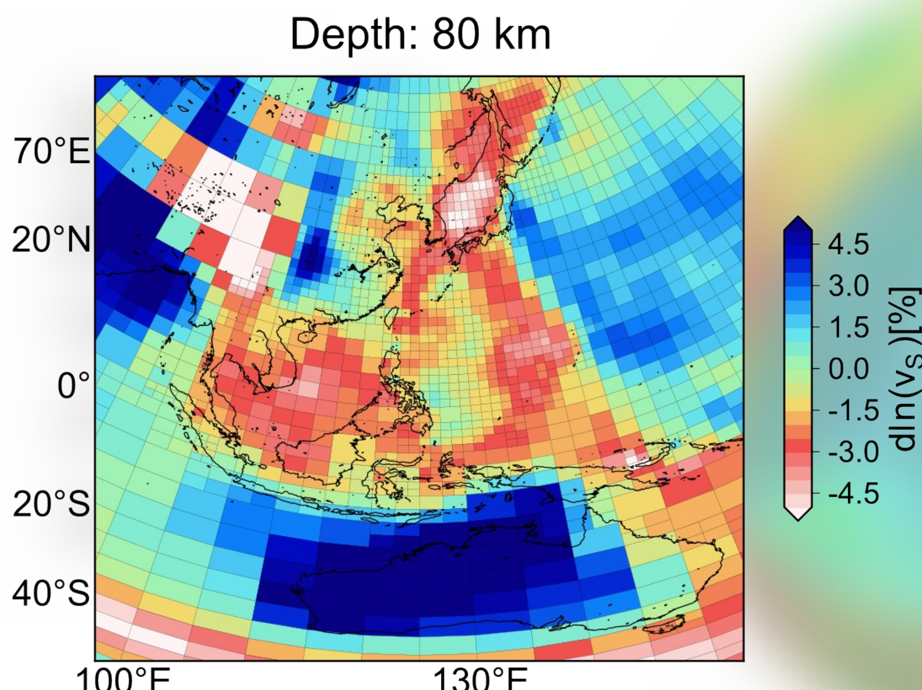

2) Radial anisotropy in the entire mantle

$$\xi = \left(\frac{v_{SH}}{v_{SV}}\right)^2$$

3) Extreme data diversity: Numerous previously published datasets

Download @ http://n.ethz.ch/~auerl

(2) Model comparison, anisotropic

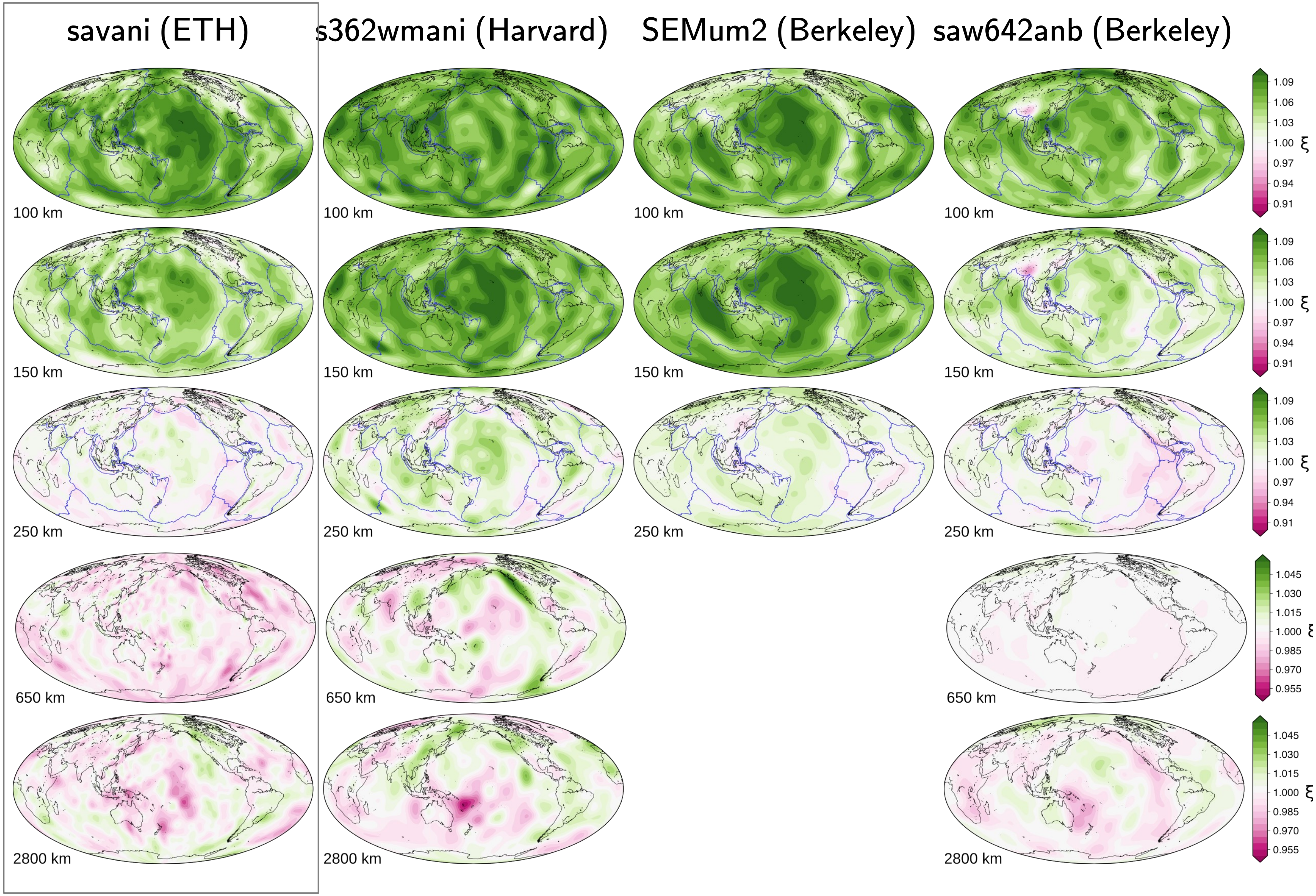

(2) Model comparison, anisotropic

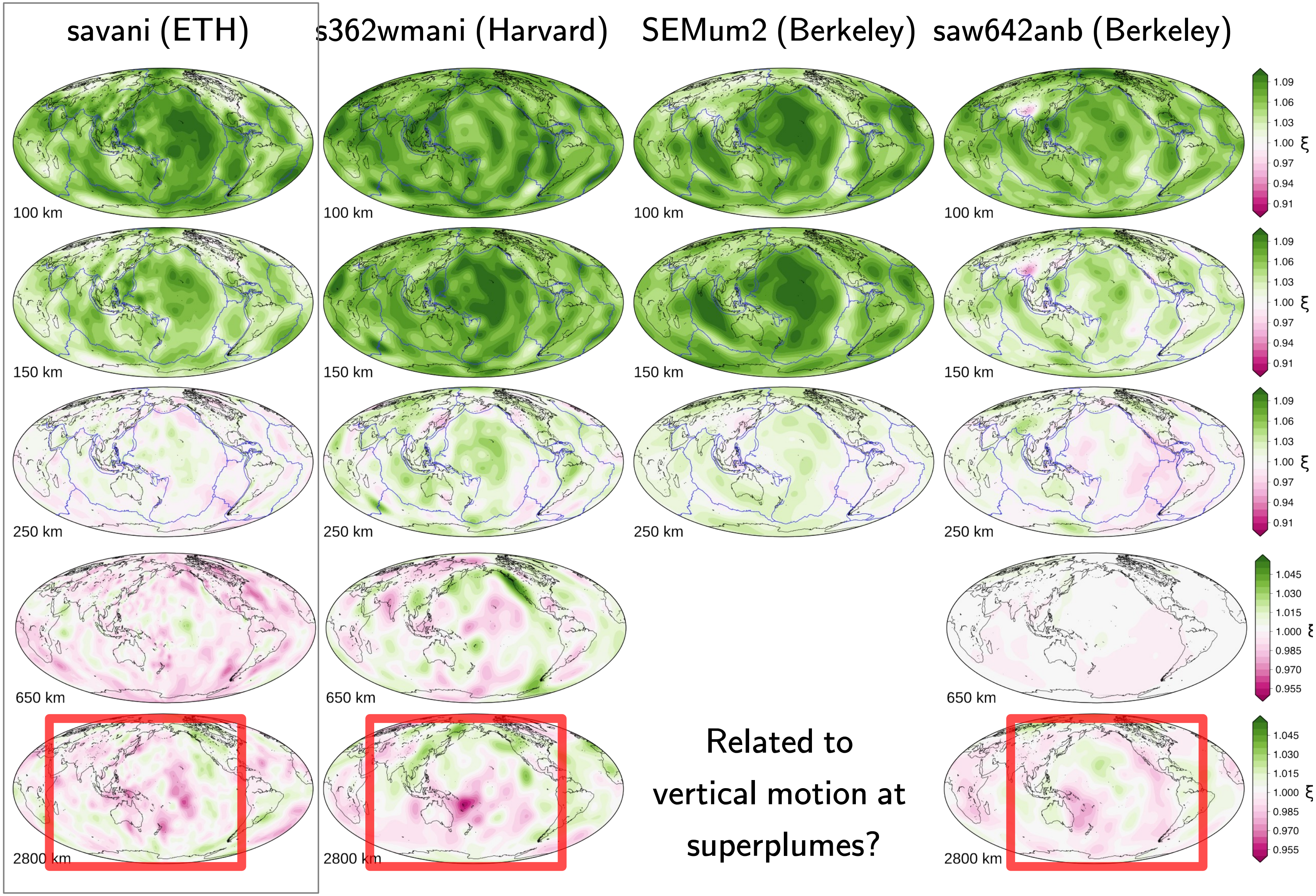

$\xi < 1$

Related to vertical motion at superplumes?

(2) Model comparison, anisotropic

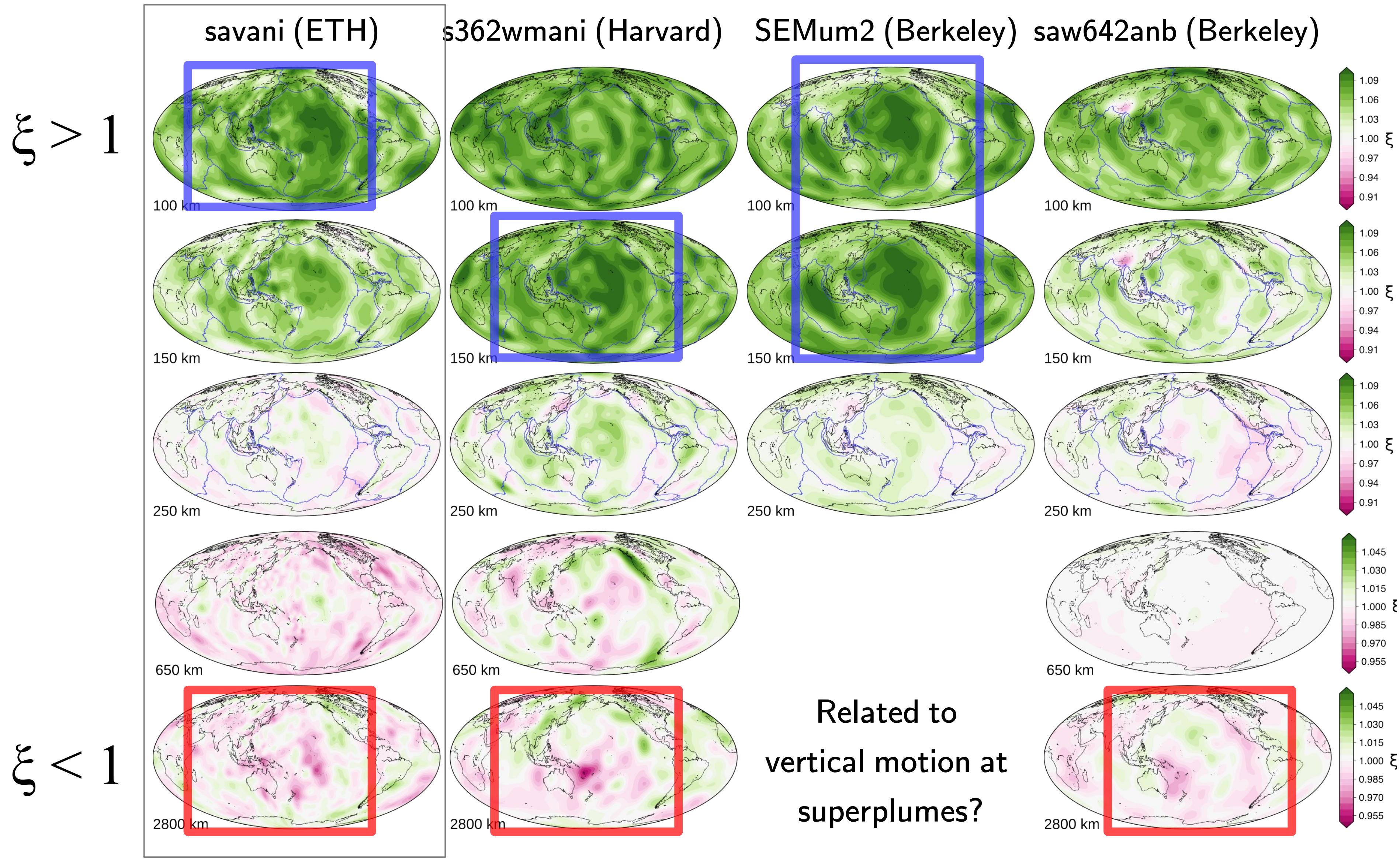

(2) Model comparison, anisotropic

Ocean anisotropy

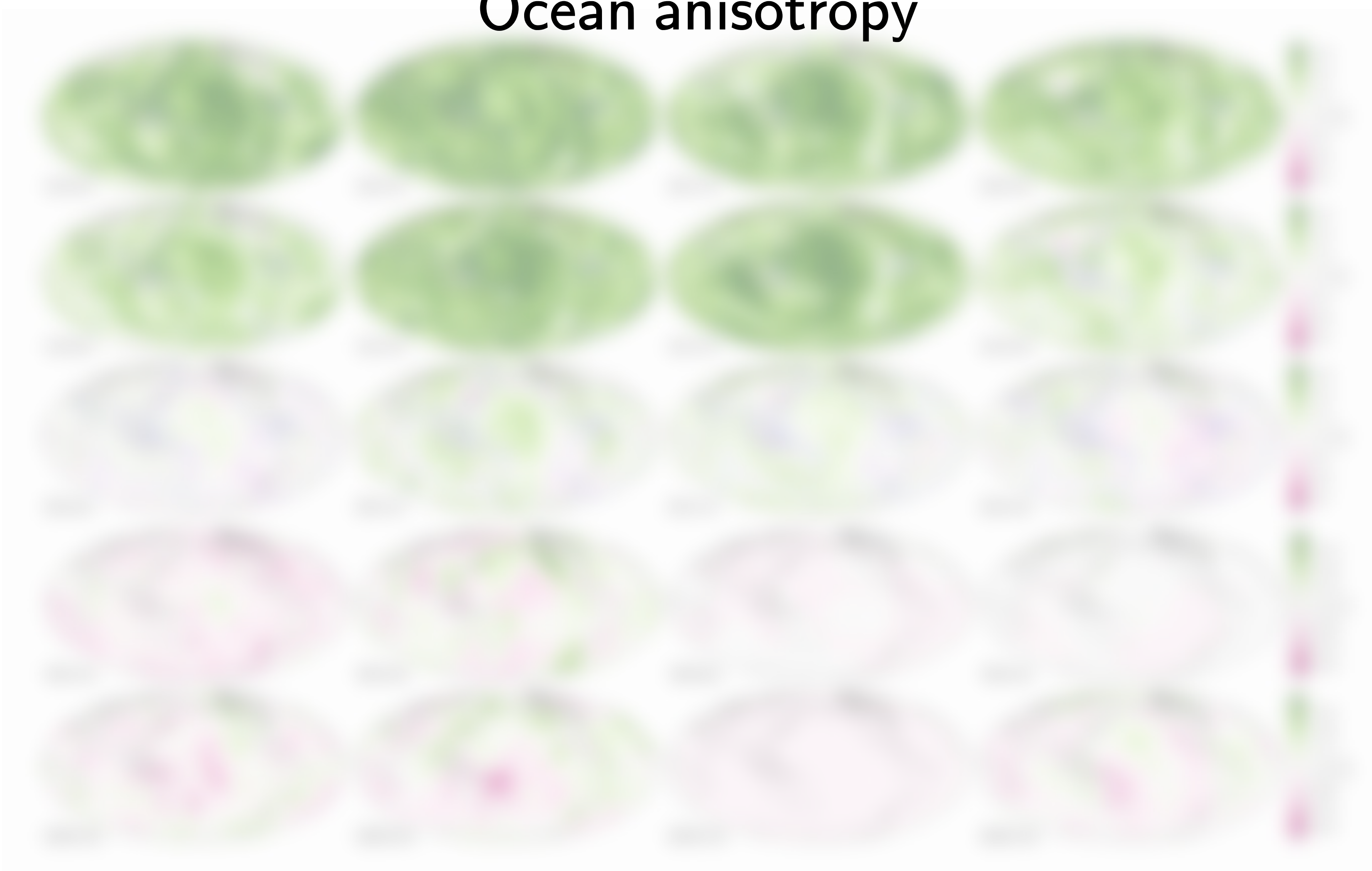

(2) Model comparison, anisotropic

Ocean anisotropy

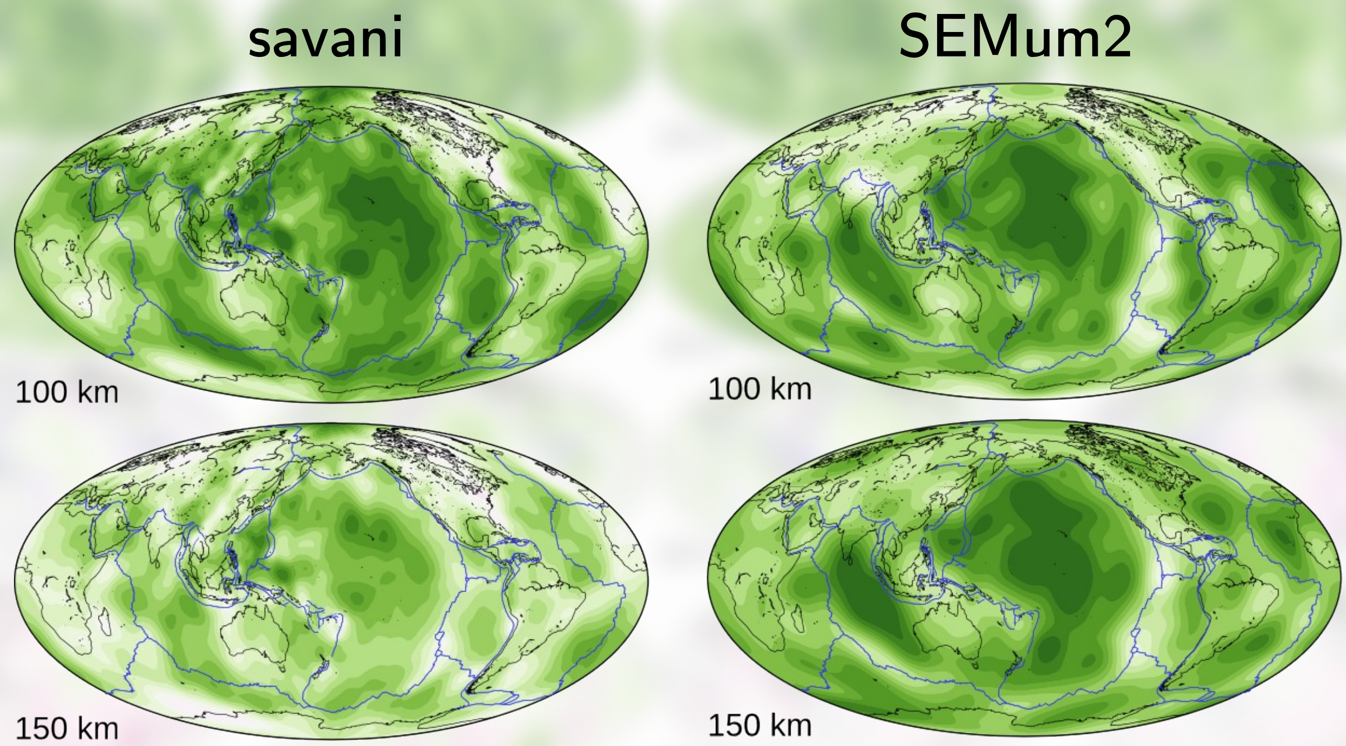

(2) Model comparison, anisotropic

Ocean anisotropy

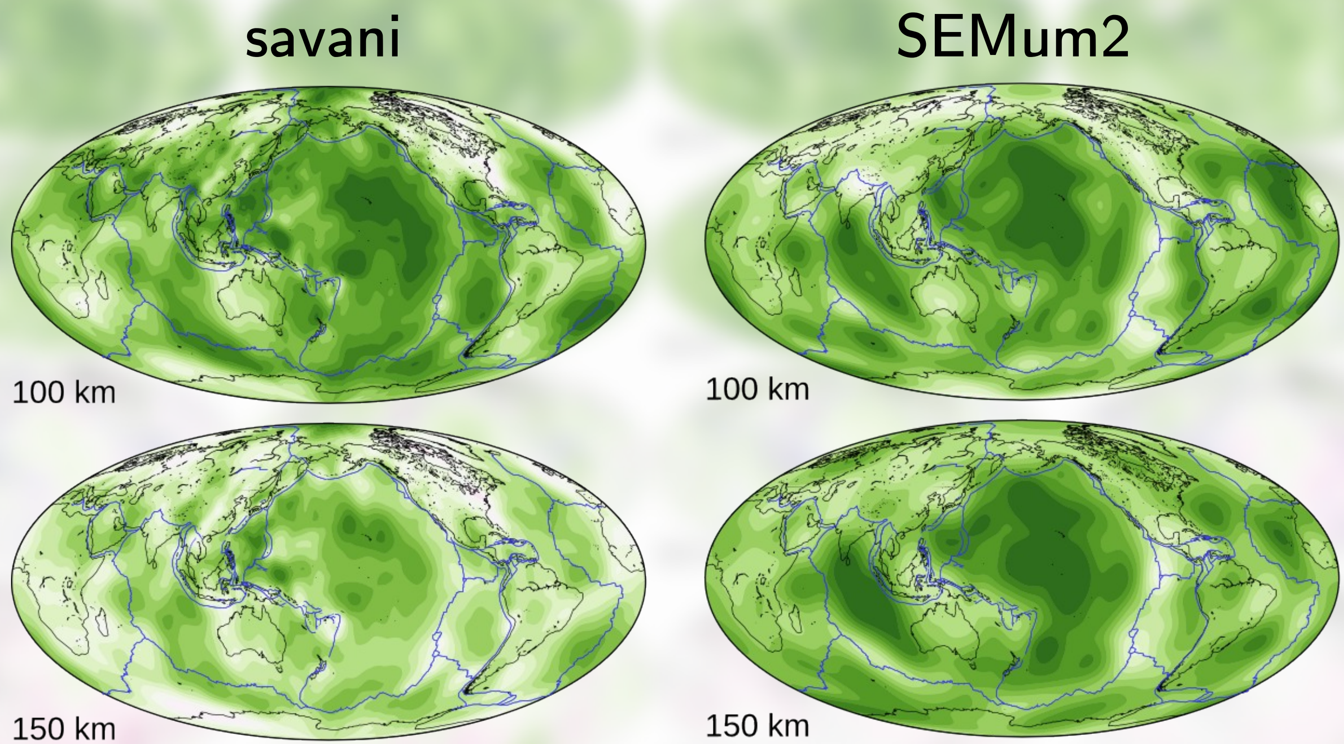

What is the ξ anomaly and how does it relate to upper-mantle dynamics?

(2) Thesis outline

Chap.

2. Whole-mantle anisotropy from surface and body waves at adaptive resolution *(Auer et al. 2014)*

3. Thermal structure, anisotropy, and dynamics of oceanic boundary layers *(Auer et al. 2015)*

4. Joint inversion of P- and S-wave constraints, hydration of marginal basins *(Tesoniero et al. 2015)*

5. Hybrid full waveform tomography combining global and regional data *(Auer et al. 2016, in preparation)*

(3) Oceanic upper-mantle structure

Other geophysical observations

Bathymetry Z

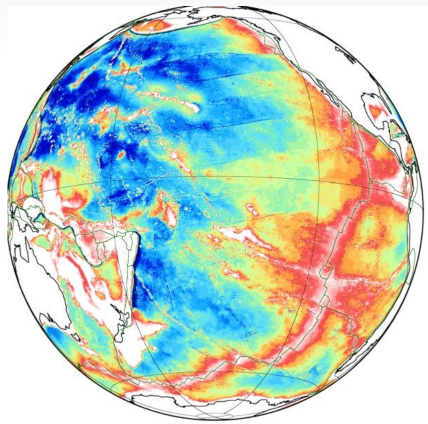

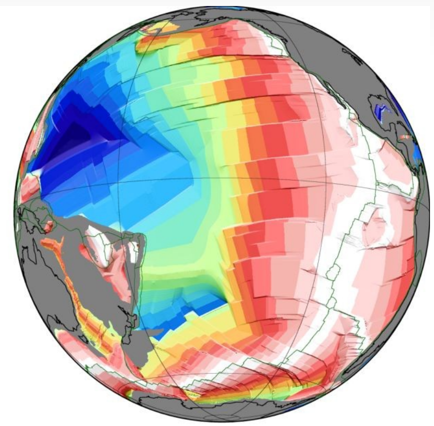

τ sea-floor ages

This study:

Wavespeeds V_S

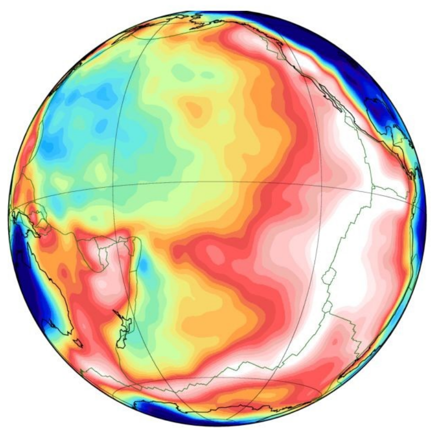

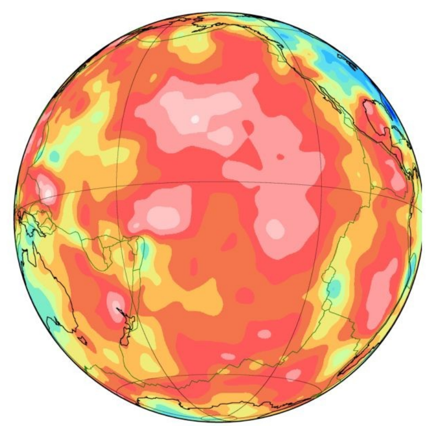

ξ anisotropy

(3) Oceanic upper-mantle structure

Other geophysical observations

Bathymetry Z

τ sea-floor ages

Half-space Cooling (HSC)!

This study:

Wavespeeds V_S

ξ anisotropy

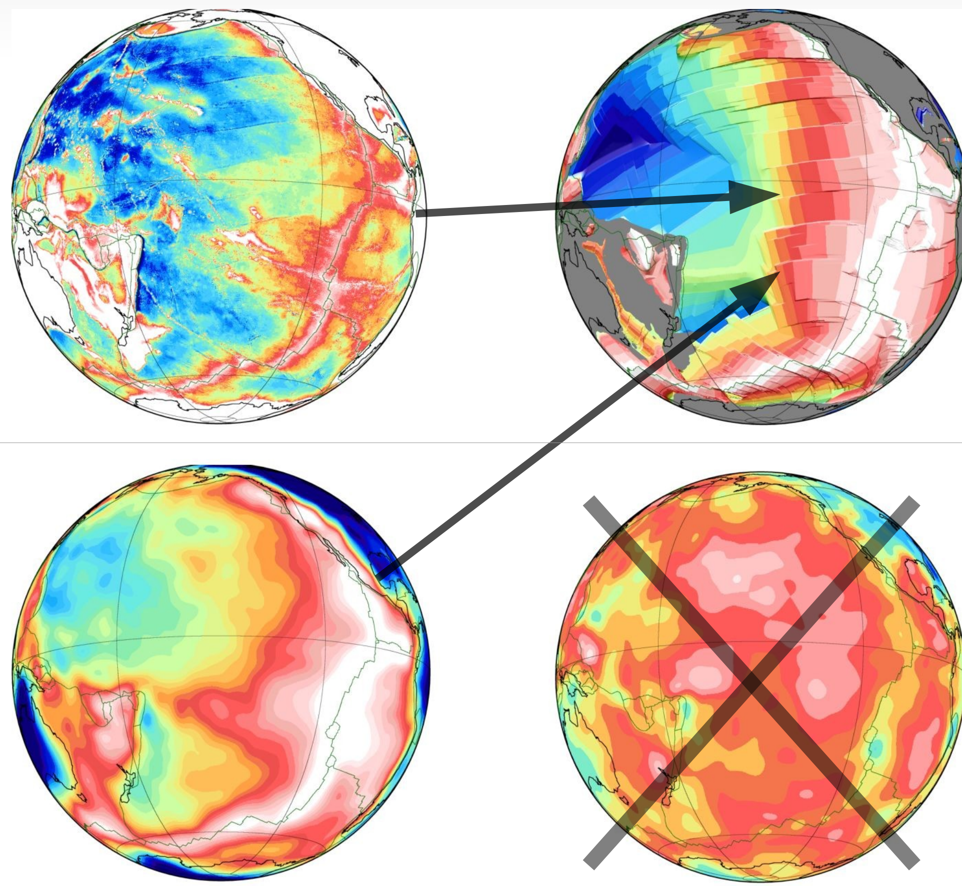

(3) Age dependence, isotropic

Reference v_s against sea-floor ages of the Pacific Ocean

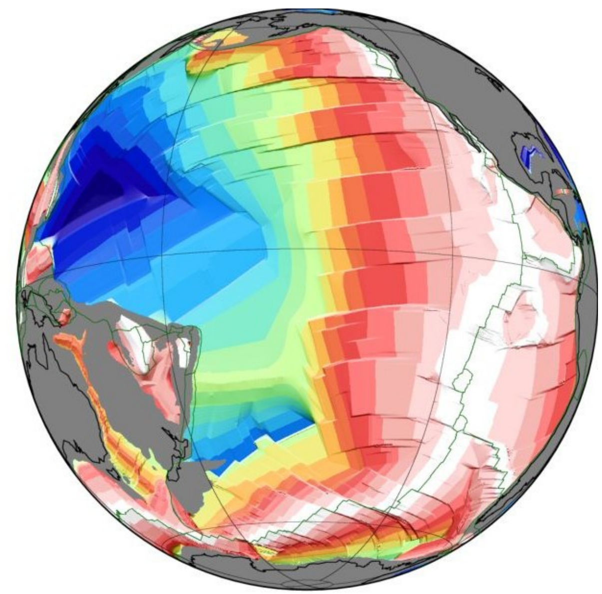

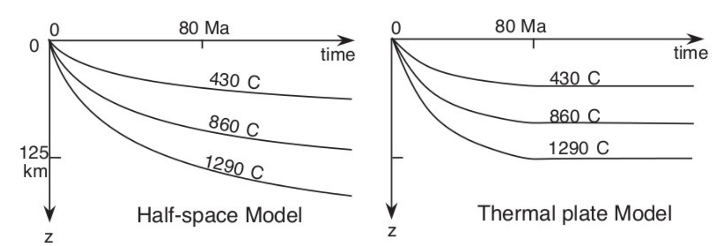

(3) Age dependence, isotropic

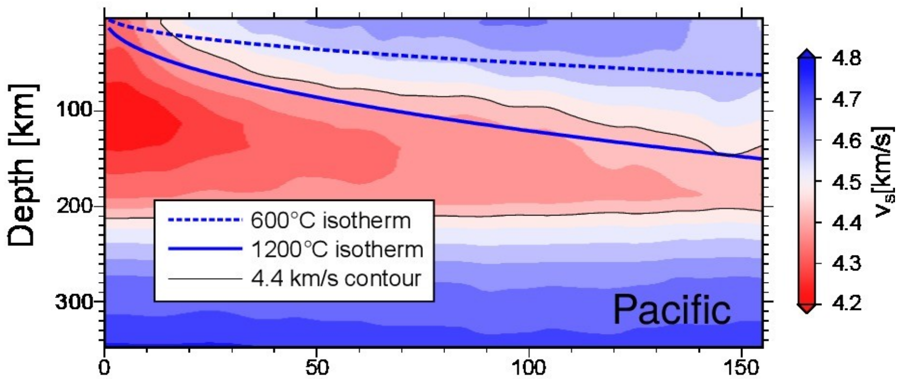

Sea-floor ages [Ma]

Reference v_s against sea-floor ages of the Pacific Ocean

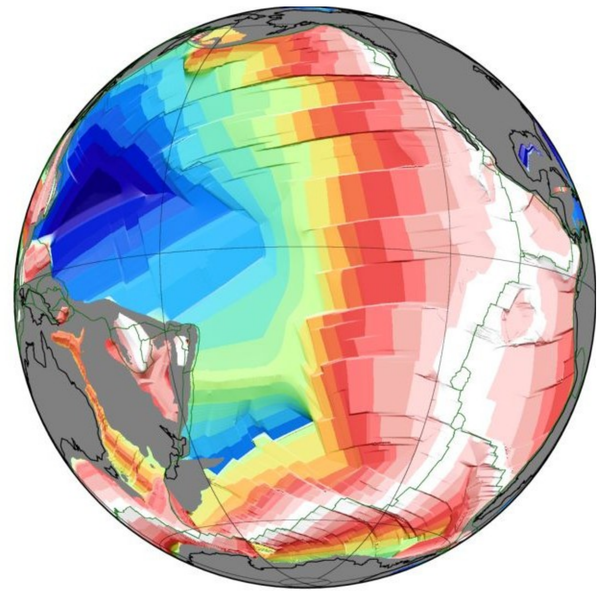

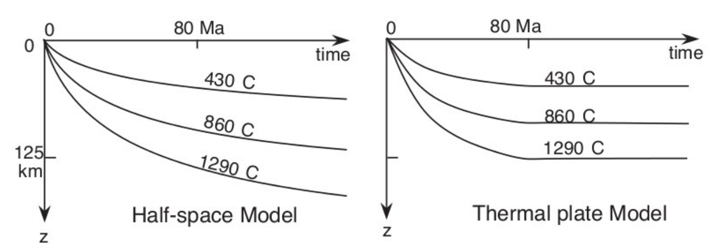

(3) Age dependence, isotropic

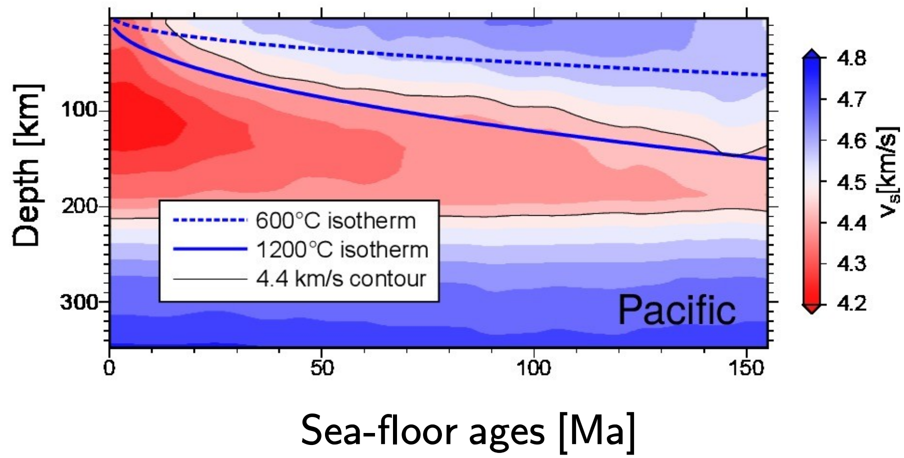

- Oceanic lithosphere agrees broadly with half-space cooling, LAB~1200°

Reference v_s against sea-floor ages of the Pacific Ocean

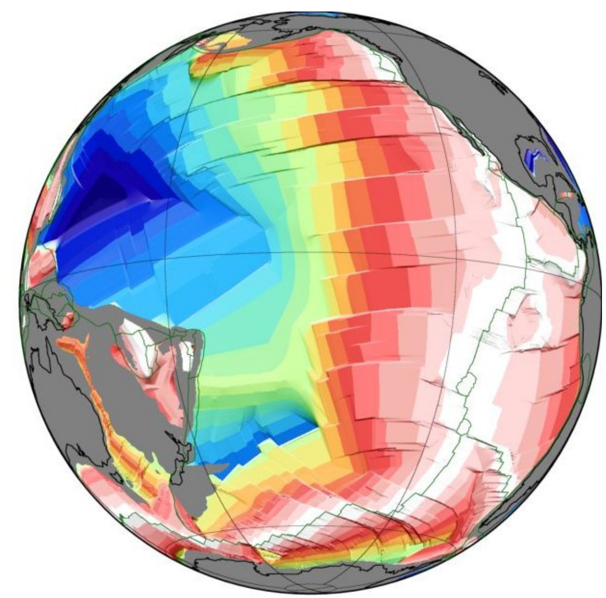

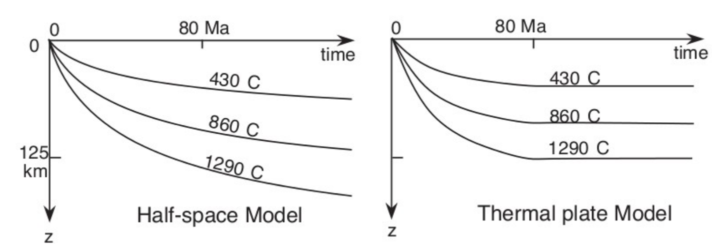

(3) Age dependence, isotropic

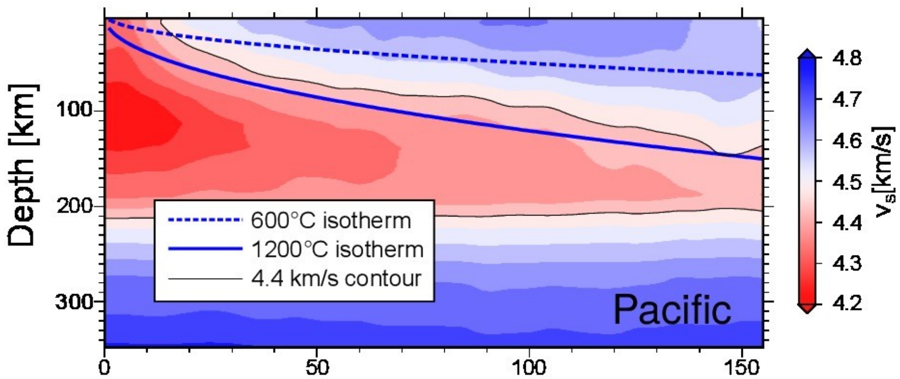

Sea-floor ages [Ma]

- Oceanic lithosphere agrees broadly with half-space cooling, LAB~1200°
- **But:** anomaly in the Pacific at sea-floor ages of~ 80 million years

Reference v_s against sea-floor ages of the Pacific Ocean

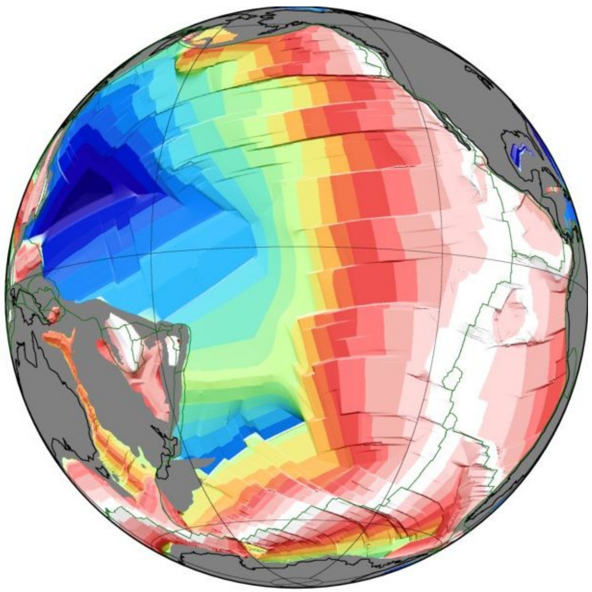

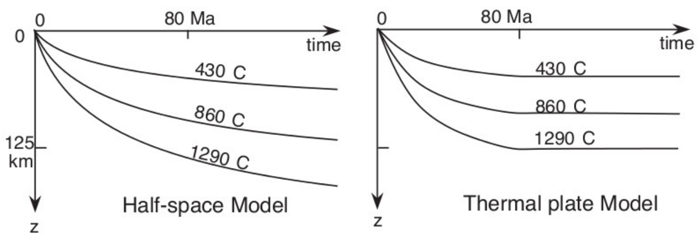

(3) Age dependence, isotropic

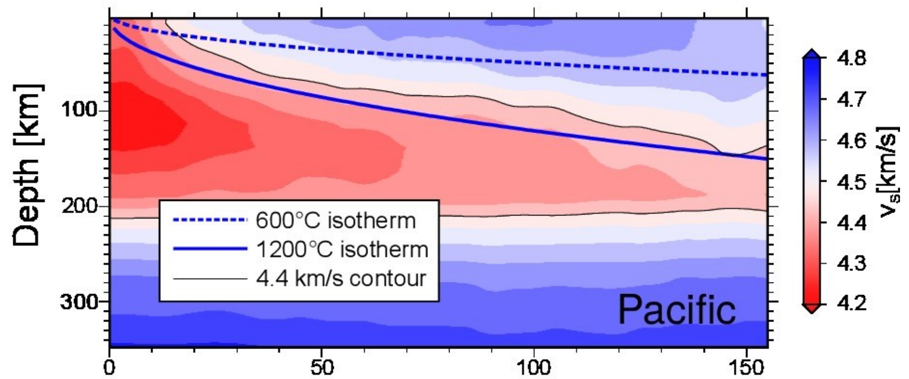

Sea-floor ages [Ma]

- Oceanic lithosphere agrees broadly with half-space cooling, LAB~1200°
- **But:** anomaly in the Pacific at sea-floor ages of~ 80 million years
- Complexity beyond half-space cooling

Reference v_s against sea-floor ages of the Pacific Ocean

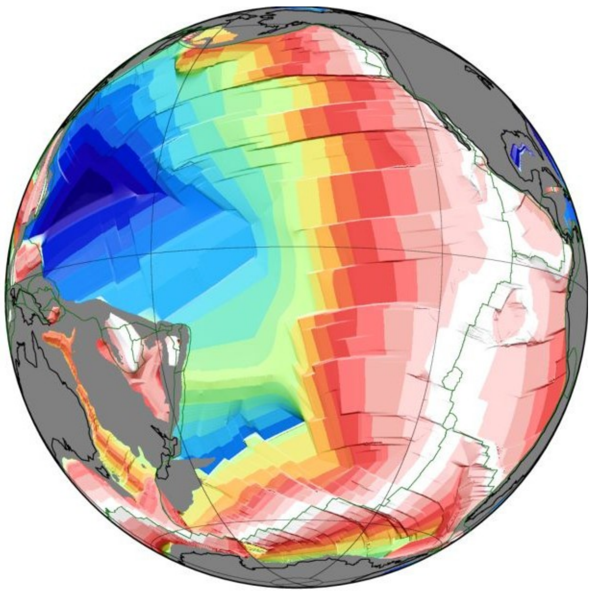

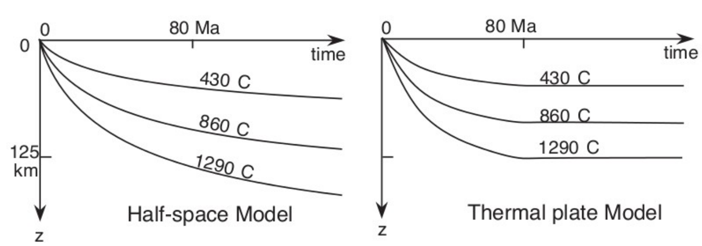

(3) Age dependence, anisotropic

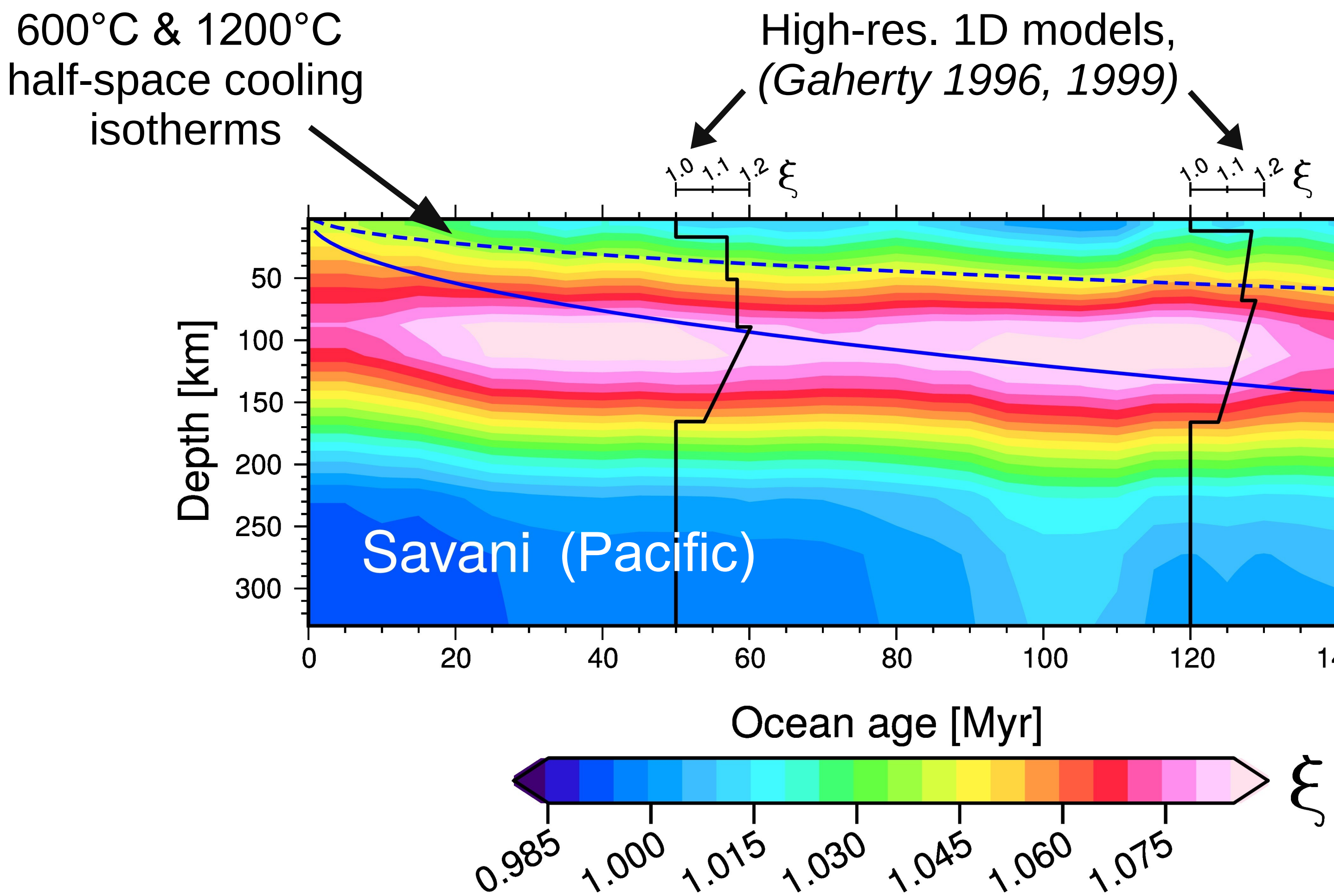

(3) Age dependence, anisotropic

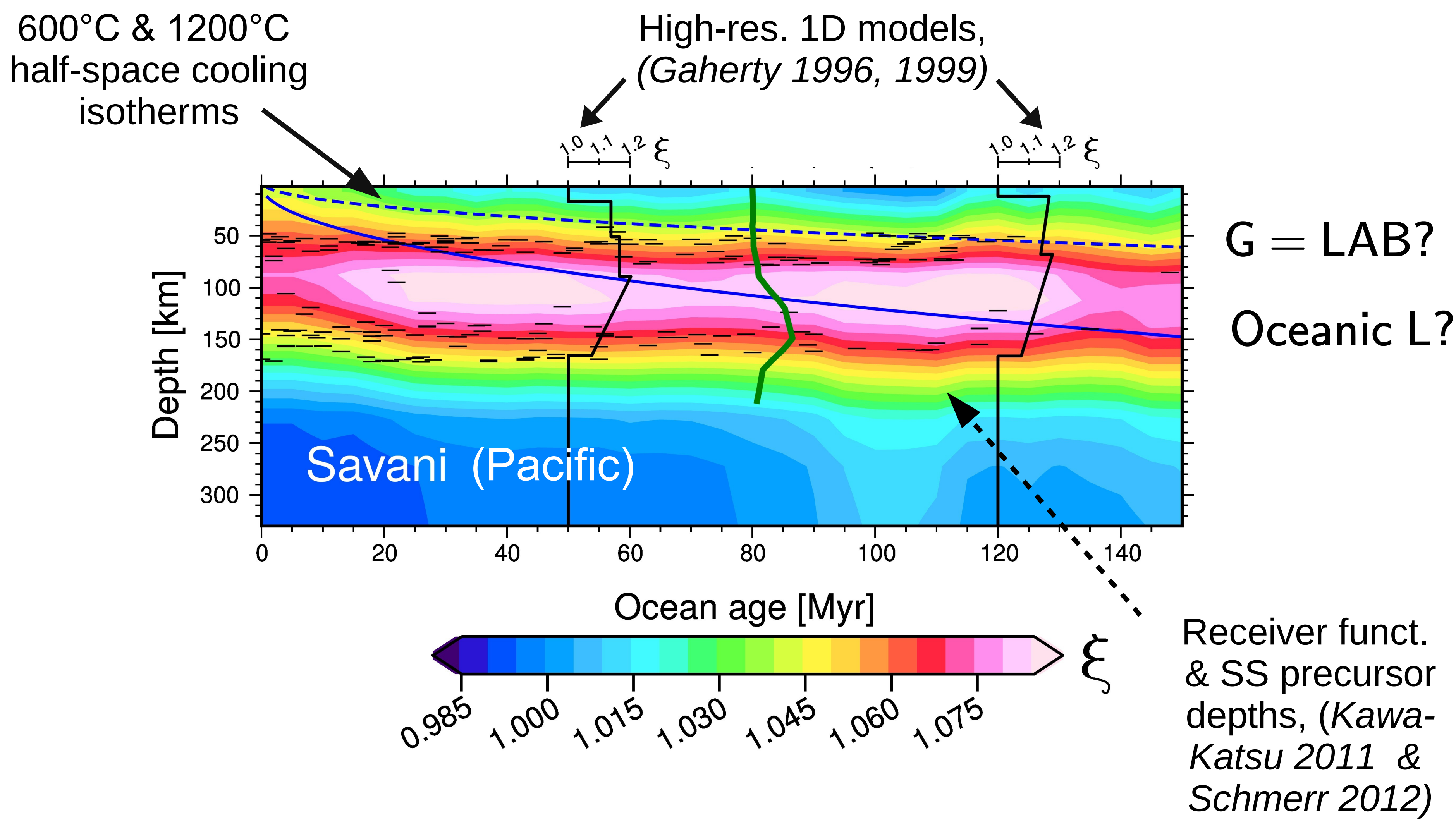

(3) Age dependence, anisotropic

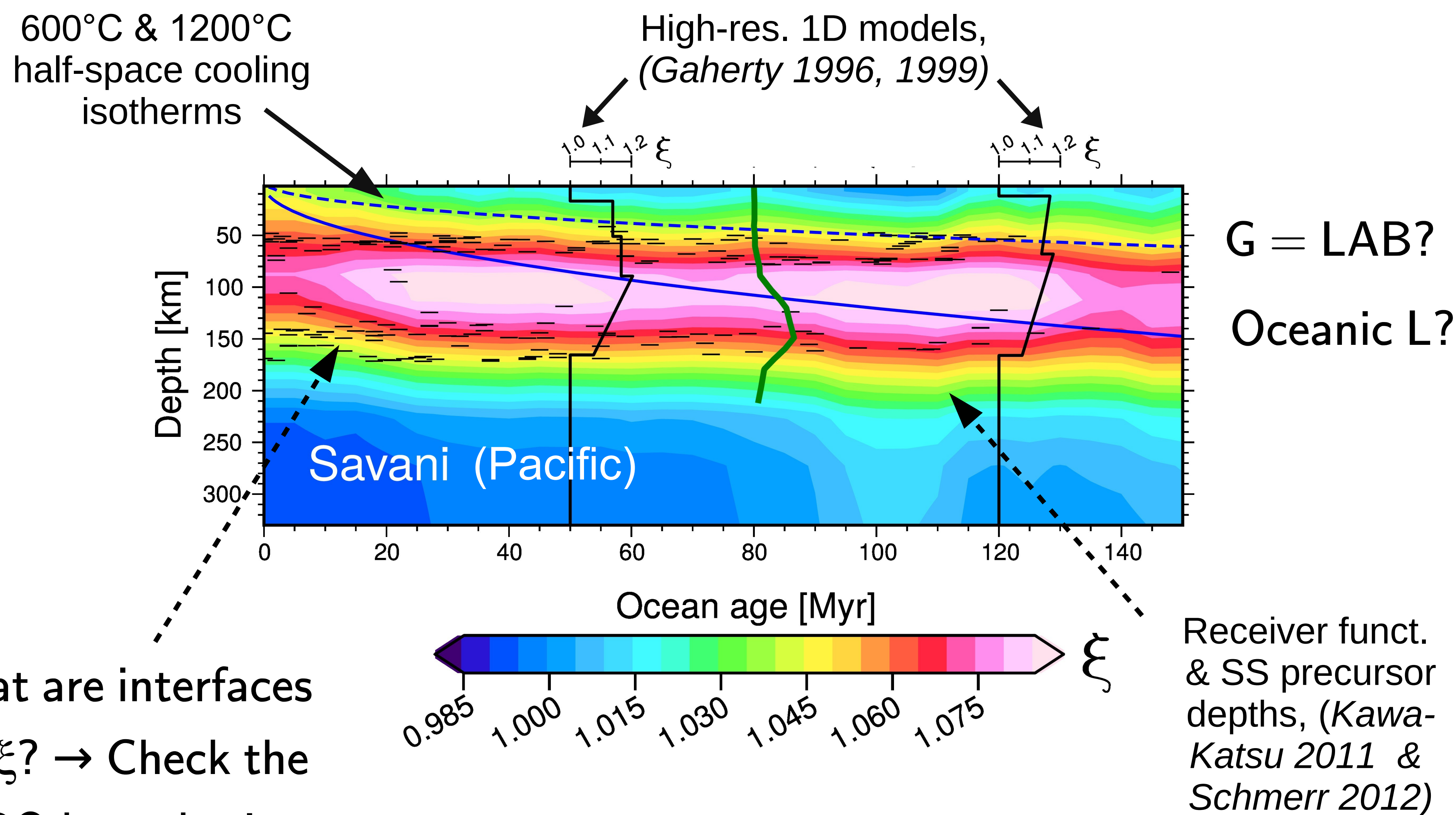

What are interfaces and ξ? → Check the LPO hypothesis

(3) Age dependence, anisotropic

600°C &
half-spac
isoth

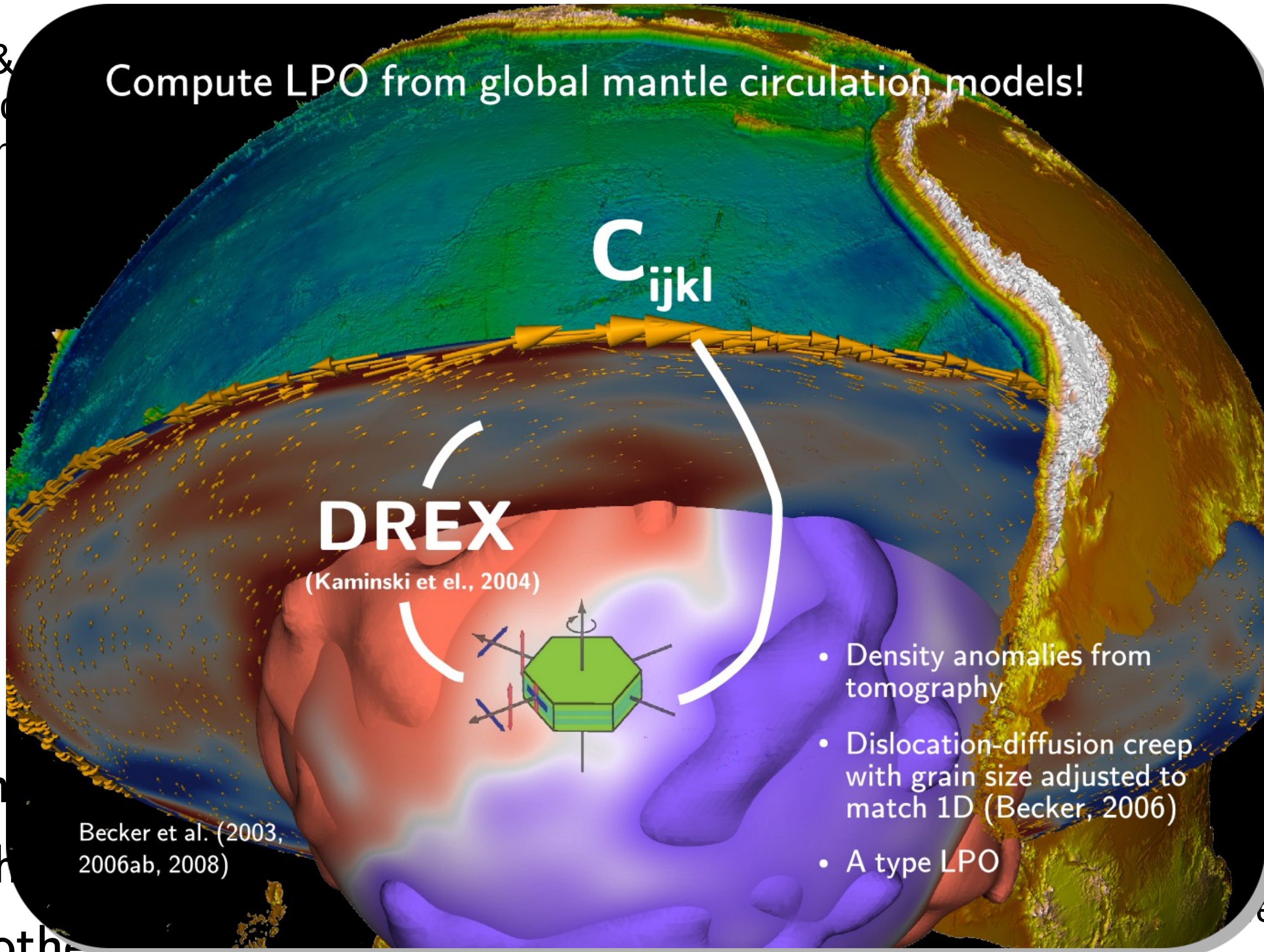

LAB?
eanic L?

er funct.
recursor
, (*Kawa-*
2011 &
err 2012)

What are in
and ξ? → Ch
LPO hypothesis

(3) Age dependence, anisotropic

600°C & 1200°C half-space cooling isotherms

High-res. 1D models, *(Gaherty 1996, 1999)*

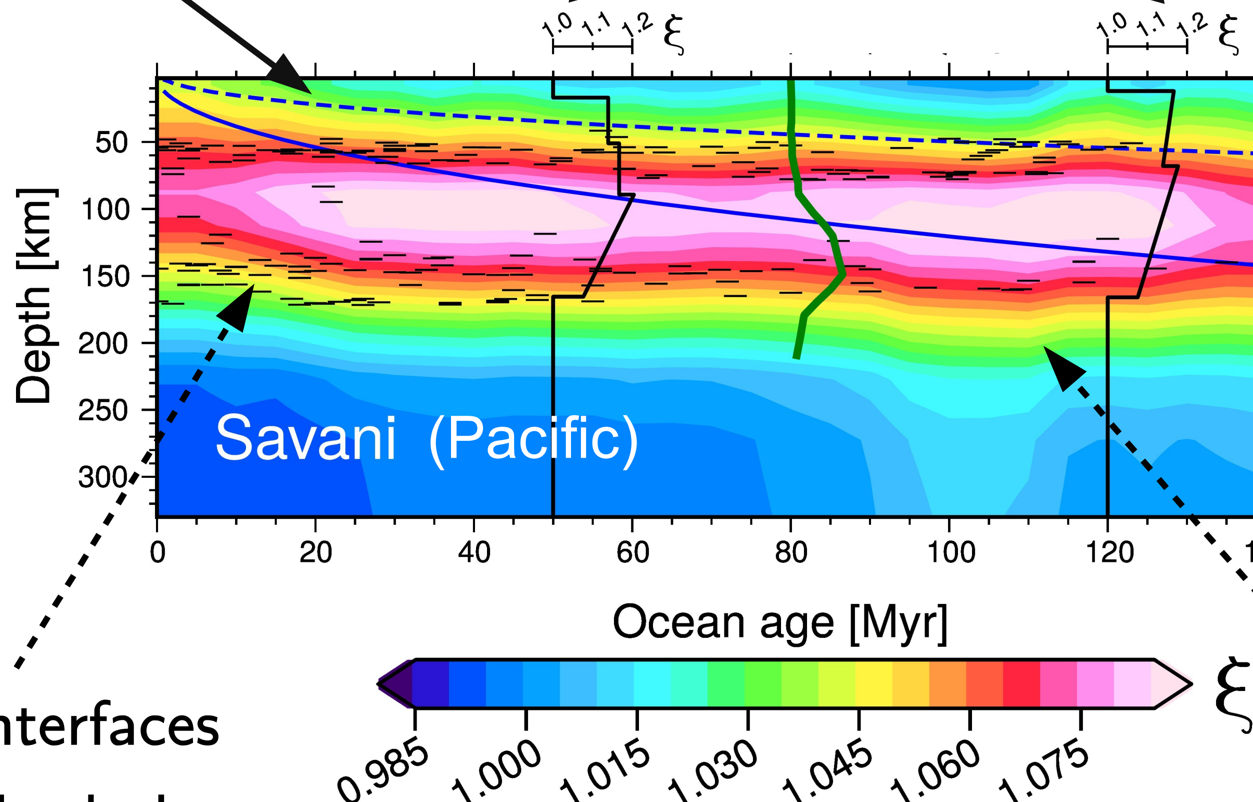

G = LAB?

Oceanic L?

What are interfaces and ξ? → Check the LPO hypothesis

Receiver funct. & SS precursor depths, (*Kawa-Katsu 2011 & Schmerr 2012)*

(3) Age dependence, anisotropic

Comparison with LPO-based prediction

Radial anisotropy comparsion (this study)

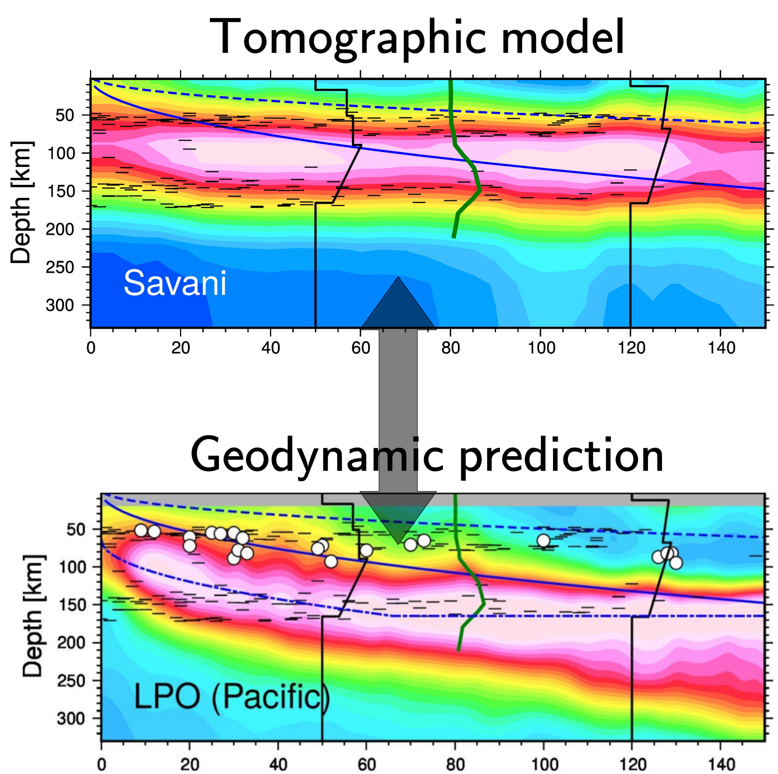

ξ too deep and not flat!

(3) Age dependence, anisotropic

Comparison with LPO-based prediction

Radial anisotropy comparsion (this study)

Tomographic model

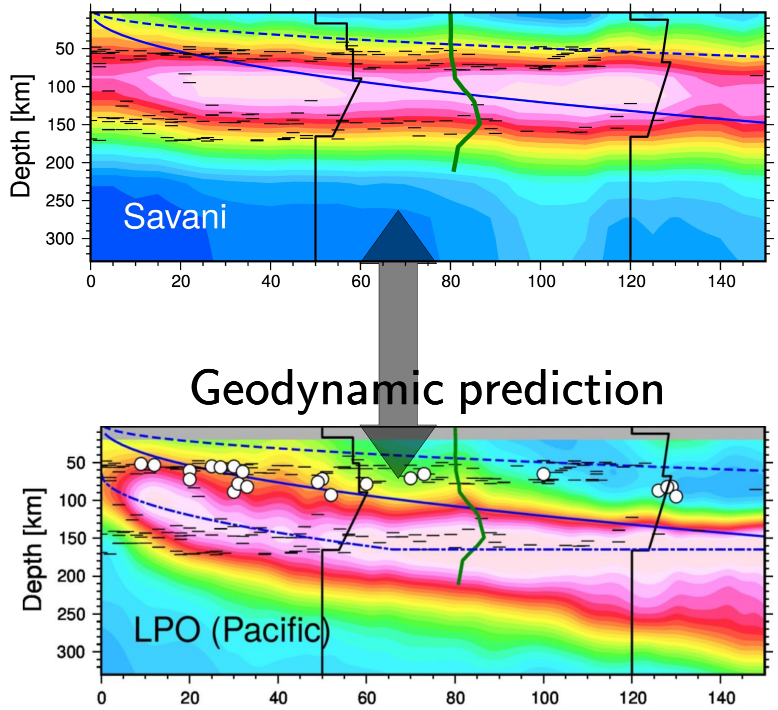

ξ too deep and not flat!

Azimuthal anisotropy, Becker et al. (2015)

(3) Age dependence, anisotropic

Comparison with LPO-based prediction

Radial anisotropy comparsion (this study)

Tomographic model

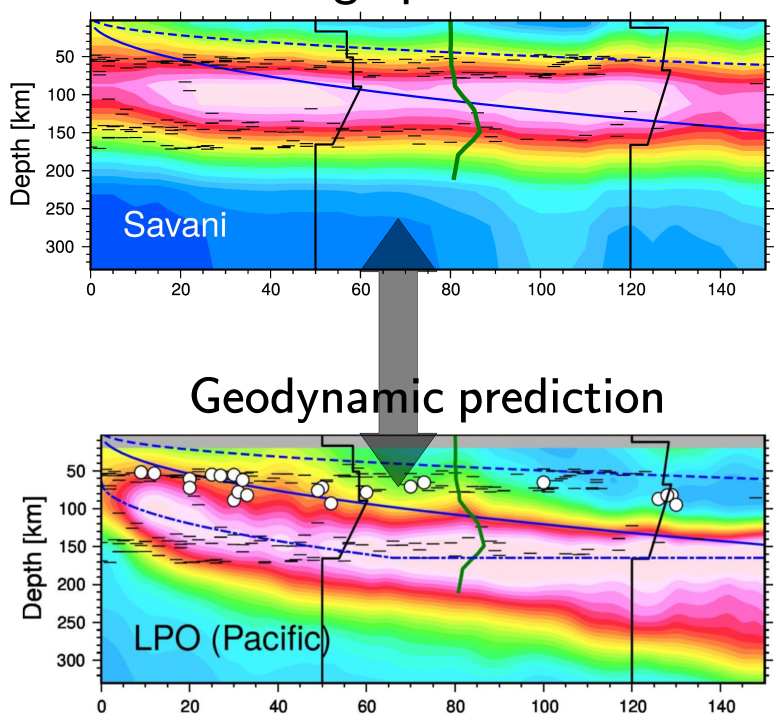

ξ too deep and not flat!

Azimuthal anisotropy, Becker et al. (2015)

Fast axes comparison

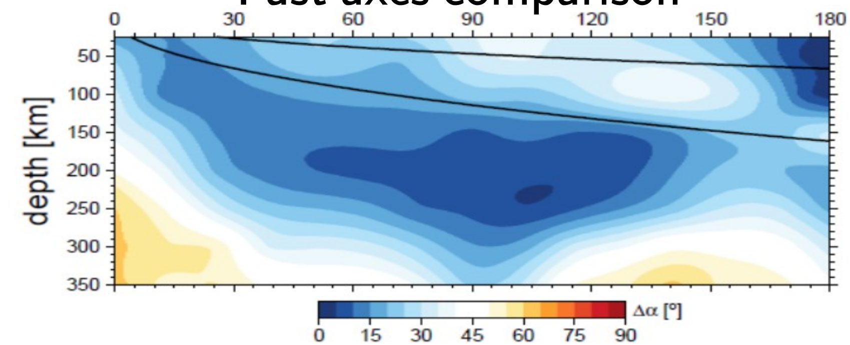

Tomographic and geodynamic fast axes directions **match** underneath the 1200°C isotherm!

(3) Age dependence, anisotropic

- Flat ξ artifact of penalizing model roughness?

- **Idea:** Circumvent regularization by conducting "probabilistic" **hypothesis tests** → solve forward problem for conceptual geodynamic models of ξ and monitor data fit

- Are flat or age-dependent models preferred?

(3) Hypothesis test: flat layer

Fit (VR) for Pacific dataset: $$VR = 1 - \frac{|\mathbf{G} \cdot \mathbf{m} - \mathbf{d_{obs}}|}{|\mathbf{d}_{obs}|}$$

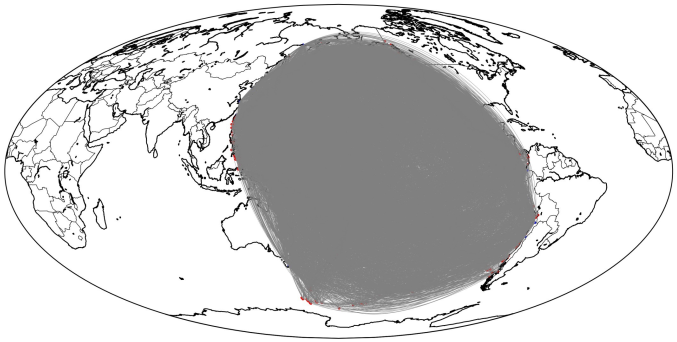

(3) Hypothesis test: flat layer

Fit (VR) for Pacific dataset:

$$VR = 1 - \frac{|\mathbf{G} \cdot \mathbf{m} - \mathbf{d_{obs}}|}{|\mathbf{d}_{obs}|}$$

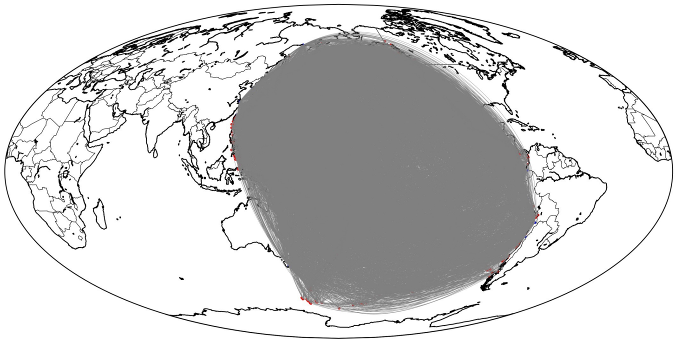

(3) Hypothesis test: flat layer

Grid search over layer depth z_0
and the anisotropy strength ξ_{max}

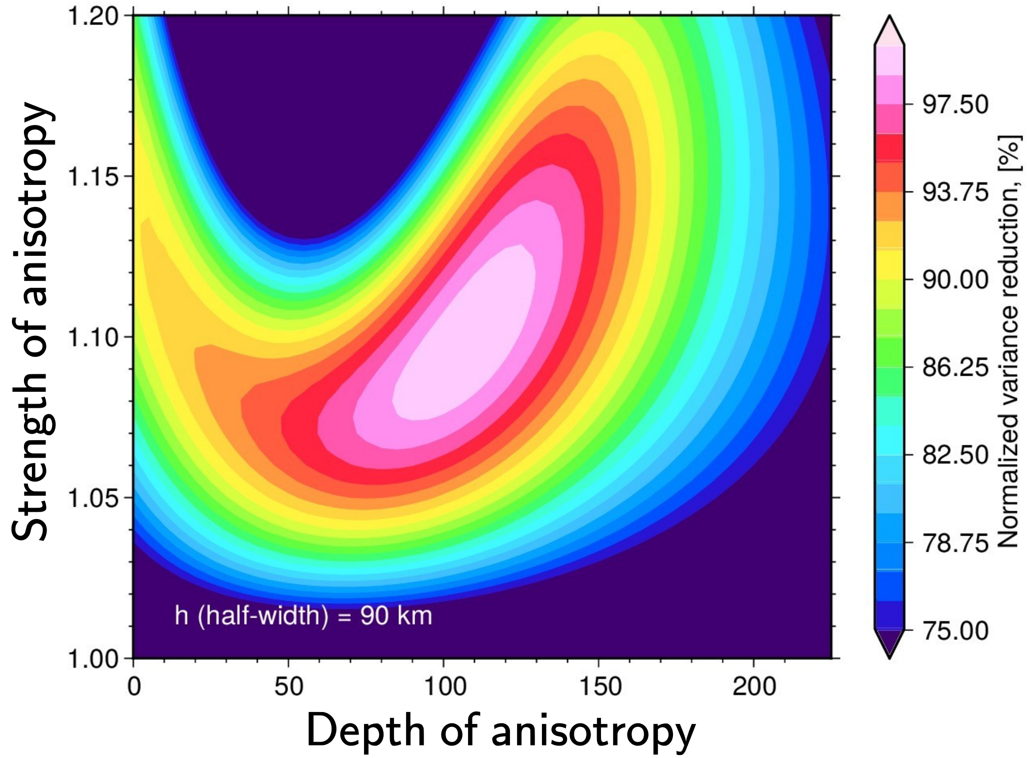

Fit (VR) for
Pacific dataset:

$$VR = 1 - \frac{|\mathbf{G} \cdot \mathbf{m} - \mathbf{d_{obs}}|}{|\mathbf{d}_{obs}|}$$

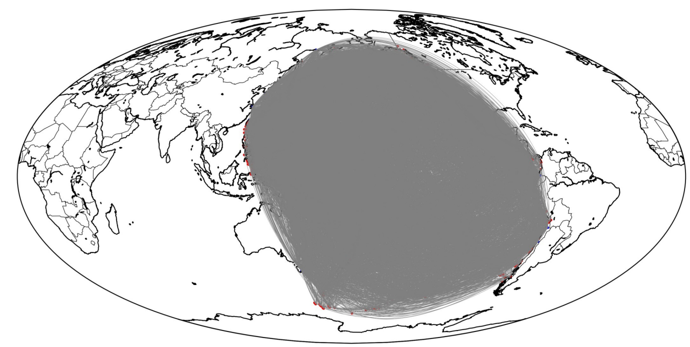

(3) Hypothesis test: flat layer

Grid search over layer depth z_0 and the anisotropy strength ξ_{max}

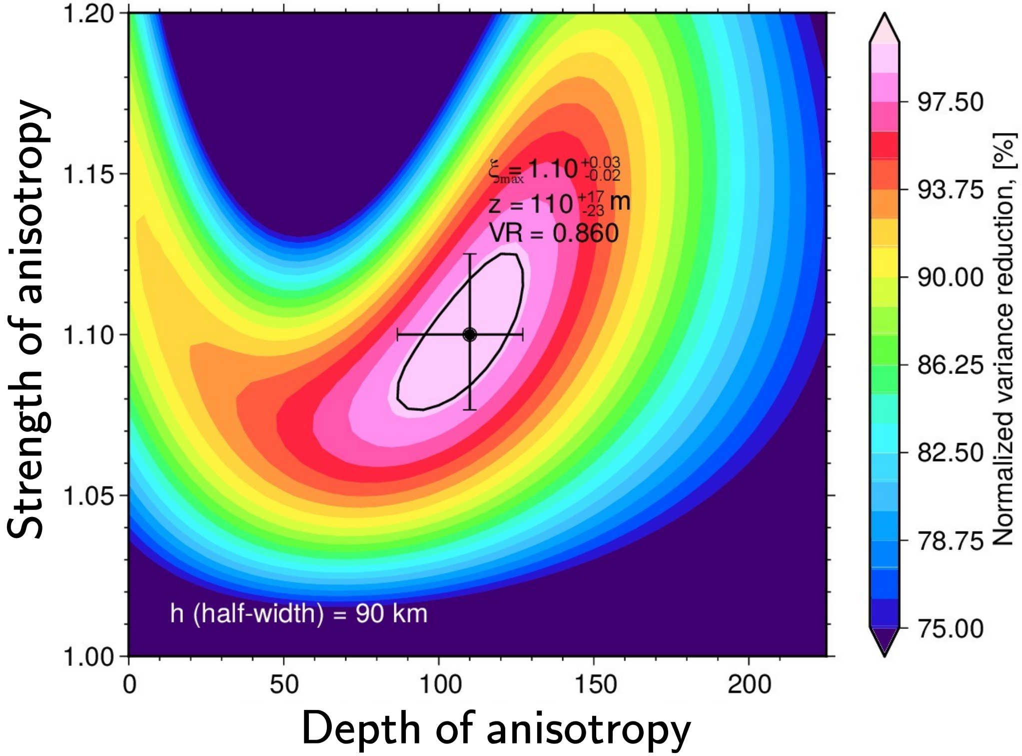

Fit (VR) for Pacific dataset:

$$VR = 1 - \frac{|\mathbf{G} \cdot \mathbf{m} - \mathbf{d_{obs}}|}{|\mathbf{d}_{obs}|}$$

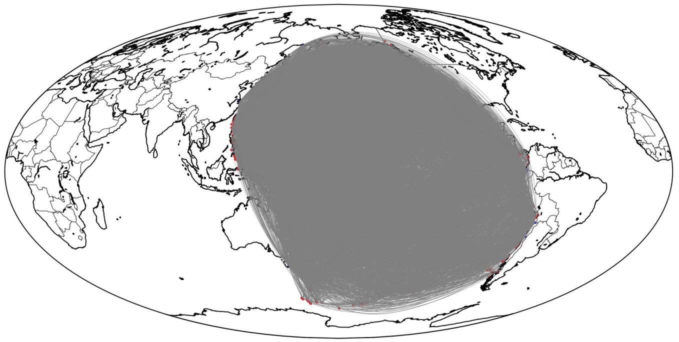

(3) Hypothesis test: flat layer

Grid search over layer depth z_0
and the anisotropy strength ξ_{max}

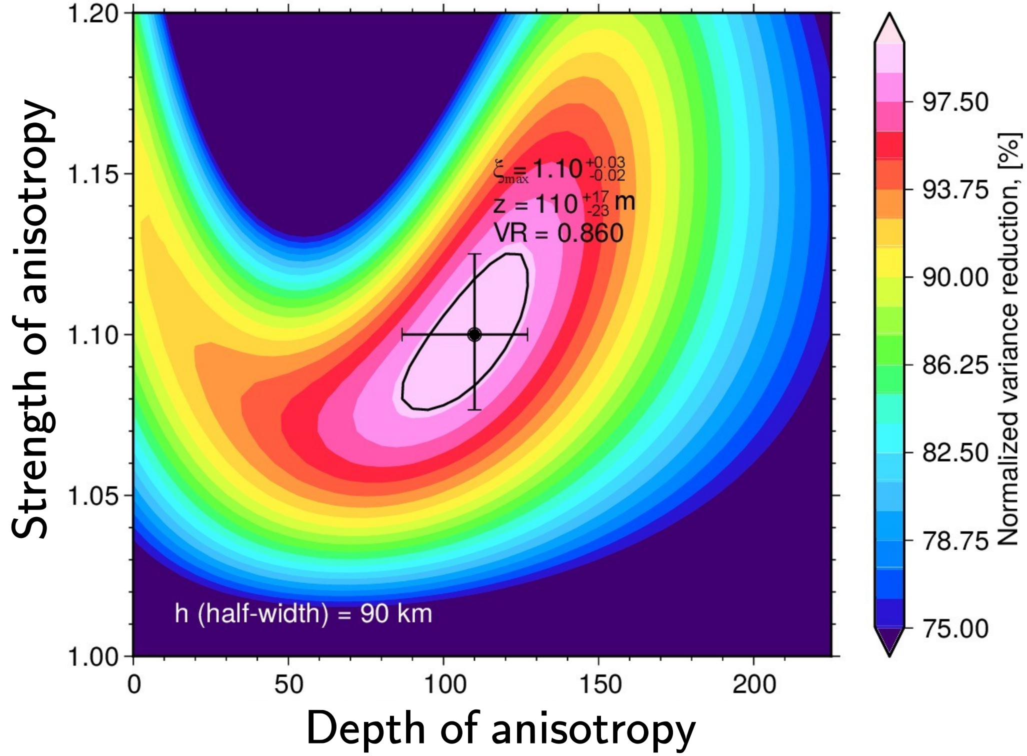

Fit (VR) for
Pacific dataset:

$$VR = 1 - \frac{|\mathbf{G}\cdot\mathbf{m} - \mathbf{d_{obs}}|}{|\mathbf{d}_{obs}|}$$

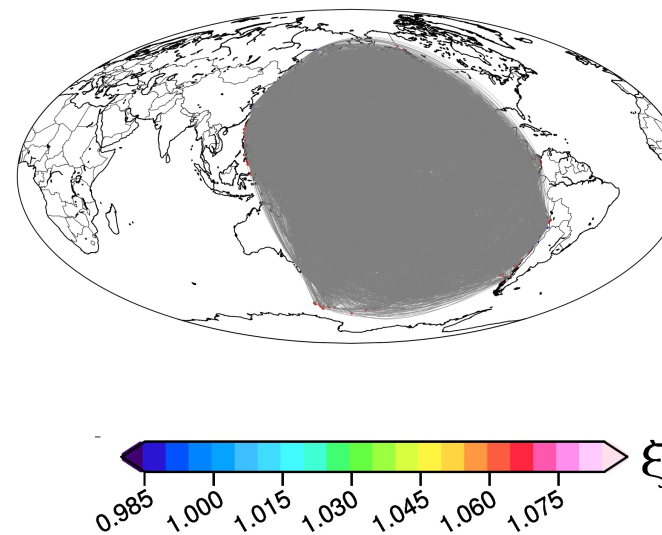

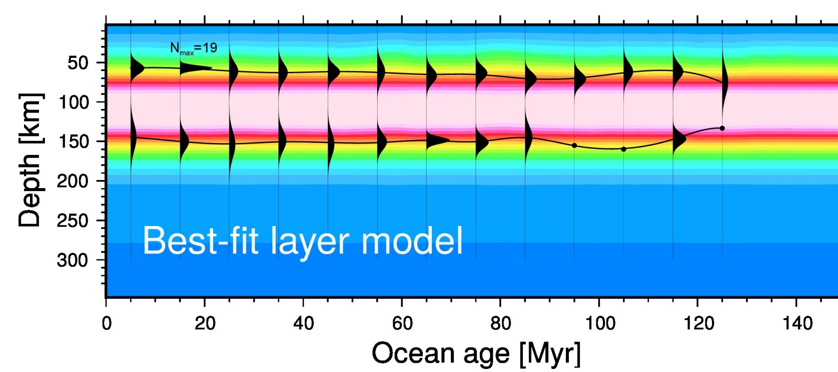

(3) Hypothesis test: flat layer

Grid search over layer depth z_0
and the anisotropy strength ξ_{max}

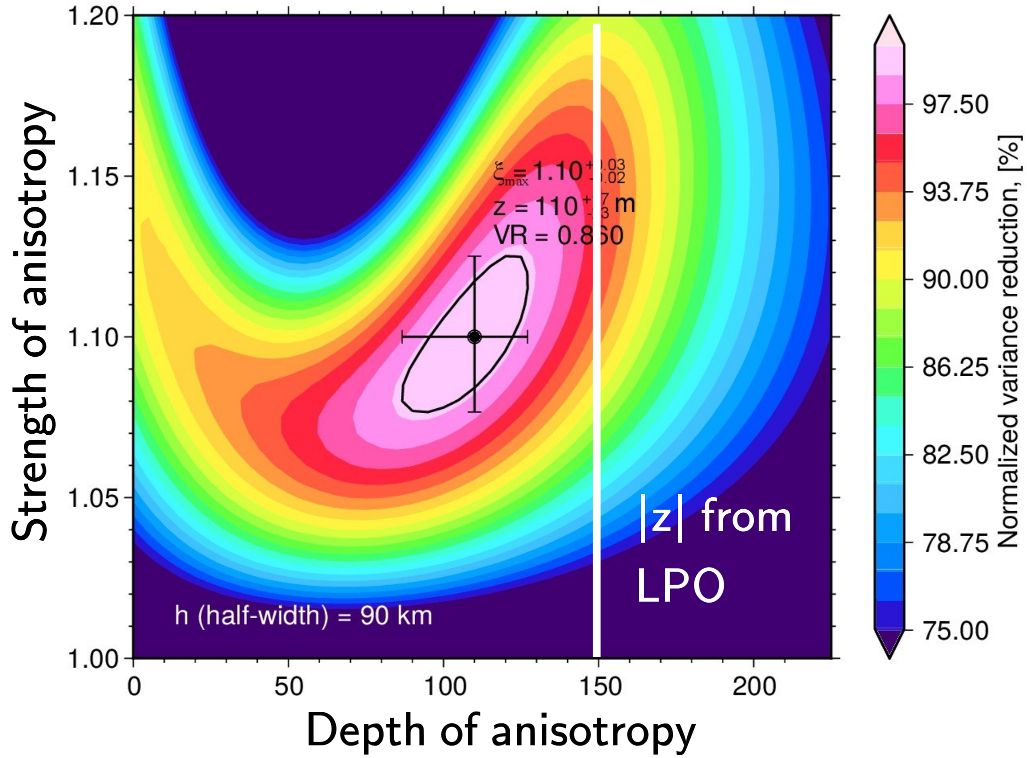

Again: LPO anisotropy too deep

Fit (VR) for
Pacific dataset:

$$VR = 1 - \frac{|\mathbf{G}\cdot\mathbf{m} - \mathbf{d_{obs}}|}{|\mathbf{d}_{obs}|}$$

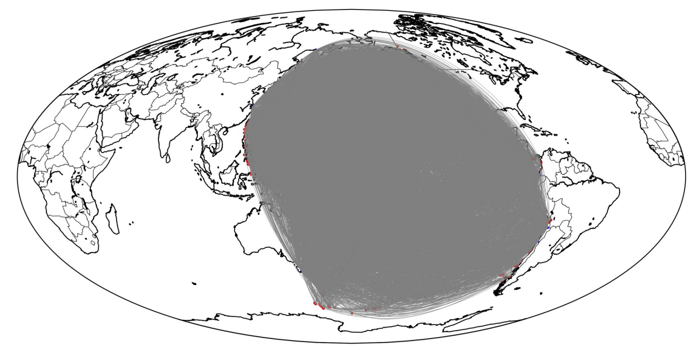

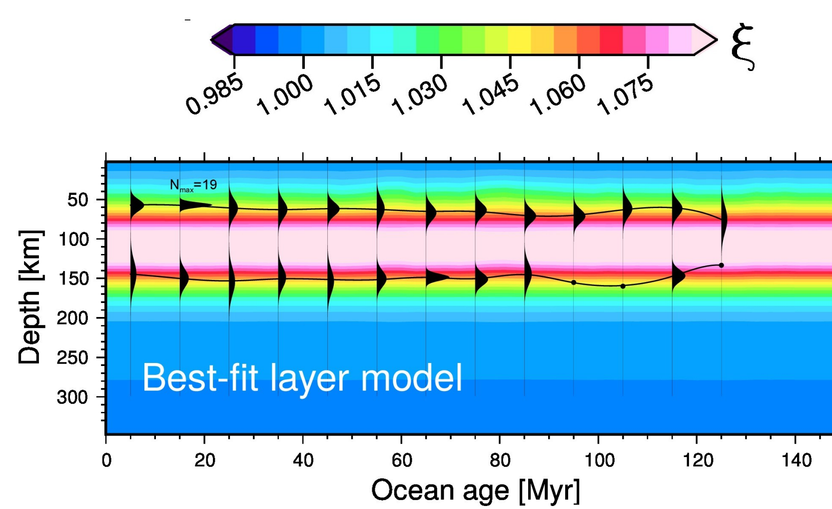

(3) Hypothesis test: $\sqrt{\tau}$ case

Model: $$z_1 = a + c\sqrt{\kappa\hat{\tau}(\mathbf{x}, f)} \qquad \hat{\tau}(\mathbf{x}, f) = \begin{cases} \tau(\mathbf{x}) & \text{for } \tau(\mathbf{x}) < f \\ f & \text{for } \tau(\mathbf{x}) \geq f \end{cases}$$

(3) Hypothesis test: $\sqrt{\tau}$ case

Model:

$$z_1 = a + c\sqrt{\kappa\hat{\tau}(\mathbf{x}, f)} \qquad \hat{\tau}(\mathbf{x}, f) = \begin{cases} \tau(\mathbf{x}) & \text{for } \tau(\mathbf{x}) < f \\ f & \text{for } \tau(\mathbf{x}) \geq f \end{cases}$$

Flattening age f

Slope factor c

(3) Hypothesis test: $\sqrt{\tau}$ case

Model:

$$z_1 = a + \boxed{c}\sqrt{\kappa\hat{\tau}(\mathbf{x}, f)} \qquad \hat{\tau}(\mathbf{x}, f) = \begin{cases} \tau(\mathbf{x}) & \text{for } \tau(\mathbf{x}) < f \\ \boxed{f} & \text{for } \tau(\mathbf{x}) \geq f \end{cases}$$

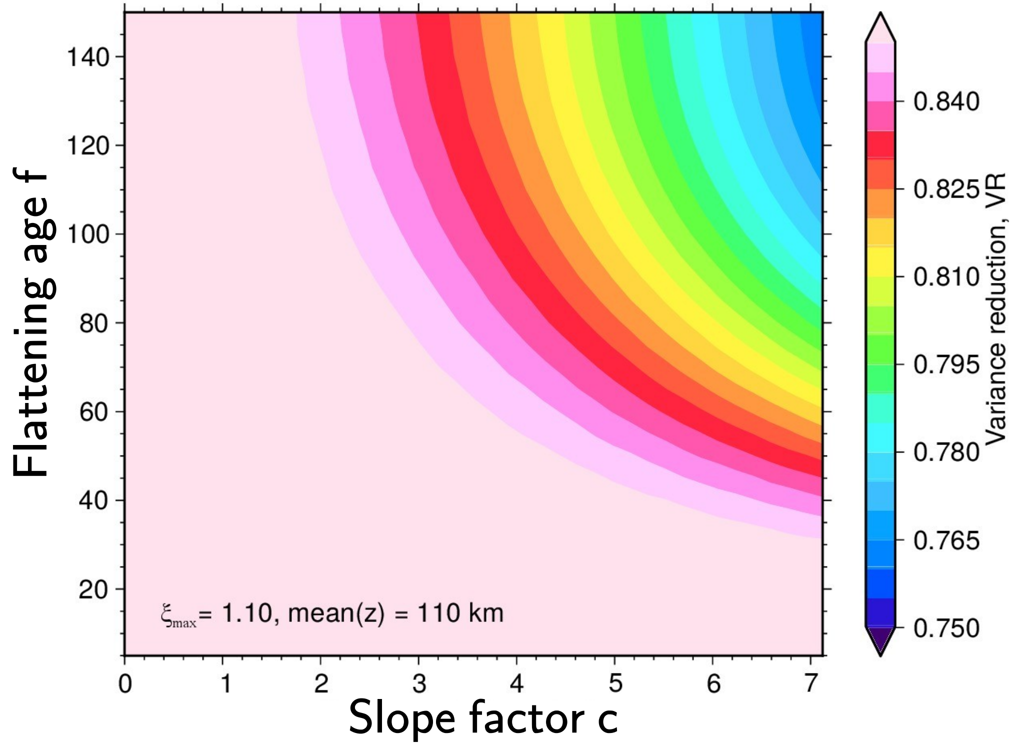

(3) Hypothesis test: $\sqrt{\tau}$ case

Model: $z_1 = a + c\sqrt{\kappa \hat{\tau}(\mathbf{x}, f)}$ $\quad \hat{\tau}(\mathbf{x}, f) = \begin{cases} \tau(\mathbf{x}) & \text{for } \tau(\mathbf{x}) < f \\ f & \text{for } \tau(\mathbf{x}) \geq f \end{cases}$

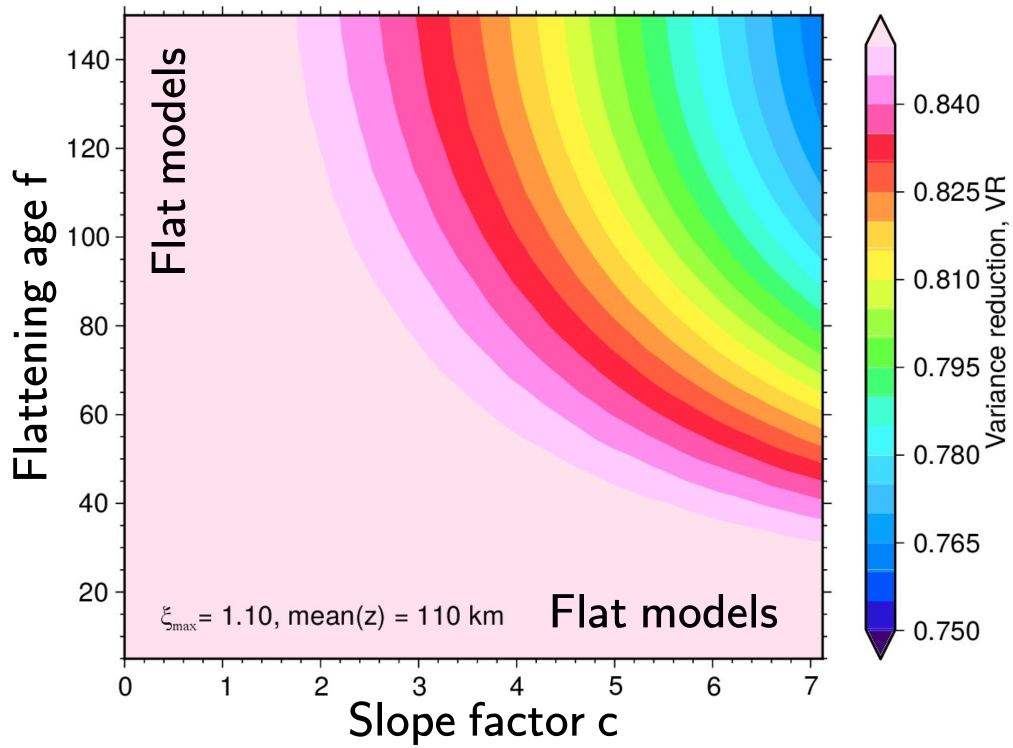

(3) Hypothesis test: $\sqrt{\tau}$ case

Model:

$$z_1 = a + c\sqrt{\kappa\hat{\tau}(\mathbf{x}, f)} \qquad \hat{\tau}(\mathbf{x}, f) = \begin{cases} \tau(\mathbf{x}) & \text{for } \tau(\mathbf{x}) < f \\ f & \text{for } \tau(\mathbf{x}) \geq f \end{cases}$$

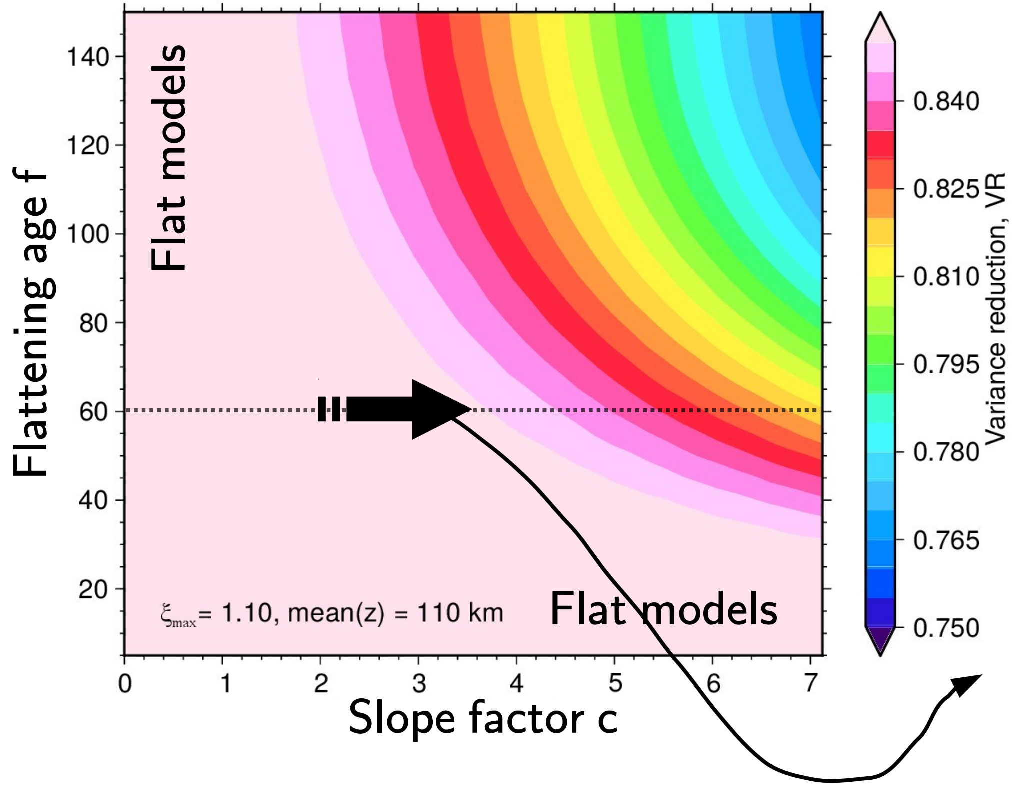

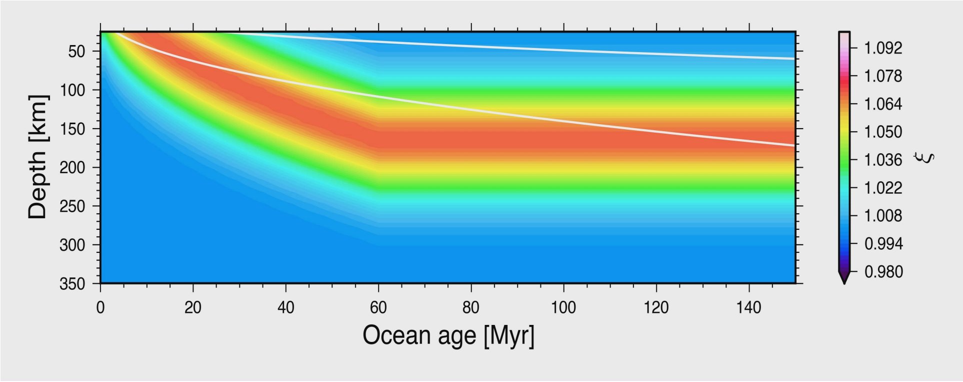

(3) Hypothesis test: summary

- Regionalized hypothesis tests confirm that depth of zone is shallower than LPO prection.
- Some age-dependent models borderline compatible with data, but there is preference for flat models.

(3) Summary of results

Isotropic structure broadly **matches HSC**

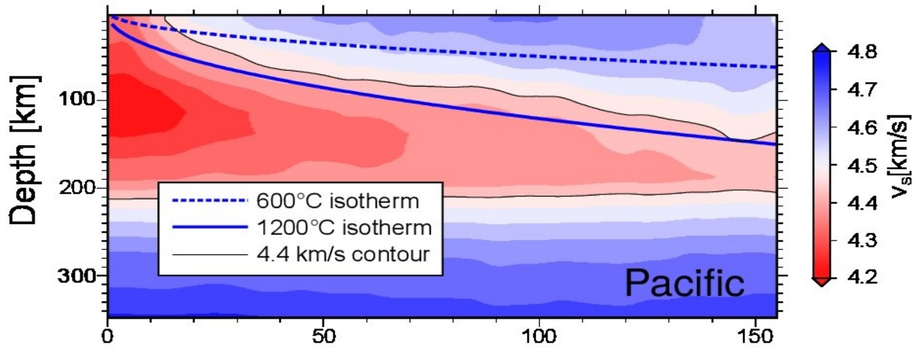

Azim. aniso. from LPO vs. sl2013sv **match**

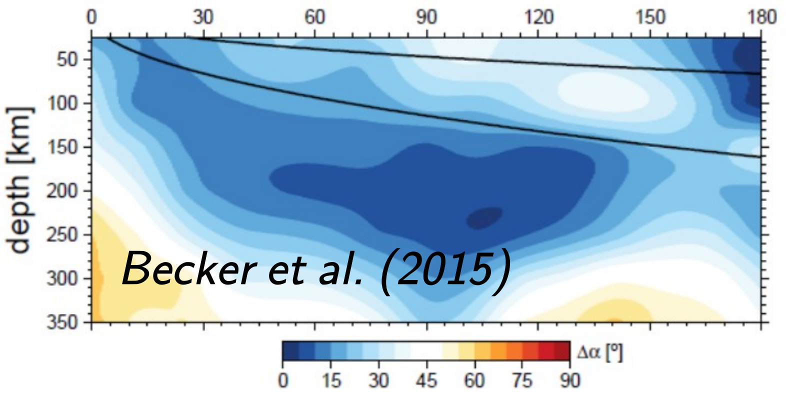

(3) Summary of results

Isotropic structure broadly **matches HSC**

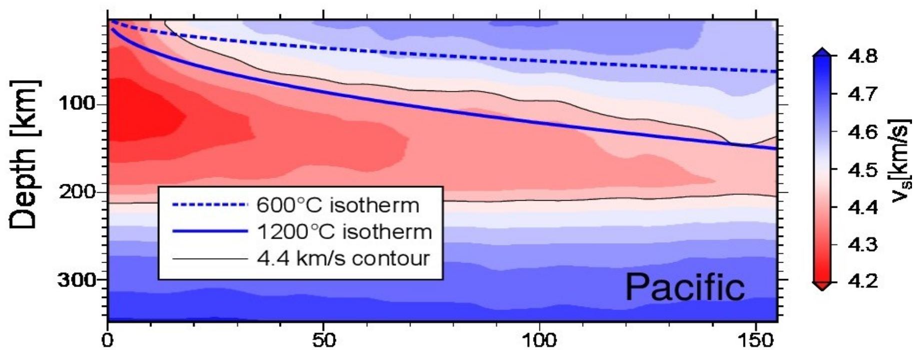

Tests indicate that flatness is **no artifact**

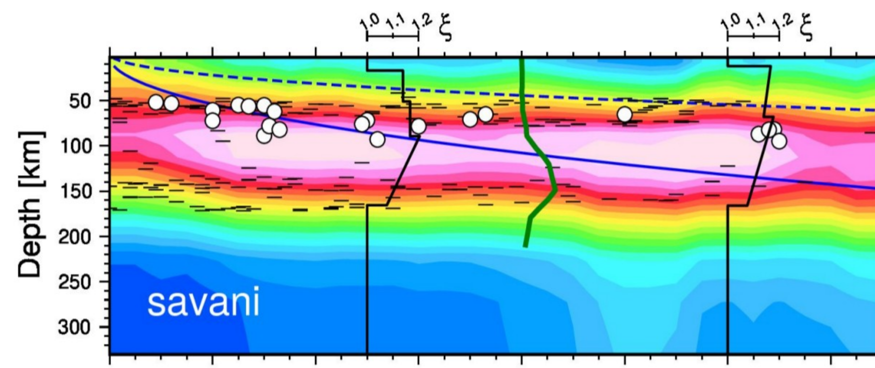

Azim. aniso. from LPO vs. sl2013sv **match**

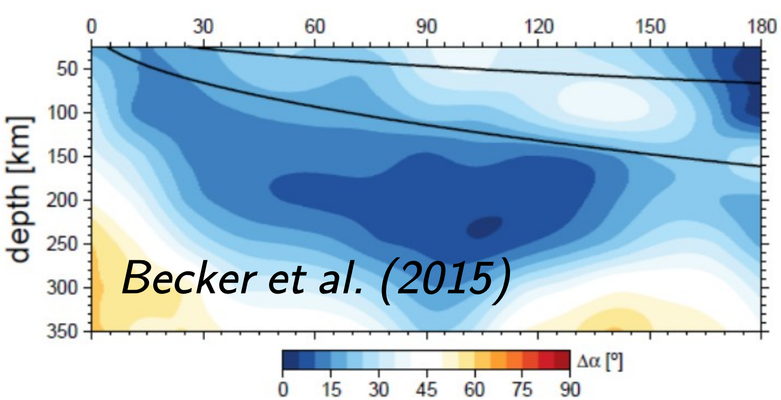

Pure LPO model doesn't work, **too deep**

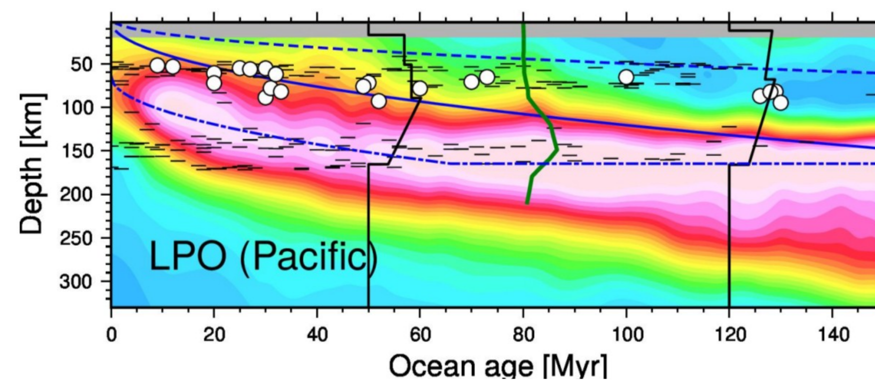

(3) Summary of results

Isotropic structure broadly **matches HSC**

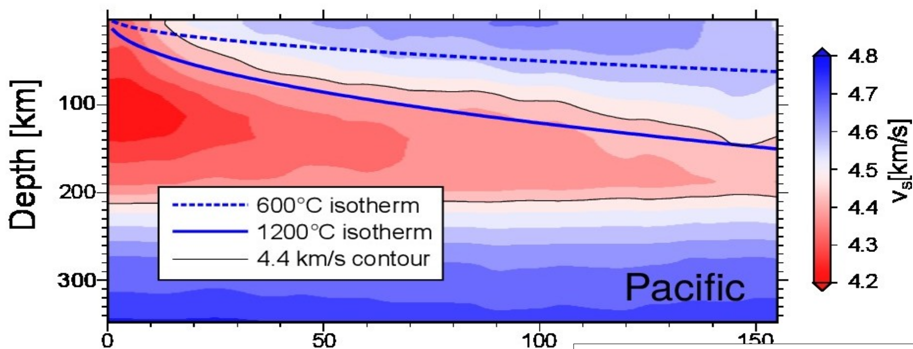

Tests indicate that flatness is **no artifact**

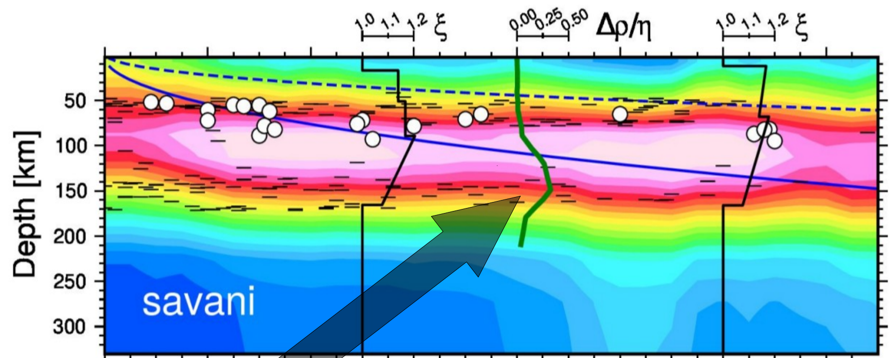

Azim. aniso. from LPO vs. sl20

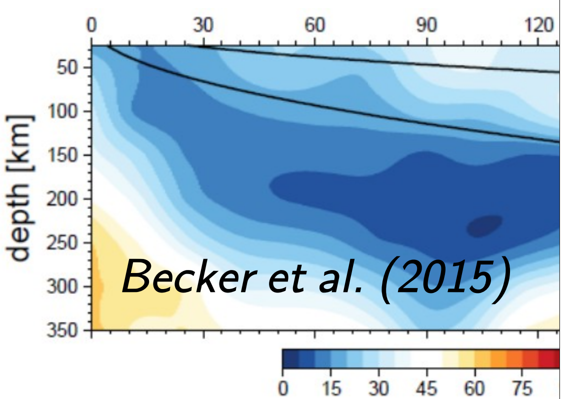

del doesn't work, **too deep**

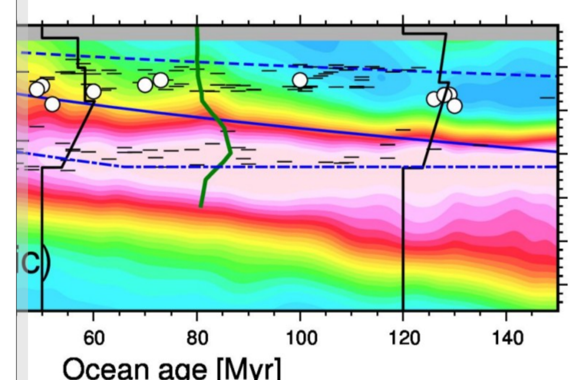

Increased partial melt mobility (Sakamaki et al. 2013)

(3) Summary of results

Isotropic structure broadly **matches HSC**

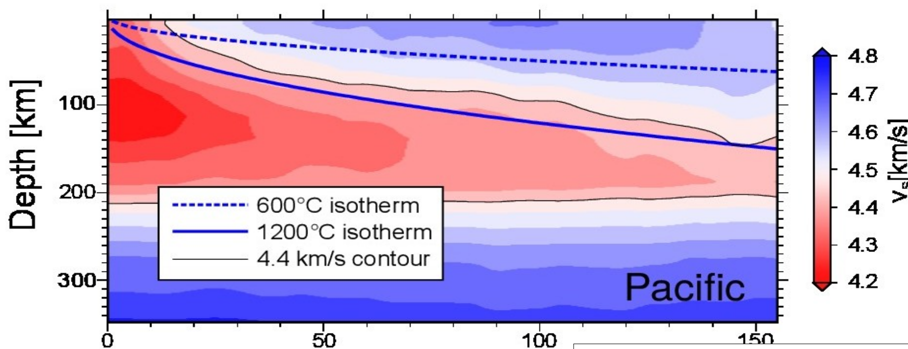

Tests indicate that flatness is **no artifact**

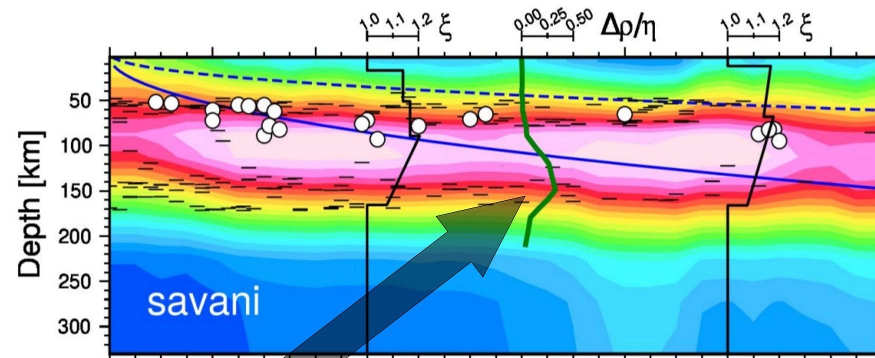

Azim. aniso. from LPO vs. sl20

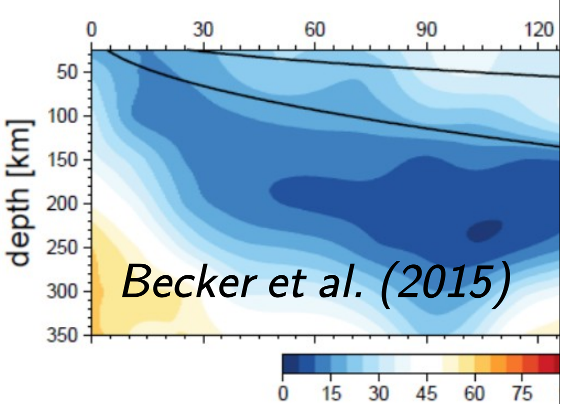

Increased partial melt mobility

(Sakamaki et al. 2013)

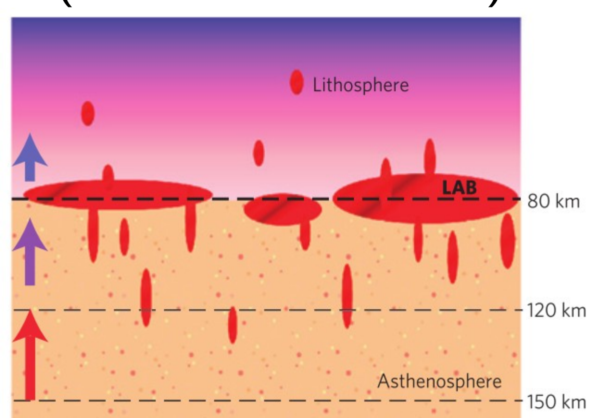

del doesn't work, **too deep**

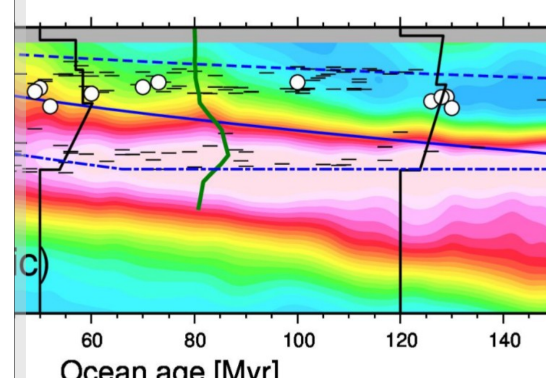

(3) Summary of results

Unified conceptual model of the upper mantle

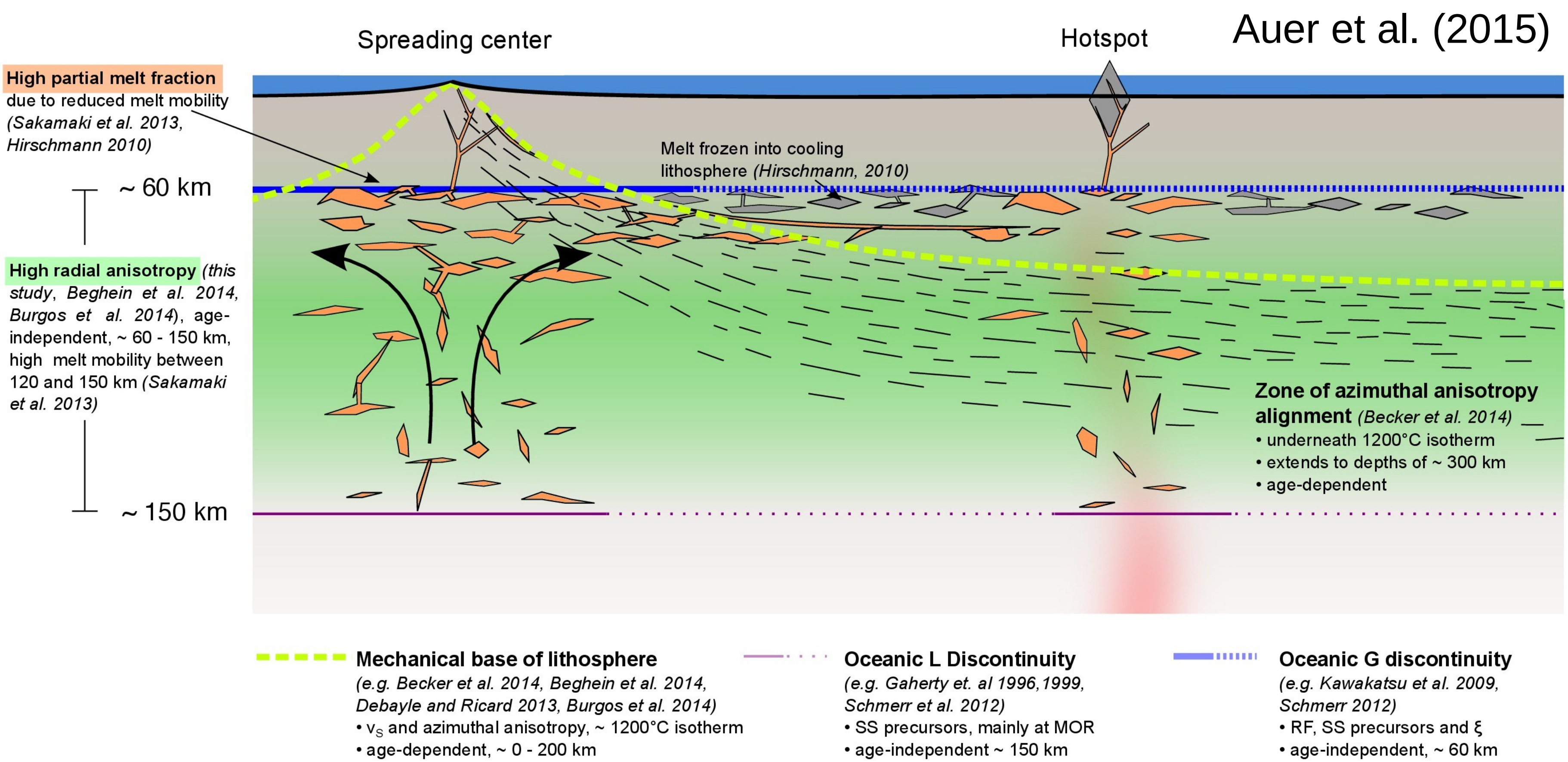

(3) Summary of results

Unified conceptual model of the upper mantle

- G is probably not the LAB, but rather a mid-lithospheric discontinuity, as seen under continents
- Radial anisotropy sees frozen-in (100Ma-1Ga) structure (petrofabrics, melt lamellae) + contributions from asthenospheric LPO
- Azimuthal anisotropy dominated LPO from recent (0-100 Ma) mantle flow, marks the “mechanical LAB”

(4) Compositional tomography

Summary of results

$(v_P - v_{P\_exp})/v_{P\_exp}$

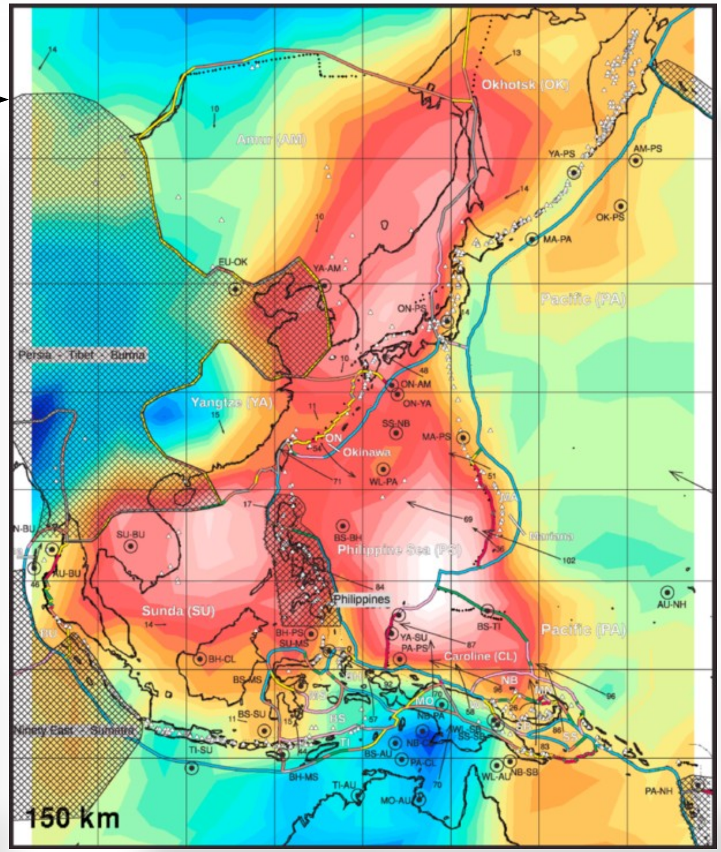

Scaling:

$$\gamma \frac{\delta \ln V_{SV}}{\delta \ln V_{PV}} = \gamma \frac{\delta \ln V_{SH}}{\delta \ln V_{PH}} = \gamma R_{S/P}$$

Key points

- *SPani*: joint model of v_P and v_S variations in the Earth's mantle
- Anomalous v_{P}/v_{S} ratios at marginal basins
- Might be related to hydration

(5) Hybrid waveform tomography

Motivation: Using regional waves?

- Resolution of tele-seismic P-waves is limited, especially in the transition zone
- Can we use new datatypes such as regional body waves to overcome this problem?

(5) Hybrid waveform tomography

Motivation: Using regional waves?

- Resolution of tele-seismic P-waves is limited, especially in the transition zone
- Can we use new datatypes such as regional body waves to overcome this problem?

... triplicated P-waves?

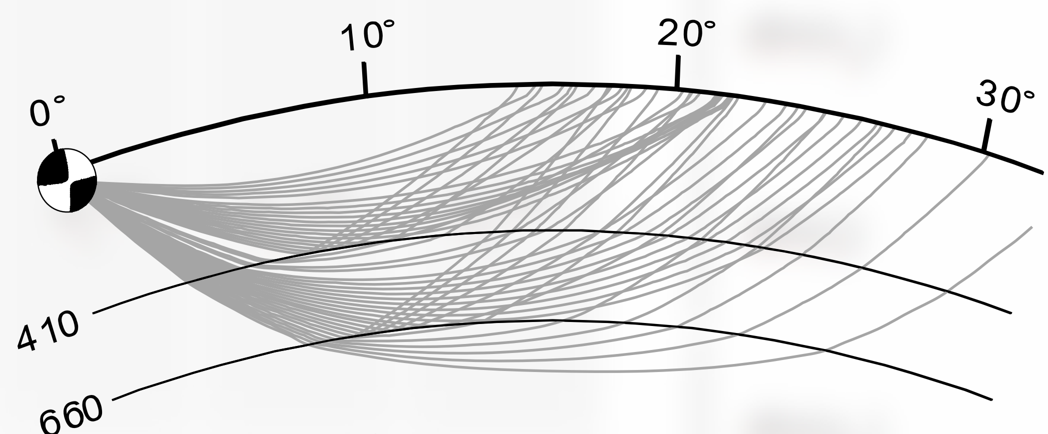

- Cannot be modeled with ray theory
- $\Delta = 14 - 32°$

(5) Hybrid waveform tomography

Motivation: Using regional waves?

- Resolution of tele-seismic P-waves is limited, especially in the transition zone
- Can we use new datatypes such as regional body waves to overcome this problem?

Yes! Cf. *Stähler et al. (2012)*

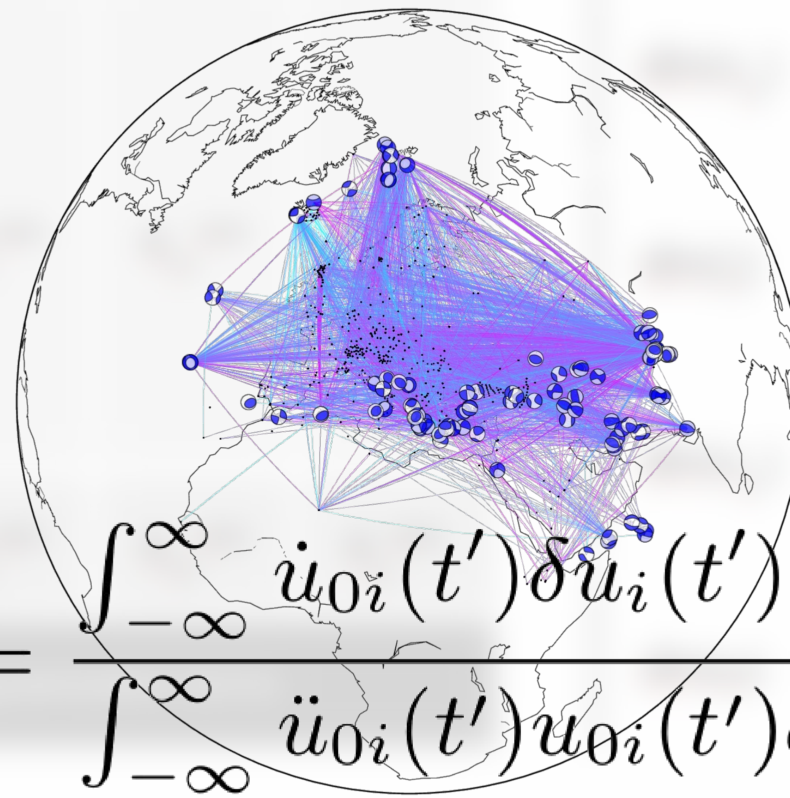

$$\delta T_r = \frac{\int_{-\infty}^{\infty} \dot{u}_{0i}(t')\delta u_i(t')dt'}{\int_{-\infty}^{\infty} \ddot{u}_{0i}(t')u_{0i}(t')dt'}$$

(5) Hybrid waveform tomography

Summary of the inverse problem

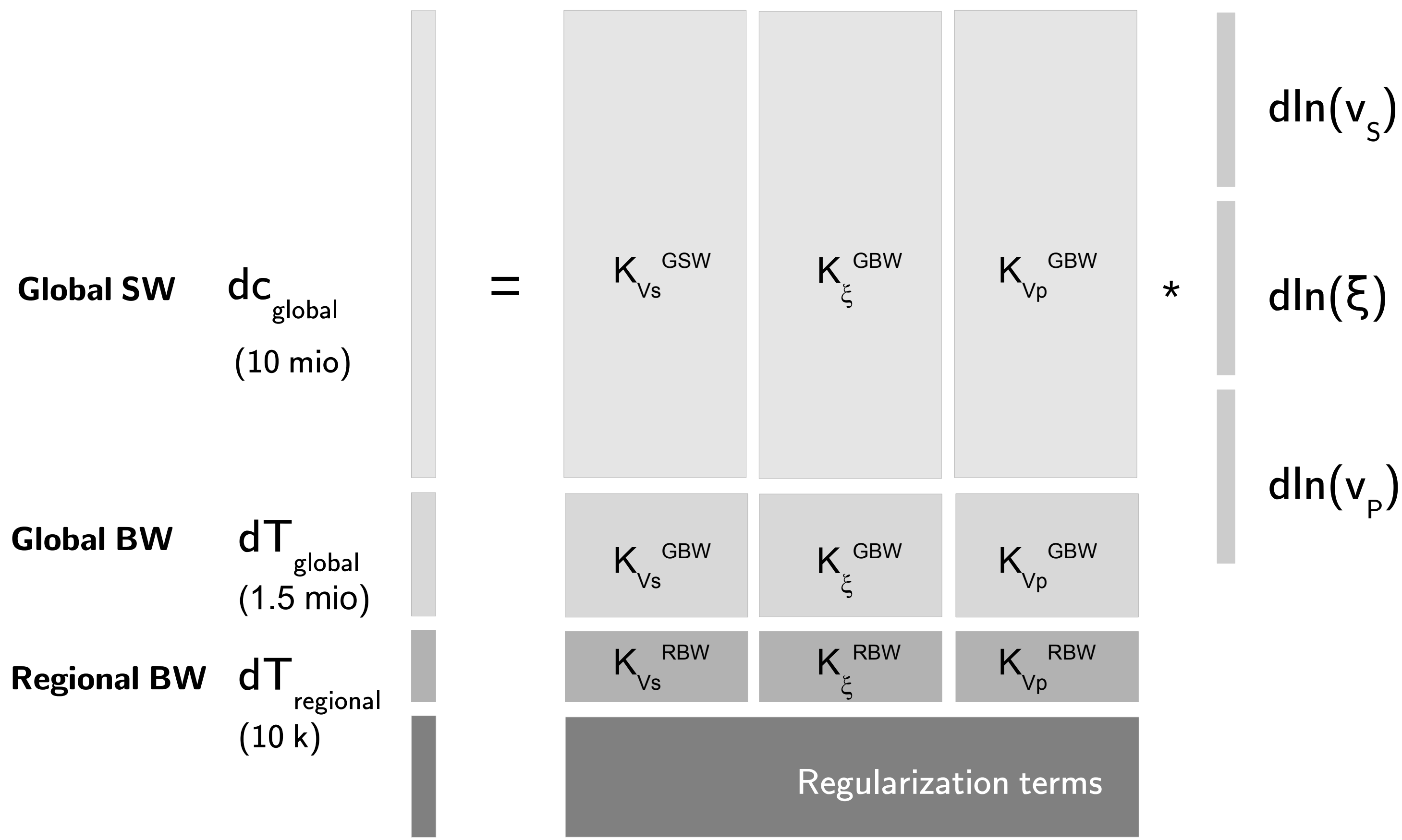

(5) Hybrid waveform tomography

Summary of the inverse problem

Cannot use ray theory for new data → AxiSEM

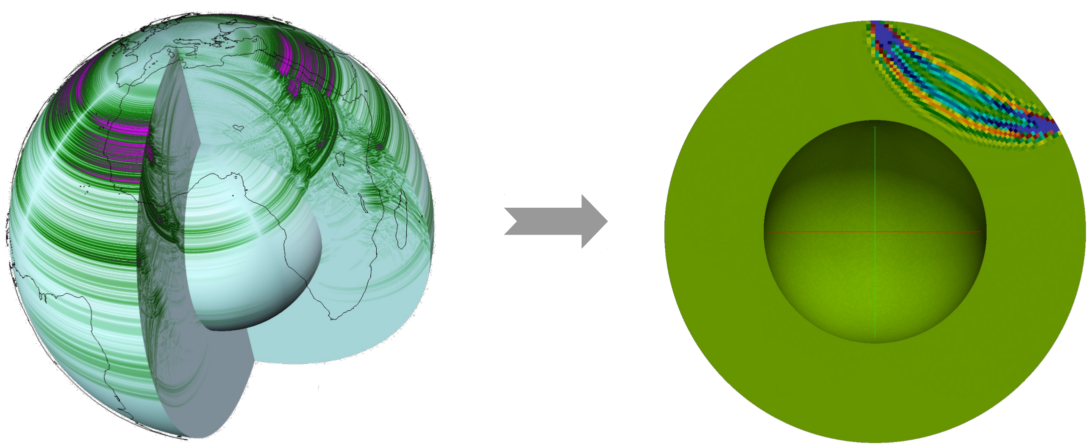

Interaction b/w 1D forward and backward wavefields

Glob

Glob

Regi

Regularization terms

(5) Hybrid waveform tomography

Summary of the inverse problem

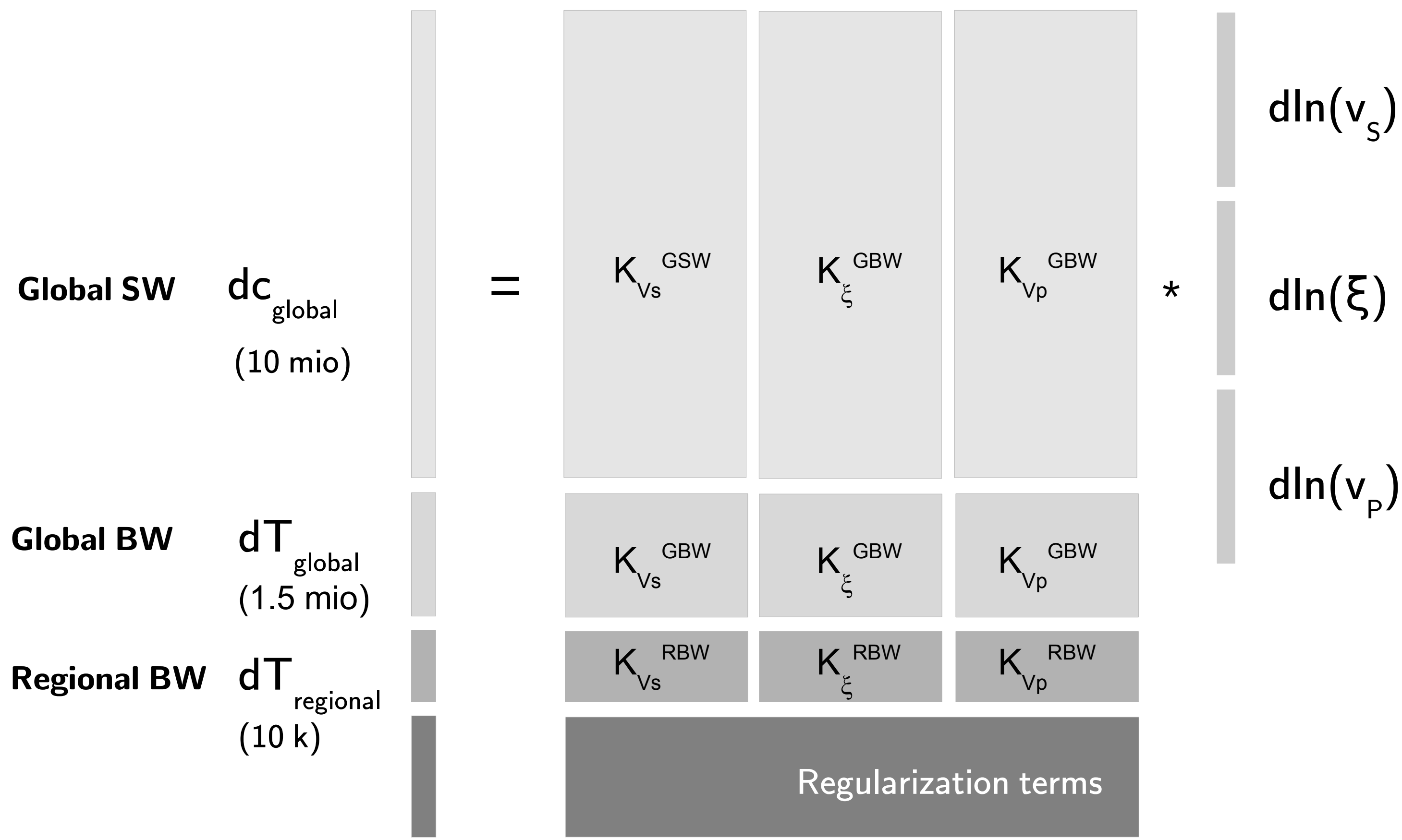

(5) Hybrid waveform tomography

MCkernel: Kernel quadrature

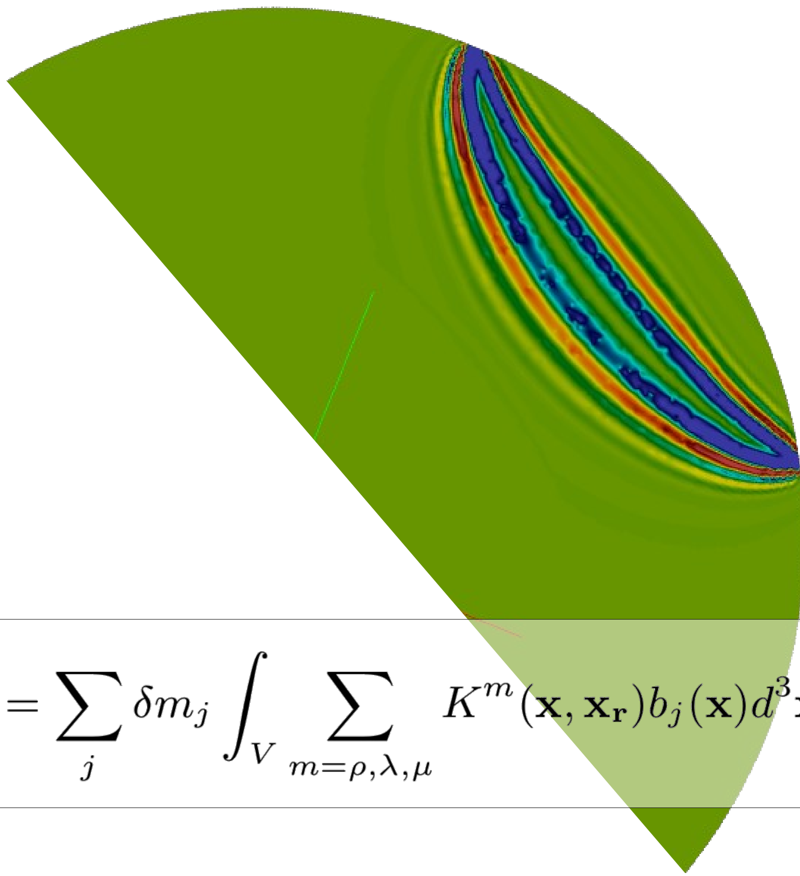

$$\delta T_r = \sum_j \delta m_j \int_V \sum_{m=\rho,\lambda,\mu} K^m(\mathbf{x}, \mathbf{x_r}) b_j(\mathbf{x}) d^3\mathbf{x}$$

(5) Hybrid waveform tomography

MCkernel: Kernel quadrature

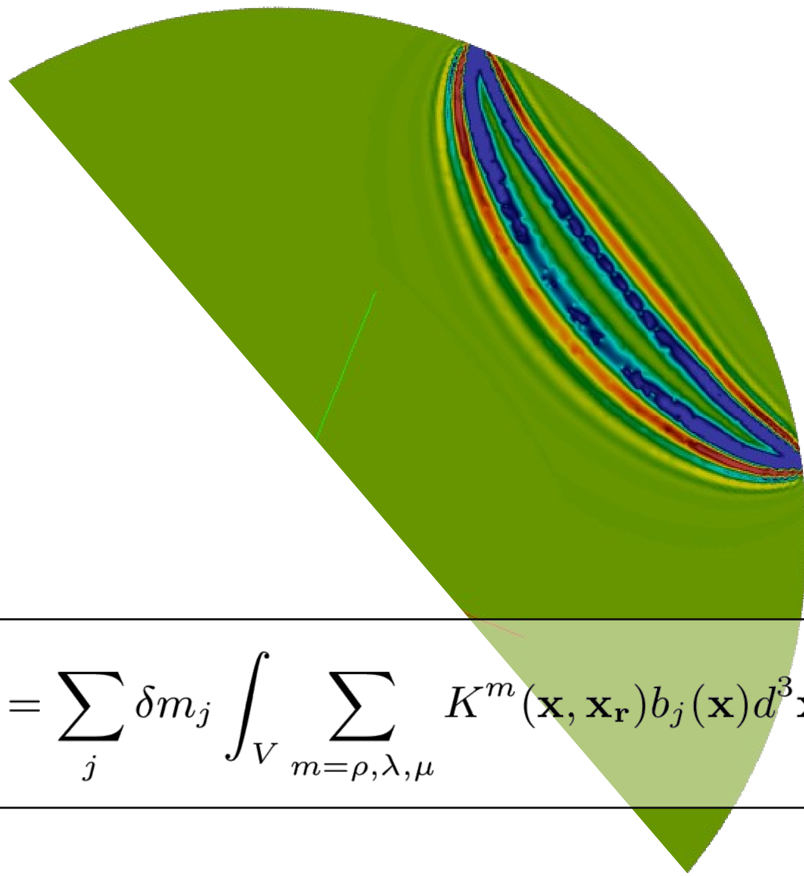

$$\delta T_r = \sum_j \delta m_j \int_V \sum_{m=\rho,\lambda,\mu} K^m(\mathbf{x}, \mathbf{x_r}) b_j(\mathbf{x}) d^3\mathbf{x}$$

- Parallel Monte-Carlo integration approach

(5) Hybrid waveform tomography

MCkernel: Kernel quadrature

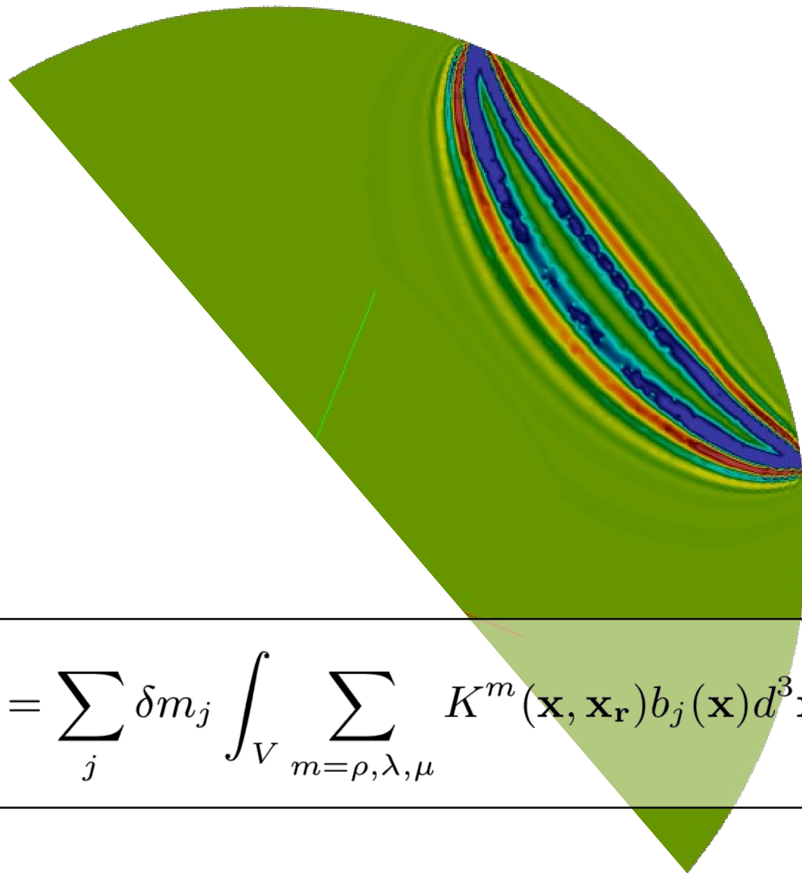

$$\delta T_r = \sum_j \delta m_j \int_V \sum_{m=\rho,\lambda,\mu} K^m(\mathbf{x}, \mathbf{x_r}) b_j(\mathbf{x}) d^3\mathbf{x}$$

- Parallel Monte-Carlo integration approach
- Supports tetrahedral and voxel meshes

(5) Hybrid waveform tomography

MCkernel: Kernel quadrature

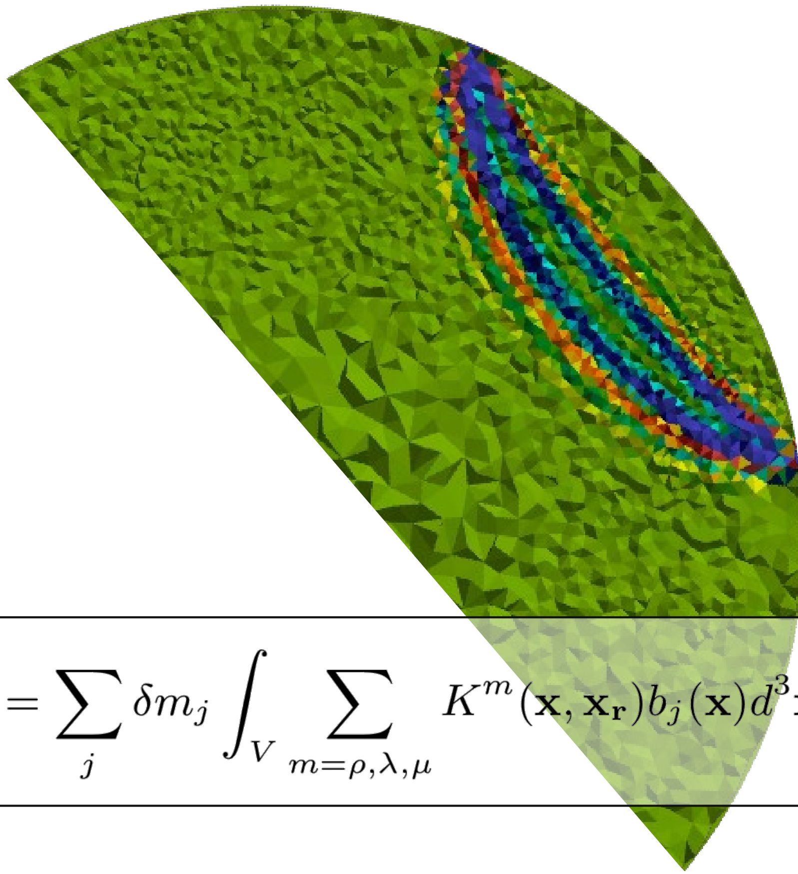

$$\delta T_r = \sum_j \delta m_j \int_V \sum_{m=\rho,\lambda,\mu} K^m(\mathbf{x}, \mathbf{x_r}) b_j(\mathbf{x}) d^3\mathbf{x}$$

- Parallel Monte-Carlo integration approach
- Supports tetrahedral and voxel meshes

(5) Hybrid waveform tomography

MCkernel: Kernel quadrature

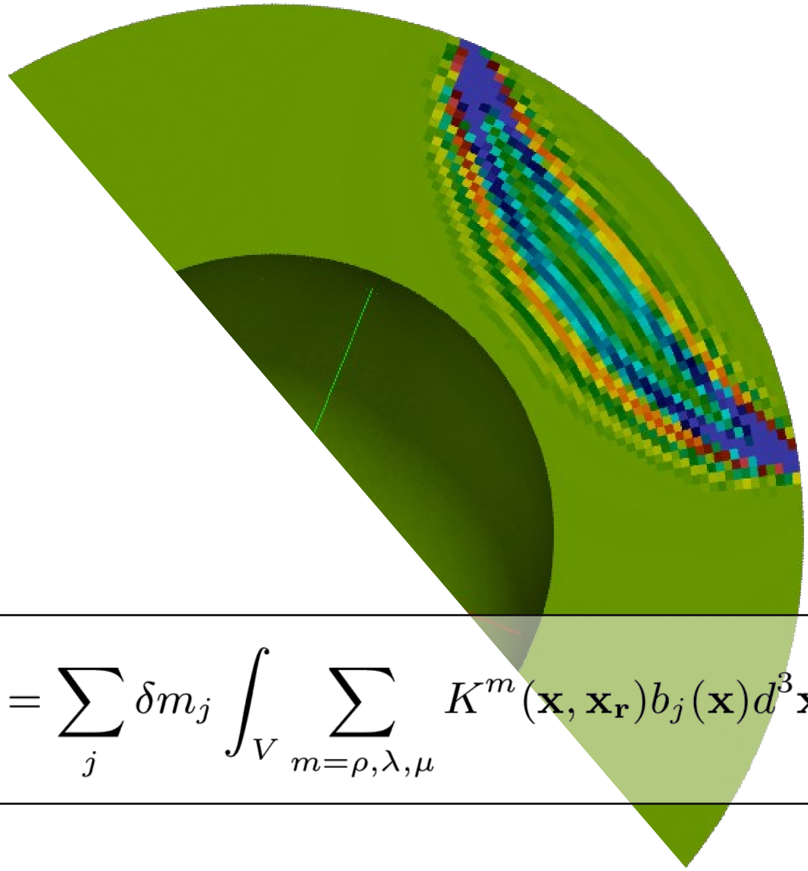

$$\delta T_r = \sum_j \delta m_j \int_V \sum_{m=\rho,\lambda,\mu} K^m(\mathbf{x}, \mathbf{x_r}) b_j(\mathbf{x}) d^3\mathbf{x}$$

- Parallel Monte-Carlo integration approach
- Supports tetrahedral and voxel meshes

(5) Hybrid waveform tomography

MCkernel: Kernel quadrature

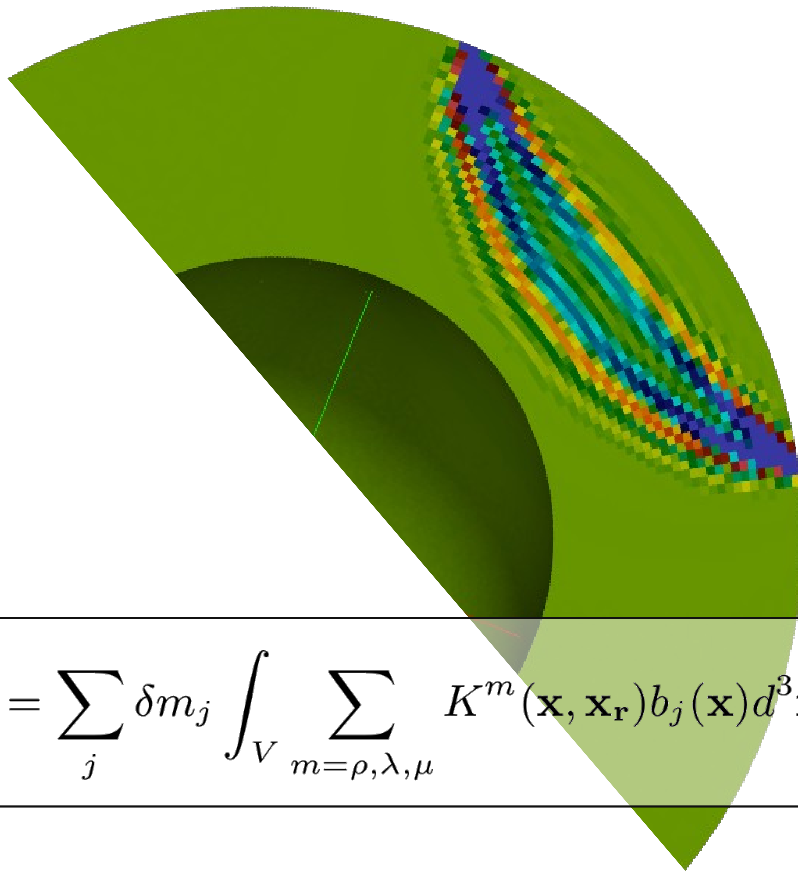

$$\delta T_r = \sum_j \delta m_j \int_V \sum_{m=\rho,\lambda,\mu} K^m(\mathbf{x}, \mathbf{x_r}) b_j(\mathbf{x}) d^3\mathbf{x}$$

- Parallel Monte-Carlo integration approach
- Supports tetrahedral and voxel meshes
- Available for download @ https://github.com/sstaehler/mckernel

(5) Hybrid waveform tomography

Prediction quality of kernels

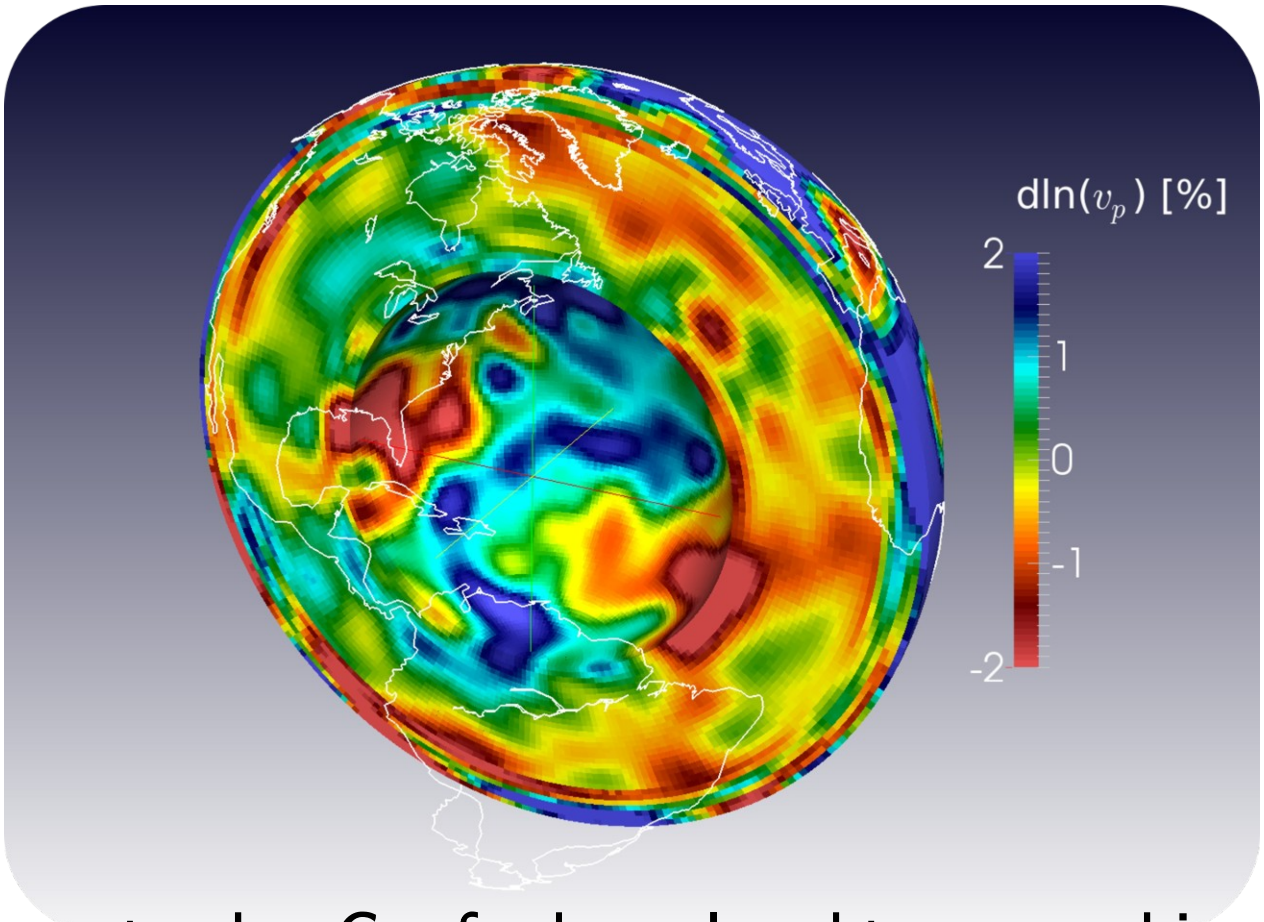

Compute d = Gm for kernel and tomographic model

(5) Hybrid waveform tomography

Prediction quality of kernels

(5) Hybrid waveform tomography

Prediction quality of kernels

(5) Hybrid waveform tomography

Prediction quality of kernels

- Compute SPECFEM synthetics for tomographic model

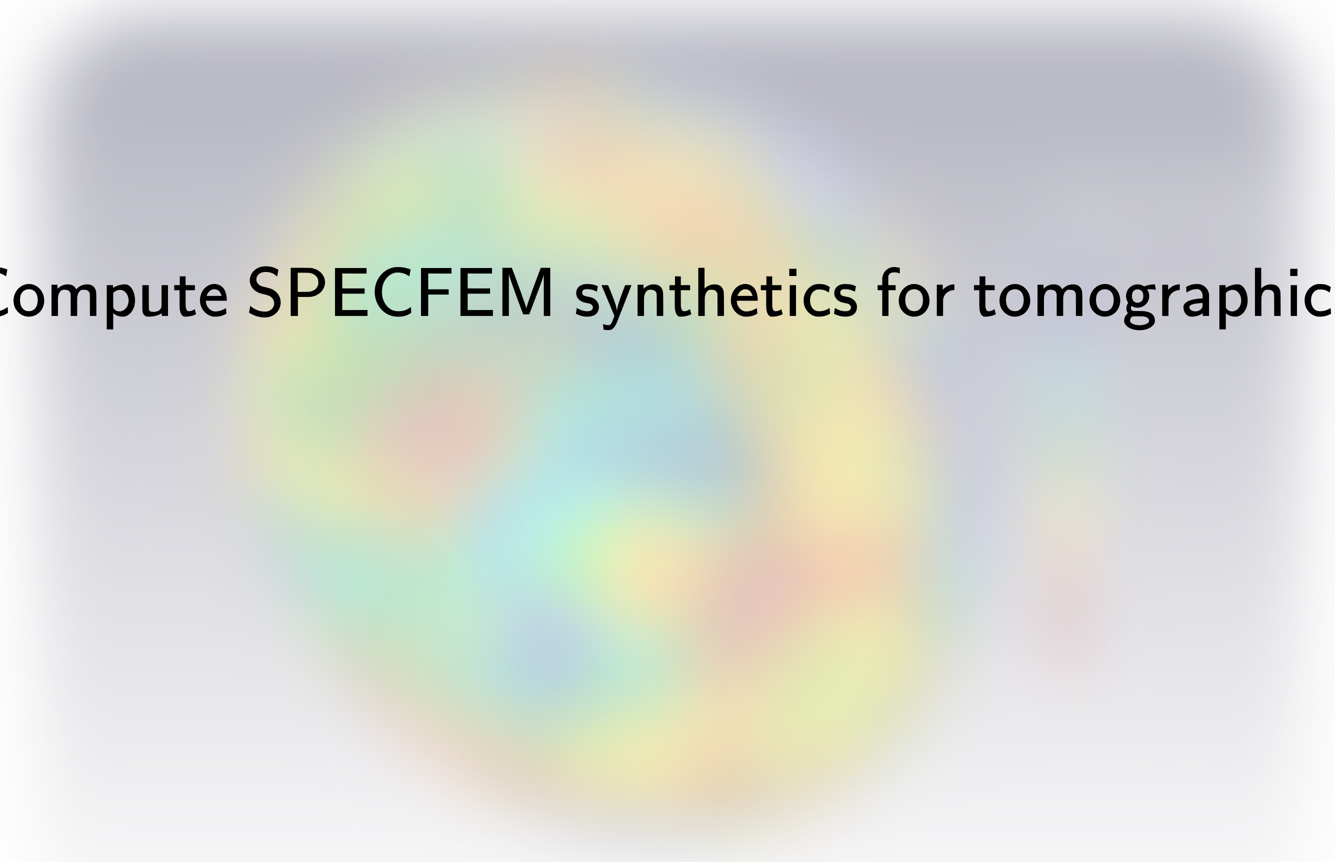

(5) Hybrid waveform tomography

Prediction quality of kernels

- Compute SPECFEM synthetics for tomographic model
- Measure cross-correlation traveltimes for synthetics

(5) Hybrid waveform tomography

Prediction quality of kernels

- Compute SPECFEM synthetics for tomographic model
- Measure cross-correlation traveltimes for synthetics
- Compare predicted and measured traveltimes

(5) Hybrid waveform tomography

Prediction quality of kernels

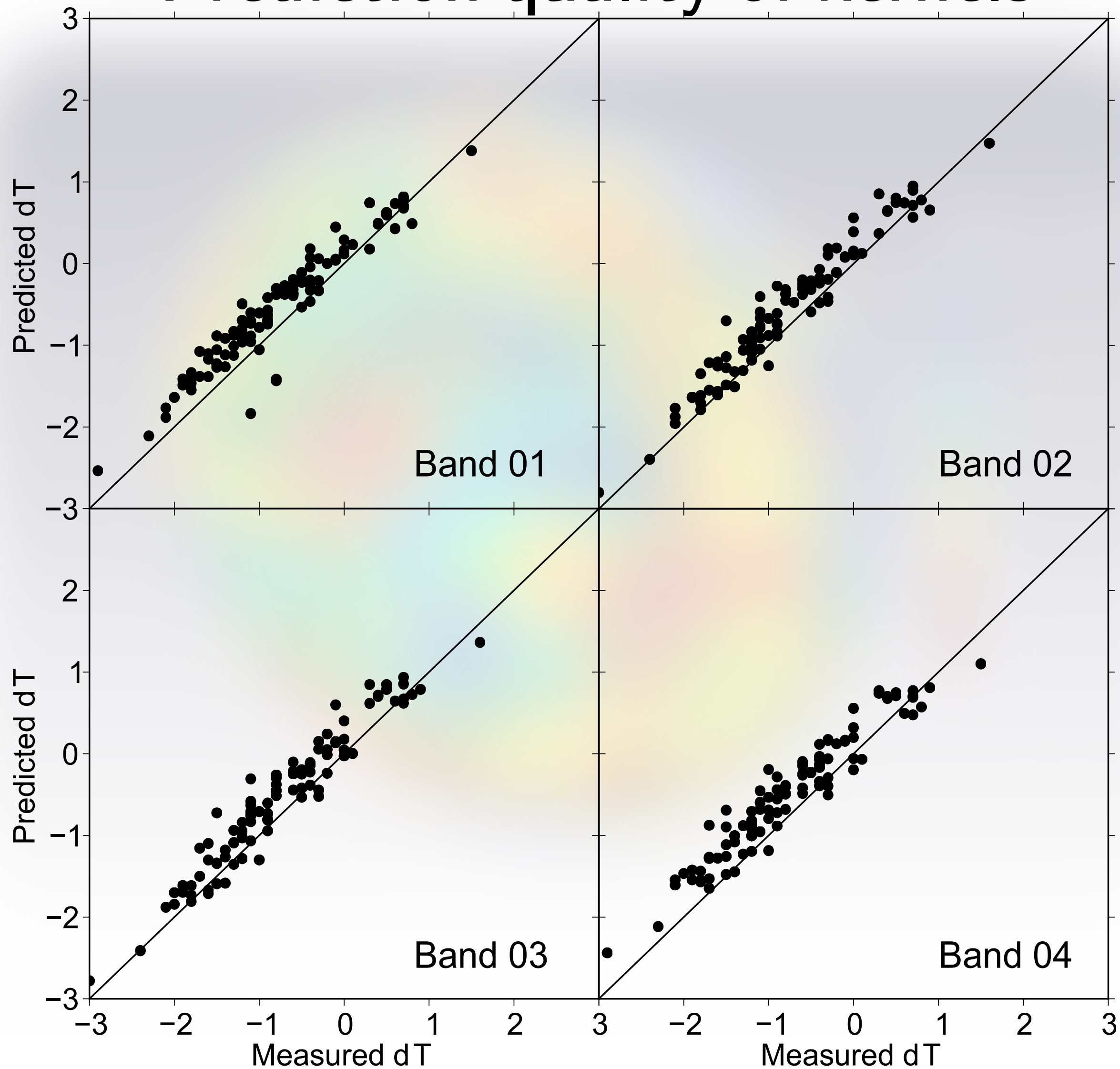

(5) Hybrid waveform tomography

Preliminary model Spani+EU (WIP)

With regional data

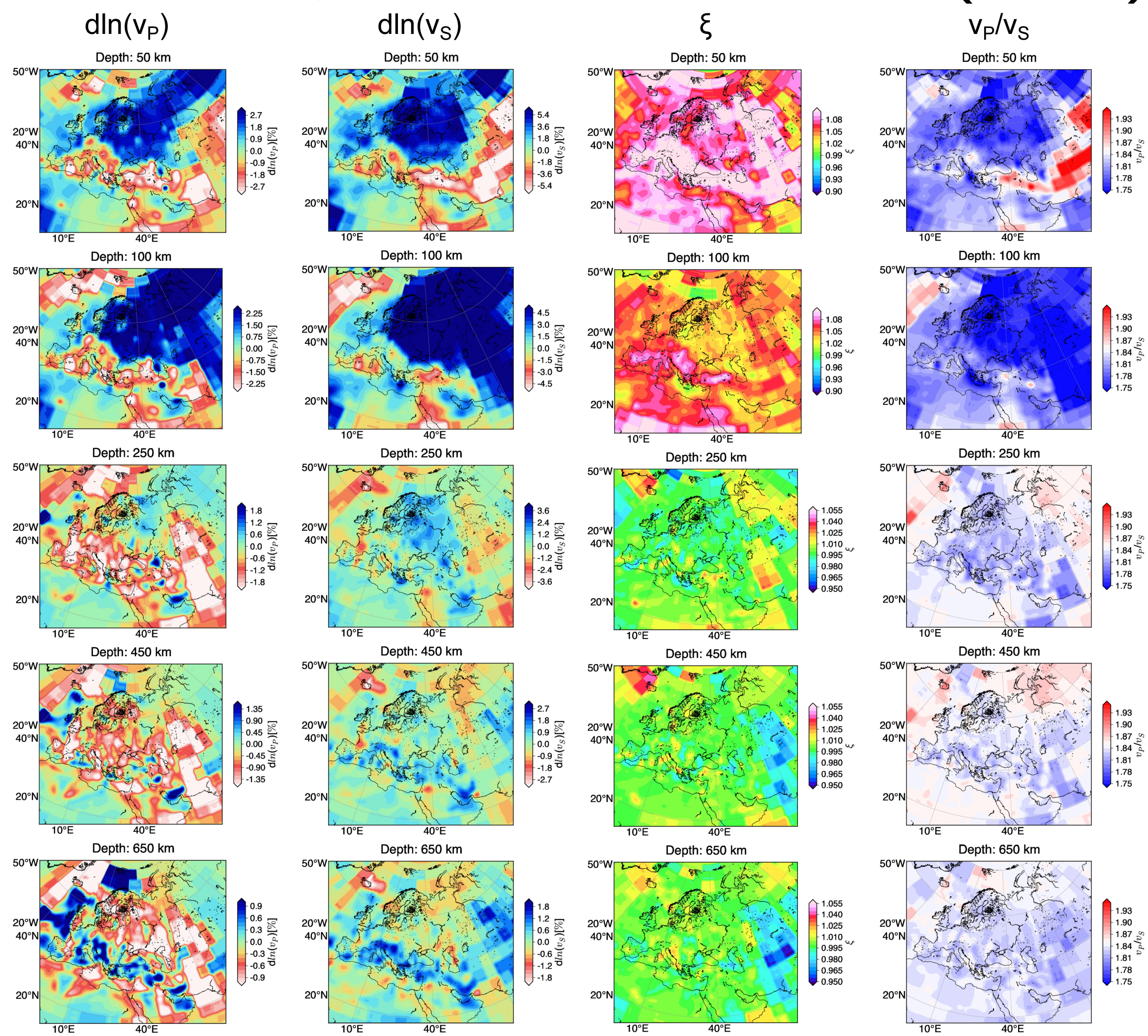

Conclusions

Conclusions

- *Savani*, a model of global whole-mantle radial anisotropy available for download

Conclusions

- *Savani*, a model of global whole-mantle radial anisotropy available for download
- New conceptual model of the oceanic lithosphere-asthenosphere system

Conclusions

- *Savani*, a model of global whole-mantle radial anisotropy available for download
- New conceptual model of the oceanic lithosphere-asthenosphere system
- A new hybrid approach to full waveform inversion, as a compromise between global and regional scale tomography

Conclusions

- *Savani*, a model of global whole-mantle radial anisotropy available for download
- New conceptual model of the oceanic lithosphere-asthenosphere system
- A new hybrid approach to full waveform inversion, as a compromise between global and regional scale tomography

Thank you!

(Apero at 19:00 in J Floor)

Backup slides

Melt mobility

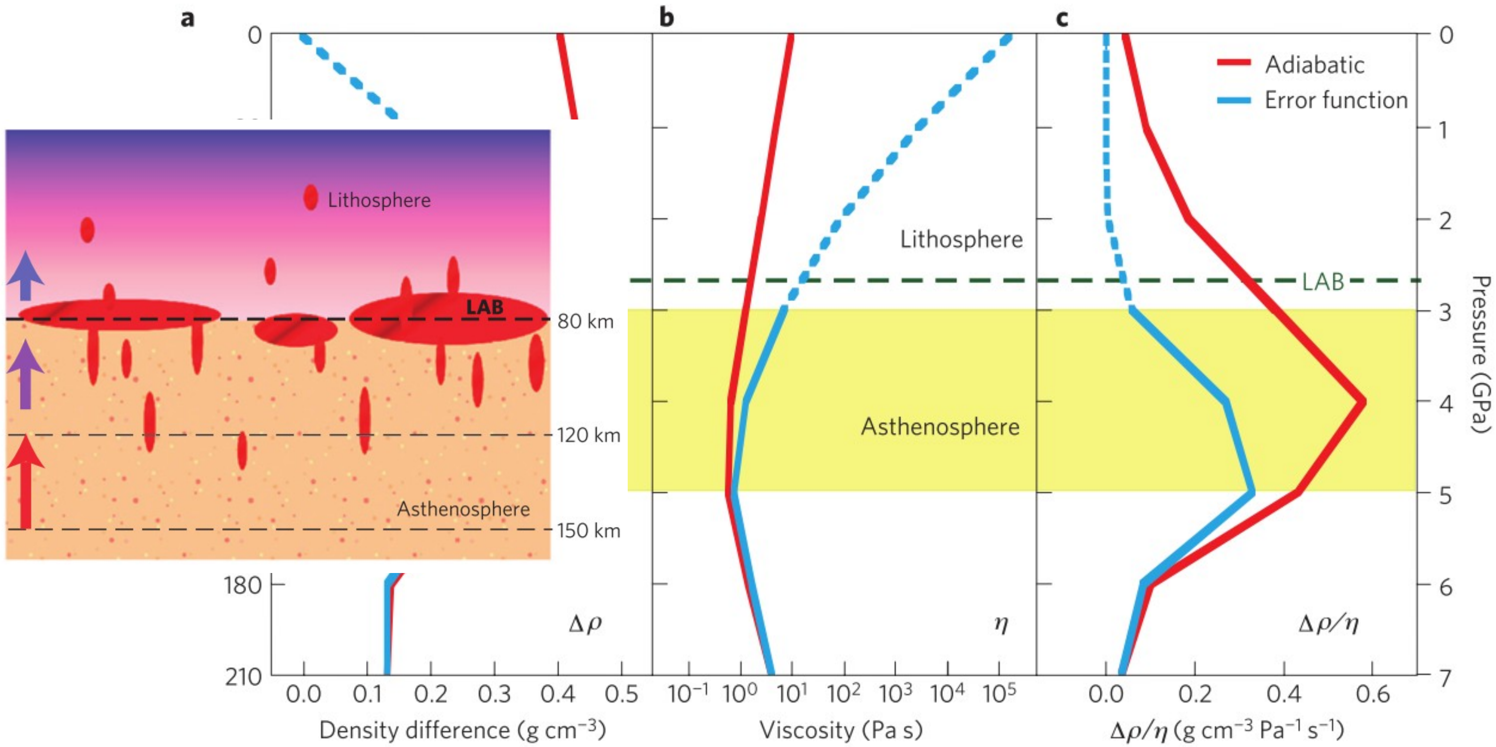

Figure 2 | Magma properties and mobility as a function of depth. a, Density difference between basaltic magma and olivine ($\Delta\rho$) as a function of depth (and pressure). The red and blue lines are based on an adiabatic temperature gradient, and a realistic error-function temperature profile for mature oceanic lithosphere, respectively. The potential temperature is 1,623 K. Yellow shading highlights the depth range with anomalous physical properties of basaltic melts due to the structural transition in Al coordination. **b**, Viscosity (η) of basaltic magma along the same two profiles. Hypothetical subsolidus density and viscosity profiles are dashed. **c**, Mobility $\Delta\rho/\eta$ of basaltic magma along the same two profiles, respectively.

LPO (1)

- LPO = Lattice preferred orientation
- Mainly due to dislocation glide (slip) along certain preferred glide plains and associated internal rotation/alignment of mineral grains
- To a first order, seismic anisotropy closely linked to the direction of shear or kinematic deformation

LPO (2)

- Olivine shows a strong single-crystal elastic anisotropy. Fastest P- and S-wave velocities parallel to [100] crystallographic axis
- 70ties: Experimental studies on olivine indicated [100] axes of crystals to be nearly || to flow direction and (010) plane || to flow plane.
- Analysis of naturally deformed peridotite → [100](010) crystallographic axis of grains often coincide with rock lineation
- MCM + VPSC modelling + simple model of LPO development. **Works well** in case of large length scales and simple dynamics (e.g. Tommasi 1998, Becker 2006)

Xi > 1 = horizontal flow   Xi < 1 = vertical flow

LPO (3)

- New findings in past ~10 years suggest that it's more difficult
- LPO type is sensitive to water, stress, temperature, pressure, melting (→ Carmen's work)
- Way of interpretation of seismic anisotropy needs major modifications!

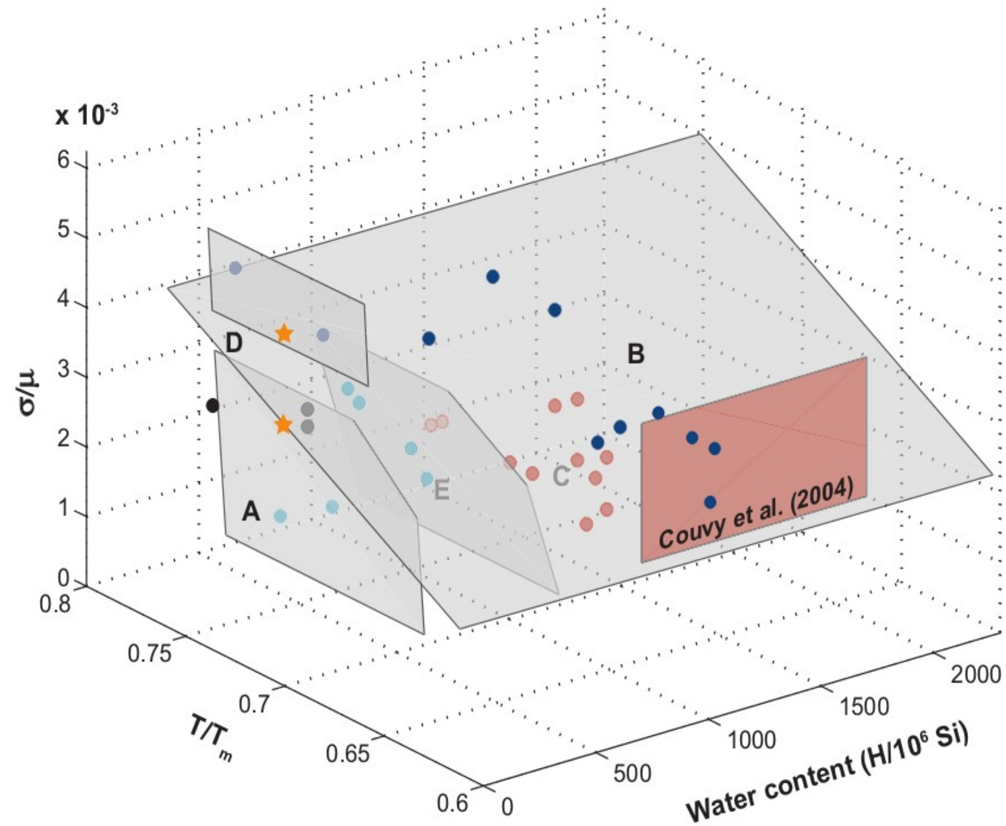

A-type: Lithosphere, low water content

E-type: Astenhosphere, higher water conent

LPO (4)

Shear wave splitting (direction of the polarization of the faster, vertically traveling shear wave)

Fabric	**Horizontal flow**	**Vertical planar flow**
A-type	Parallel to flow	Small splitting
B-type	Normal to flow	Parallel to the plane
C-type	Parallel to flow	Normal to the plane
D-type	Parallel to flow	Small splitting
E-type	Parallel to flow	Small splitting

V_{SH}/V_{SV} anisotropy

Fabric	**Horizontal flow**	**Vertical cylindrical flow**
A-type	$V_{SH}/V_{SV} > 1$	$V_{SH}/V_{SV} < 1$
B-type	$V_{SH}/V_{SV} > 1$	$V_{SH}/V_{SV} > 1$ (weak)
C-type	$V_{SH}/V_{SV} < 1$	$V_{SH}/V_{SV} > 1$ (weak)
D-type	$V_{SH}/V_{SV} > 1$	$V_{SH}/V_{SV} < 1$
E-type	$V_{SH}/V_{SV} > 1$ (weak)	$V_{SH}/V_{SV} < 1$

A & E type most abundant

LPO (5)

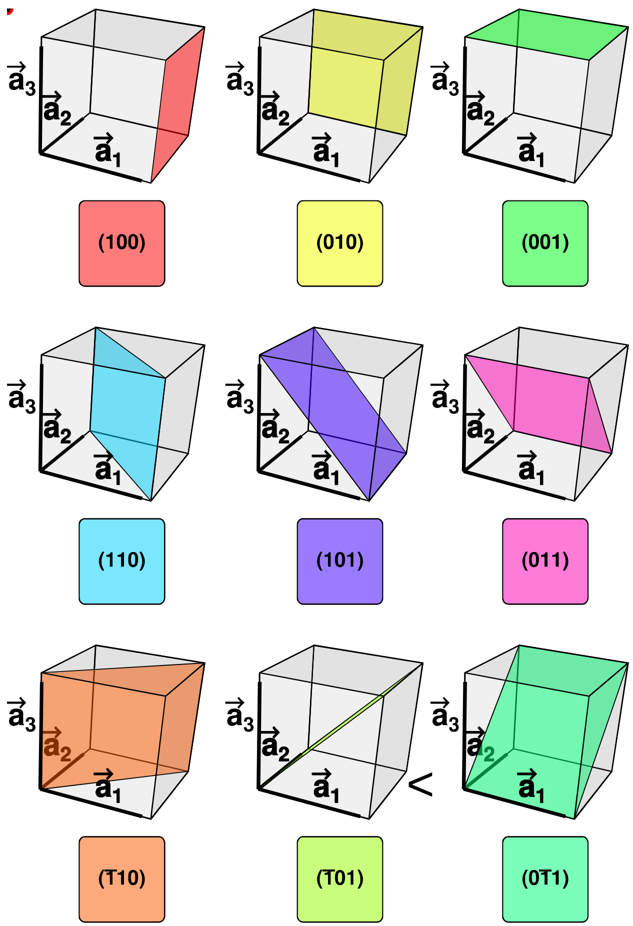

Dominant slip systems in
Various types of olivine LPO

A-type	B-type	C-type
[100] (010)	[001] (010)	[001] (100)

D-type	E-type
[100] $\{0kl\}$	[100] (001)

SKS splitting (1)

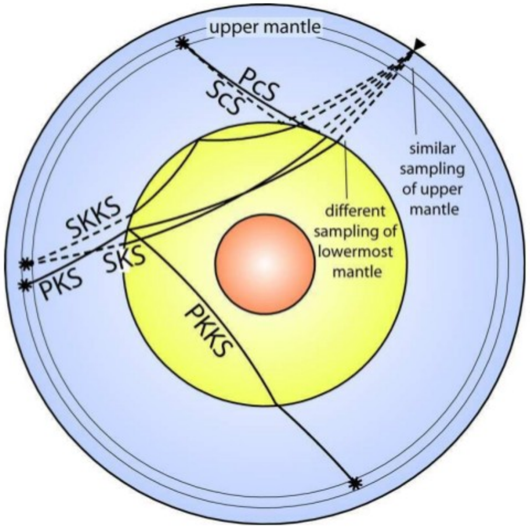

- Vertically incident s-wave, transversing an anisotropic medium
- Polarization removed by transversing the liquid core
- Initial polarization of SKS is in plane of propagation (vertical)
- Splits in fast and slow polarized shear wave
- One can measure the fast axis, the delay time and the splitting angle
- Can be done on S, ScS, SS, PKS, but most popular are SKS and SKKS.
- Differnetial splitting of SKS-SKKS to infer lowermost mantle anisotropy

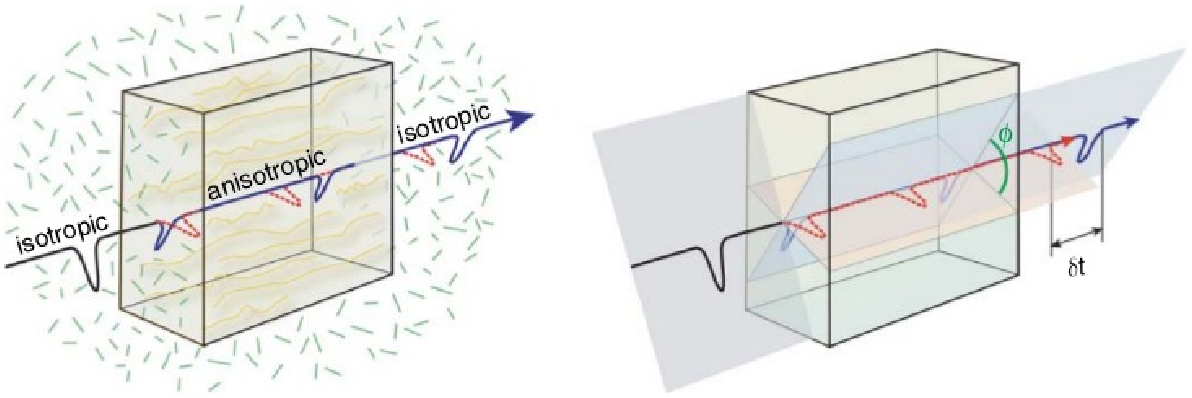

SKS splitting (2)

2ψ azimuthal anisotropy fast axes well reconciled by spatially averaged global shear wave splitting

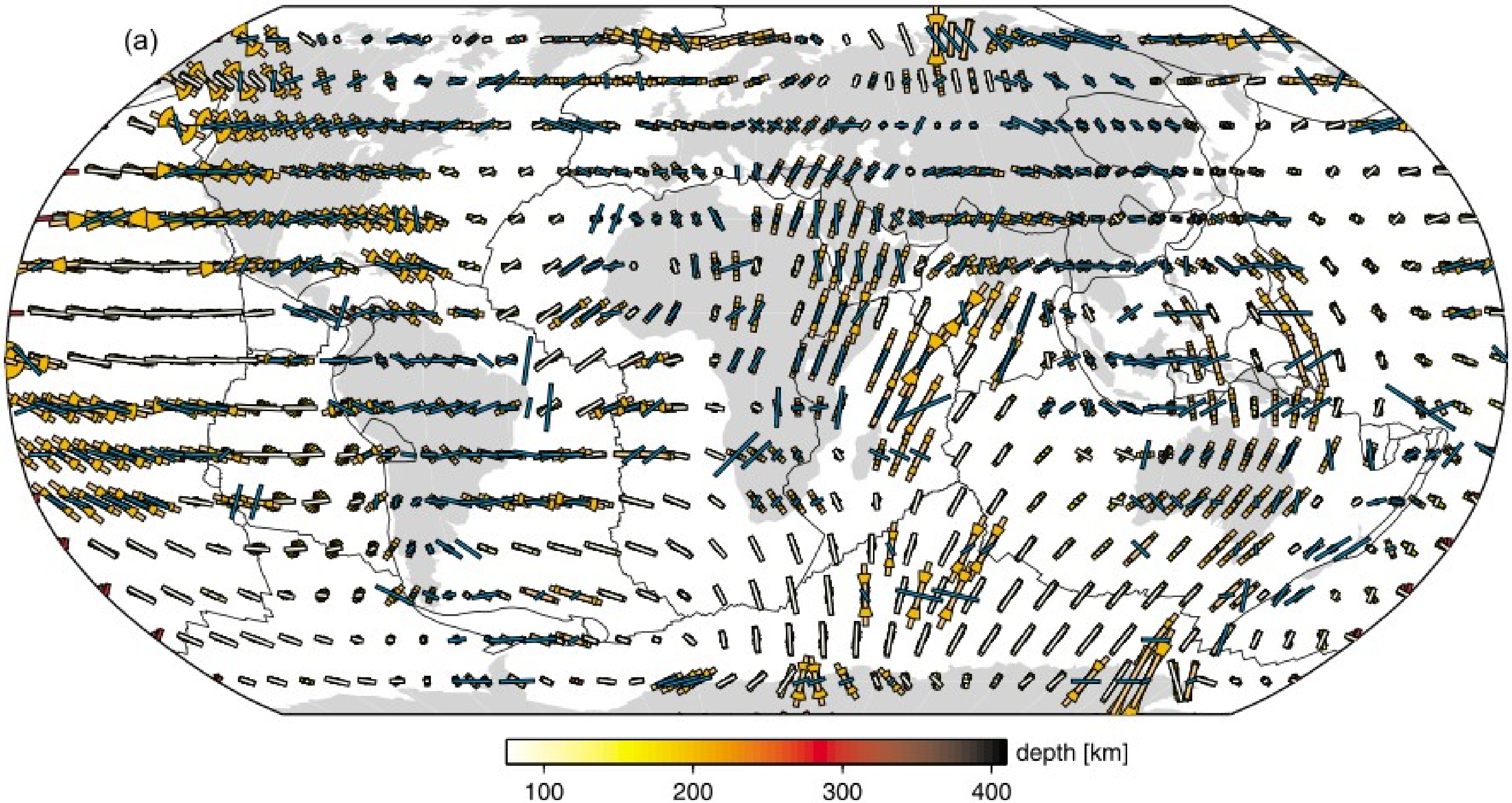

Becker (2011)

SKS splitting (2)

Favier & Chevrot (2003)

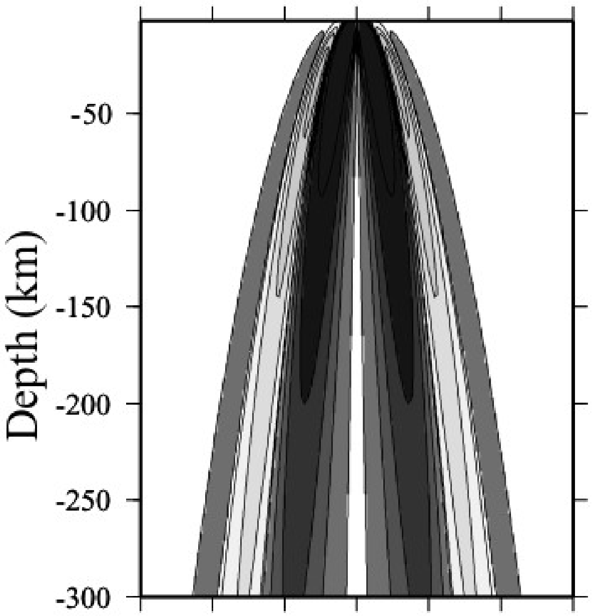

Analytical kernels,
following the formalism
of Dahlen (2000)

In the finite-frequency sense
splitting has also vertical resolution

Long (2008)

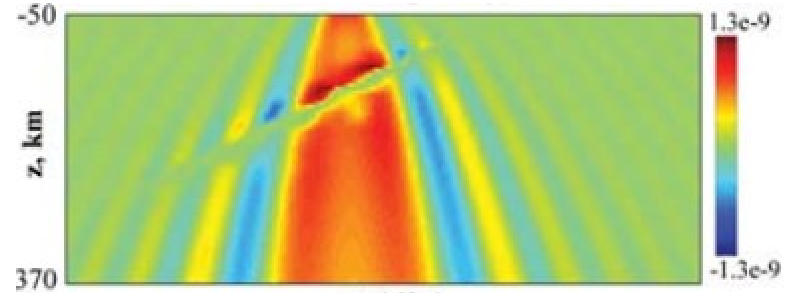

2D kernels in heterogeneous
models, adjoint method

Sieminski (2008)

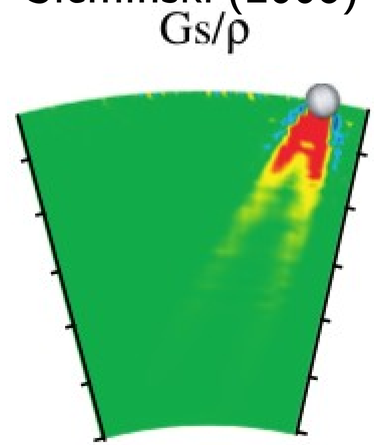

3D kernels in 3D
models, Specfem,
adjoint method

Regional datasets / Mermaids

USarray

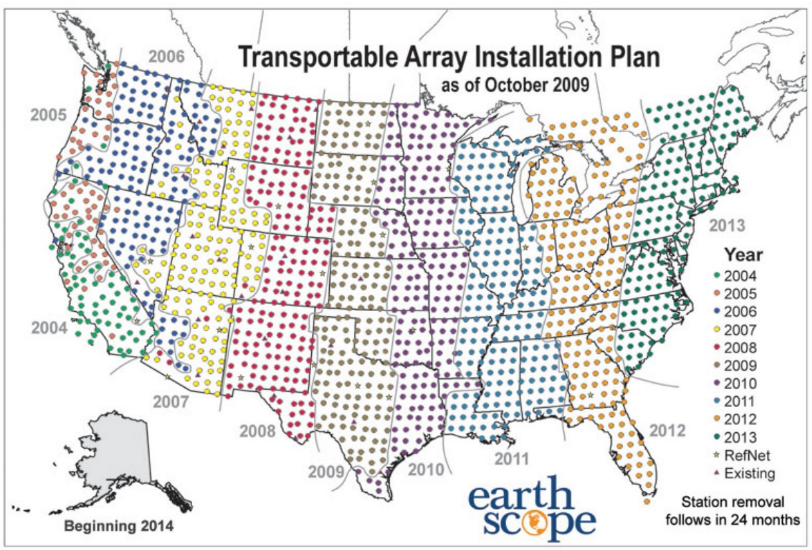

Alparray

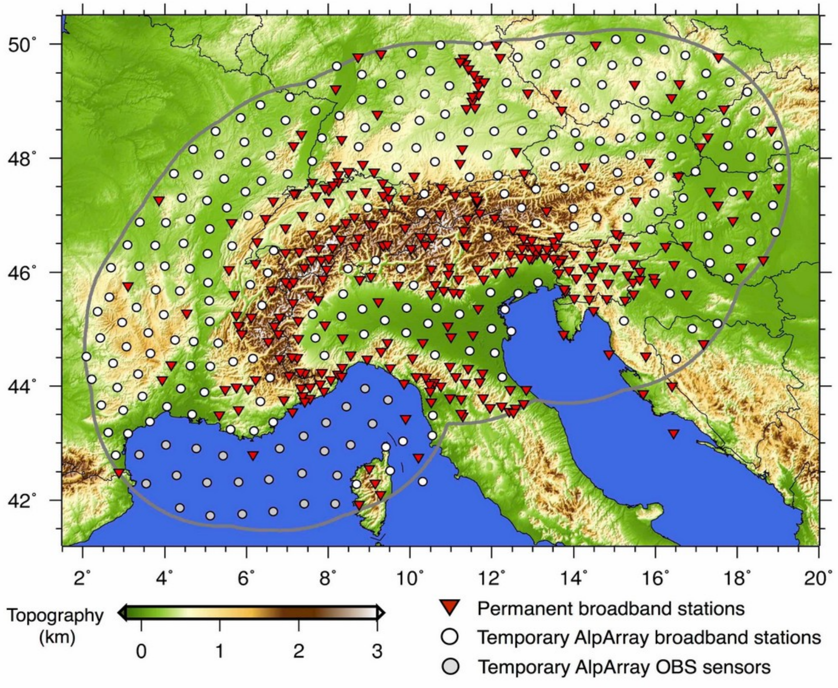

Lower-mantle anisotropy (1)

Anisotropy at 2800 km depth, degrees 2 and 3 only

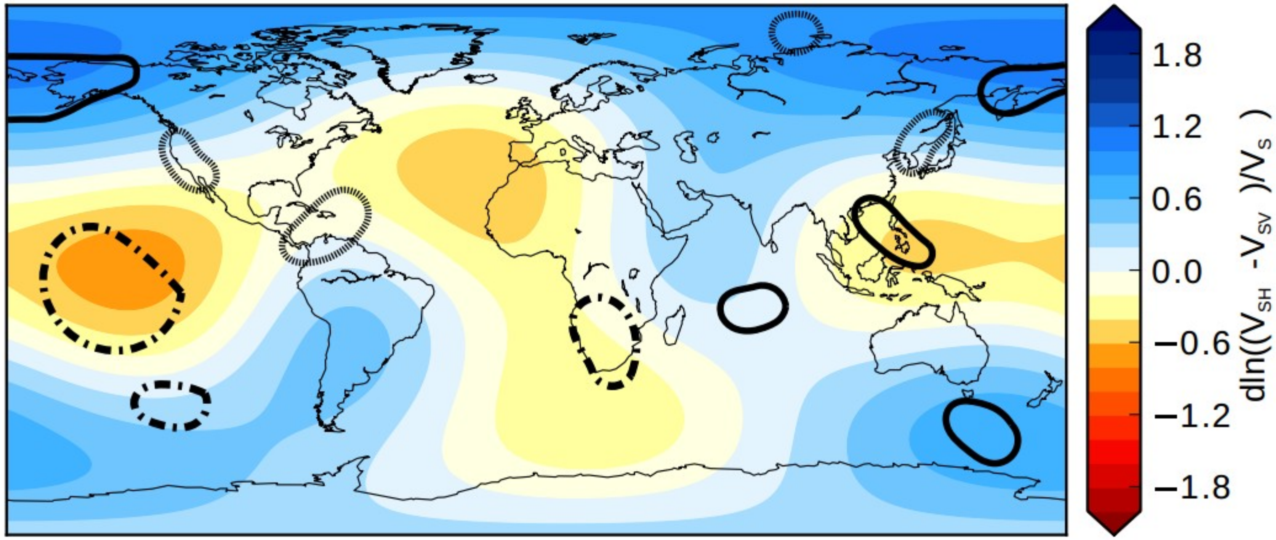

Lower-mantle anisotropy (2)

Required by the data?

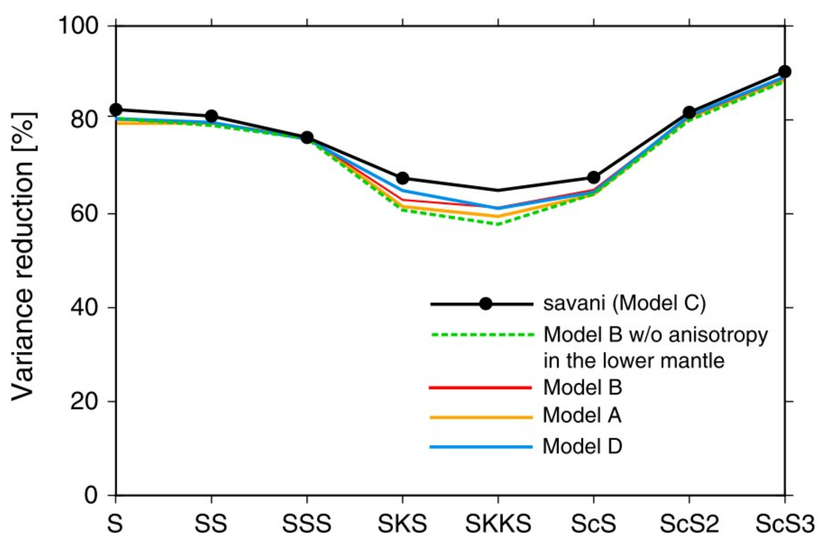

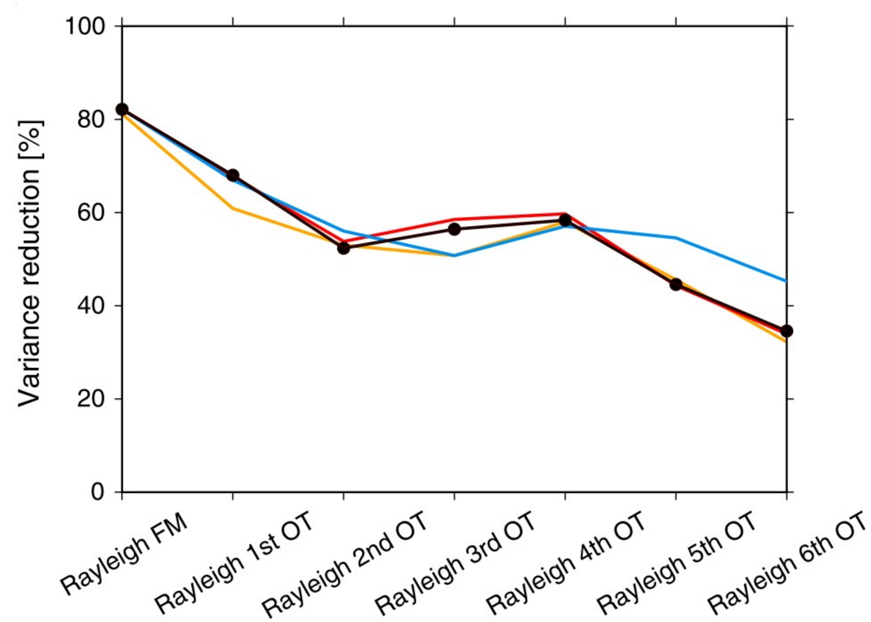

Lower-mantle anisotropy (3)

Summary of LM observations

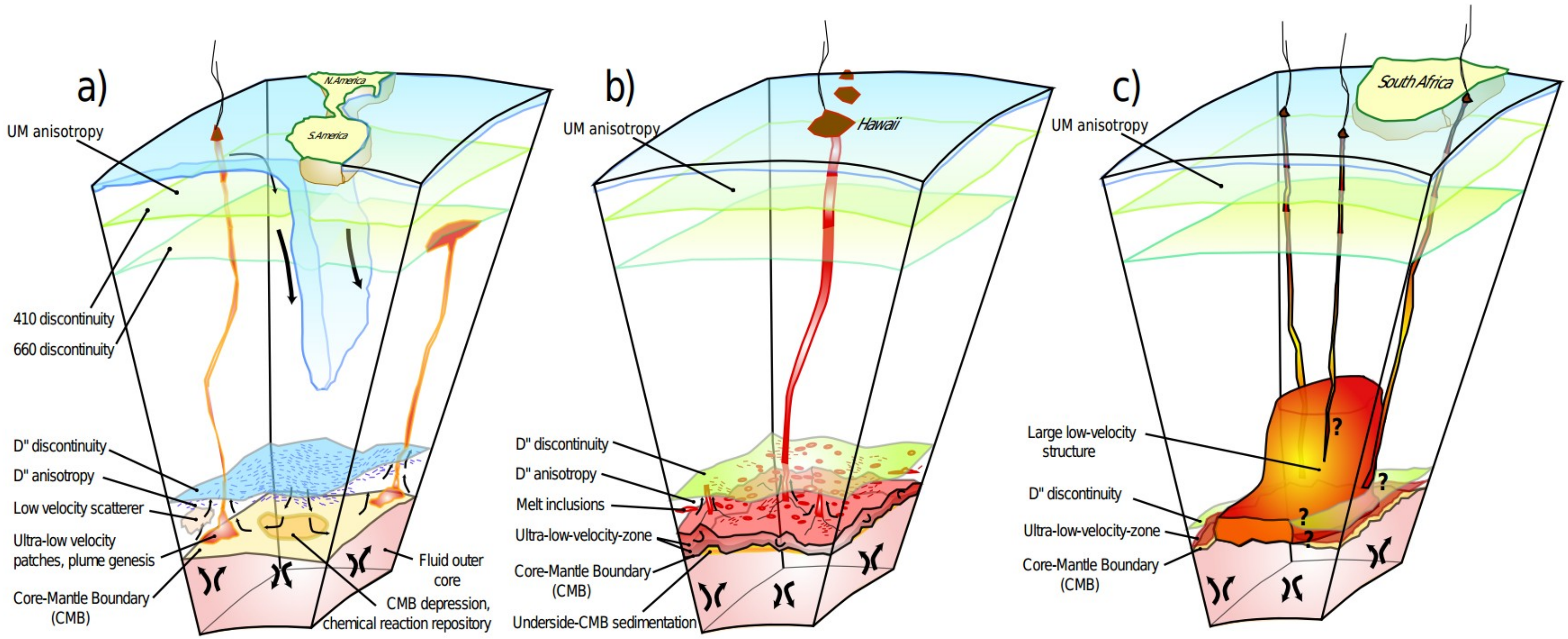

from Garnero (2004)

Lower-mantle anisotropy (2)

Why is there a faster V_{SH} (horizontal flow) associated with regions of fast seismic velocity and faster V_{SV} (vertical flow) close to LLSVP's?

- PPV is the main canditate to explain CMB parallel LPO in the lowermost mantle, being less viscous than PV and intrinsically anisotropic
- Lithosphere sinks towards the CMB, undergoes the PPV phase transition, bends, and is subjected to horizontal deformation, causing LPO type anisotropy?
- Fast V_{SV} might be associated with vertical mass transport at zones of plume genesis near edges of LLSVPS

Fossil (frozen-in) anisotropy

vs. asthenospheric flow

- Paleo-spreading model match confined to shallow regions
- Define a mechanical Lithosphereasthenosphere "boundary" based on transition

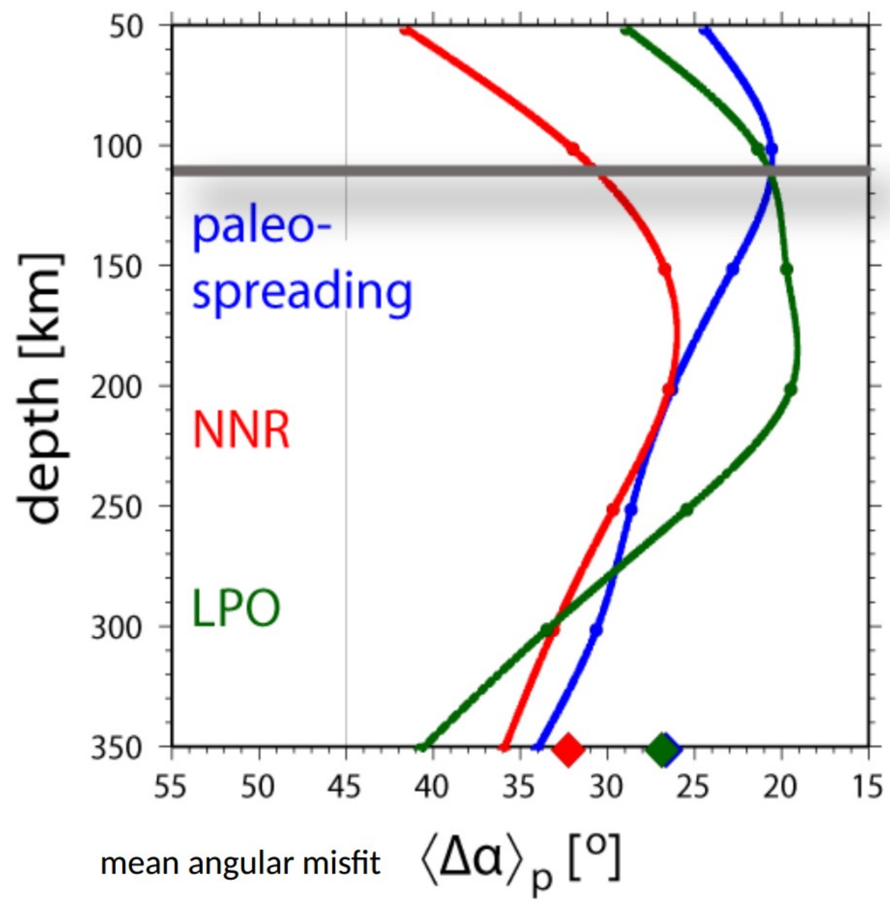

Fit for different LPO models

Azimuthal and radial

- Blue: oceanic correlation for 50-350 km
- Black: global correlation for 50-350 km

→ differently parameterized geodynamic models

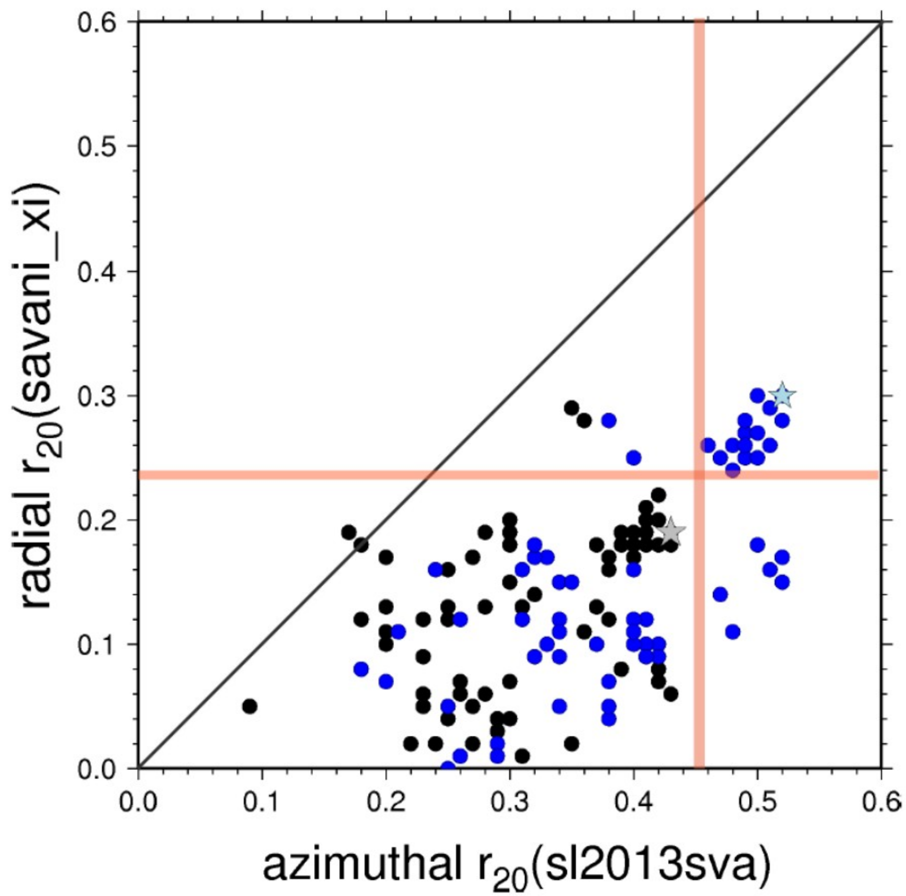

Azimuthal anisotropy (1)

Smith & Dahlen (1973) and Montagner & Nataf (1986) show that perturbations of surface wave phase velocities in media with weak hexagonal anisotropy is given by

$$\delta c = \frac{dc}{c} \approx D^0 + D_C^{2\phi}\cos(2\phi) + D_S^{2\phi}\sin(2\phi)$$
$$+D_C^{4\phi}\cos(4\phi) + D_S^{4\phi}\sin(4\phi),$$

Medium with a single fast or slow symmetry axis and isotropic velocities in the plane perpendicular to it.

Special cases: Azimuthal anisotropy (2ψ and 4ψ terms)
Radial anisotropy (0ψ terms)
No 1ψ and 3ψ terms

Coefficients in D depend on 13 independent elastic constants

Azimuthal anisotropy (2)

From 21 to 13 independent elastic parameters, of which we resolve only a couple at once

- 2Ψ-azimuthal term:

$$\alpha_1 \cos 2\Psi \qquad \alpha_2 \sin 2\Psi$$

$$B_c = \frac{1}{2}(C_{11} - C_{22}) \qquad B_s = C_{16} + C_{26}$$

$$G_c = \frac{1}{2}(C_{55} - C_{44}) \qquad G_s = C_{54}$$

$$H_c = \frac{1}{2}(C_{13} - C_{23}) \qquad H_s = C_{36}$$

- 4Ψ-azimuthal term:

$$\alpha_3 \cos 4\Psi \qquad \alpha_4 \sin 4\Psi$$

$$E_c = \frac{1}{8}(C_{11} + C_{22}) + \frac{1}{4}C_{12} - \frac{1}{2}C_{66} \qquad E_s = \frac{1}{2}(C_{16} - C_{26})$$

- Constant term (0Ψ-azimuthal term: α_0)

$$A = \rho V_{PH}^2 = \frac{3}{8}(C_{11} + C_{22}) + \frac{1}{4}C_{12} + \frac{1}{2}C_{66}$$

$$C = \rho V_{PV}^2 = C_{33}$$

$$F = \frac{1}{2}(C_{13} + C_{23})$$

$$L = \rho V_{SV}^2 = \frac{1}{2}(C_{44} + C_{55})$$

$$N = \rho V_{SH}^2 = \frac{1}{8}(C_{11} + C_{22}) - \frac{1}{4}C_{12} + \frac{1}{2}C_{66}$$

Azimuthal: 3 (Vs, Gs, Gc), horizontal symmetry, Radial: 2 (Vs, Xi) vertical symmetry
Vectorial tomography: 4 (Vs, Xi, two angles of orientation of symmetry axis).

Azimuthal anisotropy (3)

Montagner & Nataf (1986) show that A,C,L,N,F kernels are Equivalent to the aszimuthal anisotropic kernels

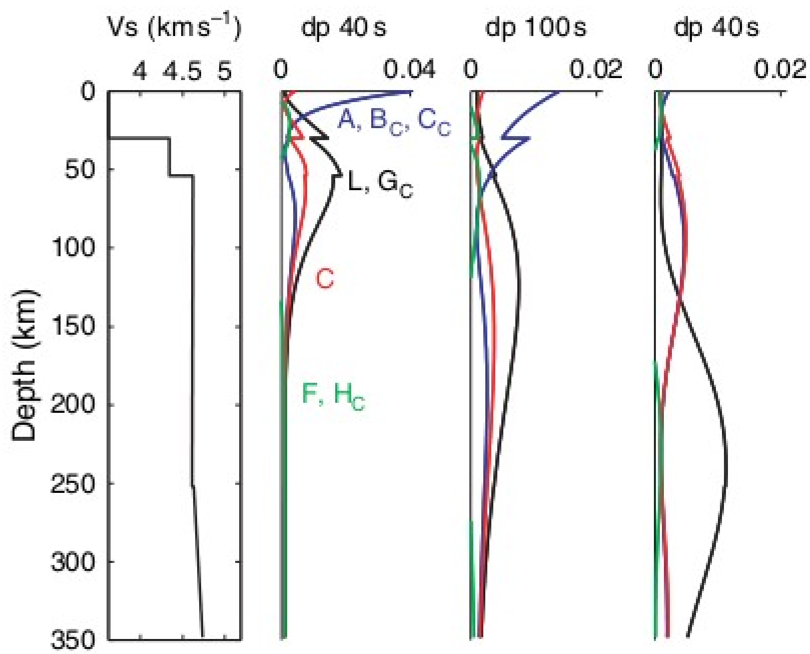

We can derive The fast axis direction and the Amplitude of azimuthal anisotropy

$$\begin{cases} \Lambda_{2\Psi} = \sqrt{A_{2\Psi}^2 + B_{2\Psi}^2} \\ \Theta_{2\Psi} = \frac{1}{2}\arctan\left(\frac{B_{2\Psi}}{A_{2\Psi}}\right) \end{cases} \text{ and } \begin{cases} \Lambda_{4\Psi} = \sqrt{A_{4\Psi}^2 + B_{4\Psi}^2} \\ \Theta_{4\Psi} = \frac{1}{4}\arctan\left(\frac{B_{4\Psi}}{A_{4\Psi}}\right) \end{cases}$$

Linearity of CC delay times (1)

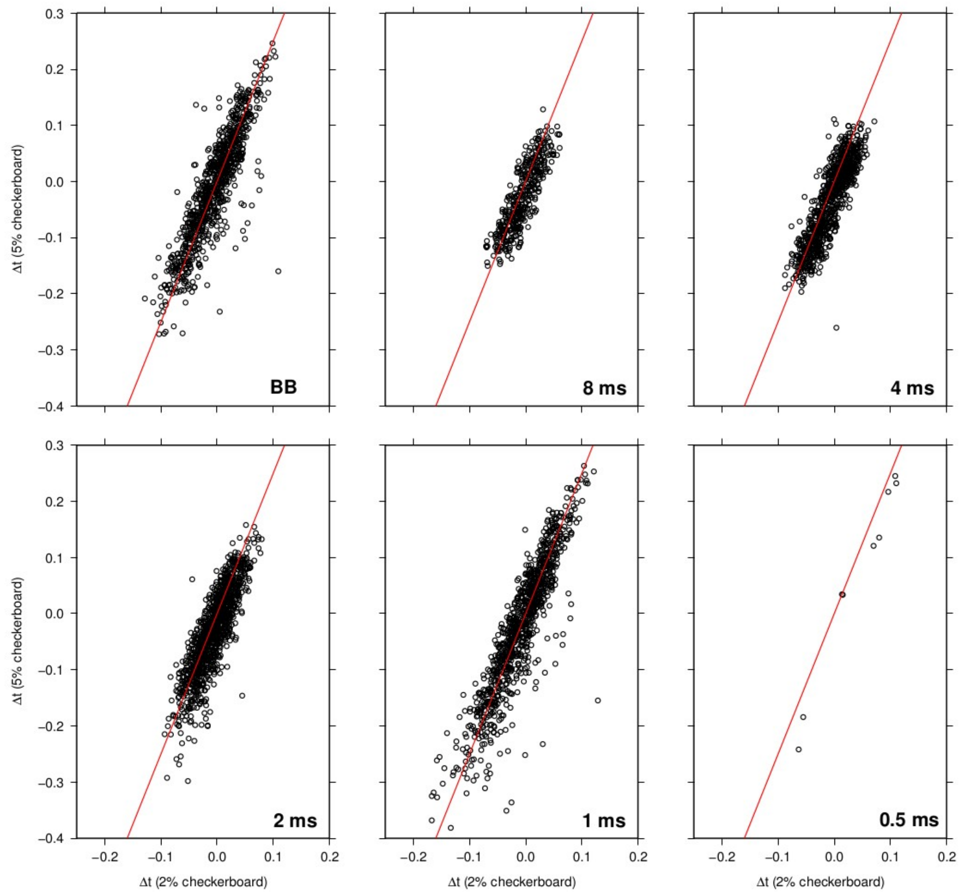

Figure 4. Cross-correlation delay times measured for the $\pm 5\%$ versus those in the $\pm 2\%$ model. The red line denotes a slope of 5/2. BB is for broadband data, and the other 5 bands with dominant periods of 8 ms, 4 ms, 2 ms, 1 ms and 0.5 ms. Very few correlations pass the condition that $R > 0.8$ for the passband with dominant period of 0.5 ms.

Regularization options

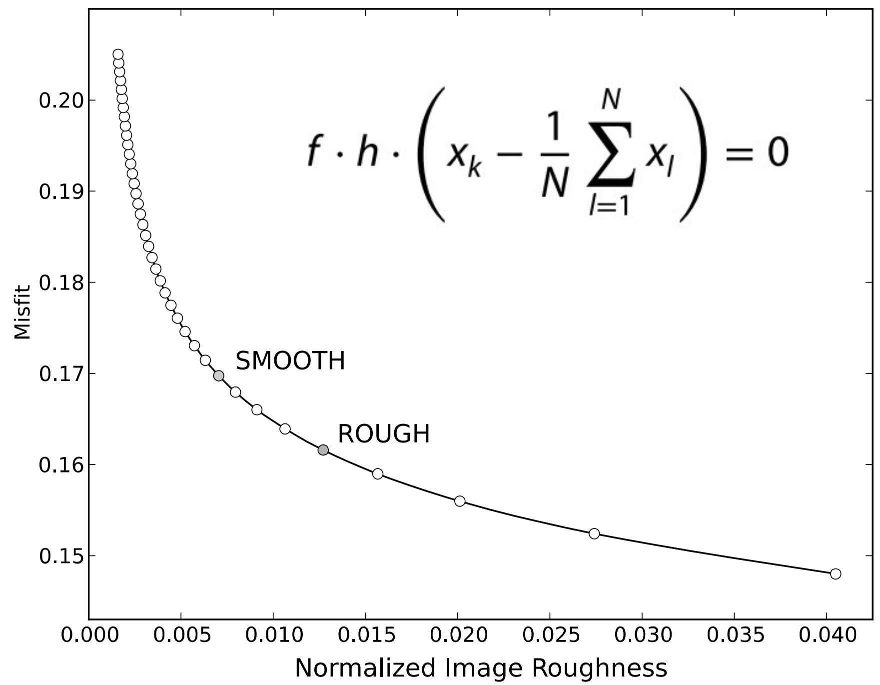

- Minimum norm model
- $\boxed{\text{Smoothest model}}$
- Fewest wavelets

LPO model of Becker (2008)

	LPO (Becker et al., 2008)
reference frame shear	none (NNR)
density inferred from	S362WANI (Kustowski et al., 2008)
upper thermal boundary layer	excluded around cratons
upper mantle	
background viscosity, η_{um}	average $\approx 1.8 \times 10^{21}$ Pas, non-Newtonian
asthenospheric viscosity	temperature and stress dependent (Becker, 2006)
	$\sim$ three orders of magnitude variations in upper mantle
velocity gradients	form LPO when in dislocation creep
method of LPO estimate	full DREX (Kaminski et al., 2004) for A type LPO

LPO model of Becker (2008)

	(Becker et al., 2008)
reference frame sh	
density inferred fr	8)
upper thermal bou	
upper mantle	
background viscos	wtonian
asthenospheric vis	(Becker, 2006)
	ions in upper mantle
velocity gradients	ep
method of LPO est	for A type LPO

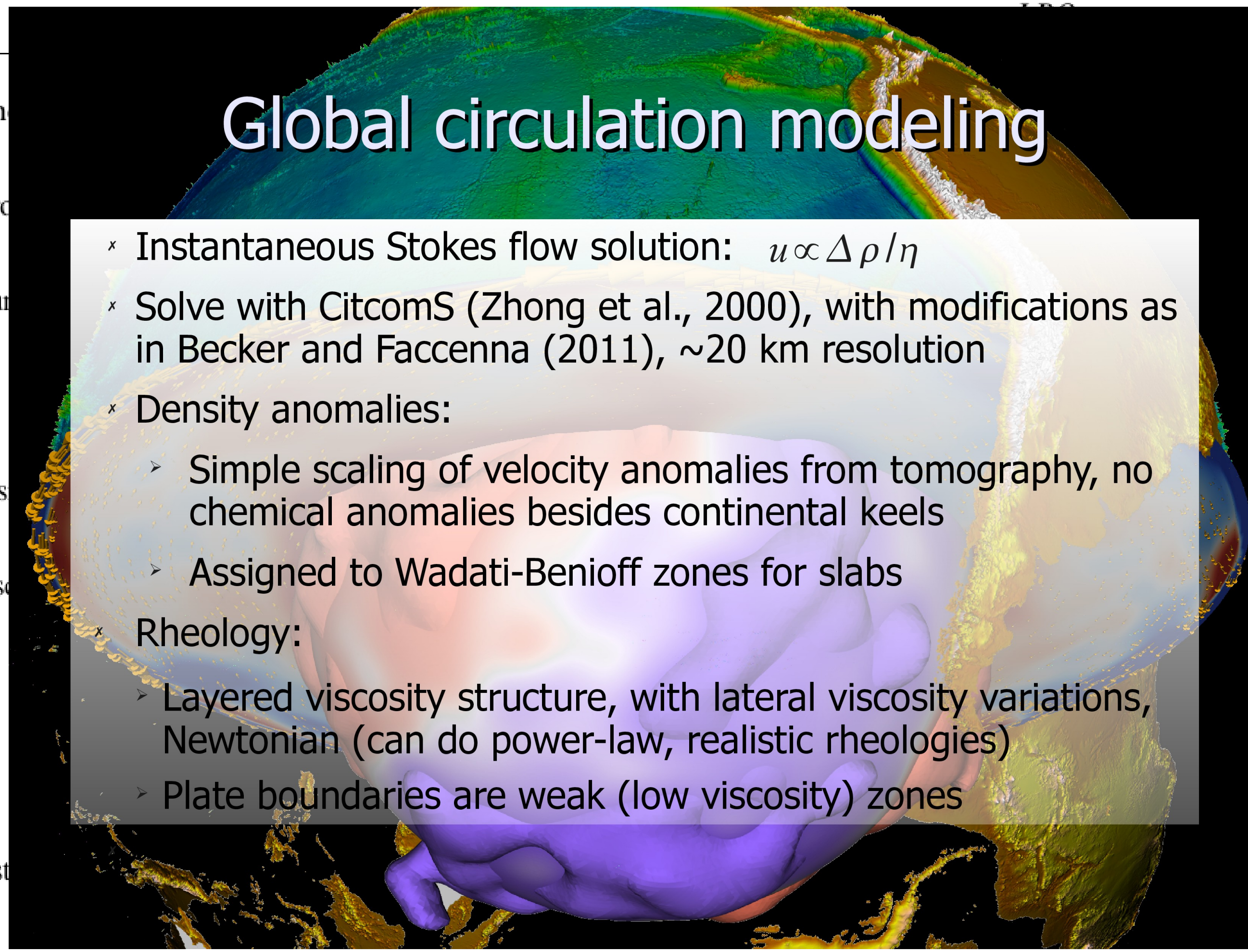

Born theory

1)

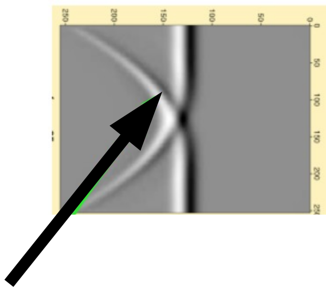

A wavefront heals because energy
Diffracts around the anomaly, making
anomaly hard to detect

2)

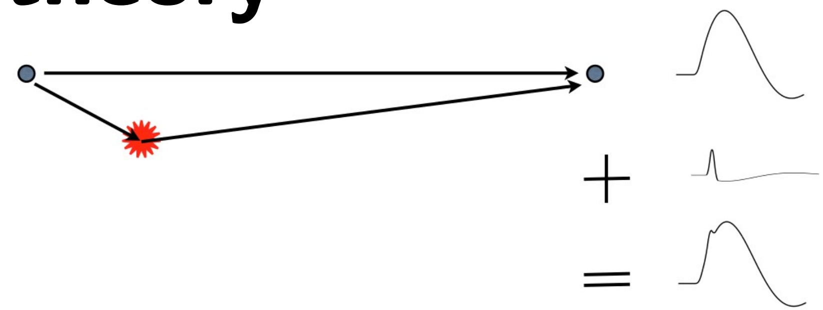

In the first-order Born approximation
this is modeled via single scattering

3)

Considering cross-correlation delay times:
Scattered wave perturbs delay time

Born

$$\delta T = -\frac{\delta\dot{\gamma}(0)}{\ddot{\gamma}(0)} = -\frac{\int_{-\infty}^{\infty}\dot{u}(t')\boxed{\delta u(t')}\mathrm{d}t'}{\int_{-\infty}^{\infty}\ddot{u}(t')u(t')\mathrm{d}t'}$$

$$\delta\bar{u}^{\mathrm{PP}}(\omega) = \frac{\omega^2}{4\pi r V_{\mathrm{P}}^2}\left[\frac{\delta\rho}{\rho} - \frac{\delta\lambda}{\lambda+2\mu} - 2\frac{\delta\mu}{\lambda+2\mu}\right]\mathrm{e}^{\mathrm{i}k_{\mathrm{P}}r}\,\mathrm{d}V$$

Can also use Adjoint method

4)

Line integrals

$$T \approx \int_{P_0}\frac{\mathrm{d}s}{c(\boldsymbol{r})}\,.$$

Turn into volume integrals

$$\delta T = \int K_{\mathrm{P}}(\boldsymbol{r}_{\mathrm{x}})\frac{\delta V_{\mathrm{P}}}{V_{\mathrm{P}}}\mathrm{d}^3\boldsymbol{r}_{\mathrm{x}}$$

Rays vs. finite-frequency kernels

Does replacing 0-th with 1st order (single scattering) theory play a role, globally?

Ray theory

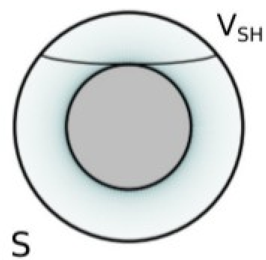

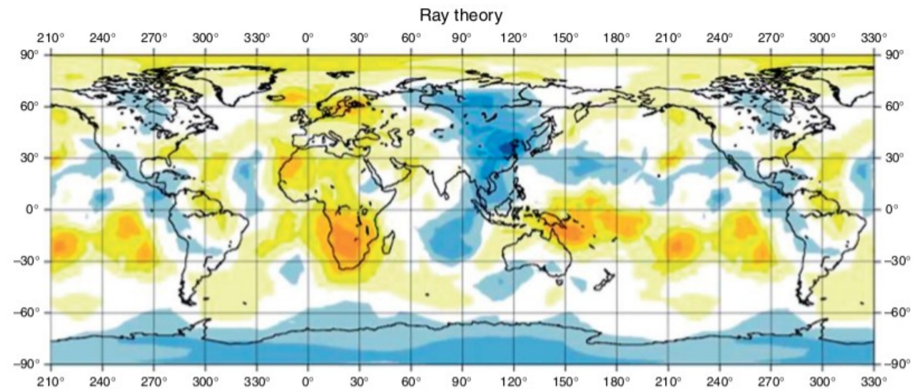

Van der Hilst (2002)

FF-theory

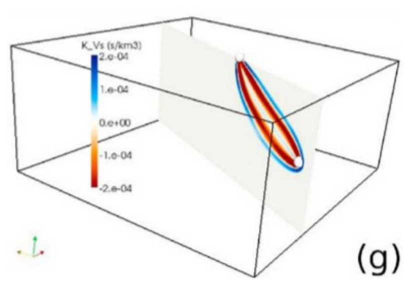

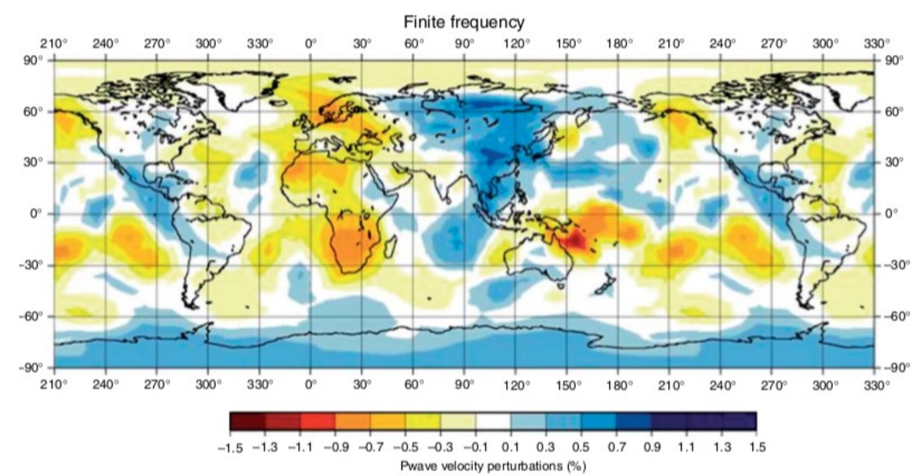

Montelli (2005)

Data coverage is much more of a problem. But regionally, it makes a difference!

→ Ray theory where sufficient, FF-theory, where required!

Linearity of CC delay times (1)

Quality of kernel linearity

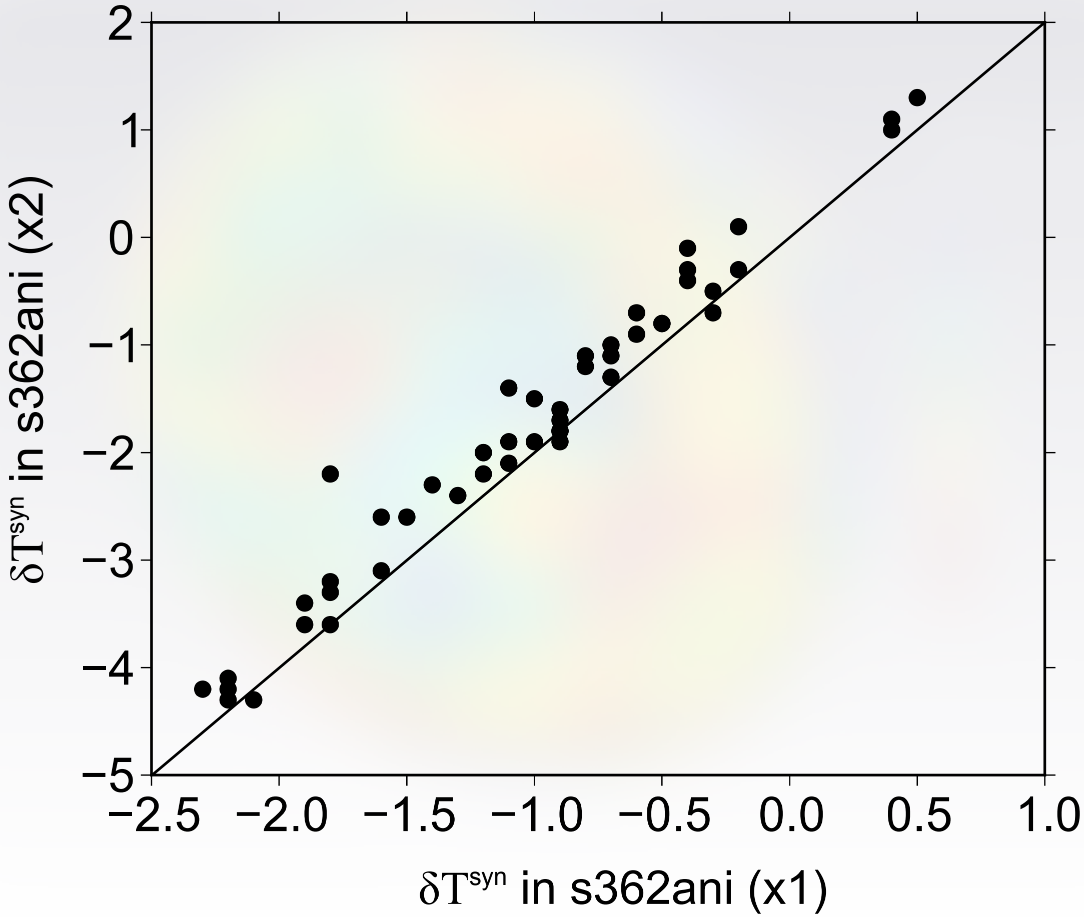

Linearity of CC delay times (2)

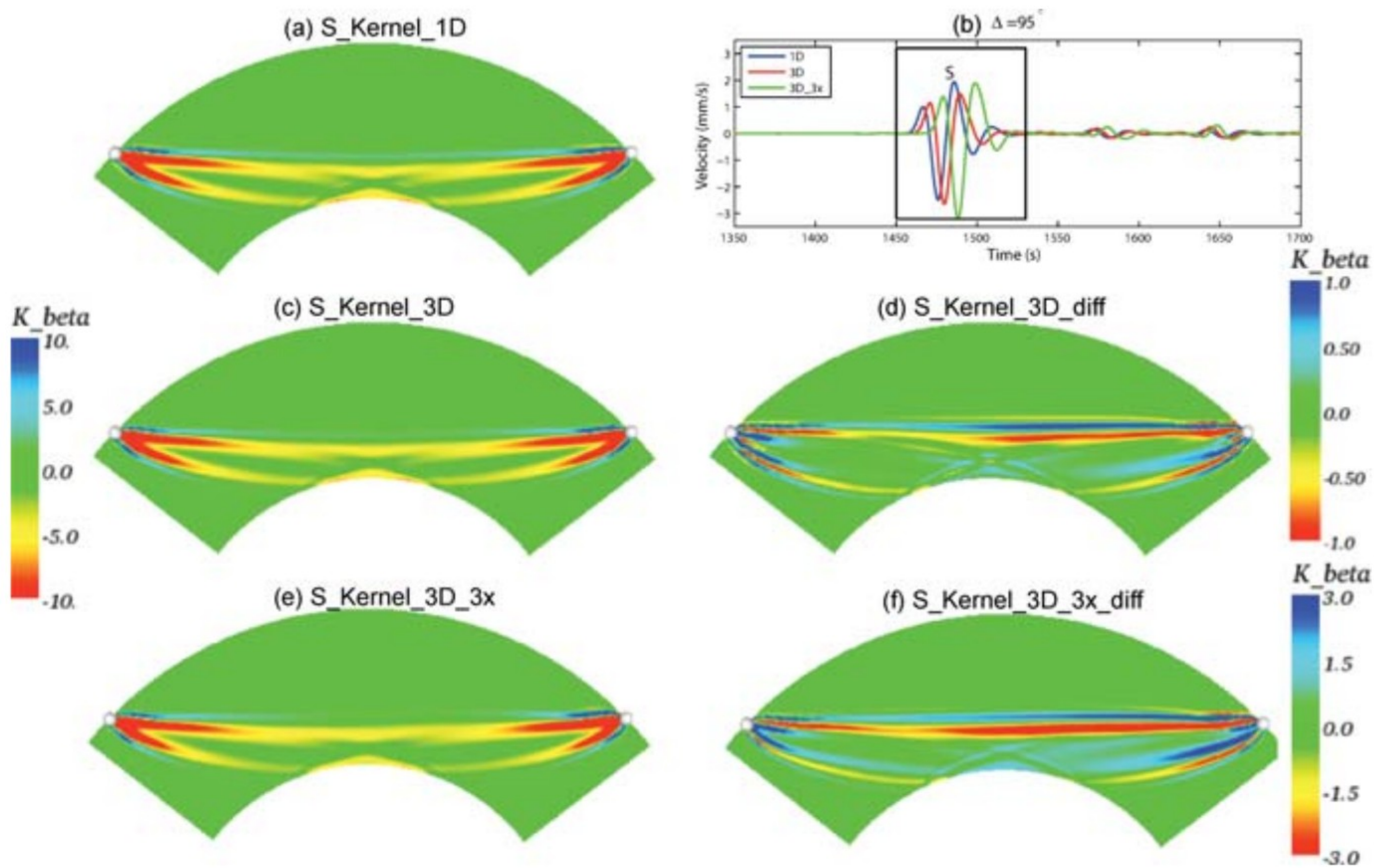

Figure 15. (a) 9 s K_β kernel for the S phase at a distance $\Delta = 95°$ for the 1-D PREM model. (b) Transverse-component velocity seismograms for the source–receiver pair described in Fig. 14 for various reference models: 1-D (PREM), 3-D (S20RTS) and 3D_3x (S20RTS enhanced by a factor of 3). (c) Same as (a), but for the 3-D model. (d) The difference between the kernels in (c) and (a). (e) Same as (a), but for the 3D_3x model. (f) The difference between the kernels in (e) and (a). Note that the colour bars for figures (d) and (f) are different from the colour bar for figures (a), (c) and (e).

Old results: Model of Beghein (2014)

- Supplementary Material (42 pages) here - Article usage stats here

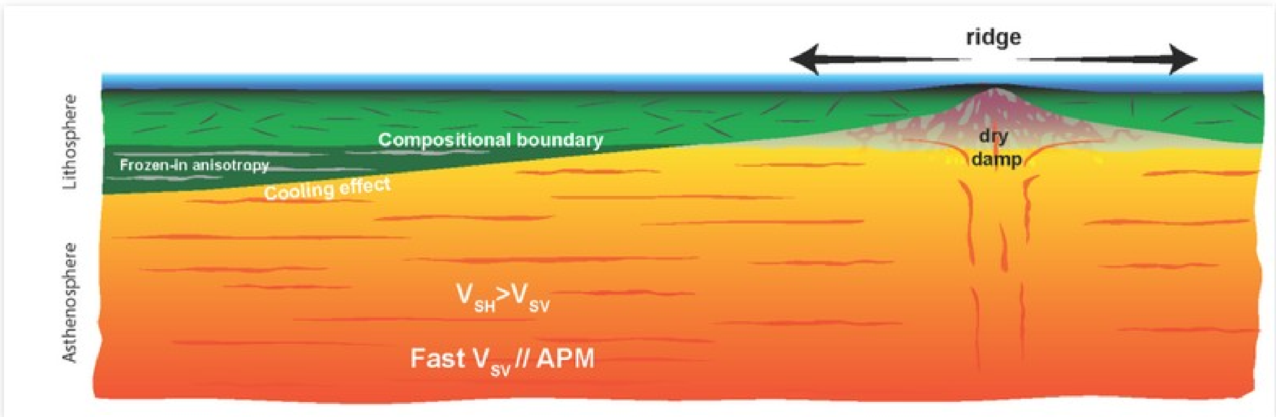

This figure illustrates the Earth's upper mantle beneath the Pacific ocean. The orange layer represents the deformable, warm asthenosphere in which there is active mantle flow. The green layer on top represents the lithospheric plate, which forms at the mid ocean ridge, then cools down and thickness as it moves away from the ridge. The cooling of the plate overprints a compositional boundary that forms at the ridge by dehydration melting and is preserved as the plate ages. The more easily deformable, hydrated rocks align with mantle flow. The directions of past and present-day mantle flow can be detected by seismic waves, and changes in the alignment of the rocks inside and at the bottom of the plate can be used to identify layering. CREDIT: Nicholas Schmerr (University of Maryland)

Old results: Ekström (1998)

Radial anisotropy in the Central Pacific

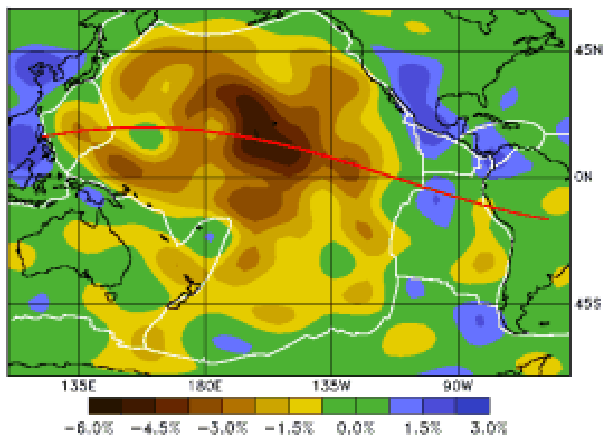

Isotropic cross-section

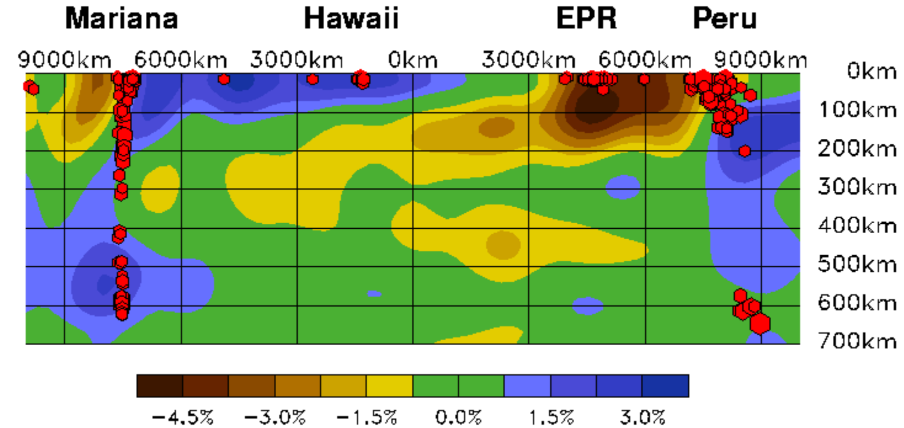

Anisotropic cross-section

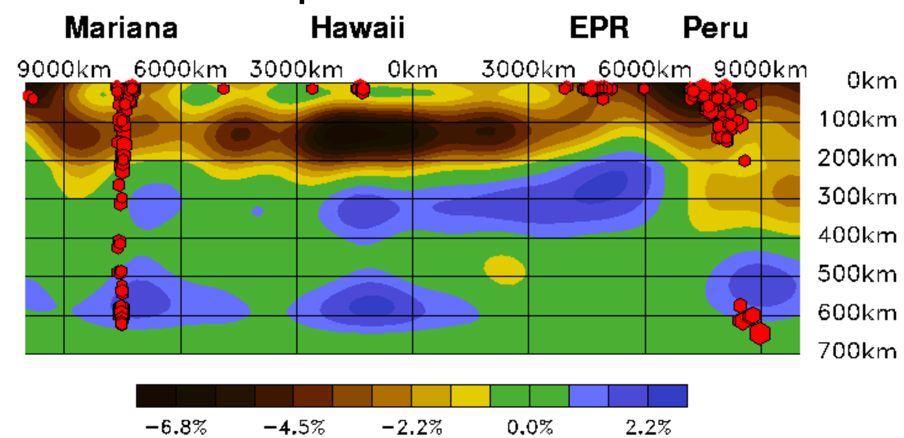

"Pancake" like structure of

Above average xi with a

Peak at ~ 150 km depth

Old results: Beghein (2015)

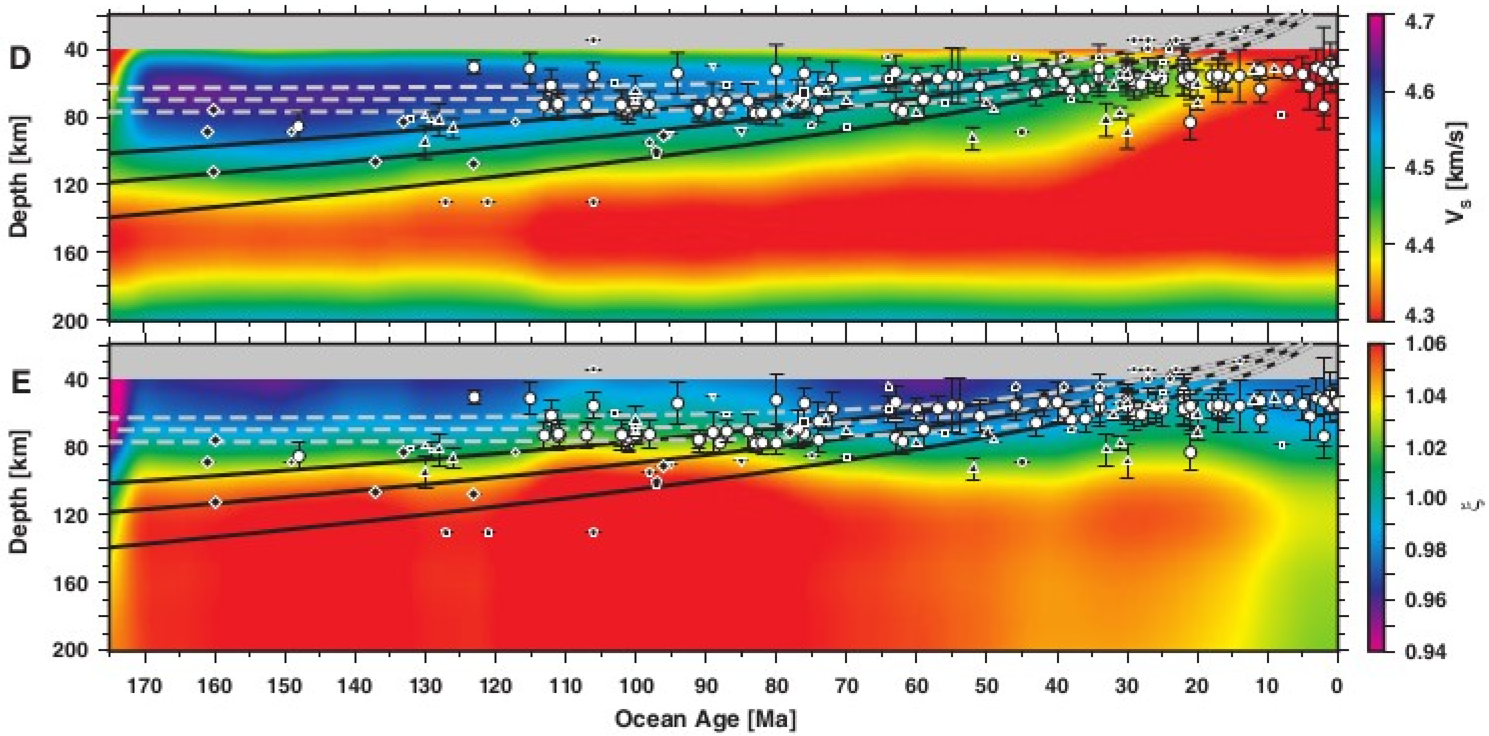

Old results: Burgos (2014)

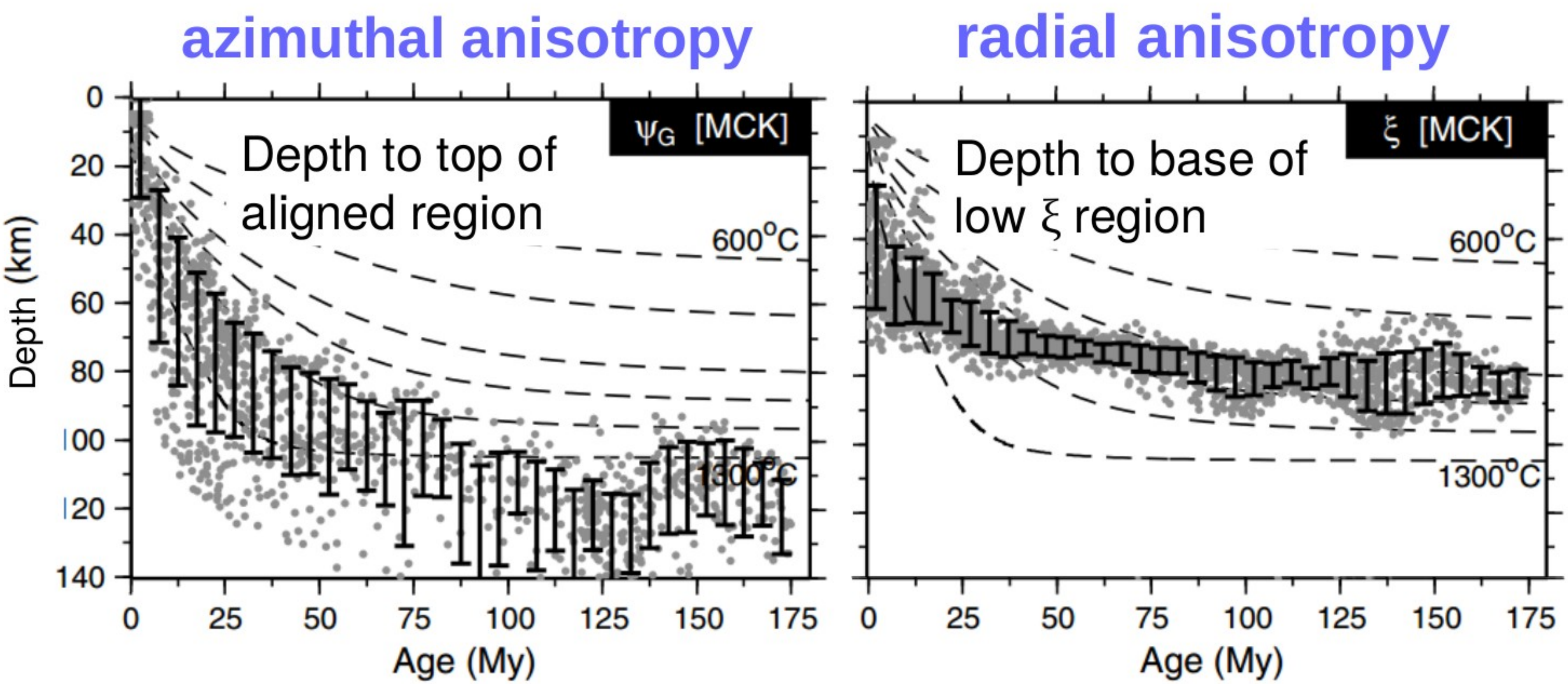

seems to follow thermal model – OK!

does not seem to follow thermal model - ?!

SS precursor modeling, Schmerr (2012)

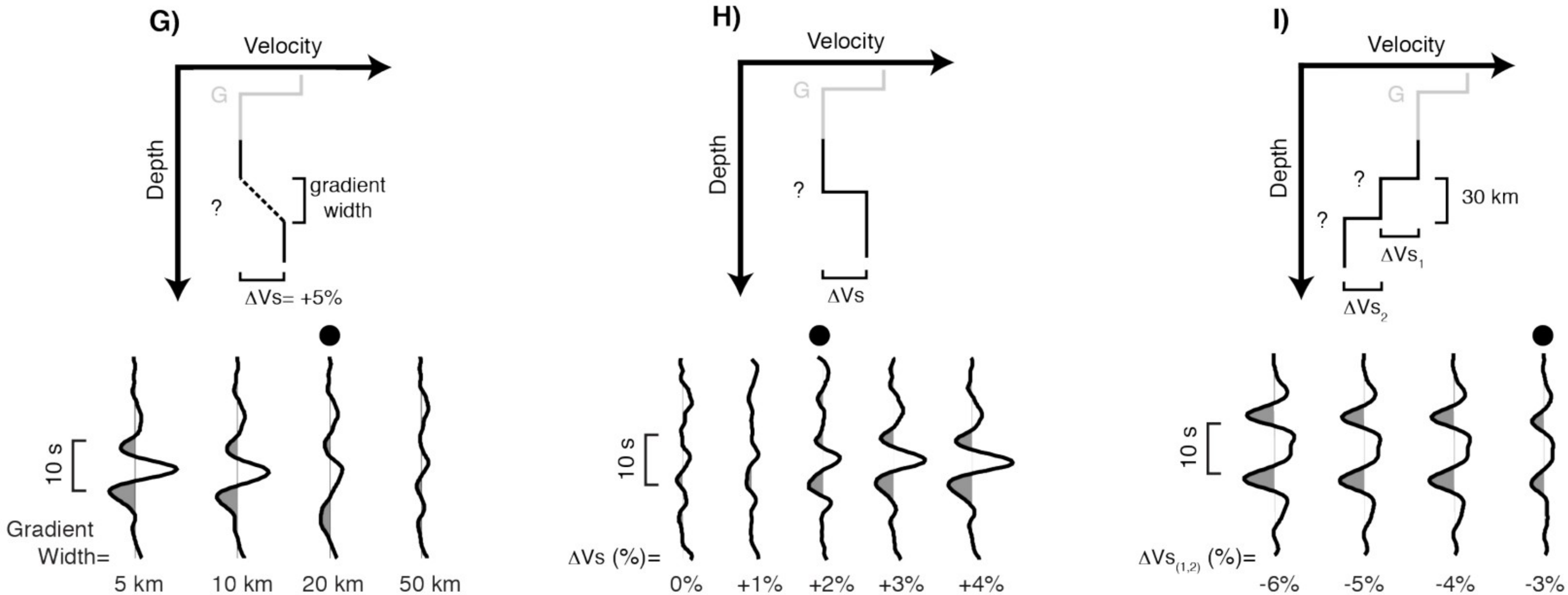

Which of them are compatible with our model?

SS precursors, Receiver functions

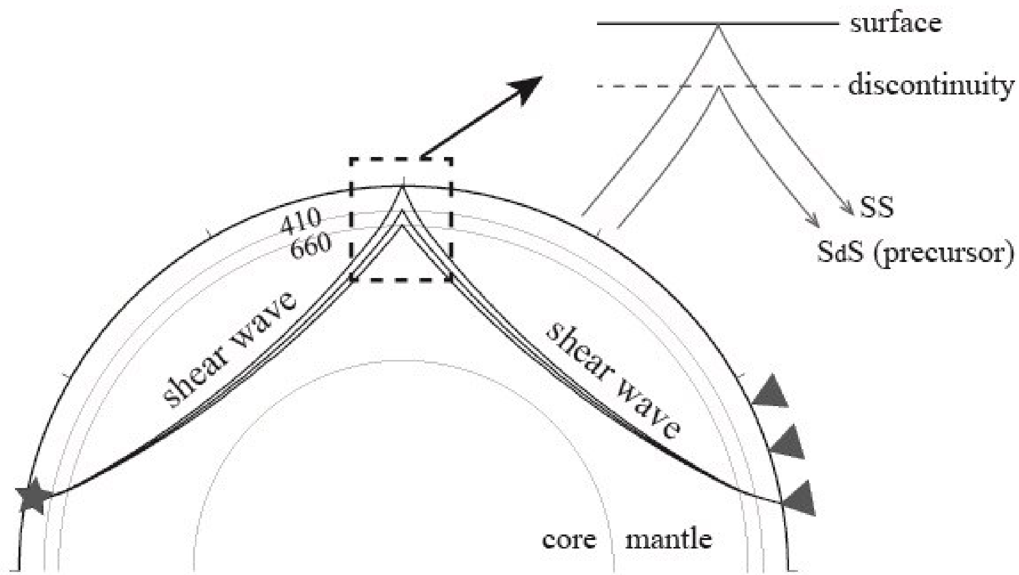

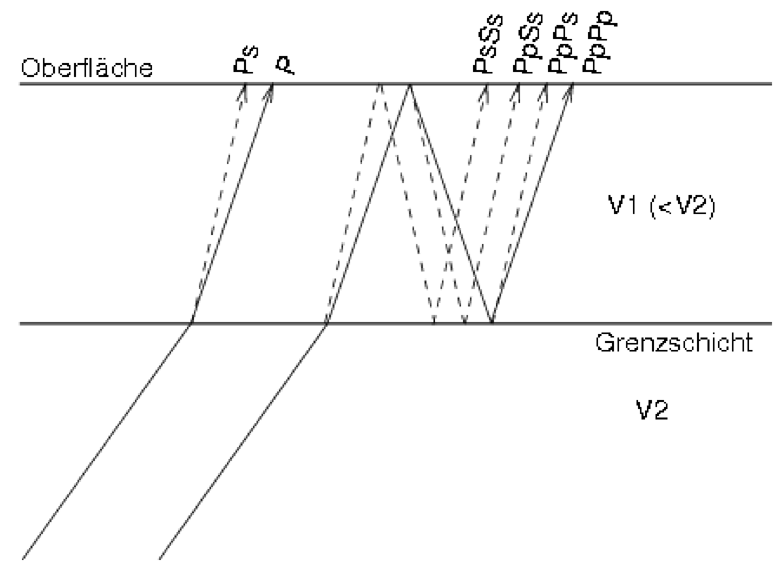

Look at SS precursors
reflected at interfaces

Look at time difference
With converted waves

Recent approaches to global modeling

Adjoint (Bozdag, 2012)

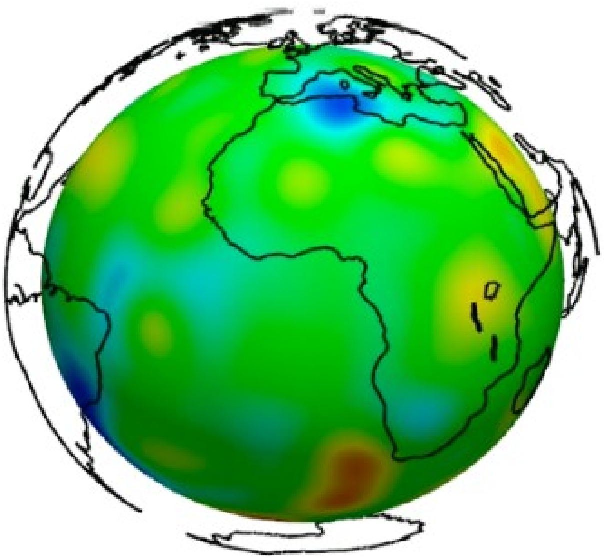

Global adjoint tomography
T<30 s, 300 EQ's, 1 it.

CEM (Afanasiev et al. 2015)

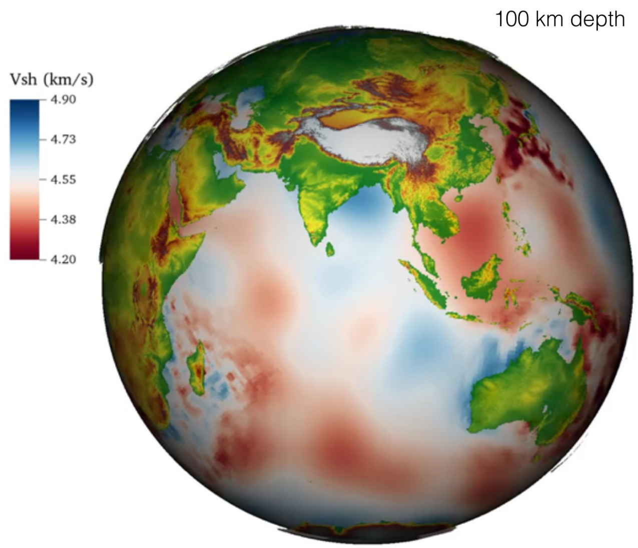

Method agnostic composite model from regional waveform tomographys and S20RTS

SAVANI *(Auer et al., 2014)*

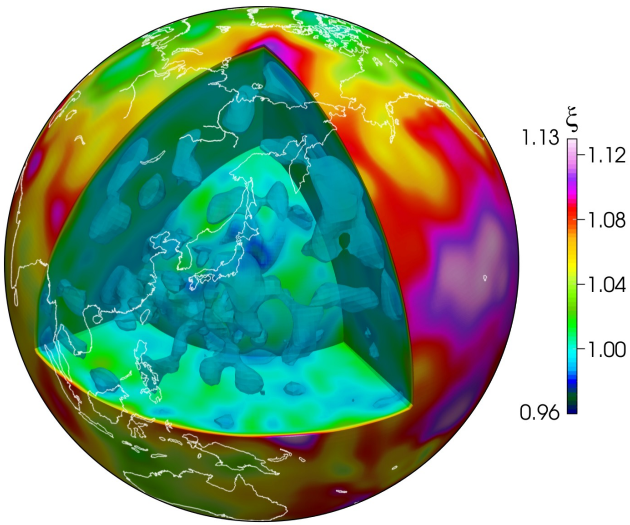

Compilation of multiple Global datasets, reinversion; Next: add regional data

Adjoint vs. classical tomography

	classical tomography	adjoint tomography
reference model	1D	3D
physical domain	3D	3D
Born approximation	yes	yes
forward modelling technique	e.g., ray theory, modes, or banana-doughnut kernels	fully numerical (e.g., SEM)
gradient method	$\mathbf{g} = -\mathbf{G}^T\mathbf{d}$ $G_{ik} = \int_V K_i B_k \, \mathrm{d}^3\mathbf{x}$	$g_k = \int_V K B_k \, \mathrm{d}^3\mathbf{x}$
Newton method	$\mathbf{G}^T\mathbf{G}\,\delta\mathsf{m} \approx -\mathbf{g}$	(too costly)
number of iterations	1	multiple

Adjoint vs. classical tomography

Classical tomography

We can accumulate the full approximate Hessian

In the framework of non-linear optimization theory one would call it a "Gauss-Newton type" method

The approximate nature of our forward theory restricts ourselves to 1D reference models, thus we can only do 1 inversion step

Adjoint tomography

One is restricted to compute so called "Event Kernels" i.e. a sum of misfit Kernels

Computing individual kernels for all different event station pairs would be to expensive

Would theoretically work with every available wiggle in the record but in practice people employ more robust misfit functionals (e.g. traveltimes)

Limited to rather low frequency and small domains

Focuses on the background model

Kernel expressions

Table B.1: Sensitivity kernel expressions for three different parameterizations of elastic structure. $\mathbf{D}$ is the deviatoric strain (e.g., *Liu and Tromp*, 2006, Eq. 28).

Model Parameter		Notation	Kernel Expression
Bulk modulus	κ	$K_{\kappa(\mu\rho)}(\mathbf{x})$	$-\kappa \int_0^T [\boldsymbol{\nabla} \cdot \mathbf{s}^\dagger(\mathbf{x}, T-t)][\boldsymbol{\nabla} \cdot \mathbf{s}(\mathbf{x}, t)]\, dt$
Shear modulus	μ	$K_{\mu(\kappa\rho)}(\mathbf{x})$	$-2\mu \int_0^T \mathbf{D}^\dagger(\mathbf{x}, T-t) : \mathbf{D}(\mathbf{x}, t)\, dt$
Density	ρ	$K_{\rho(\kappa\mu)}(\mathbf{x})$	$-\rho \int_0^T \mathbf{s}^\dagger(\mathbf{x}, T-t) \cdot \partial_t^2 \mathbf{s}(\mathbf{x}, t)\, dt$
Bulk sound speed	c	$K_{c(\beta\rho)}(\mathbf{x})$	$2\, K_{\kappa(\mu\rho)}$
S wavespeed	β	$K_{\beta(c\rho)}(\mathbf{x})$	$2\, K_{\mu(\kappa\rho)}$
Density	ρ	$K_{\rho(c\beta)}(\mathbf{x})$	$K_{\rho(\kappa\mu)} + K_{\kappa(\mu\rho)} + K_{\mu(\kappa\rho)}$
P wavespeed	α	$K_{\alpha(\beta\rho)}(\mathbf{x})$	$\left(2 + \frac{8\mu}{3\kappa}\right) K_{\kappa(\mu\rho)}$
S wavespeed	β	$K_{\beta(\alpha\rho)}(\mathbf{x})$	$2\, K_{\mu(\kappa\rho)} - \frac{8\mu}{3\kappa} K_{\kappa(\mu\rho)}$
Density	ρ	$K_{\rho(\alpha\beta)}(\mathbf{x})$	$K_{\rho(\kappa\mu)} + K_{\kappa(\mu\rho)} + K_{\mu(\kappa\rho)}$

“Bayesian” generalized non-linear
least-squares inversion (vs. discrete regularization)

Assume: a posteriori model parameters are distributed according to a Gaussian PDF

$$\rho(\mathbf{m}) \propto \exp\left(-\frac{1}{2}\mathbf{m}\cdot\mathbf{C}_{\mathrm{m}}^{-1}\cdot\mathbf{m}\right) \qquad C_{\mathrm{m}}(\mathbf{r}_1,\mathbf{r}_2) = \sigma^2\exp\left(-\frac{|\mathbf{r}_1,\mathbf{r}_2|^2}{2L^2}\right)$$

For a linear problem the solution is given by (Tarantola & Valette, 1982)

$$\begin{aligned}\mathbf{m} &= \mathbf{C}_{\mathrm{m}}\cdot\mathbf{G}^{\mathrm{T}}\cdot\left(\mathbf{C}_{\mathrm{d}}+\mathbf{G}\cdot\mathbf{C}_{\mathrm{m}}\cdot\mathbf{G}^{\mathrm{T}}\right)^{-1}\cdot\mathbf{d}\\ &= \left(\mathbf{C}_{\mathrm{m}}^{-1}+\mathbf{G}^{\mathrm{T}}\cdot\mathbf{C}_{\mathrm{d}}^{-1}\cdot\mathbf{G}\right)^{-1}\cdot\mathbf{G}^{\mathrm{T}}\cdot\mathbf{C}_{\mathrm{d}}^{-1}\cdot\mathbf{d}\end{aligned}$$

- To solve slightly non-linear problems, this algorithm can be iterated
- Provides a formalized way to introduce prior knowledge

Compare to “Classic” formulation:
Solving the linear system

$$\begin{bmatrix}\mathbf{A}^{-1/2}\cdot\mathbf{G}\\ \mathbf{B}^{-1/2}\end{bmatrix}\cdot\mathbf{m} = \begin{bmatrix}\mathbf{A}^{-1/2}\cdot\mathbf{d}\\ 0\end{bmatrix} \xrightarrow{\text{LSQR}} \mathbf{m} = \left(\alpha\mathbf{I}+\beta\mathbf{D}_1^2+\mathbf{G}^{\mathrm{T}}\cdot\mathbf{C}_{\mathrm{d}}^{-1}\cdot\mathbf{G}\right)^{-1}\cdot\mathbf{G}^{\mathrm{T}}\cdot\mathbf{C}_{\mathrm{d}}^{-1}\cdot\mathbf{d}$$

$$\mathbf{C}_{\mathrm{m}}^{-1} = \alpha\mathbf{I}+\beta\mathbf{D}_1^2$$

Computational aspects (petscinv)

SPQLSR vs. PETSc (KSP-LSQR)

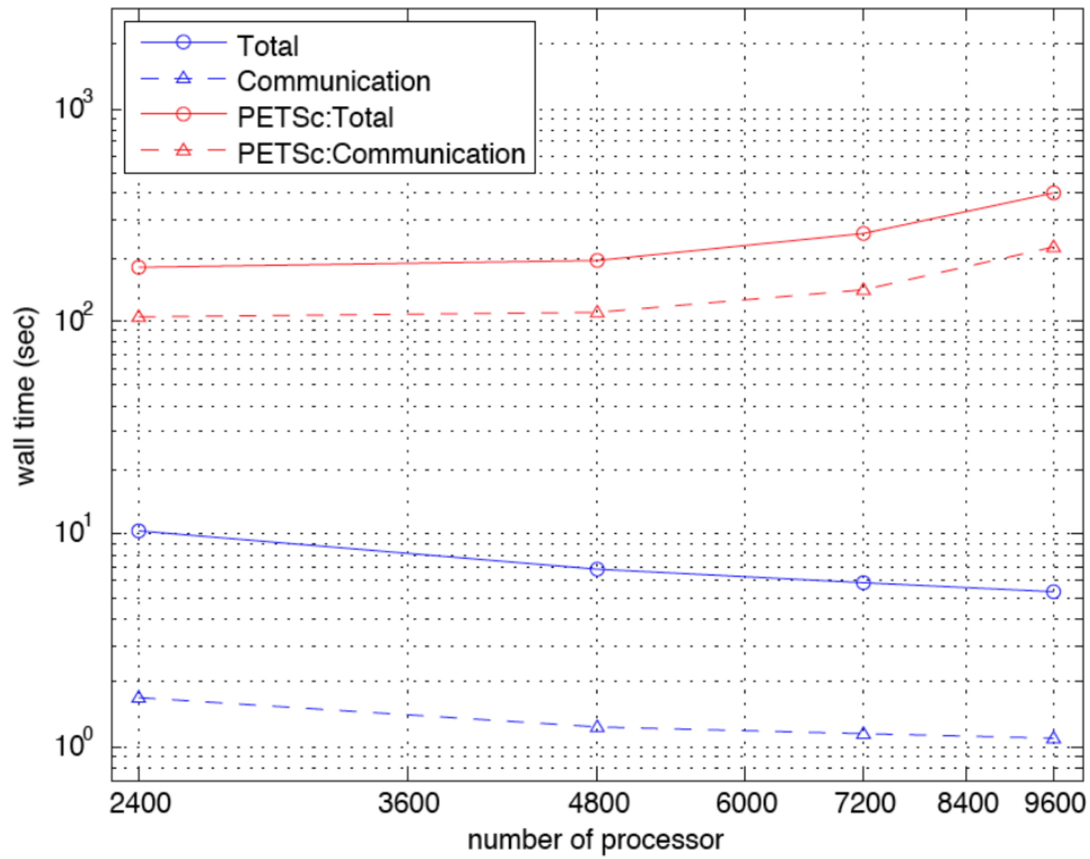

Tomography solver from Univ. of Wyoming

Tested our code on system matrices up to around 200 GB, takes around 10 hrs for one point in the L-curve on 12 Cores 3.45 GHz shared memory node

Computational aspects (MCkernel)

Strong scaling test, fixed problem size:

- 587 SRC-REC pairs
- 4 period bands from 10 – 30 s
- Triangular mesh with n=7260

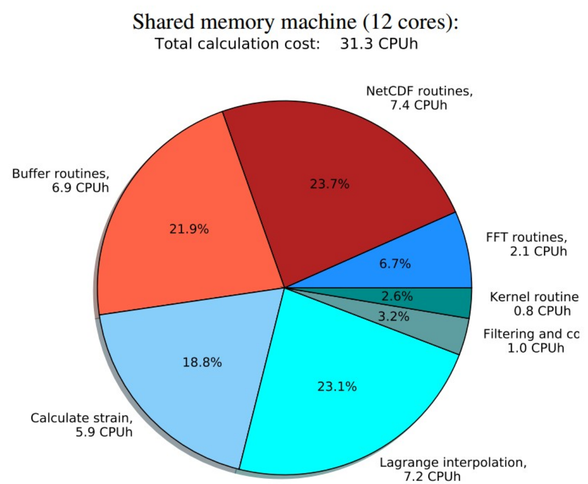

Figure 6. Time shares of different program parts on a small-scale run with 5 receivers and 160 kernels. Reddish colors show program parts related to IO, while blueish show CPU-intensive parts. It can be seen that the code benefits highly from a low-latency file system, as the one on the shared-memory machine. Note that the CPU frequency of the Shared memory machine was 3.45 GHz, compared to 2.2 GHz for the HPC one.

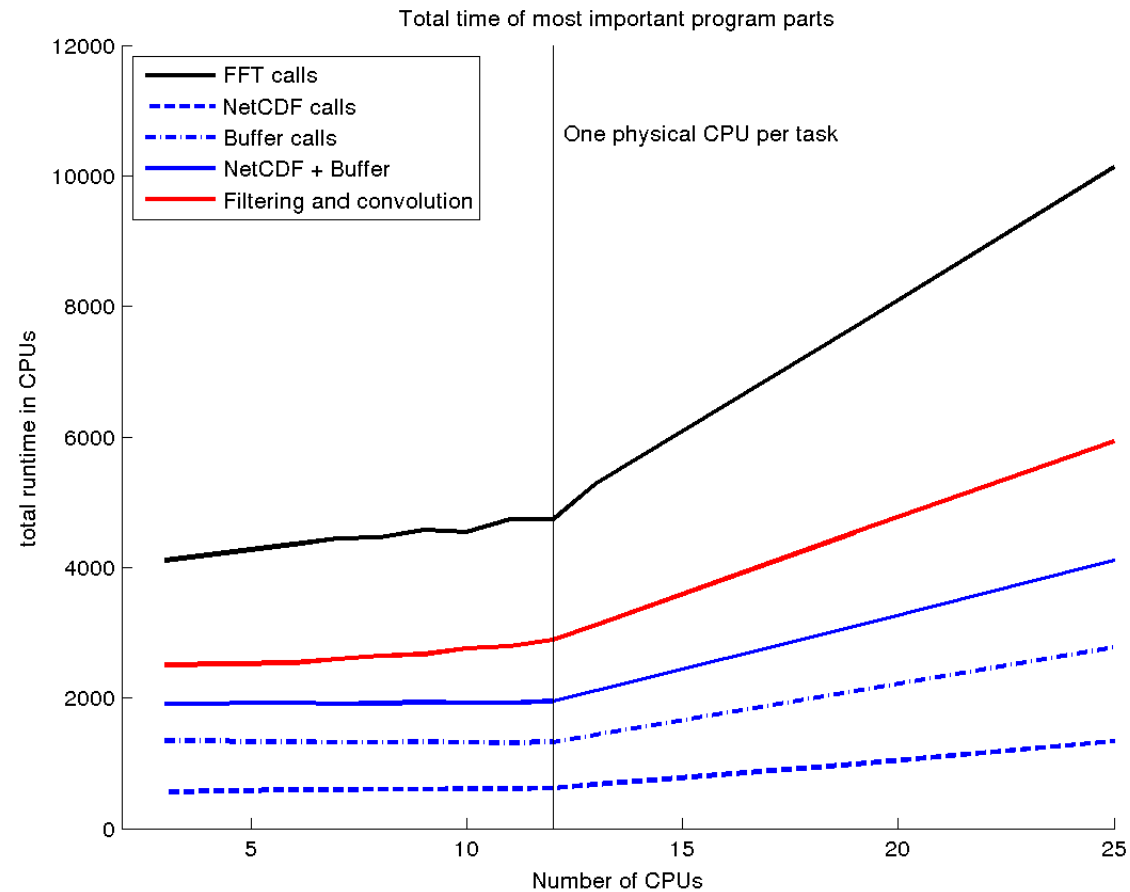

Mckernel: How it works

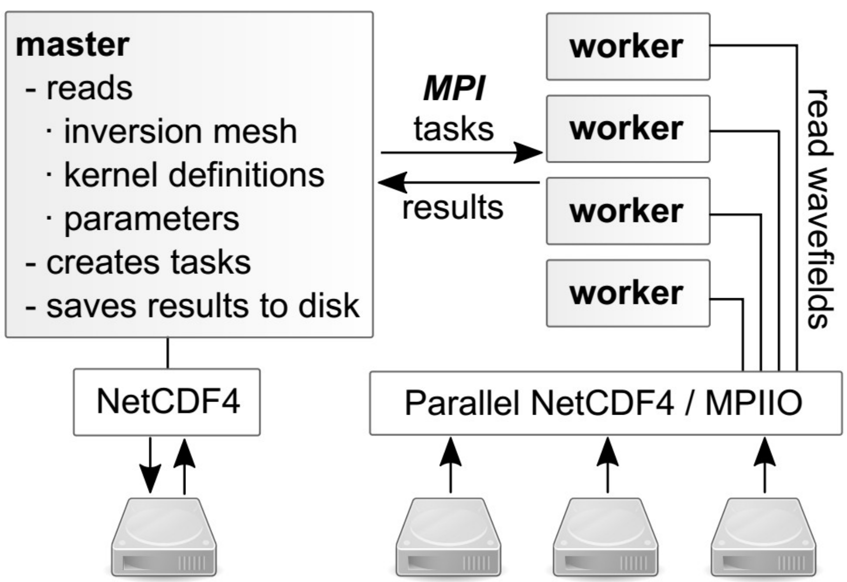

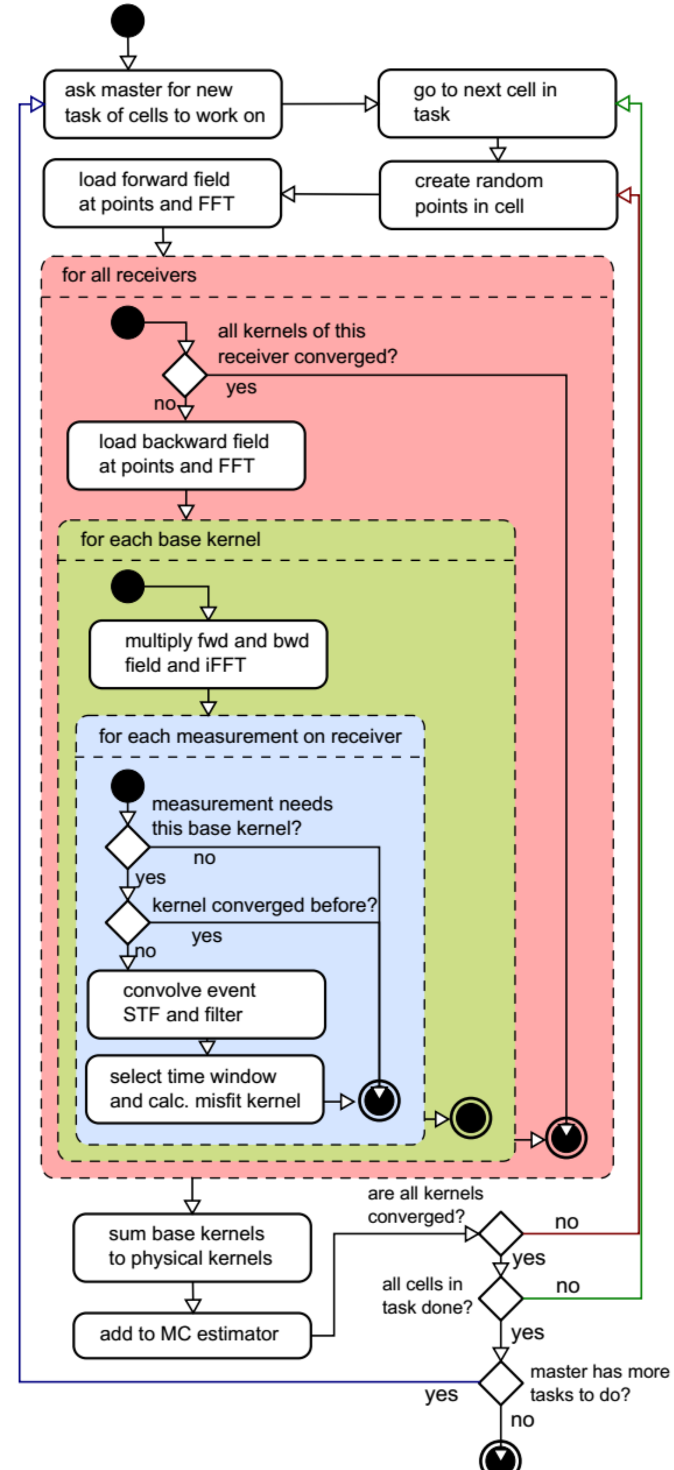

AxiSEM, basic principle

Source Decomposition:

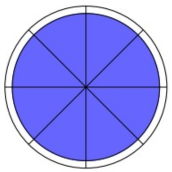

$$\mathbf{u} = \mathbf{u}(s, z)$$

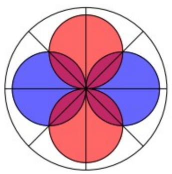

$$\mathbf{u} = \mathbf{u}(s, z) \cdot f(\sin\phi, \cos\phi)$$

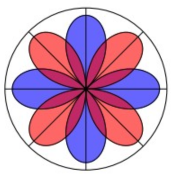

$$\mathbf{u} = \mathbf{u}(s, z) \cdot f(\sin(2\phi), \cos(2\phi))$$

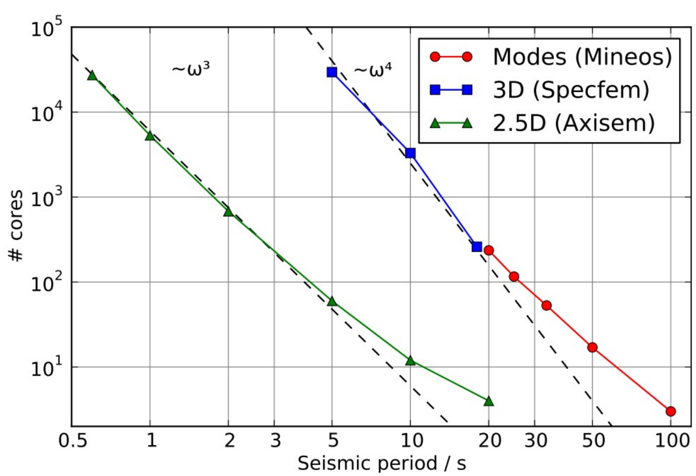

2D numerical problems:

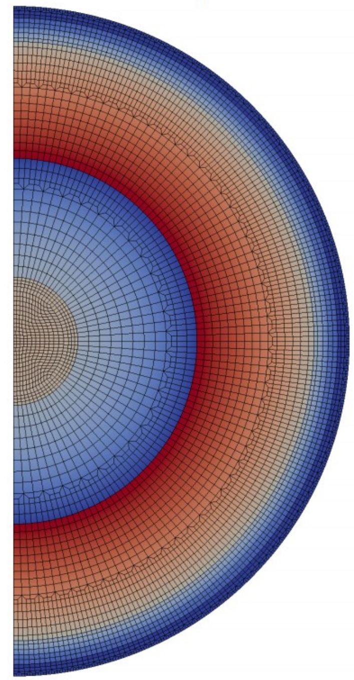

→ Global 1D wavefields up to 2 Hz

1D models → one can use properties arising from axial symmetry (where source is located on a axis through the center of the earth) to decompose moment tensor sources in a series of multipole sources that can be solved on a 2D disk.

3D wavefields reconstructed from 2D solutions viat Analytical relations

HSC comparsion (1)

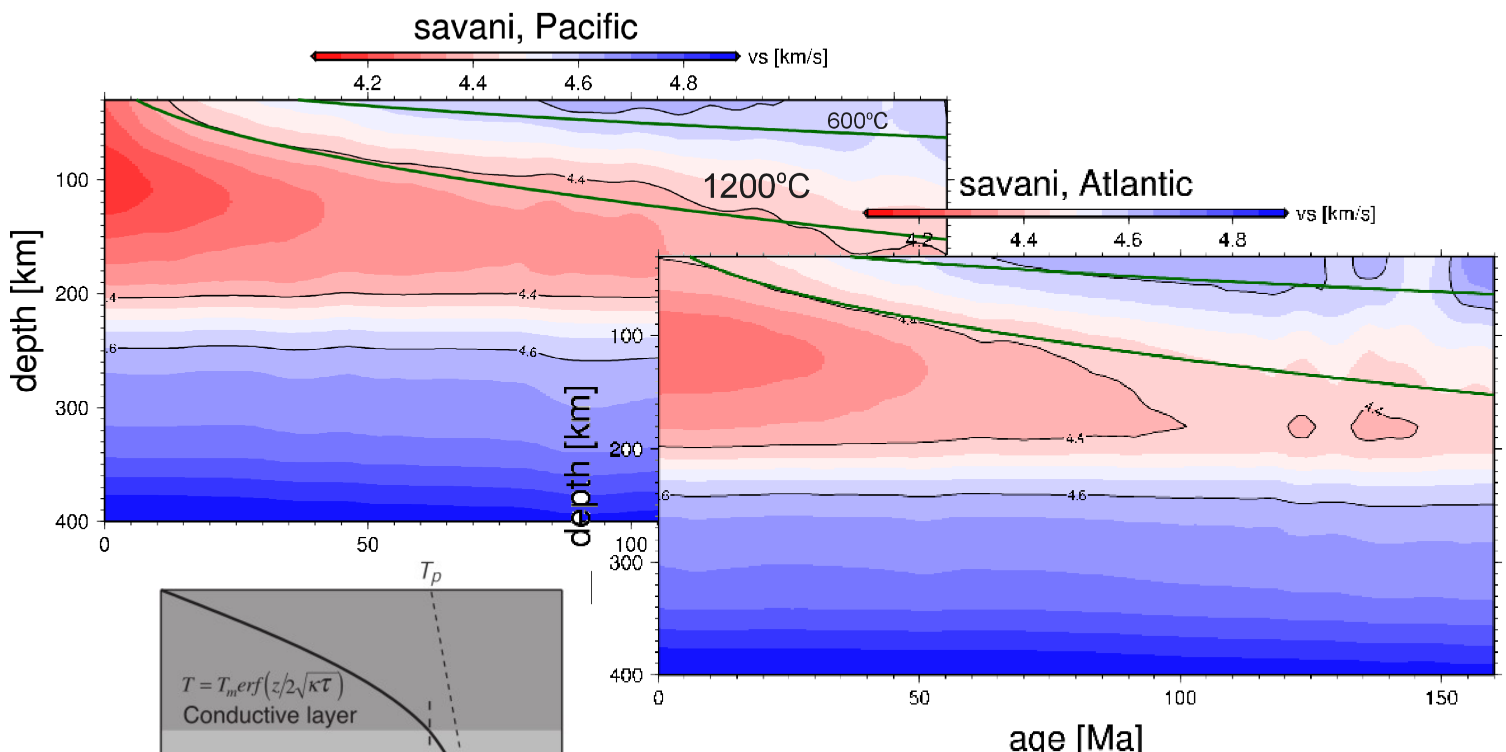

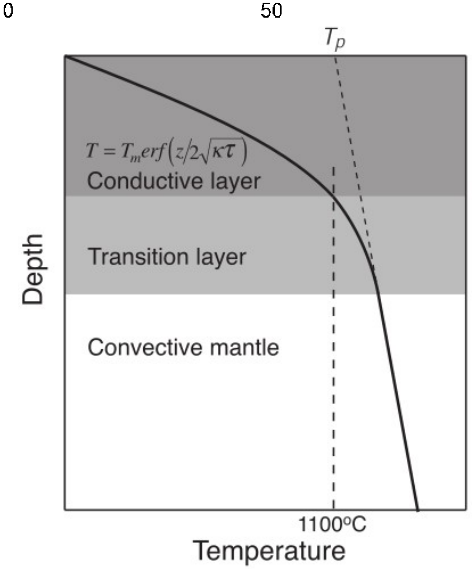

Half-space cooling works fine, but not at > ~80 Ma

Reference against sea-floor age, combine with a thermal Reference model, and vS-to-T scaling relationship

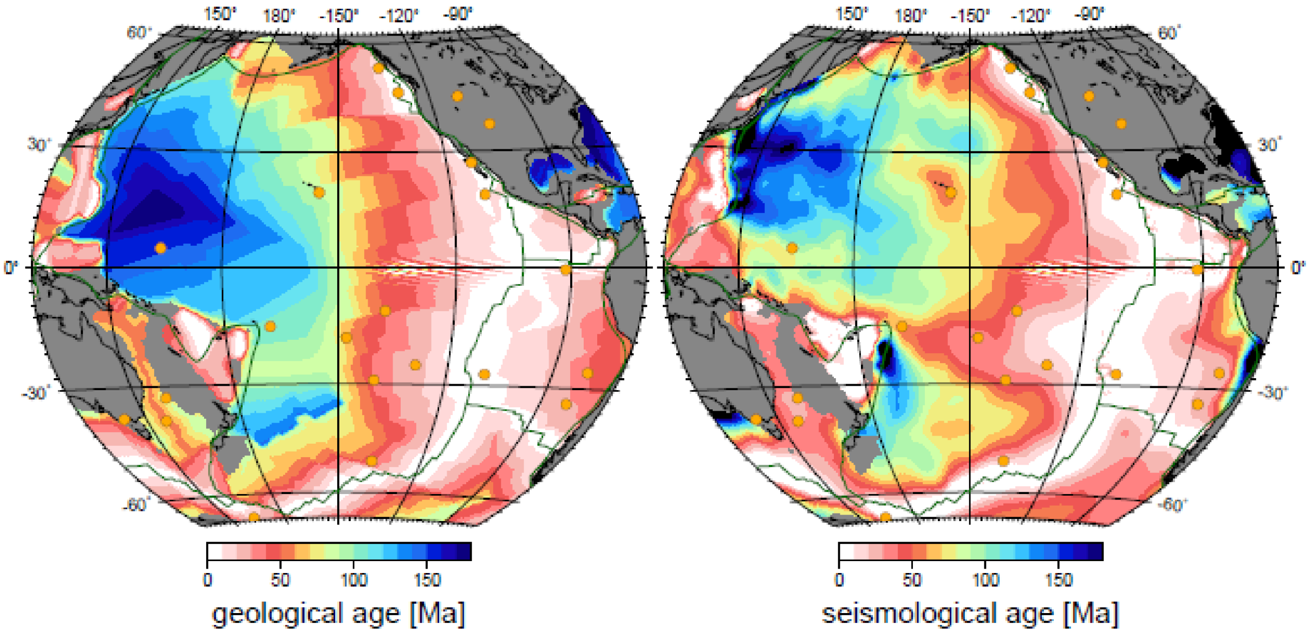

SAVANI, equivalent half-space cooling age, referenced to Pacific

cf. Ritzwoller et al. (2004)

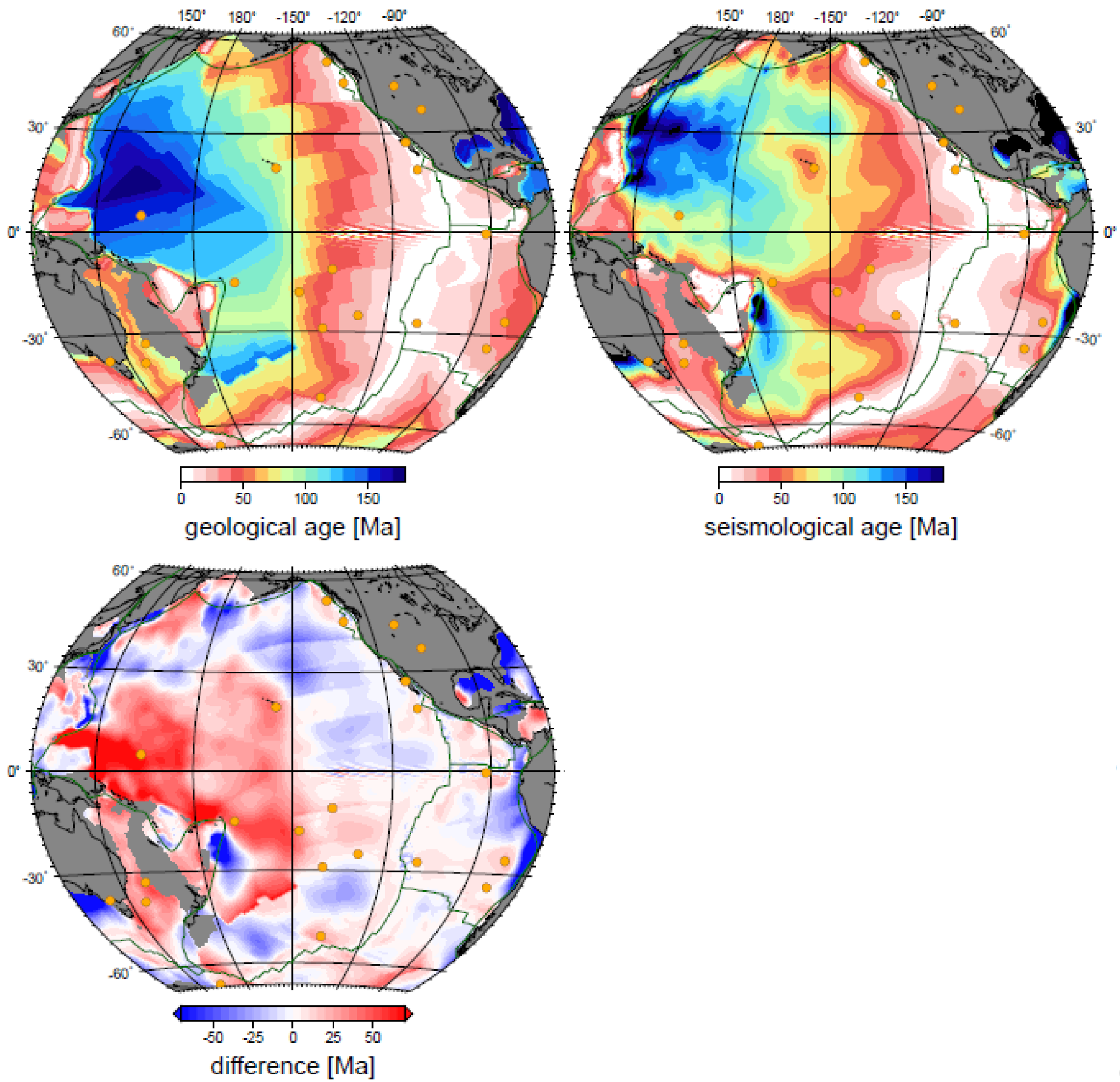

SAVANI, equivalent half-space cooling age, referenced to Pacific

cf. Ritzwoller et al. (2004)

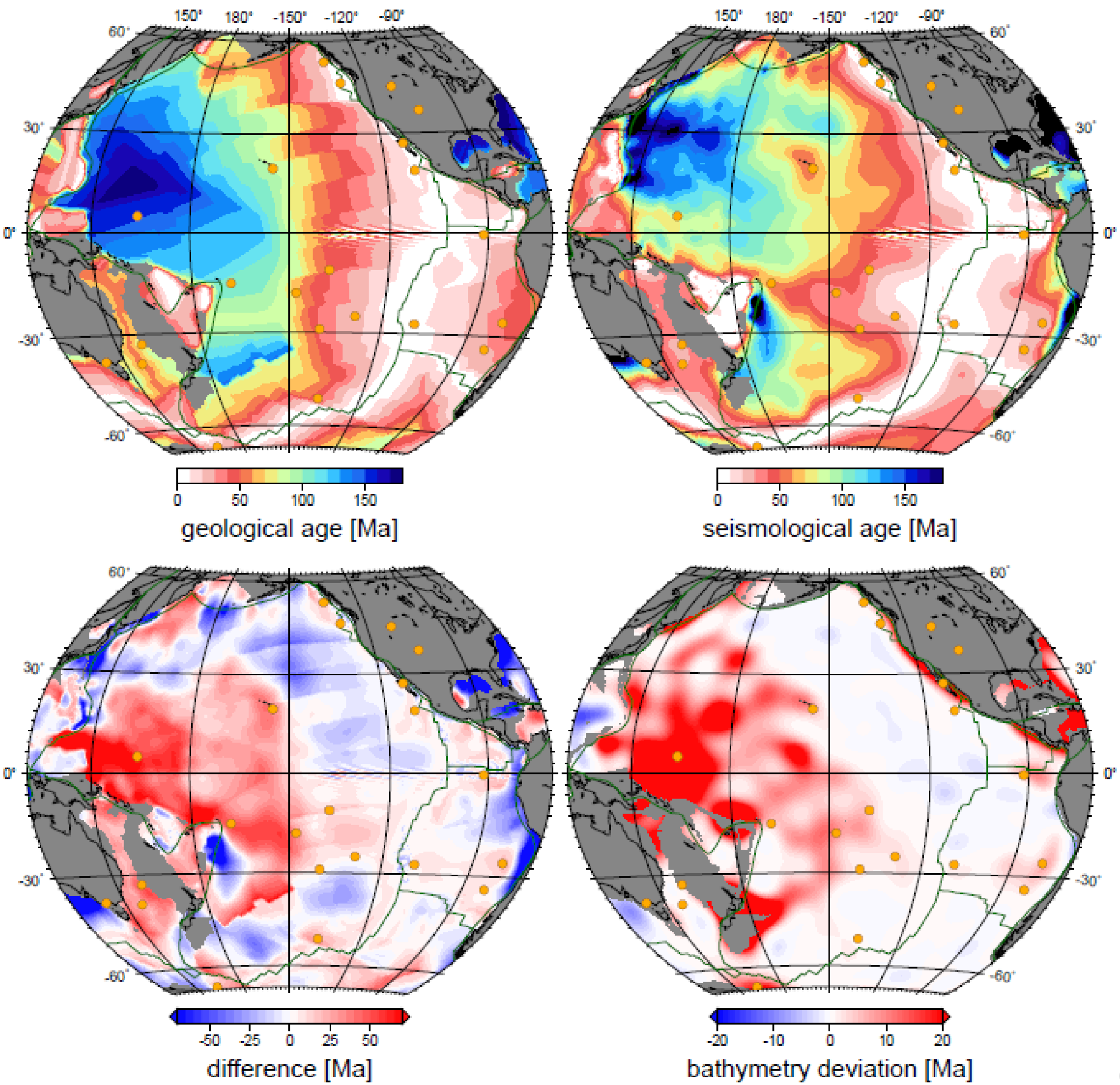

SAVANI, equivalent half-space cooling age, referenced to Pacific

cf. Ritzwoller et al. (2004)

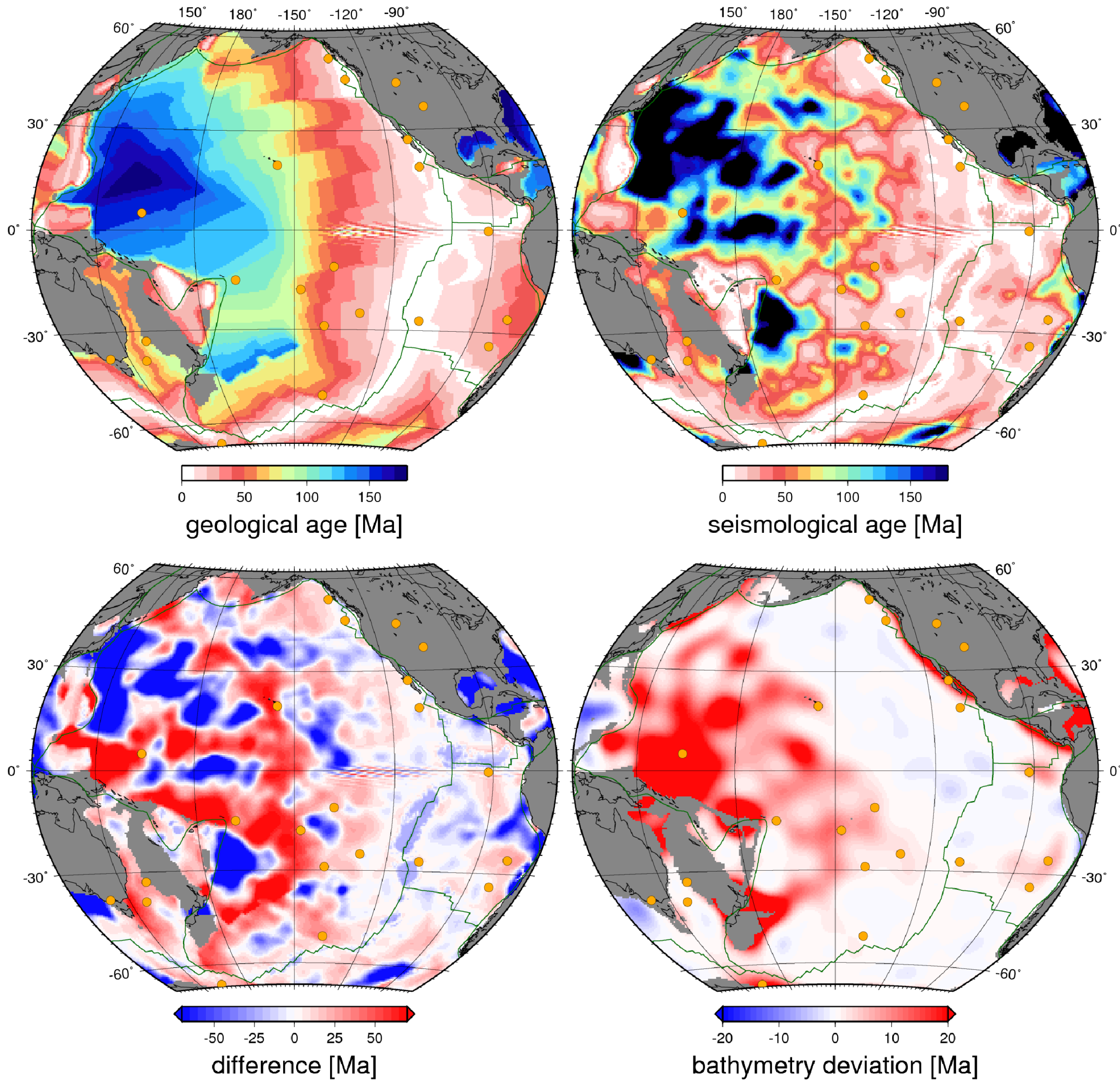

SEMum2, equivalent half-space cooling age, referenced to Pacific

Ritzwoller et al. (2004)

SH cross-model comparsions

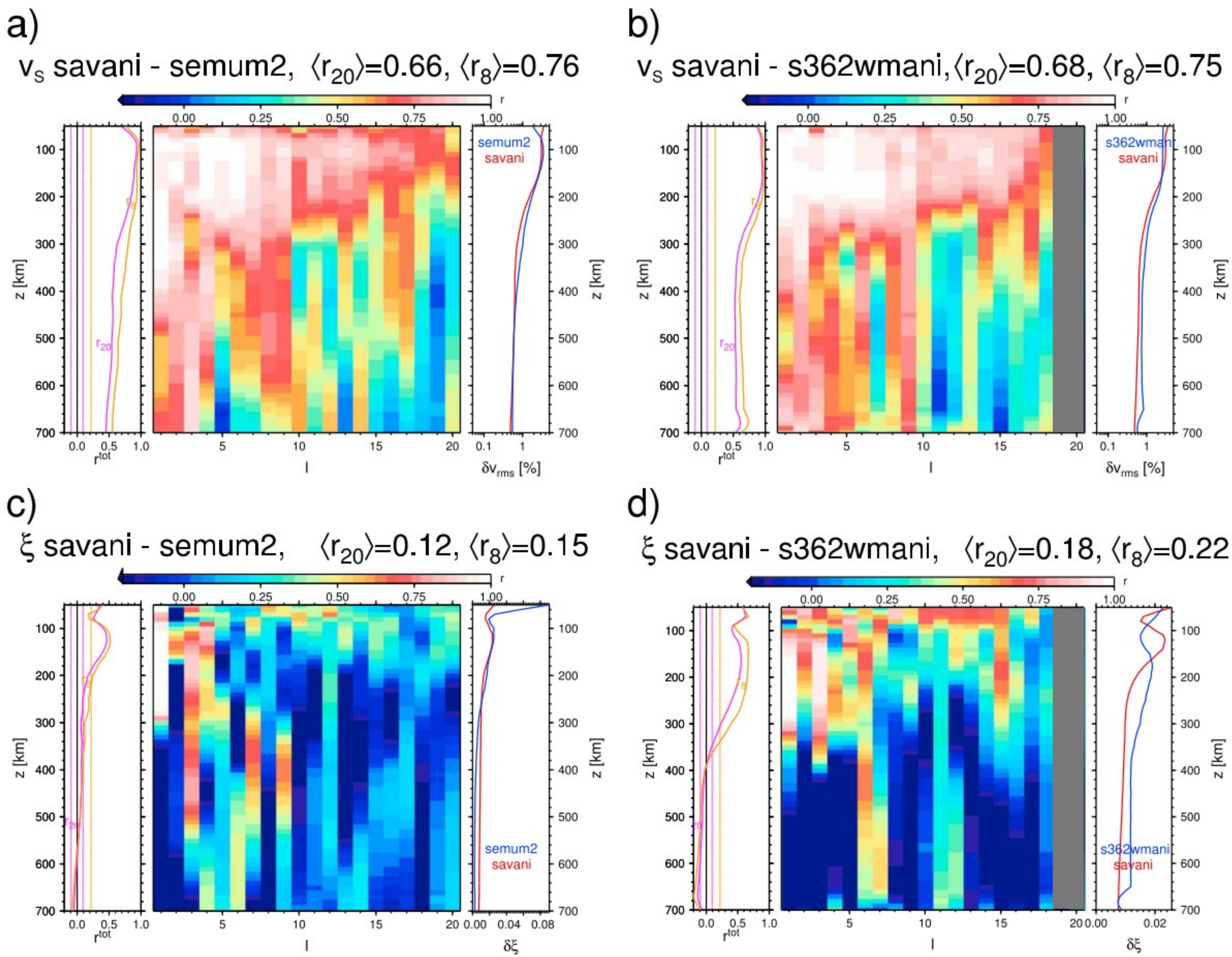

Model power, comparison

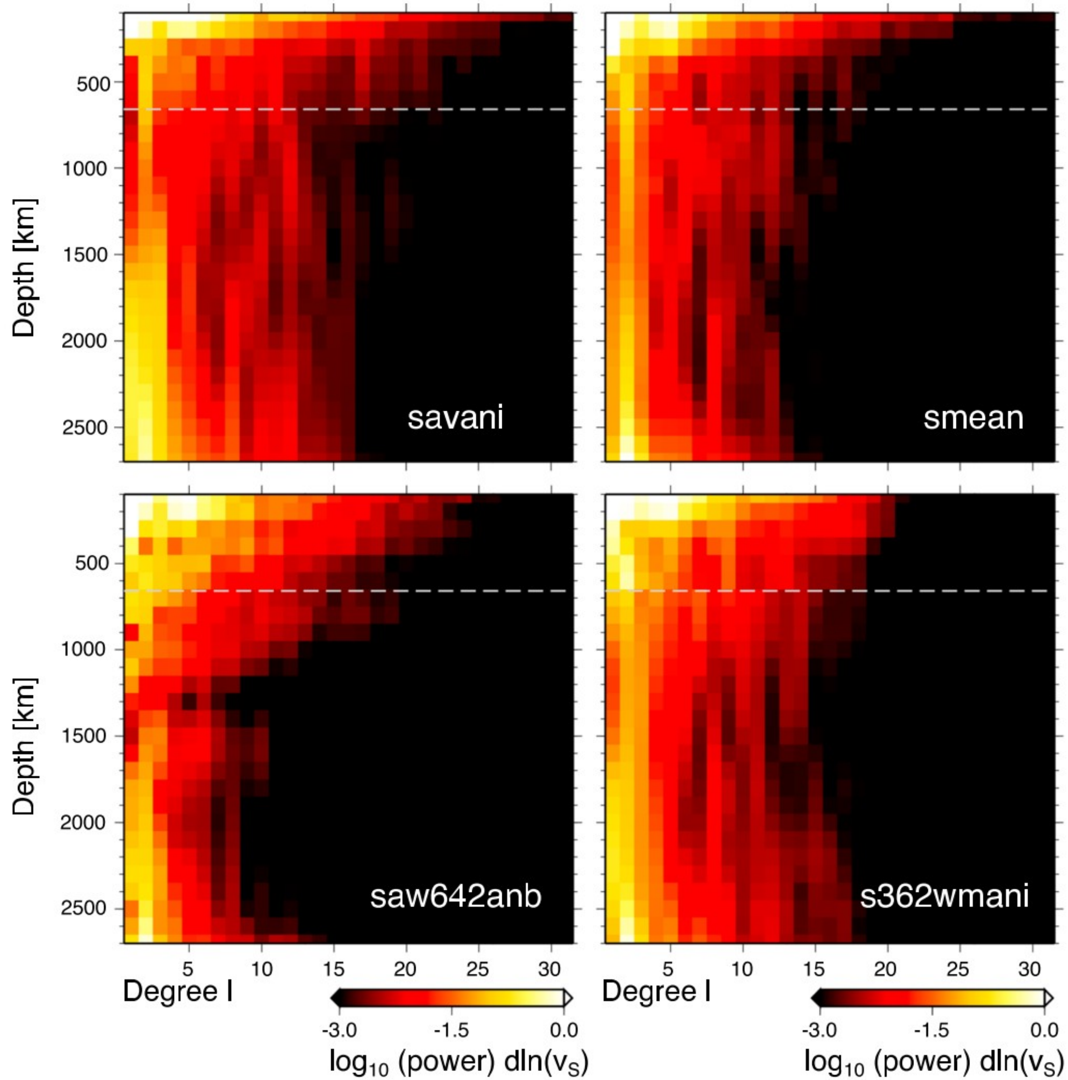

CRUST2.0 vs CRUST1.0

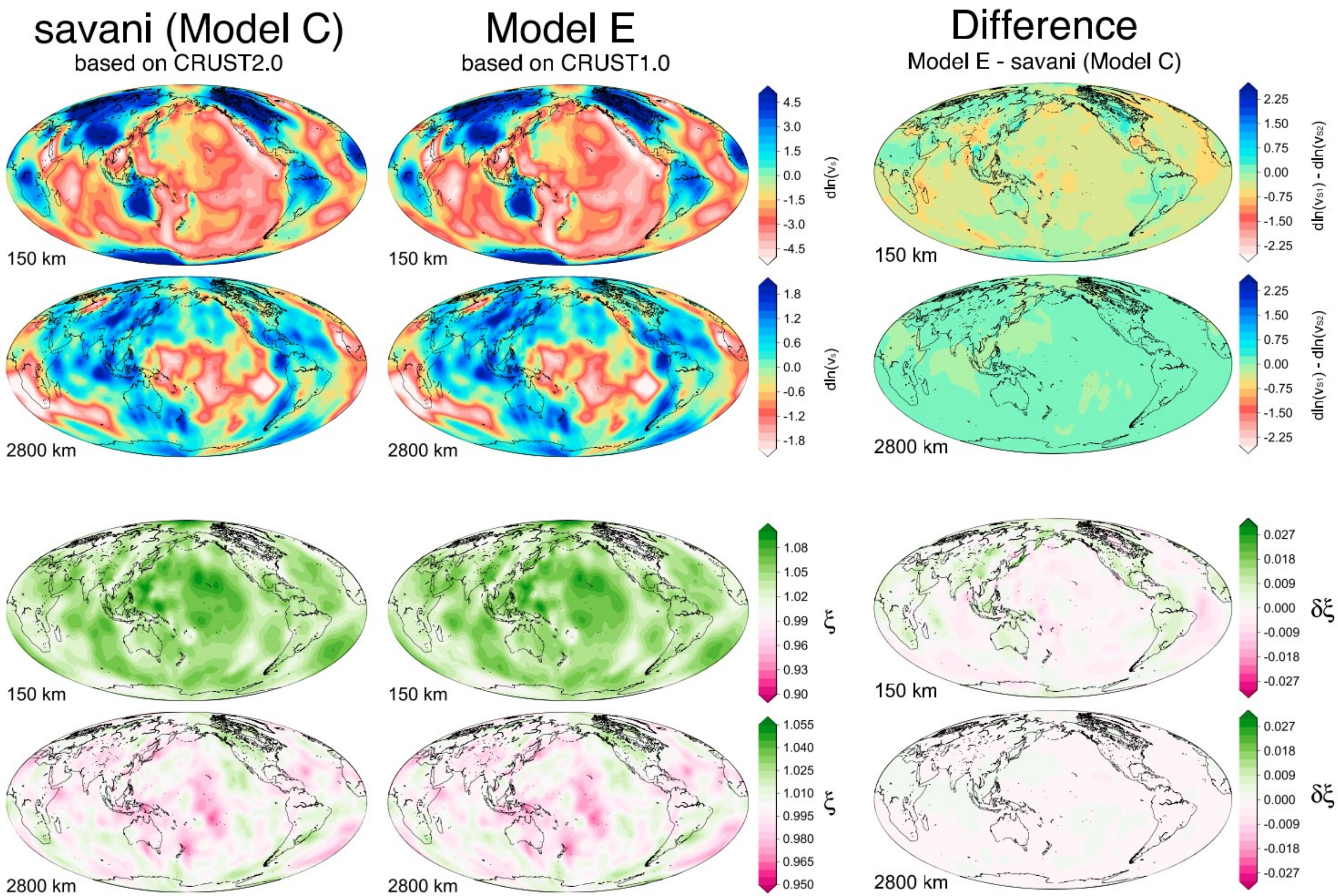

Figure A1. Map view comparison of *savani* (model C) with a preliminary test model in which the crustal model CRUST2.0 is replaced with its successor CRUST1.0.

Azimuthal anisotropy correction

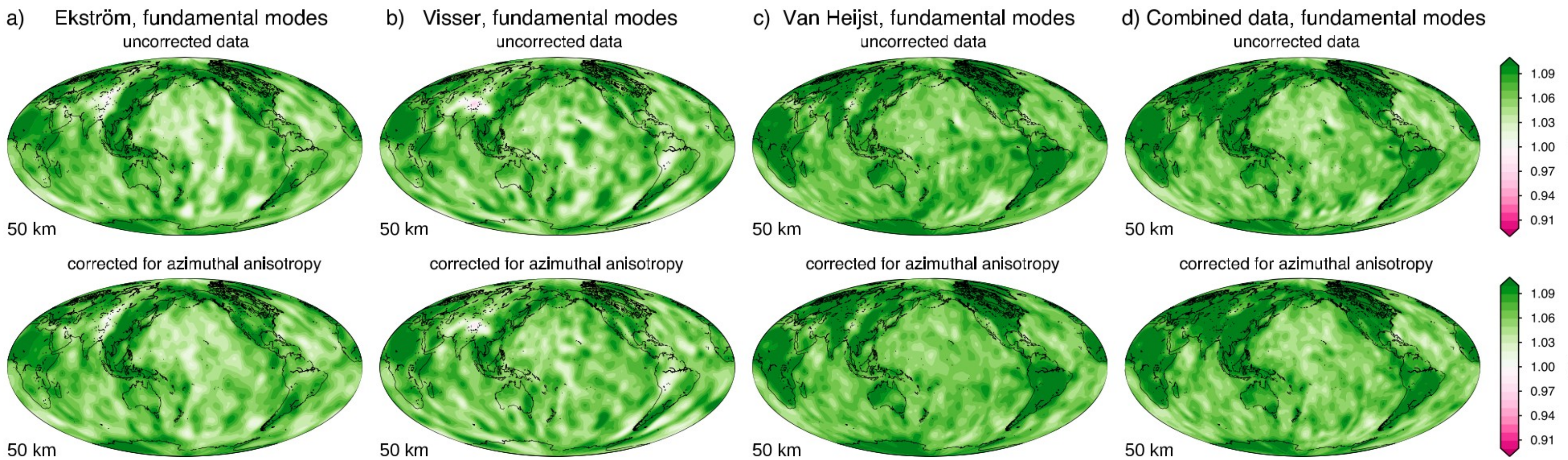

Figure 8. Anisotropic variations at a depth of 50 km, (a–d, top) before and (a–d, bottom) after correcting fundamental modes for azimuthal anisotropy. The corrections have profound effects [*Ekström*, 2011] and seem to remove a number of spurious anomalies such the streak-like feature extending from Tasmania toward the East Pacific Rise (Ekström data set). Combining all data sets sharpens the continental signature at shallow depths.

Checkerboard tests (Savani)

$$\mathbf{d} = \mathbf{A}\mathbf{m}; \qquad \mathbf{m}^\dagger = \mathbf{A}^\dagger\mathbf{d} = \mathbf{A}^\dagger\mathbf{A}\ \mathbf{m} = \mathfrak{R}\ \mathbf{m}$$

$\mathfrak{R}$ describes how the “real” Earth $\mathbf{m}$ is project

into the tomographic model $\mathbf{m}^\dagger$ (Menke, 1989)

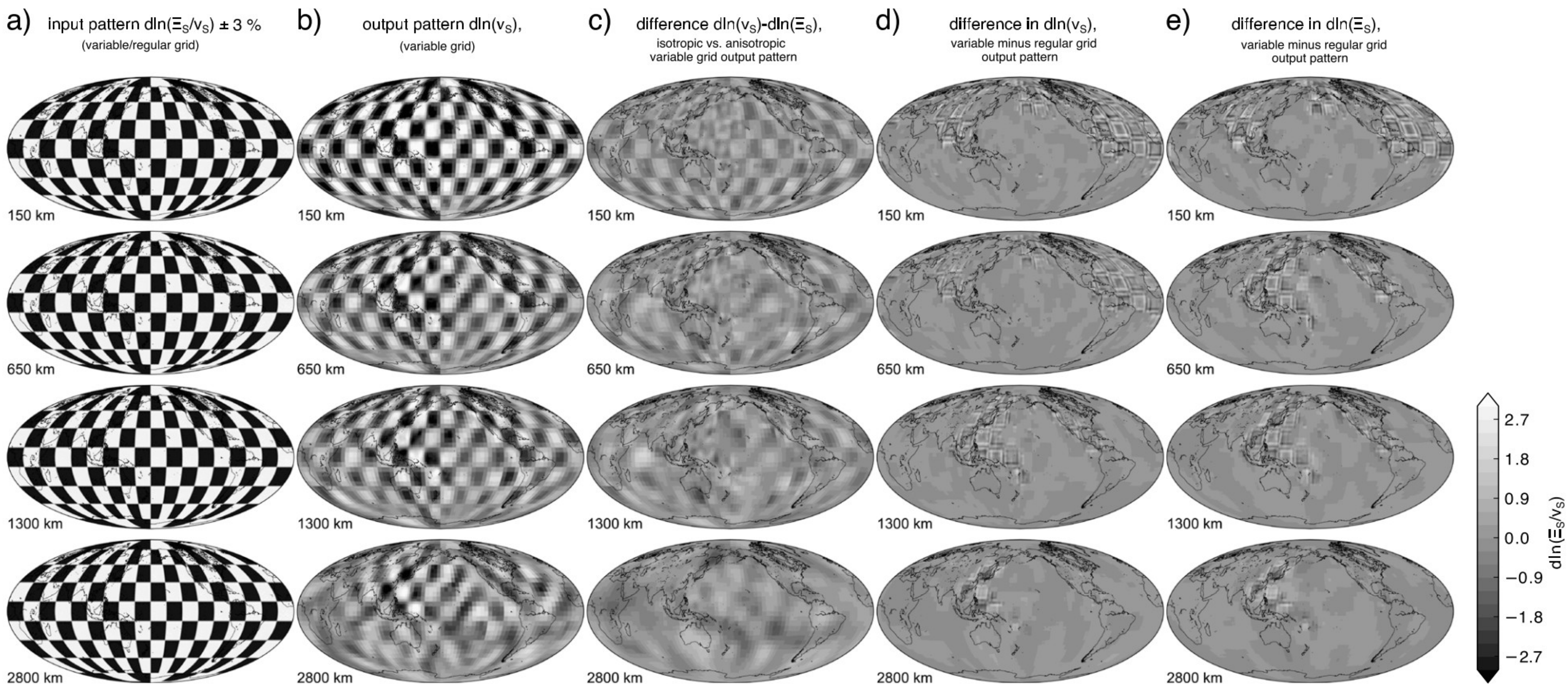

Leakage tests (Savani)

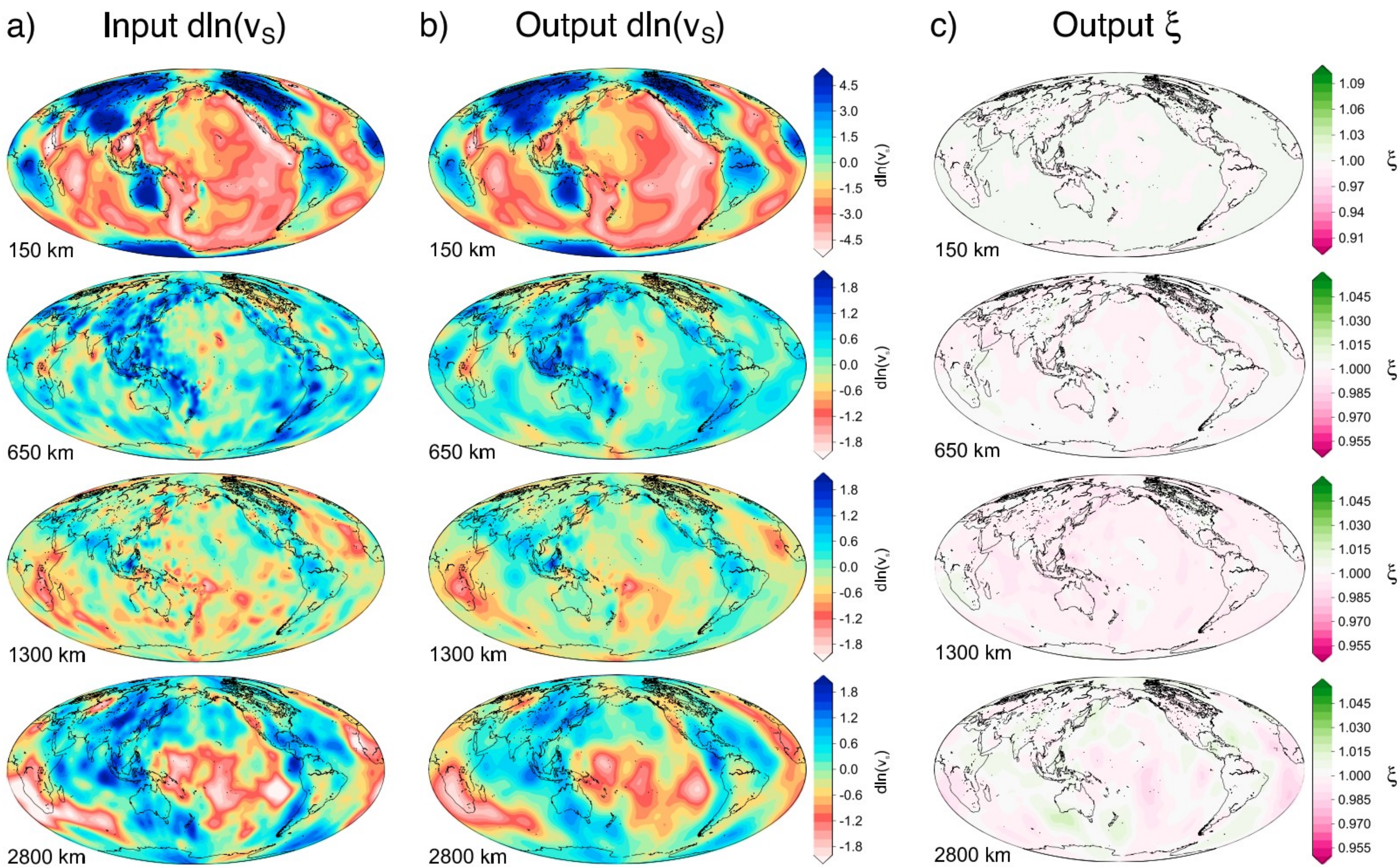

Ray hitcounts (SPani)

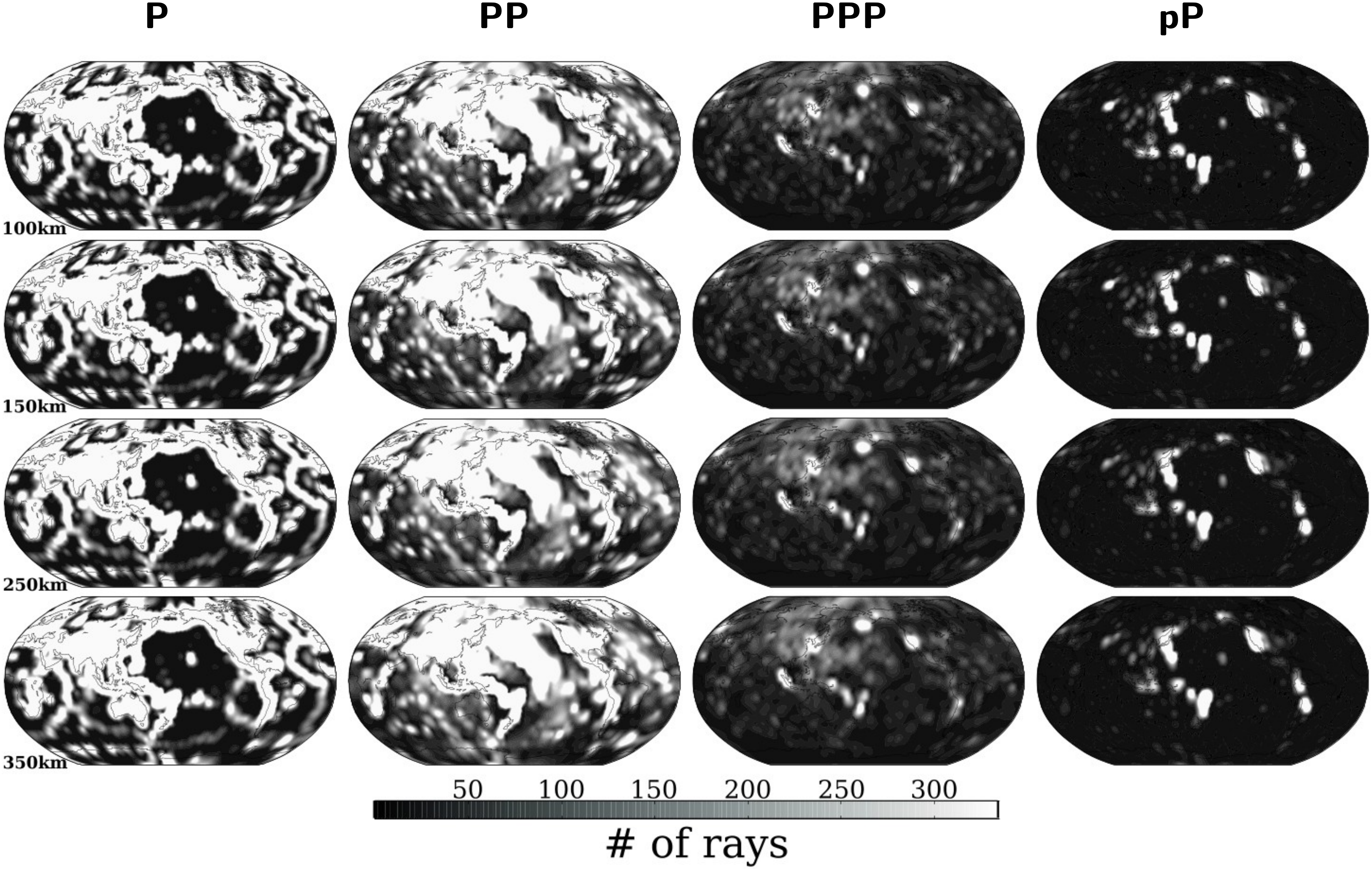

Tomographic filtering (SPani)

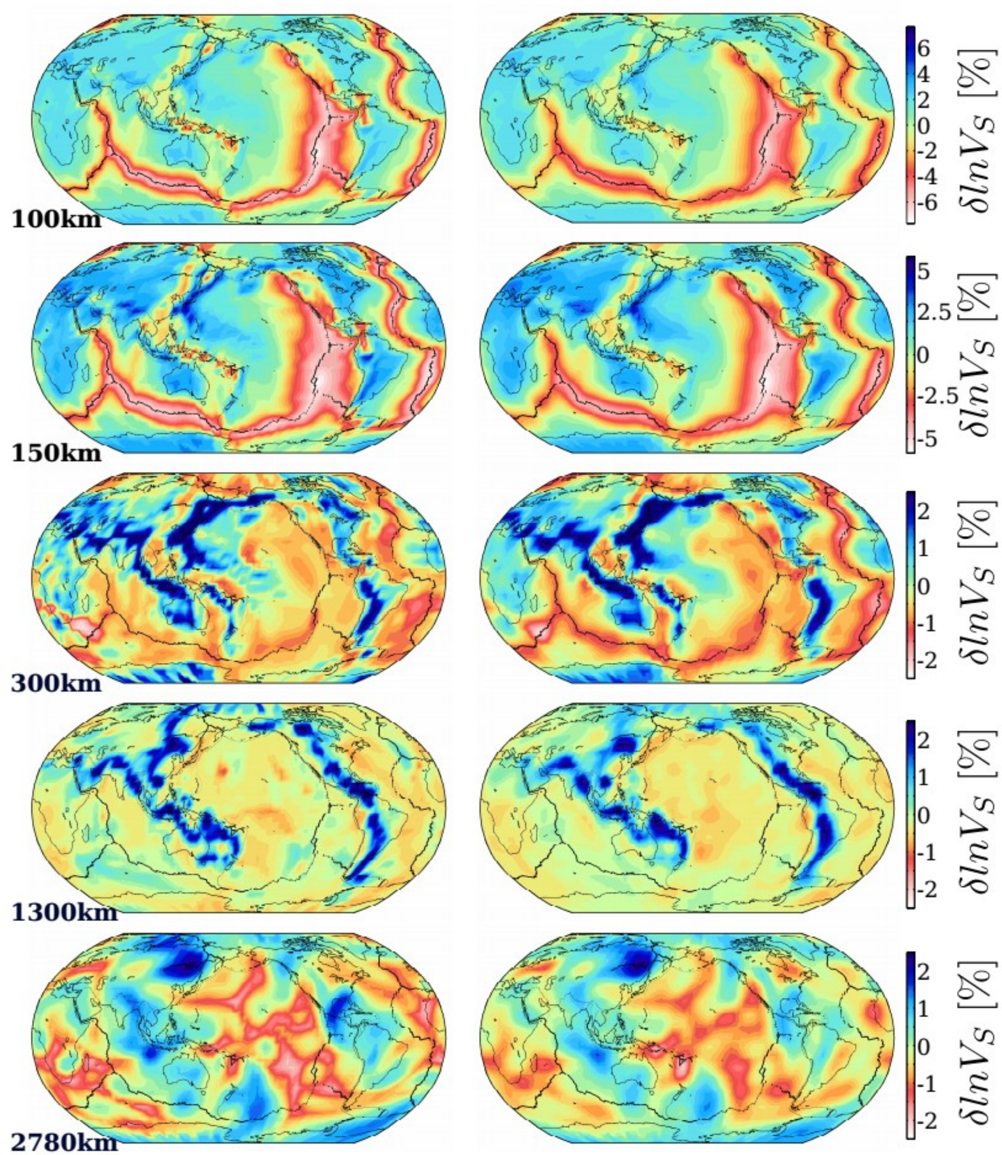

Leakage test (SPani)

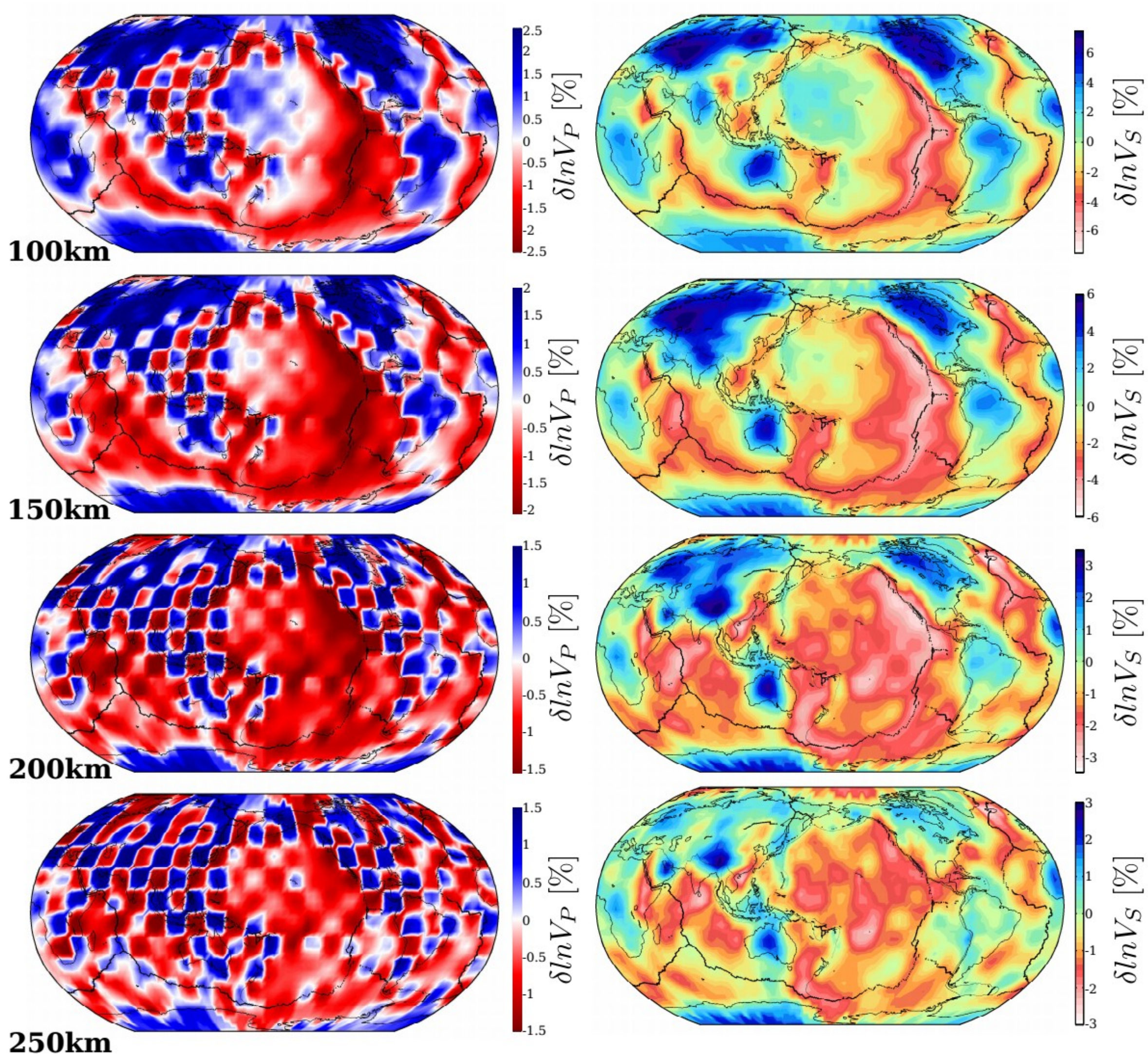

Leakage test (SPani)

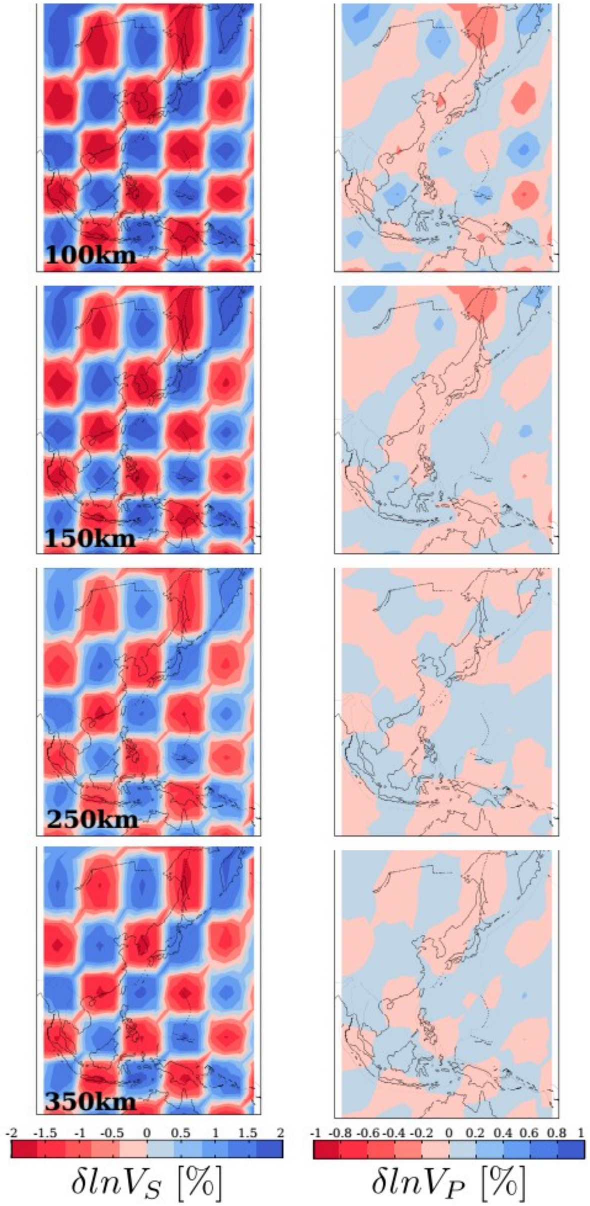

L-curve analysis (SPani)

Rayleigh + P have sensitivity
For P-wave structure, but not
Enough to resolve it.

We “help” the inversion to
converge to a geological
plausible model

Need to find a balance
between perfect scaling
(leading poor data fit) but not
to hide contribution from P-
waves in the regions where
we have large sensitivity

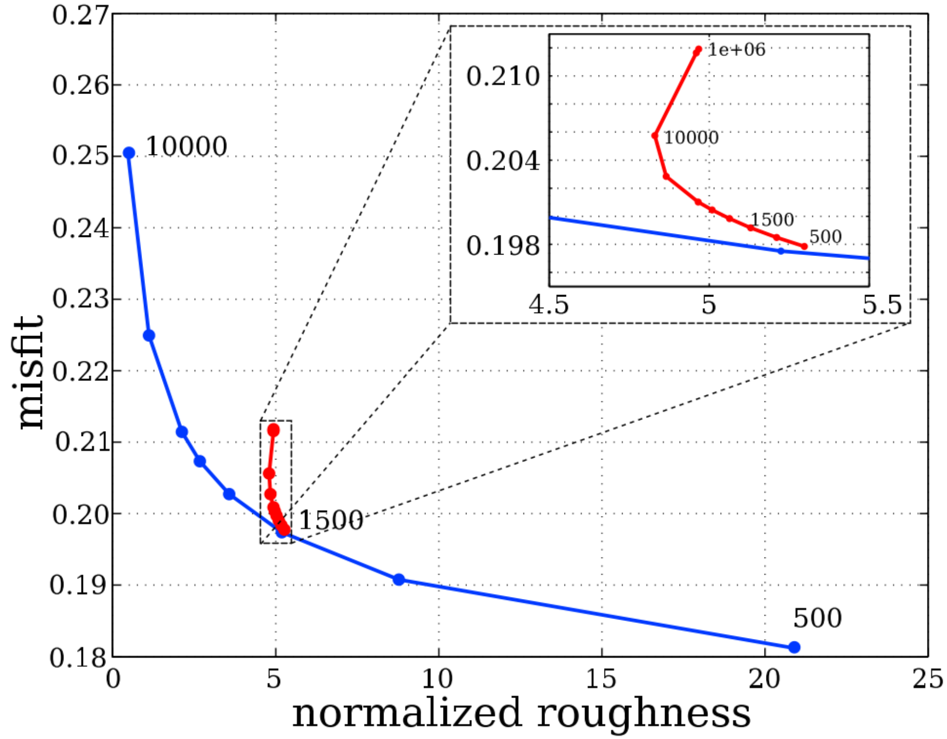

SPani test (without scaling constraints)

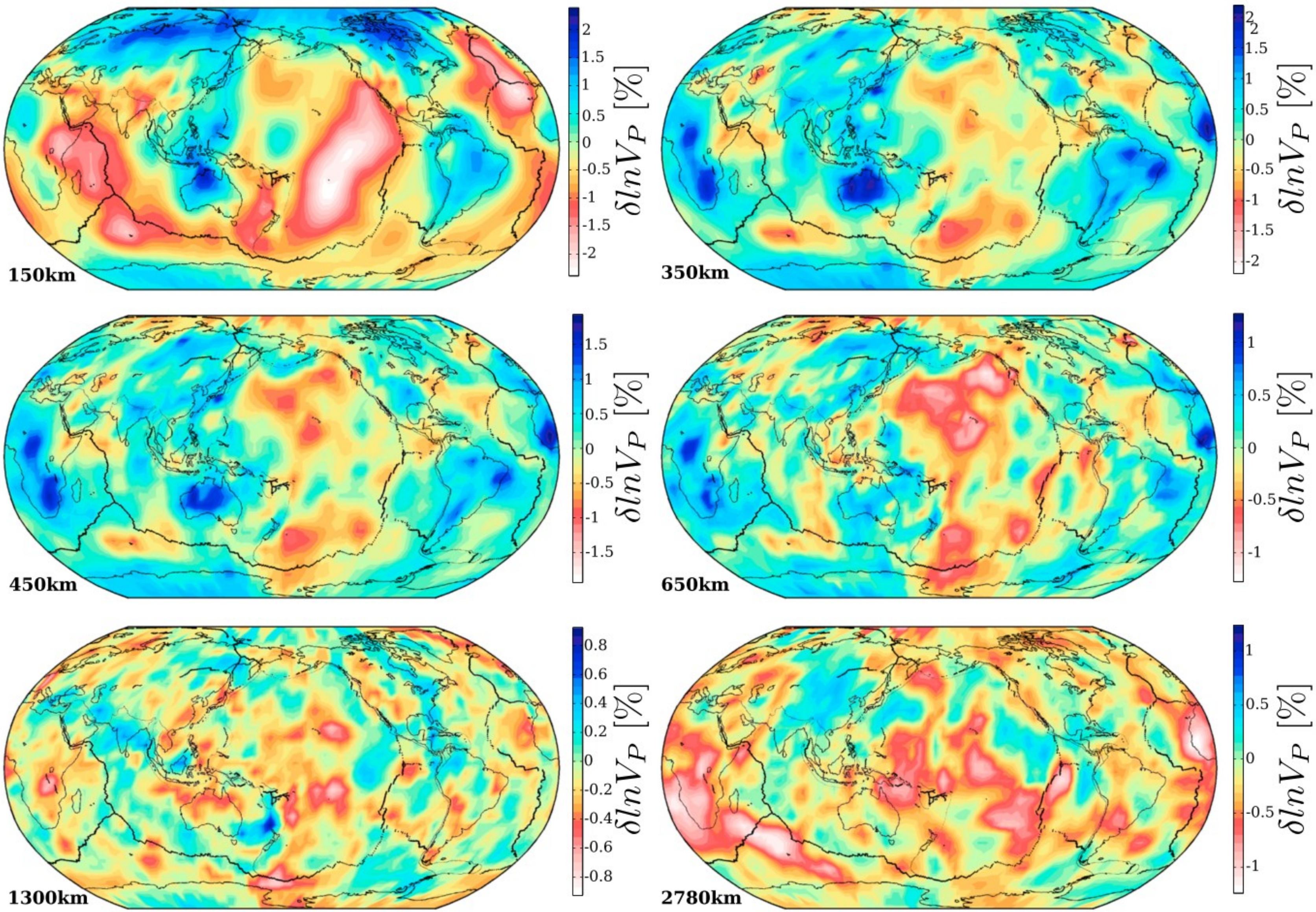

SPani (with scaling constraints)

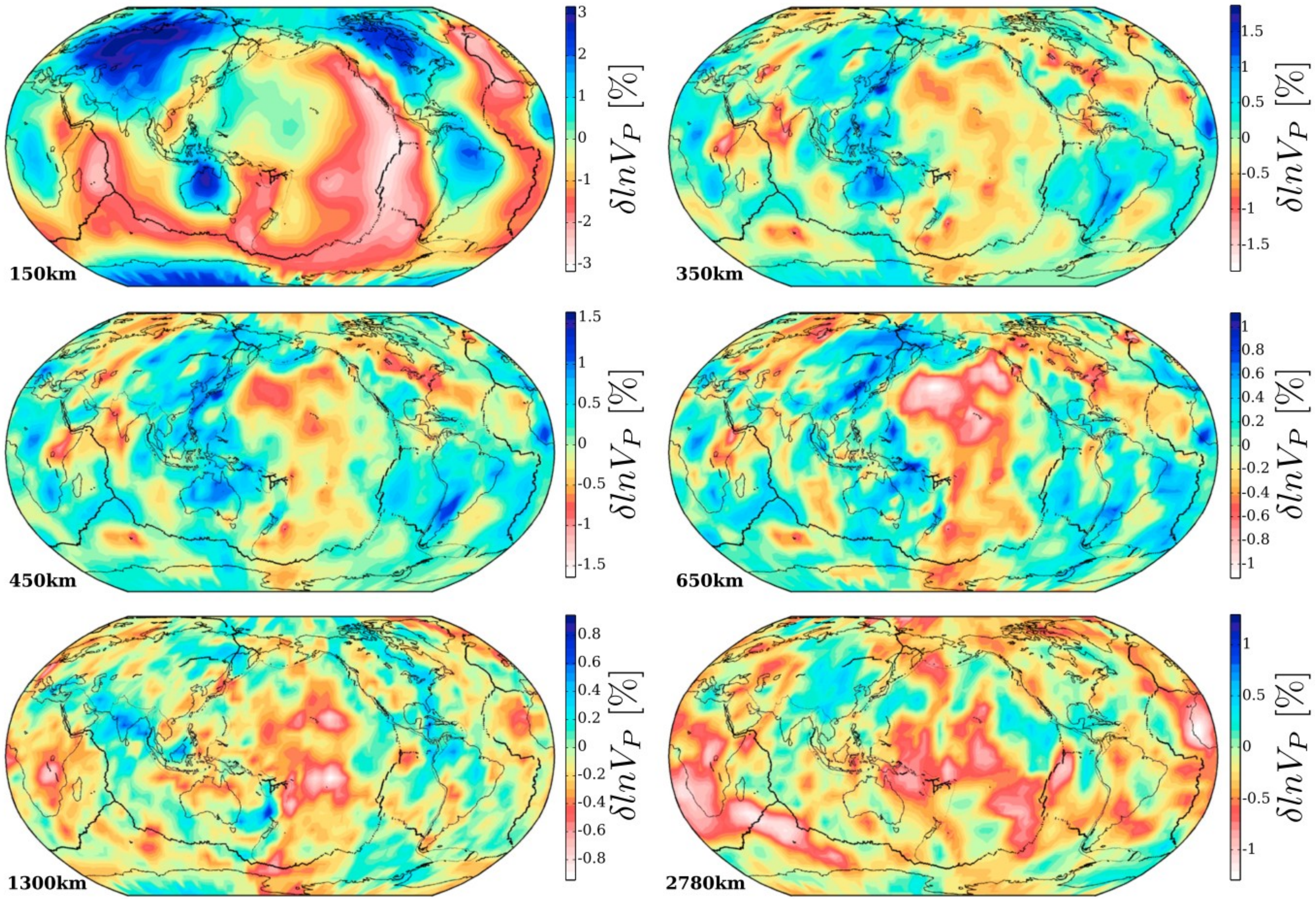

SPani (with scaling constraints)

Partial melting occuring in the subducting slab creates a volcanic arc. The stetching of the crust caused by the upwelling of molten magma creates a basin behind the volcanic chain (e.g. Japan sea, Philippine sea)

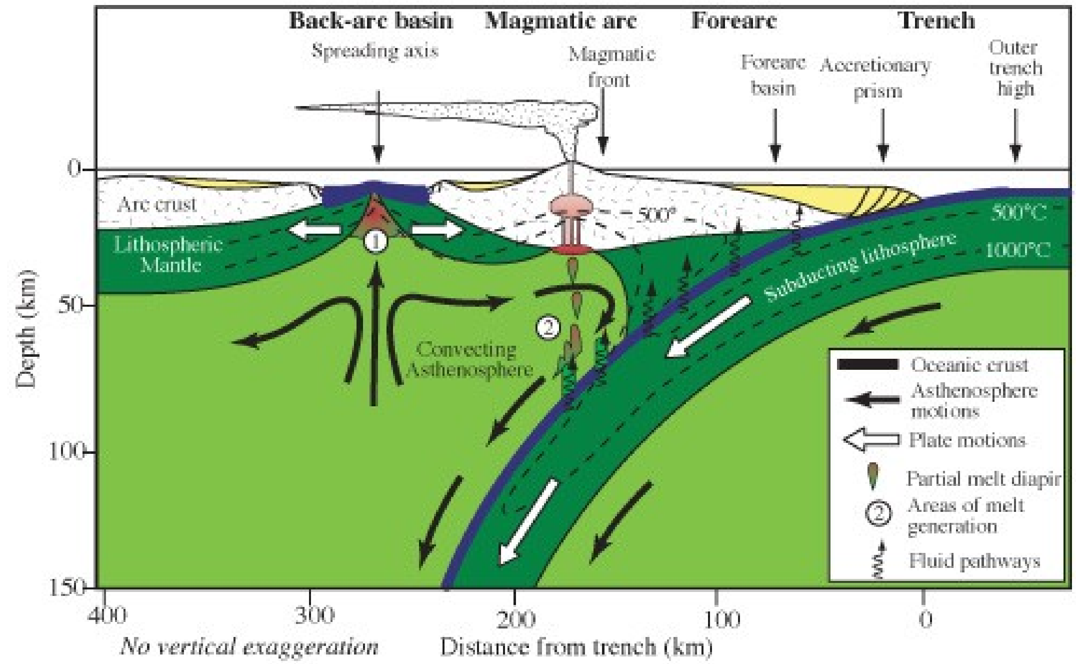

Water transported down via the subducted slab, enables partial melting and the creation of a magmatic. Probably not degassed entirely, since we find a lot of Serpentinized sea mountains (only forms if water present). Water trapped inside the mantle in the form of hydrous minerals? Fast eastward retreatment → lowered Viscosity? → small scale convection?

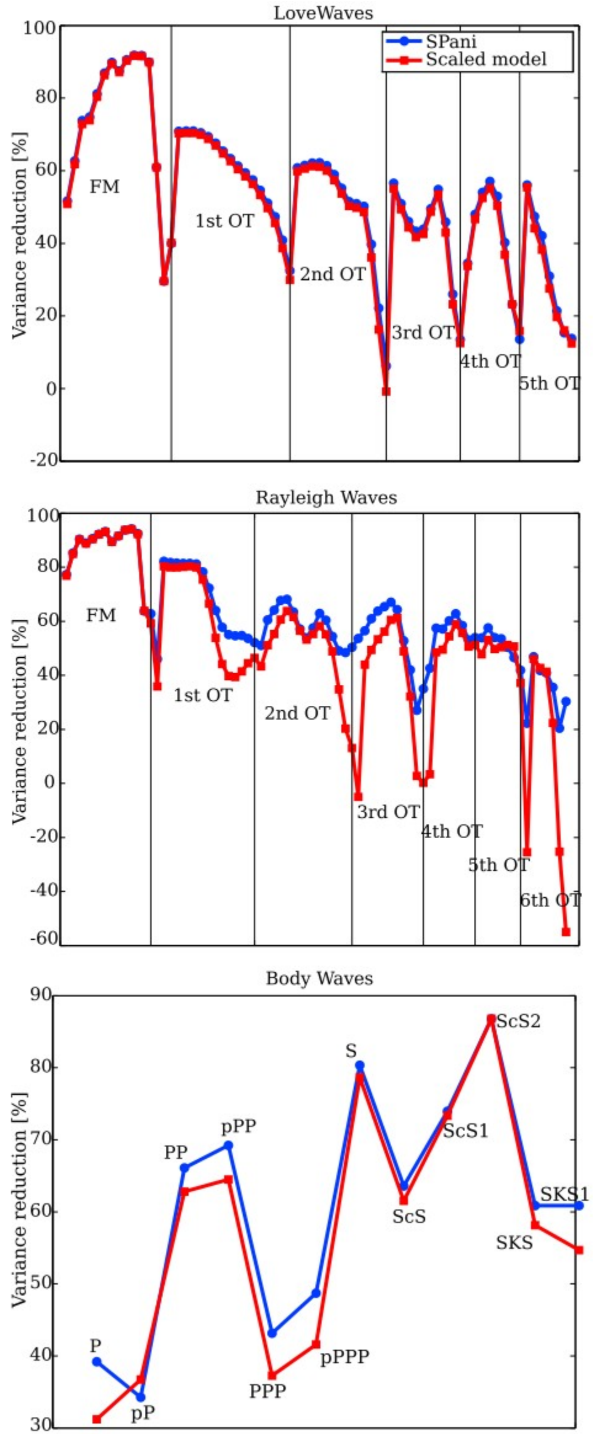

SPani + scaled model: datafit

A statistical condundrum

We assume normally distributed errors, define

$$\chi^2 = \sum_i \frac{|\sum_j A_{ij} m_j - d_i|^2}{\sigma_i^2}$$

And accept models with $\chi^2 \approx N$ we now take an acceptable model, and remove one anomaly (e.g. the Tahiti plume): Small enough that Chi squared remains acceptable!

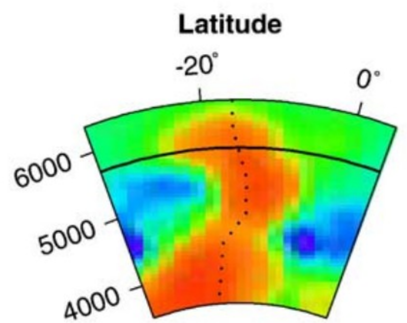

Does this mean Tahiti is not resolved?

A statistical condundrum

We

χ

And

take

anom

ough that Chi squared remains acceptable!

Does this mean Tahiti is not resolved?

Could be done for any anomaly! Nothing resolved?

However there are subsets of the data, that violate the criterion (e.g. the station under Tahiti)

→ Create subset criterion, regionalized datasets!

Measuring CC traveltimes

Frequency response

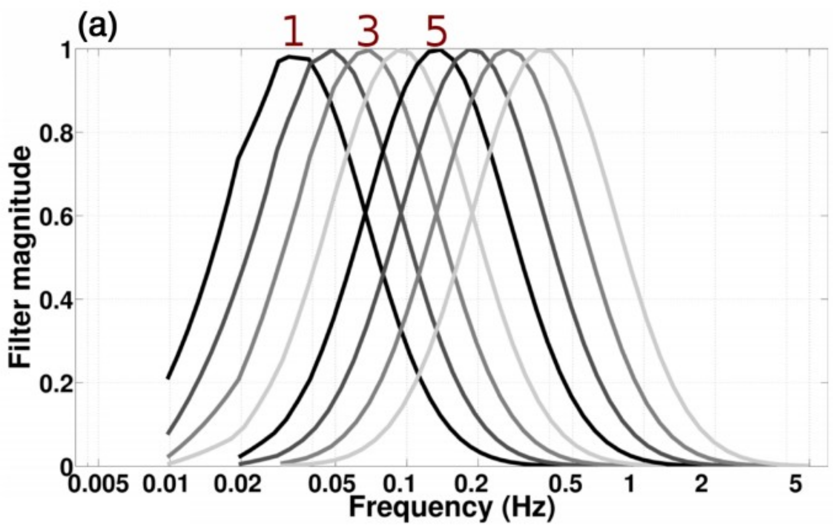

Constant fractional bandwidth

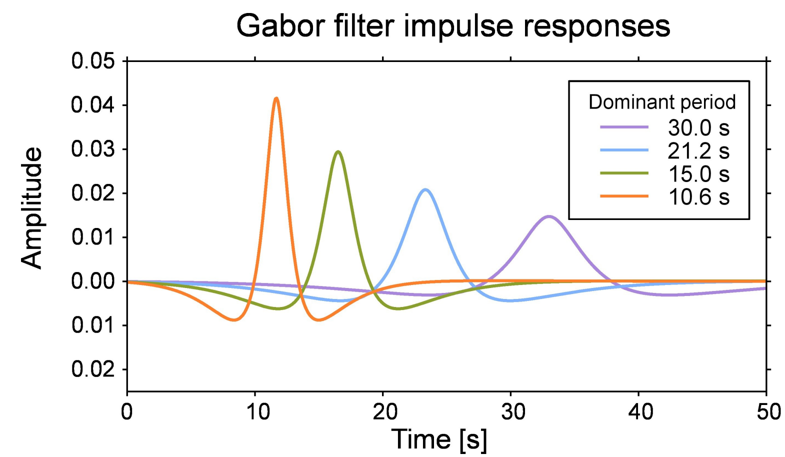

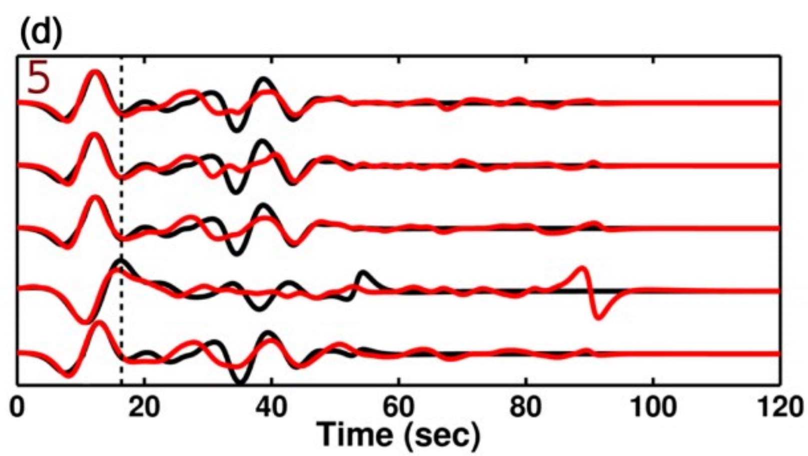

Measuring phase anomalies

Using ray theory on a sphere (e.g. Tromp & Dahlen, 1993) we can write surface wave displacement, for a reference earth, as a function of frequency as

$$u(\omega) = A(\omega)\exp\left[\frac{i\omega\Delta}{c(\omega)}\right]$$

Source Phase/Receiver Phase/Propagation Phase

The observed surface wave displacement, is given as a perturbation to the reference

$$u(\omega) + \delta u(\omega) = [A(\omega) + \delta A(\omega)]\exp\left[\frac{i\omega\Delta}{c(\omega)} + \delta\Phi(\omega)\right]$$

→ Compare seismogram with its reference synthetic in a waveform fitting procedure, that involves phase- and amplitude matching procedure in different frequencies

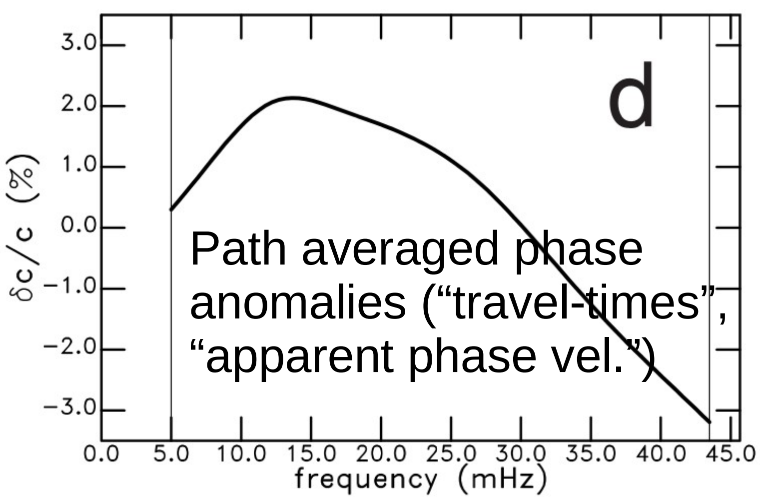

Path averaged phase anomalies ("travel-times", "apparent phase vel.")

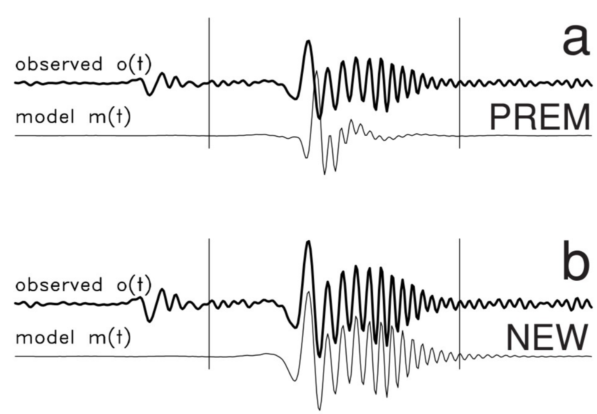

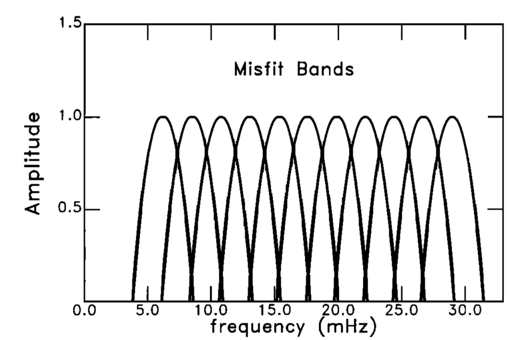

Dispersion properties of 1D medium iteratively modified until synthetic fits measured waveform

Phase anomaly → 2D phase velocity maps

Phase anomaly is related to local slowness perturbation via

$$\delta\Phi(\omega) = \omega \int_0^{\Delta} \delta p(\theta(s), \phi(s); \omega) \mathrm{d}s$$

Phase slowness p is expanded
in some basis functions, e.g.: splines
Pixels, Spherical Harmonics, or ...

Slowness perturbation is related to structure

$$\delta p(\theta, \phi; \omega) = \int_0^{a} \sum_{i=1}^{I} K_i(r; \omega) \delta\pi_i(r, \theta, \phi) dr,$$

K_i can be freqency dependent
frechet derivatives or 1D-sens-
Itivity functions

2 options: Inversion can be done using a 3D parameterization in one step or via the detour of first making 2D phase velocity “maps” or regionalized dispersion curves

$$\delta\Phi(\omega) = \omega \int_0^{\Delta} \int_0^{a} \sum_{i=1}^{I} K_i(r; \omega) \delta\pi_i[r, \theta(s), \phi(s)] drds$$

Savani: modeling details (1)

- Horizontally: Local blocks, either constant 3° or with size depending on coverage (1.25°-5.0°); Vertically: 12/27 layers
- Physical parameterization: Radial anisotropy in V_{SH} and V_{SV} or $V_{S_{Voigt}}$ and χ
- Weighting: downweighting outliers and upweighting for differential number of measurements
- Regularization: Roughness minimization $x_i - \sum_{l=1}^{N} x_l = 0$
- Reference model: PREM

Savani: modeling details (2)

Surface wave phase velocity perturbation $\delta c(\omega)$ related to selected inversion parameter $\delta\pi_i(r,\theta,\phi)$, using

$$\frac{\delta c_j(\omega)\Delta}{\omega} = \sum_{i=1}^{I}\sum_{k=1}^{K} x_{ik} \int_0^{\Delta_j}\int_0^{a} K_i(r;\omega) f_k(r,\theta,\phi)\,dr\,ds \qquad (1)$$

For body waves we get the similar expression

$$\delta T = -\sum_{k=1}^{K} x_{ik} \int_0^{\Delta_j} K_i(r;\omega) f_k(r,\theta,\phi)\,ds \qquad (2)$$

Leads to a linear system to be solved in a least-squares sense

$$\mathbf{x} = (\mathbf{A}^T \cdot \mathbf{A})^{-1} \cdot \mathbf{A} \cdot \mathbf{d} \qquad (3)$$

Sensitivity (2)

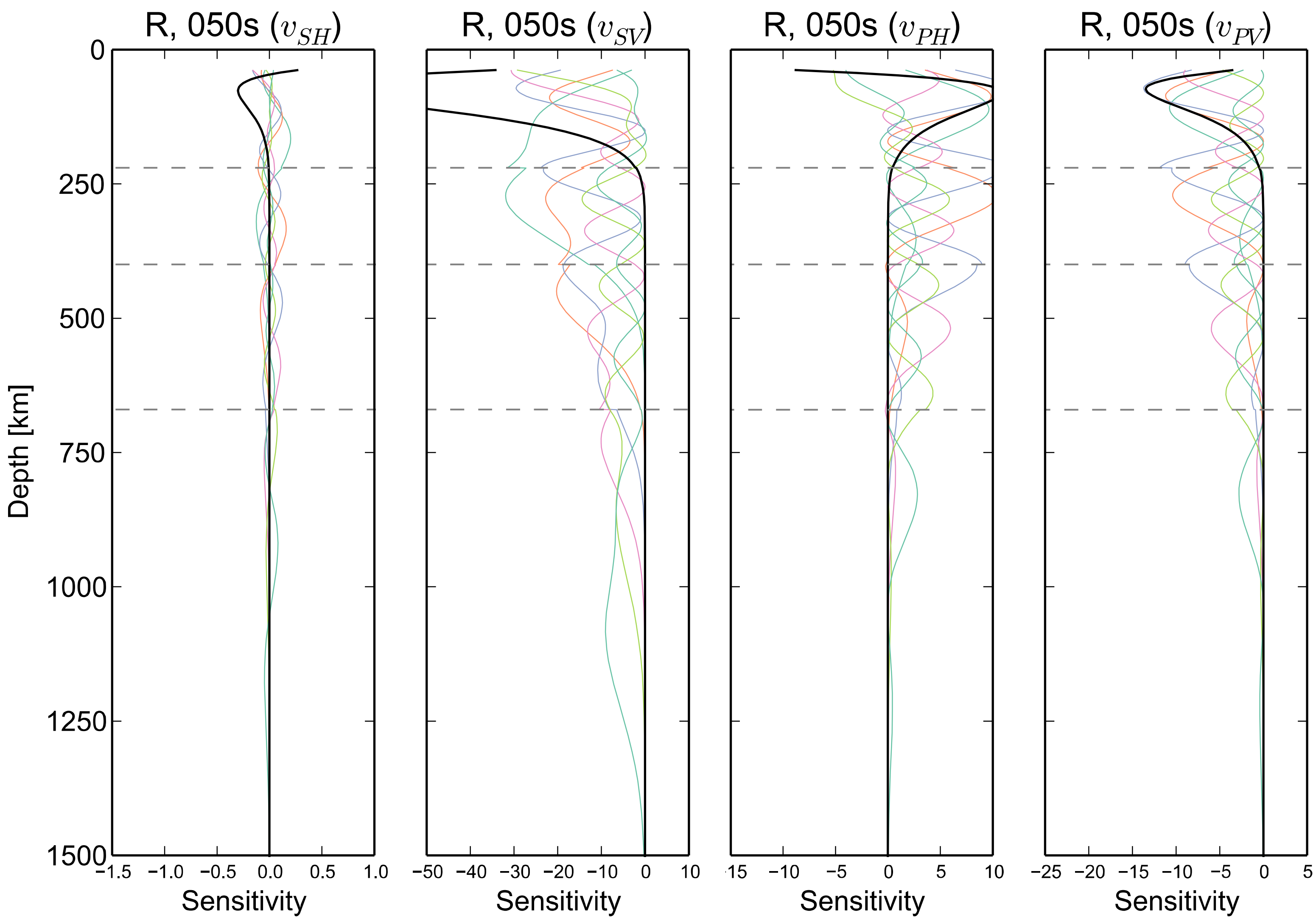

Sensitivity (1)

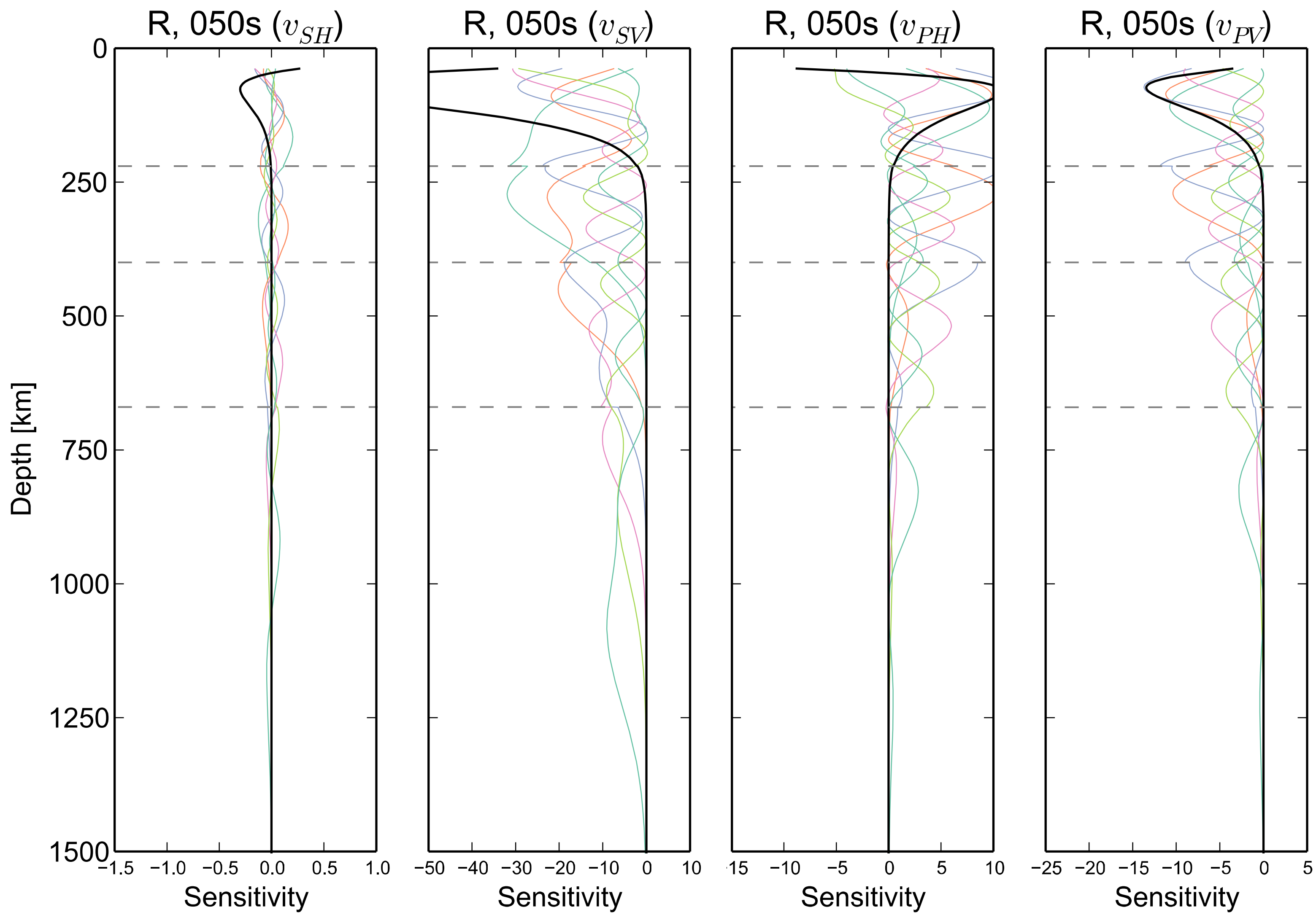

RMS comparsion

RMS profiles of our global model compared to previously published global models of radial anisotropy

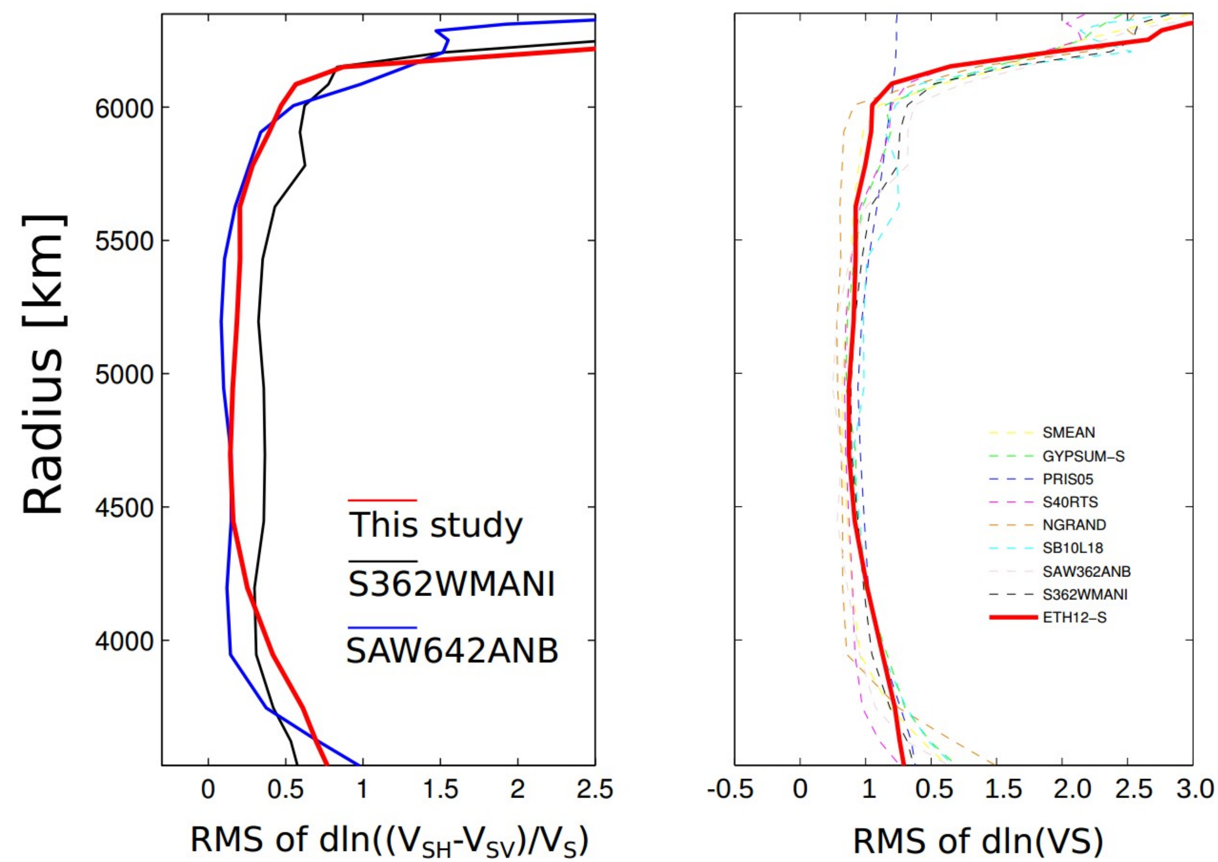

(1) Introduction: Tomography approach

Imaging multi-scale structure and dynamics

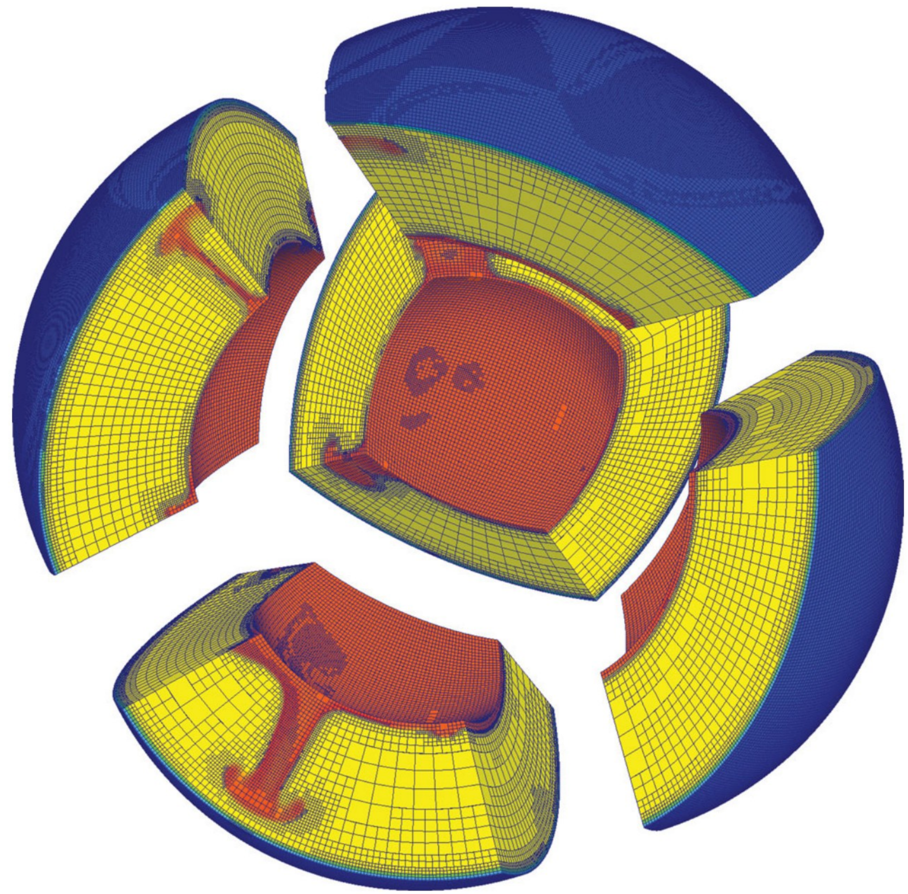

(1) Introduction: Tomography approach

Imaging multi-scale structure and dynamics

- Global mantle convection embraces multiple, coupled scales

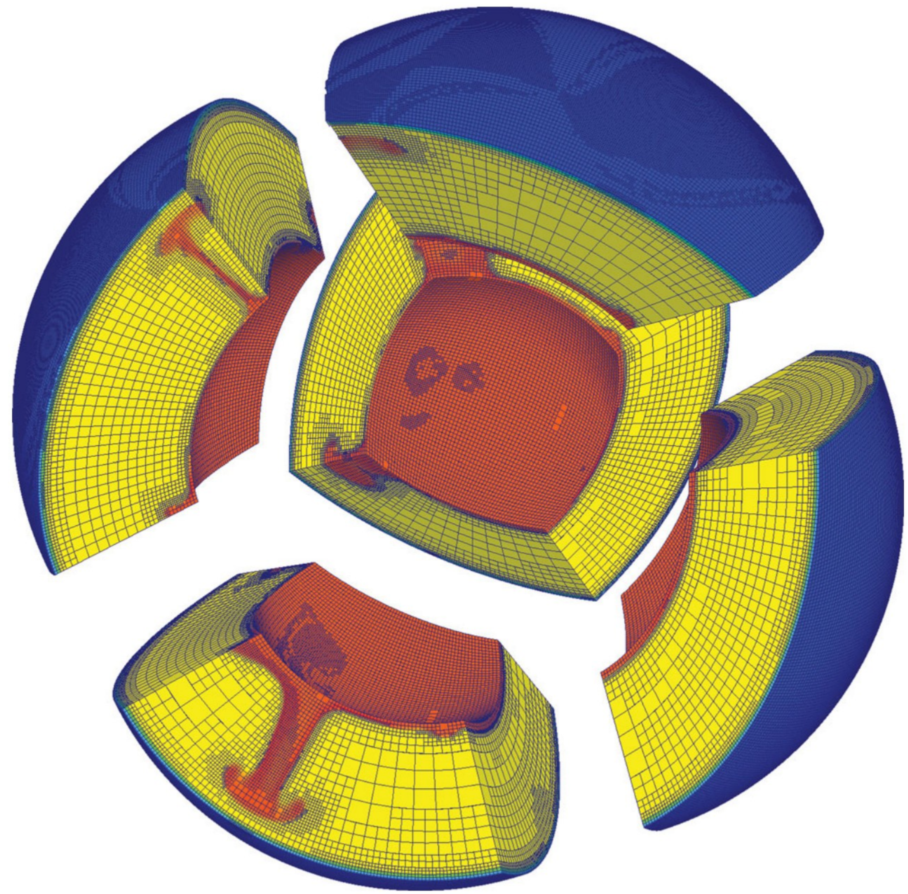

(1) Introduction: Tomography approach

Imaging multi-scale structure and dynamics

- Global mantle convection embraces multiple, coupled scales
- Convection models optimally account for them *(see, e.g. Burstedde et al. 2013)*

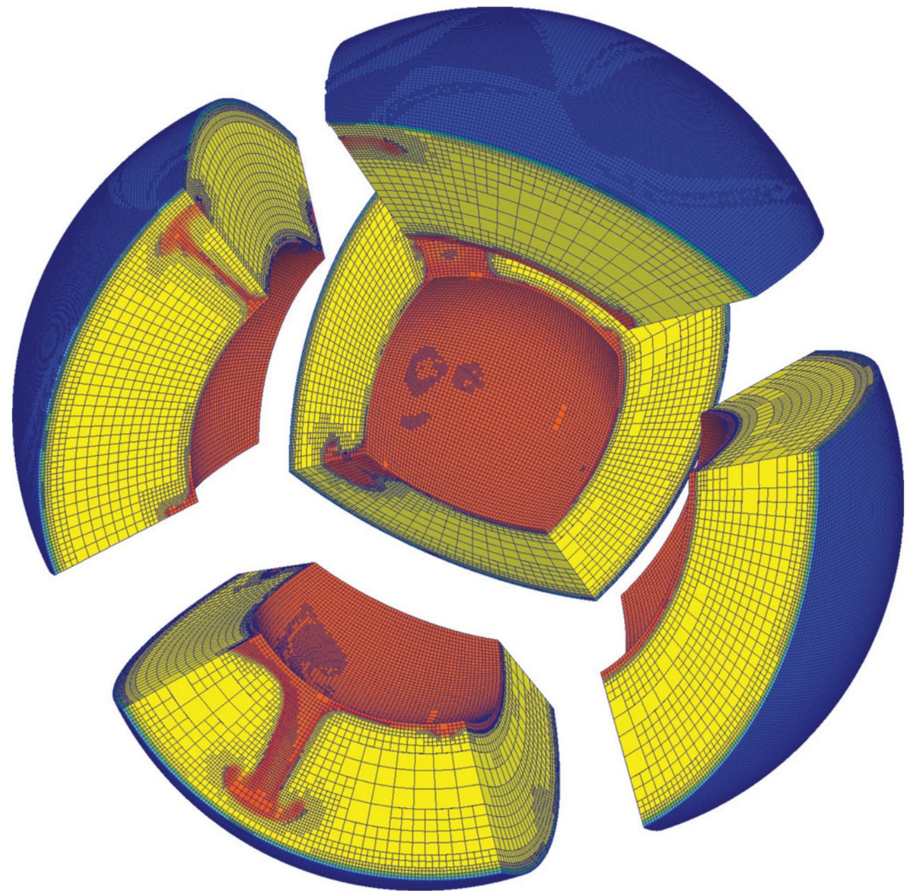

(1) Introduction: Tomography approach

Imaging multi-scale structure and dynamics

- Global mantle convection embraces multiple, coupled scales
- Convection models optimally account for them *(see, e.g. Burstedde et al. 2013)*
- Tomography models also should reflect multiple scales

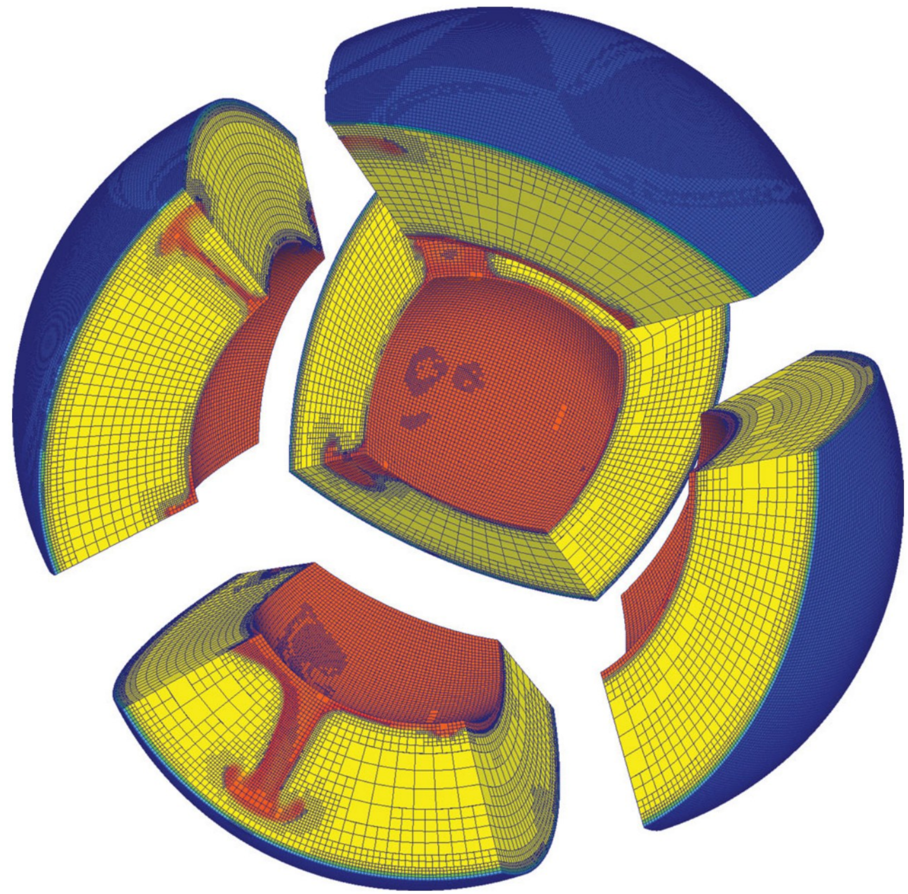

(1) Introduction: Tomography approach

Geodynamically relevant parameters

Anisotropy, e.g. $\xi = \left(\frac{v_{SH}}{v_{SV}}\right)^2$

- Provides a more direct link to mantle kinematics
- Common to assume azimuthal anisotropy or radial anisotropy

Composition, e.g. $R = \frac{d \ln v_P}{d \ln v_S}$

- Provides a more direct link to mantle composition
- Can be inferred through ratios of shear and compressional wave-speeds

(1) Introduction: Tomography approach

Summary of the inverse problem

1. Symbolic representation

$$\begin{pmatrix} \mathbf{C}_d^{-1/2}\mathbf{G} \\ \beta\mathbf{D} \\ \alpha\mathbf{I} \end{pmatrix} \cdot (\delta\mathbf{m}) = \begin{pmatrix} \mathbf{C}_d^{-1/2}\delta\mathbf{d} \\ 0 \\ 0 \end{pmatrix}$$

2. Regularization

$$\mathbf{D} = \begin{pmatrix} \dots & 0 & 0 & 0 \\ -1 & 1 & 0 & 0 \\ 0 & -1 & 1 & 0 \\ 0 & 0 & -1 & 1 \\ 0 & 0 & 0 & \dots \end{pmatrix}$$

3. Normal equations

$$\delta\mathbf{m} = [\mathbf{G}^T\mathbf{C}_d^{-1}\mathbf{G} + \mathbf{C}_m^{-1}]\mathbf{G}^T\mathbf{C}_d^{-1}\delta\mathbf{d}$$

4. Solver

Parallel solver PETSCINV available for download @ https://github.com/auerl/petscinv

(3) Hypothesis test: flat layer

Grid search over layer depth z_0
and the anisotropy strength ξ_{max}

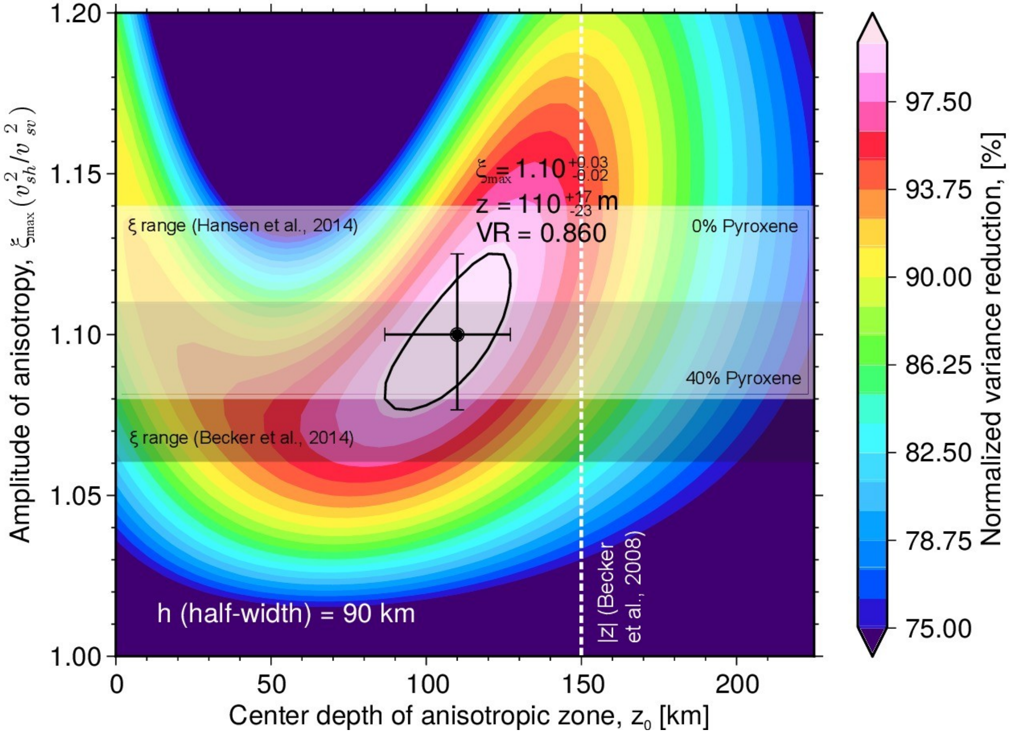

<u>Again:</u> LPO anisotropy too deep

Misfit (VR) for Pacific dataset:

$$VR = 1 - \frac{|\mathbf{G} \cdot \mathbf{m} - \mathbf{d_{obs}}|}{|\mathbf{d}_{obs}|}$$

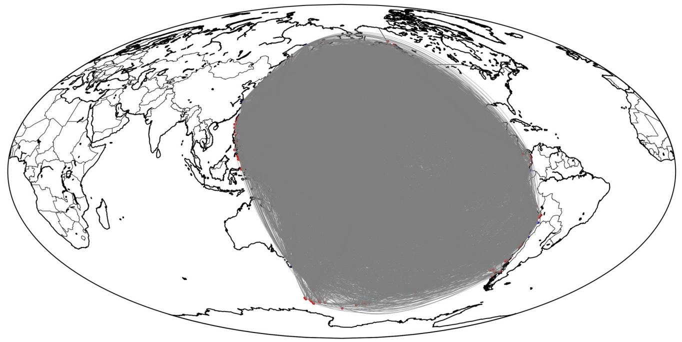

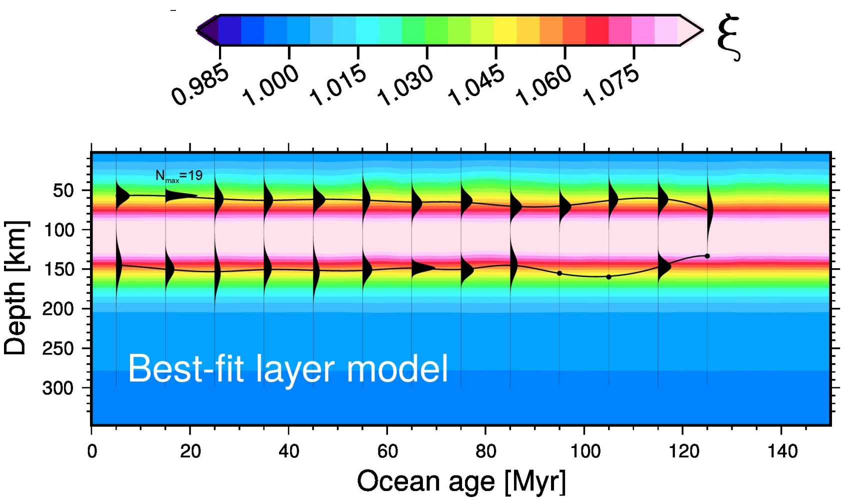

(3) Hypothesis test: $\sqrt{\tau}$ case

Model:

$$z_1 = a + c\sqrt{\kappa\hat{\tau}(\mathbf{x}, f)} \qquad \hat{\tau}(\mathbf{x}, f) = \begin{cases} \tau(\mathbf{x}) & \text{for } \tau(\mathbf{x}) < f \\ f & \text{for } \tau(\mathbf{x}) \geq f \end{cases}$$

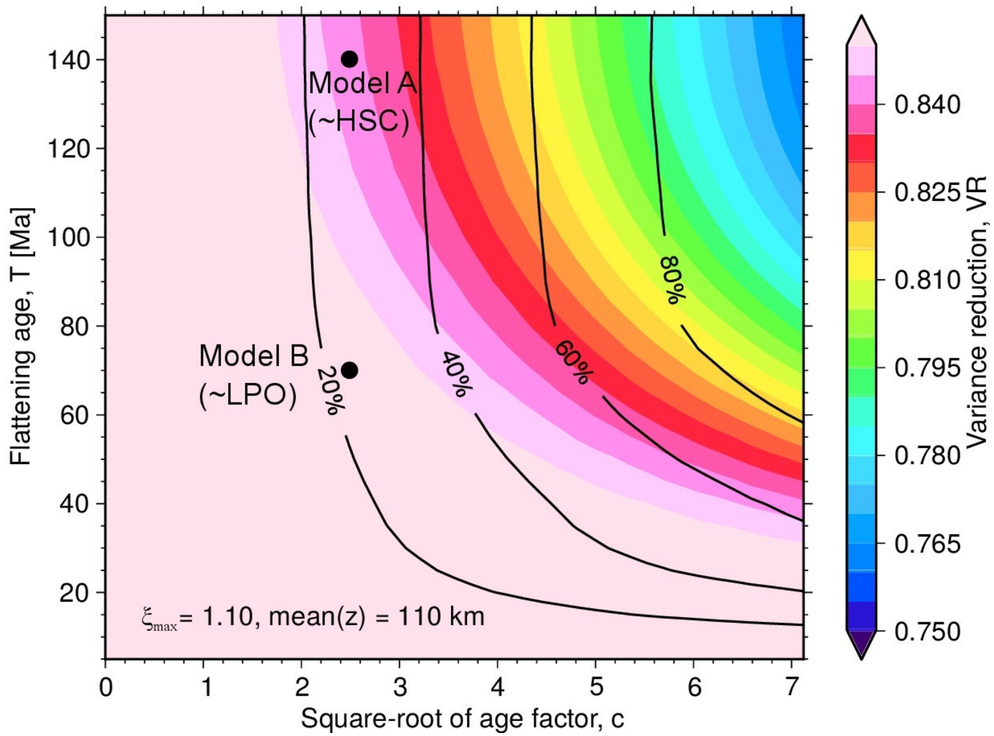

Grid search over age-slope, c, and flattening age, T

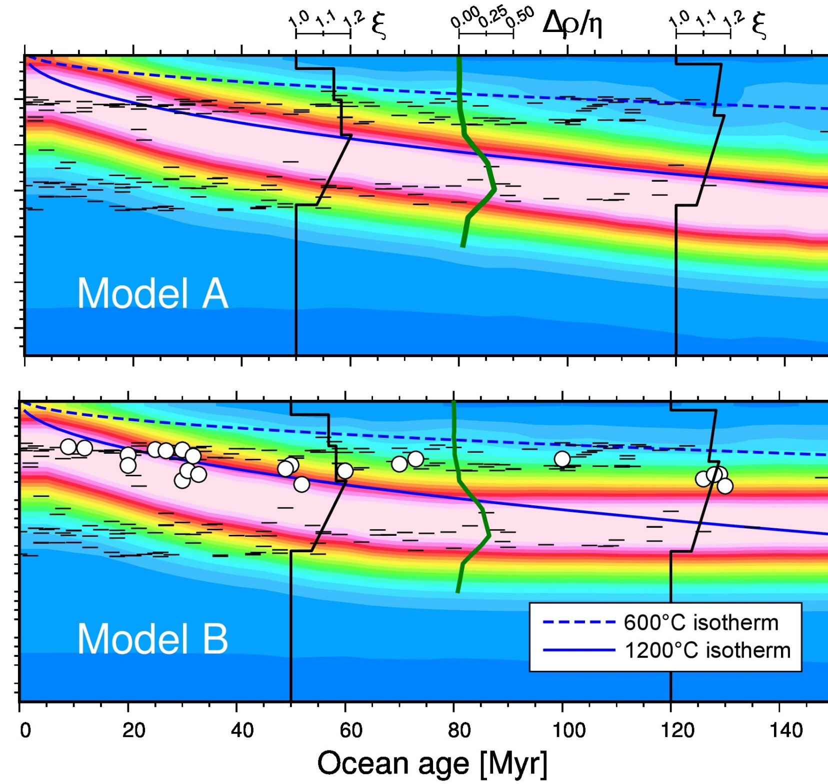

Geodynamic LPO model borderline compatible with data!

(3) Hypothesis test: $\sqrt{\tau}$ case

Model:

$$z_1 = a + c\sqrt{\kappa\hat{\tau}(\mathbf{x}, f)} \qquad \hat{\tau}(\mathbf{x}, f) = \begin{cases} \tau(\mathbf{x}) & \text{for } \tau(\mathbf{x}) < f \\ f & \text{for } \tau(\mathbf{x}) \geq f \end{cases}$$

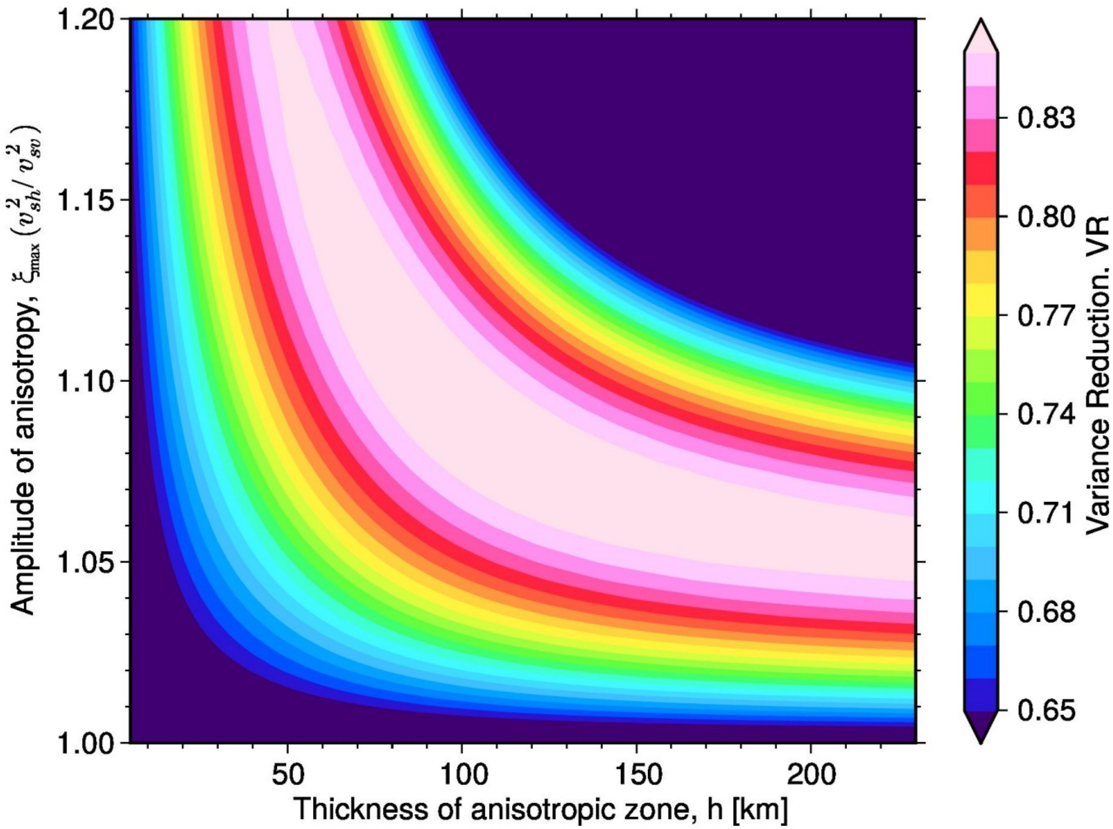

(3) Hypothesis test: $\sqrt{\tau}$ case

Model:

$$z_1 = a + c\sqrt{\kappa \hat{\tau}(\mathbf{x}, f)} \qquad \hat{\tau}(\mathbf{x}, f) = \begin{cases} \tau(\mathbf{x}) & \text{for } \tau(\mathbf{x}) < f \\ f & \text{for } \tau(\mathbf{x}) \geq f \end{cases}$$

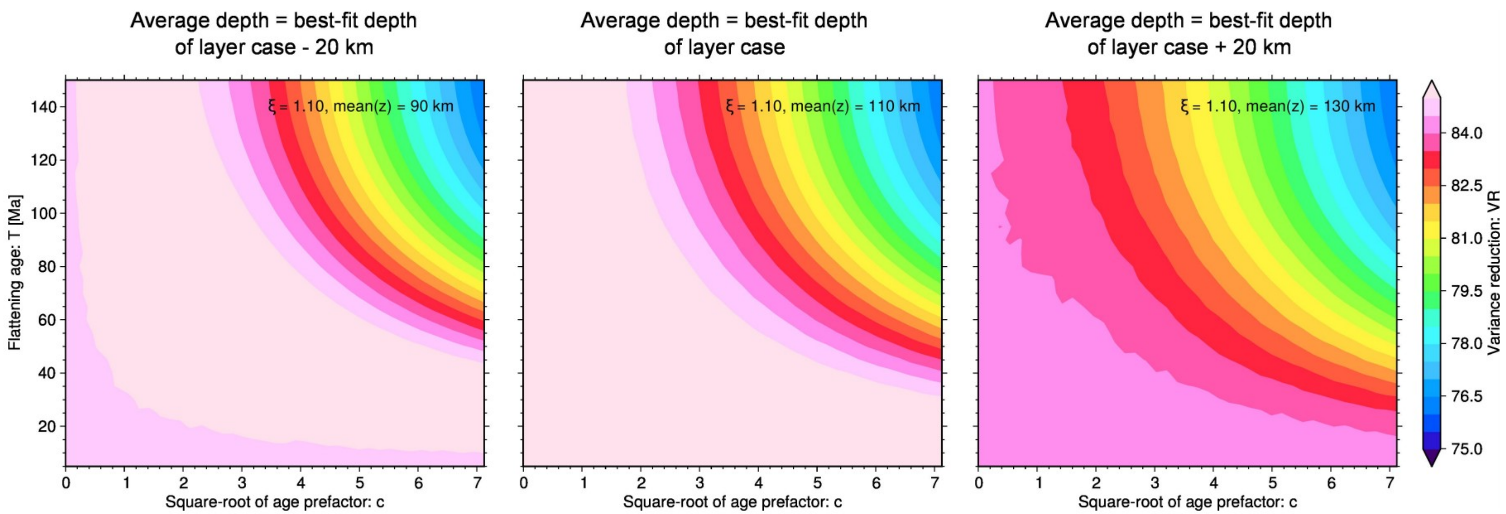

Figure 3.13.: Additional age-dependent hypothesis test (Pacific region), where the parameter z_0, controlling the average depth of the zone, was chosen to be 20 km shallower (leftmost panel) or 20 km deeper (rightmost panel) than the best-fit depth of the layer case (middle panel). The latter case shows the highest variance reductions and the general shape of the misfit contours remains the same.

(3) Hypothesis test: flat layer

Application to different oceanic regions

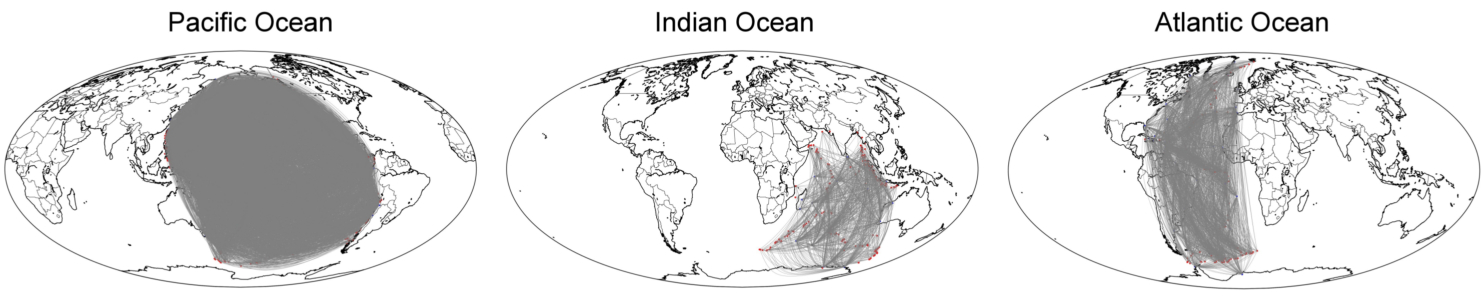

Model case	Pacific	Indian	Atlantic	Global
depth z_0 [km]	110	85	80	105
radial anisotropy, ξ_{max}	1.1	1.09	1.07	1.09
variance reduction, VR	0.860	0.733	0.781	0.854

(1) Introduction: Earth's 3D structure

Visualization in the spherical-harmonic domain

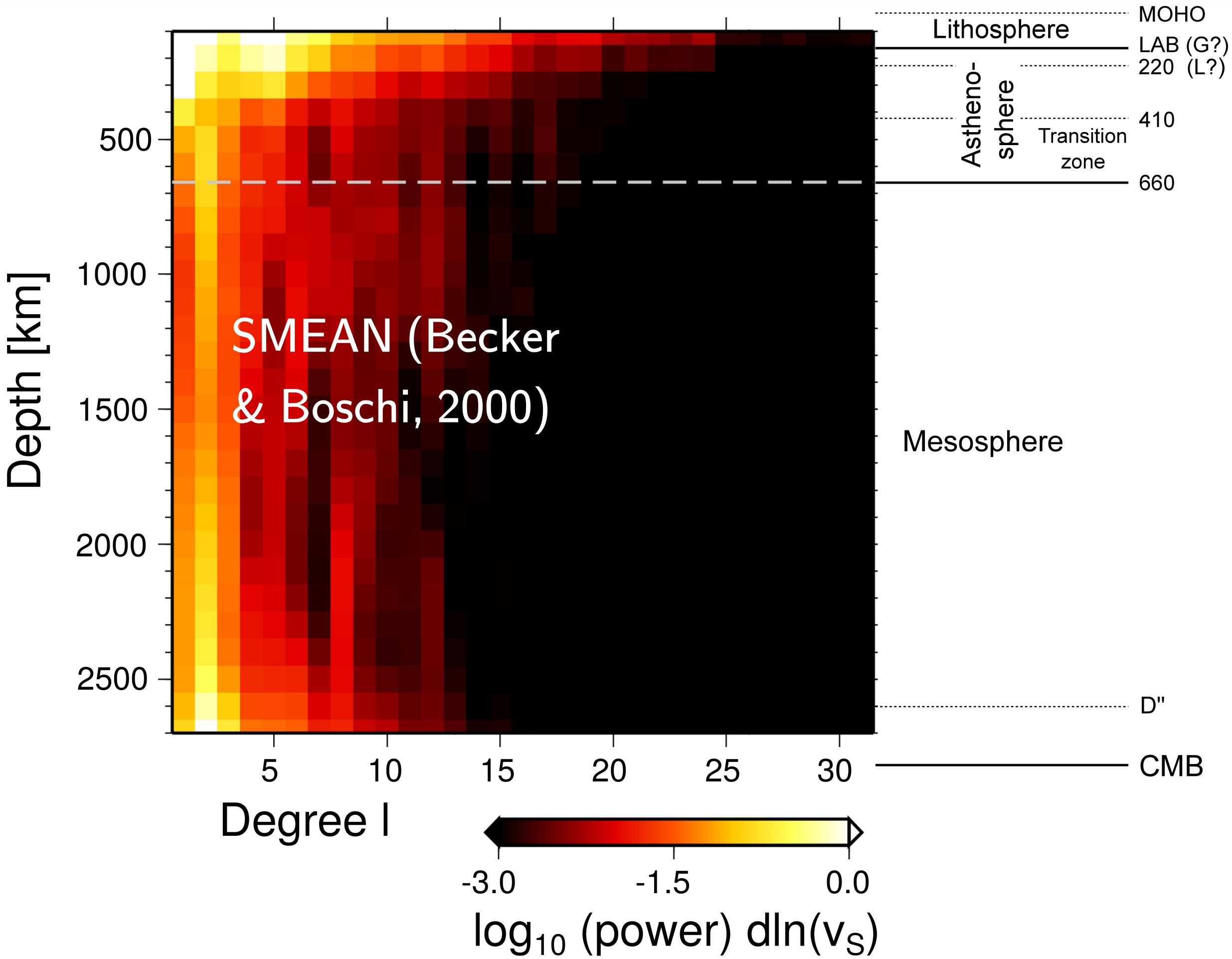

(1) Introduction: Earth's 3D structure

Visualization in the spherical-harmonic domain

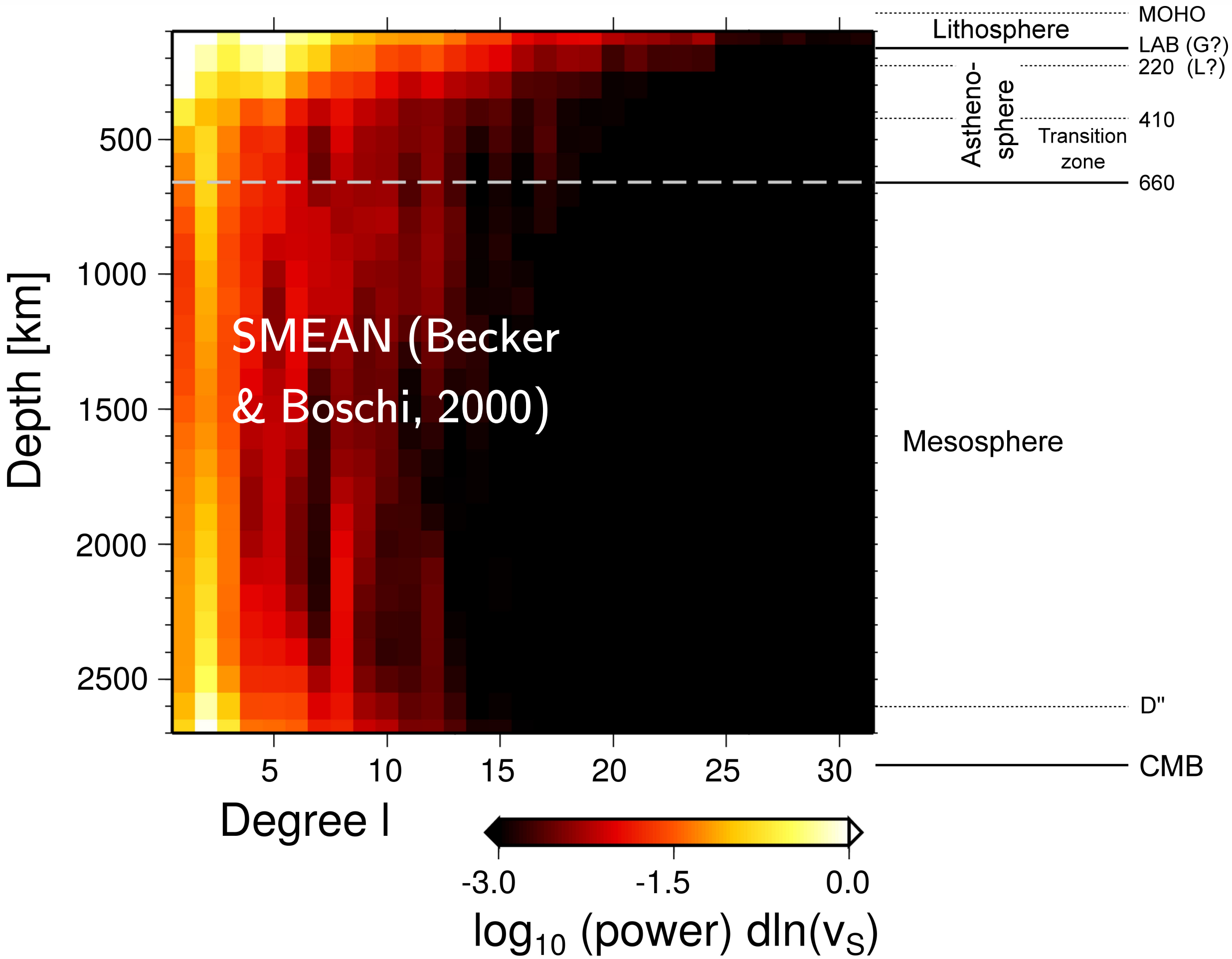

- Strong degree 5 in the upper mantle

(1) Introduction: Earth's 3D structure

Visualization in the spherical-harmonic domain

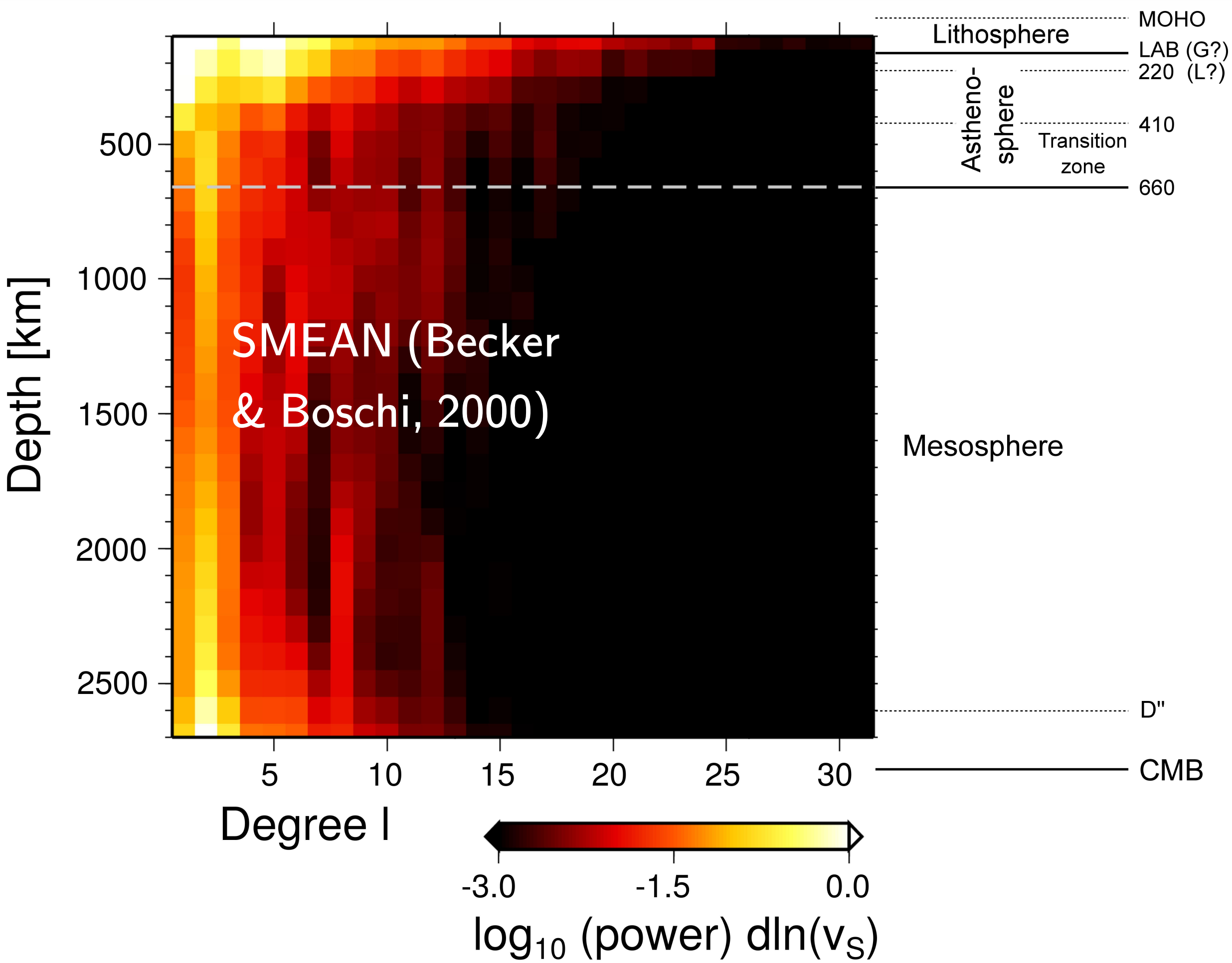

- Strong degree 5 in the upper mantle
- Strong degree 2 in the lower mantle

(1) Introduction: Earth's 3D structure

Visualization in the spherical-harmonic domain

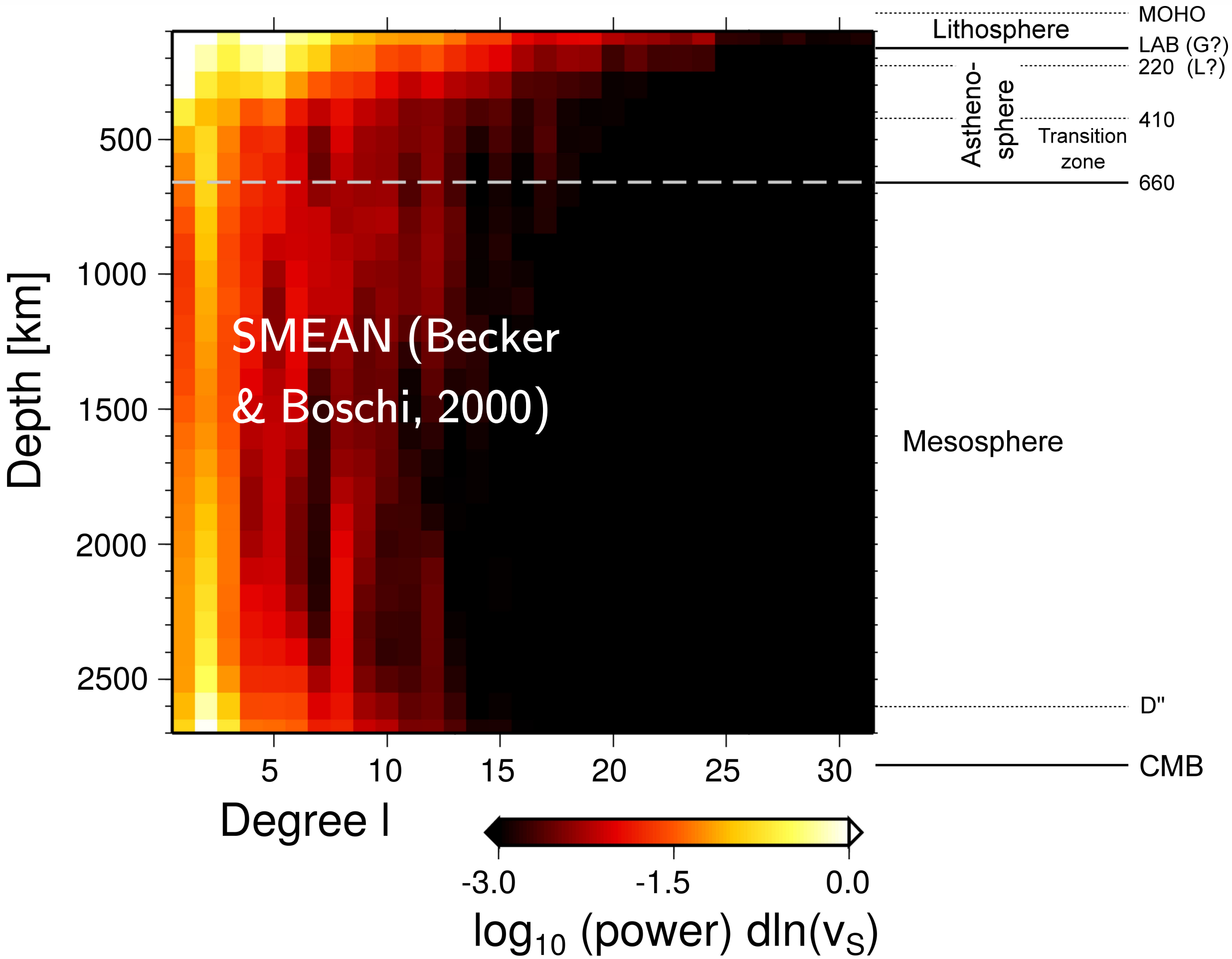

- Strong degree 5 in the upper mantle
- Strong degree 2 in the lower mantle
- Large model power near thermal boundary layers